8-2013

Tuning Cell Fate on Self-assembled Structures

Xiaohui Wu
xwu9@utk.edu

To the Graduate Council:

I am submitting herewith a dissertation written by Xiaohui Wu entitled "Tuning Cell Fate on Self-assembled Structures." I have examined the final electronic copy of this dissertation for form and content and recommend that it be accepted in partial fulfillment of the requirements for the degree of Doctor of Philosophy, with a major in Materials Science and Engineering.

Shanfeng Wang, Major Professor

We have read this dissertation and recommend its acceptance:

Roberto S. Benson, Andy Sarles, Peter K. Liaw, Shanfeng Wang

Accepted for the Council:
Carolyn R. Hodges

Vice Provost and Dean of the Graduate School

(Original signatures are on file with official student records.)

Tuning Cell Fate on Self-assembled Structures

A Dissertation Presented for the

Doctor of Philosophy

Degree

The University of Tennessee, Knoxville

Xiaohui Wu

August 2013

ACKNOWLEDGEMENTS

I would never have been able to complete my dissertation without the careful guidance of my committee members, kind help from my friends, and support from my family members.

First of all, I would like to express my gratitude to my advisor, Dr. Shanfeng Wang. You have not only given broad knowledge about polymer engineering in couses including Lab Methods and Polymer Engineering II, but also spent considerable time on guiding me in doing research, from designing tentative projects to writing manuscripts.

I would like to thank my committee members, Dr. Benson, Dr. Sarles, and Dr. Liaw for serving on my proposal and dissertation defenses and reviewing my dissertation carefully. I also learned much from Dr. Benson in his courses including Polymer Chemistry and Polymer Solutions, which helped a lot in conducting my research.

I would like to express my frank gratitude to my teammates: Dr. Xifeng Liu, Dr. Jinbo Dou, Dr. Kan Wang, and Dr. Lei Cai for their assistance, collaboration, and discussion regarding reseach projects.

I would like to thank my friends: Dr. Lijuan Zheng, Sheng Hu, Ling Li, Chao Zhu, Weidong Li, Bilin Chen, Ziqian Sun, Guoqin Xu, Yang Tong, Lili Zhang, and Shijia Yi. They have always given me support in life and research.

Finally, I would like to thank my parents and siblings. They have been supporting me and encouraging me with their best wishes.

ABSTRACT

This dissertation presents novel biodegradable copolymers with dendritic architecture, classic polymers, and inorganic materials with controlled surface topography, stiffness, and surface energy for investigating cell-material interactions and targeting tissue engineering applications. Chapter I reviews the recent progress in bone and nerve regeneration, the key factors of materials influencing cell-material interaction, and self-assembled polymer structures. Chapter II presents a divergent method to synthesize biodegrable com-dendritic tri-block copolymers consisting of poly(ethylene glycol) and poly(L-lactide) or poly(ε[epsilon]-caprolactone) and the MC3T3-E1 cell response to their spherulites. Chapter III presents the fabrication of deformable poly(ε-caprolactone) honeycomb films prepared via a surfactant-free breath figure method in a water-miscible solvent and how the tunable topography regulates MC3T3-E1 cell functions. Chapter IV investigates the fabrication of photo-cured poly(ε-caprolactone) triacrylate films with tunable pore size via breath figure method and how the pore size regulates MC3T3-E1 cell behavior. Chapter V invented a facile method to fabricate honeycomb films with submicron pores using monodisperse silica nanoparticle as template and studied the MC3T3-E1 cell functions on those honeycomb films. Chapter VI described a novel method to fabricate microgrooves with honeycomb patterns and investigated the MC3T3-E1 cell functions on this special topography. Chapter VII introduces a facile method to obtain controllable surface energy on poly(ε-caprolactone) substrates via controlling the composition of edge-on and flat-on lamellae and how MC3T3-E1 cells behave on those substrates with different surface energy. Chapter VIII

synthesizes biomimetic calcium carbonate concentric microgrooves with tunable width via self-assembly and studies the MC3T3-E1 cell response to those microgrooves. Chapter IX describes one method to fabricate controllable topographical features and mechanical properties on poly(ε-caprolactone) substrates using uniaxial and biaxial stretching and how those substrates regulate MC3T3-E1 cell functions. Chapter X studies rat pheochromocytoma (PC12) response to the banded spherulites of poly(ε-caprolactone) and polyhydroxybutyrate. Chapter XI presents the preparation of honeycomb-patterned copolymer films with tunable pore size and how the pore size regulates NPC cell attachment, proliferation, and differentiation.

TABLE OF CONTENTS

LIST OF TABLES

LIST OF FIGURES

LIST OF SCHEMES

CHAPTER I
INTRODUCTION

1.1Bone Regeneration

Bone, a complex tissue, consists of a mineral composition of hydroxyapatite and amorphous calcium phosphate crystals, which deposit on an organic matrix. Bone performs vital functions in maintaining body system, including protection of important organs, providing substrata of muscle attachment for locomotion, retaining reserve stores of calcium and some other inorganic ions, and regeneration of blood cells for oxygenation and immunoprotection of tissues [1-3]. Constantly remodeling endows bone a dynamic tissue, which requires cooperation among osteoblasts, osteocytes, and osteclasts to maintain homeostasis of bone tissue. Bone resorption from osteoclasts and their precursor always accompanies body metabolic process, while bone remodeling as one integral part of calcium homestatic system can produce new bone matrix and subsequent mineralization through the differentiation of osteoblasts and their precursor [4-6]. In the remodeling process, osteoblasts are trapped in calcified matrix, change phenotype and develop into osteocytes, which gradually reduce their organelles and production of matrix proteins, but still communicate with bone-lining cells. Osteoblasts adhere to and communicate with each other mainly through adherens junctions, which require calcium-dependent cell-cell adhesion via cadherins [5,7]. Therefore, calcium plays an important role in the elaboration of a full osteoblastic phenotype. Calcium involved ceramic implants, such as Calcium carbonate, hydroxyapatite, and calcium phosphate, were developed for bone repair in the early times [8]. Metallic and polymeric

biomaterials were also invent and are being applied as implants. However, long-term observation of these materials indicated some defects, such as mismatch of mechanical properties with native bone causing stress shielding and bone resorption and poor interaction with the tissue environment [2]. Facile and biomimetic synthetic approaches are emphasized for developing composite biomaterials with improved mechanical properties and great biocompatibility as well as bioactivity which enhance cell-material interaction and communication.

1.2 Nerve Regeneration

The nervous system consists of central nervous system (CNS) and peripheral nervous system (PNS) [9]. The CNS including spinal cord, brain, optic, and olfactory and auditory systems is crucial in conducting and interpreting signals and stimulating the PNS. The PNS includes spinal nerves arising from spinal cord, cranial nerves arising from brain, and sensory nerve cell bodies [9].

1.2.1 Peripheral Nerve Regeneration

Typical clinical treatment for nerve repair is either use of an autologous nerve graft or direct reconnection of damaged nerve ends. Reconnecting the nerve ends with small gaps can be an effective approach. However, it is not perfect for longer nerve gaps in that the extra tension on the nerve cable play a role in prohibiting nerve regeneration [9,10]. In case of longer nerve gaps, the autologous nerve graft shows advantage compared with reconnection of nerve ends. However, this cause loss of function at the donor site and the amount is limited [9].

1.2.2 Central Nerve Regeneration

Compared with peripheral nerve regeneration, the clinical treatment for central nerve regeneration becomes less promising. CNS axons cannot be produced in native environment. The worse point is that several glycoproteins in CNS are inhibitory for nerve regeneration [11-13]. Macrophages permeate the injury site more slowly than that in PNS, which delays the removal of inhibitory myelin [14]. In addition, astrocytes in CNS generate glial scars inhibiting regeneration [15].

1.2.3 Materials for Nerve Regeneration

To date, the research in term of nerve regeneration is focused on inventing advanced scaffolds which guide regeneration of nerves across lesions to replace autologous nerve graft. These materials mainly include non-autologous/acellular grafts, natural-based materials, and synthetic materials [9].

Non-autologous tissue and acellular grafts such as allogenic tissues from cadavers and xenogeneic tissues from animals can substitute autologous tissue. However, these tissues have one vital disadvantage that they cause risk of disease transmission. For application in nerve regeneration, they must be processed to remove immunogenic components or used together with immunosuppressants. Many methods such as thermal techniques, radiation, and chemical process have been employed to remove or destroy the immunogenic cells and preserve the ECM components [16-19].

The term of natural materials is used to describe one category of nerve regeneration materials which consist of natural molecules and materials. For example, widely used natural molecules are ECM proteins, such as laminin, collagen, and fibronectin as they

are important in axonal guidance [20,21]. Silicone tubes which were filled with ECM proteins were demonstrated to improve the nerve repair of rat sciatic nerve gap with 10 mm in length compared with control groups without ECM proteins [22]. Collagen filaments improved the axon regeneration and guidance across nerve gap with 20-30 mm in length [23,24]. The neurite extension was guided instead of randomly growth on oriented fibers of collagen within gels. Other natural molecules used for nerve regeneration mainly include hyaluronic acid, fibrin gels, fibrinogen, alginate, agarose, and chitosan. Current challenge of natural-based materials is to modify them for engineering applications [25-32].

Synthetic materials have drawn tremendous attraction due to the controllable chemical and physical properties for specific application. The promising synthetic materials generally possess some crucial characteristics, such as formation of conduit with tunable dimensions, feasibility of sterilization, resistance to tear, and feasibility of suturing. Materials without degradability may have high risk for infection and provoke a chronic inflammatory response [9]. Therefore, a promising material for nerve regeneration should be biodegradable. A variety of synthetic materials have been developed for nerve regeneration. Poly(glycolic acid) (PGA), poly(lactic-*co*-glycolic acid) (PLGA), and poly(lactic acid) (PLA) were approved by the FDA to be used due to their processibility, biodegradation ability, and availability [33,34]. Poly(ε-caprolactone) (PCL) has also been demonstrated to be promising materials for nerve regeneration applications [35-37]. In addition to these polyesters, biodegradable polyurethane, hydrogels, poly(organo phosphazene), and poly(3-hydroxybutyrate) have also been demonstrated to guide nerve regeneration [36, 38-40]. Materials with electrical charges showed potential application

in nerve regeneration, because the charges improved the cellular differentiation and neurite extension. For example, neurite growth was greatly enhanced on pizoelectric materials, such as poly(vinylidene fluoride), electrically conducting polymers, such as polypyrrole, and polymers with natural charges, such as poly(L-lysine) (PLL) [41-43].

1.3 Cell-Material Interactions

When cells are exposed to cell culture medium, they first generate extracellular matrix (ECM) proteins and the ECM proteins are subsequently distributed on the substrate surface to form interface. The integrin receptors mediating the adhesive interactions can transduce signals into and out of the cell. The fate of anchorage-dependent cells is hence strongly affected by the initial adhesion on substrates. It is demonstrated that the surface chemistry, mechanical properties, Surface energy, and topography can influence cell survival, proliferation, and differentiation through intimate interactions between surface and ECM proteins [44,45].

1.3.1 Surface Energy

The material surface presents chemical bonds of atoms asymmetrically directed toward the interior of the substrate, which attract the surface atoms inward and generate surface tension. After the surface reacts with ambient molecules, the surface energy gradually decreases. Once biomaterials are implanted into biological fluids, the material surface is coated with a protein layer, which plays a crucial role in mediating cell functions, such as cell attachment, and subsequently proliferation and differentiation [46-48]. The role of surface energy in the regulation of cell adhesion is contradictory. The

substrate with surface energy gradient was prepared by ozonolysis to convert the CH_3 group into OH and COOH layers and further coated the surface gradient with a fibronectin layer [48]. Because the surface with lower surface energy had higher protein adsorption, conformational changes in the proteins, and irreversible protein adsorption, the gradient fibronectin layer was formed before cell study. The findings suggested that cells showed the best spreading when water contact angle was around 60° and lower surface energy supported better cell adhesion and proliferation. Quartz with different surface energy was prepared via plasma-discharge-treatment. Cell functions of human fetal obsteoblastic (hFOB) indicated that hydrophilic surfaces caused homogeneous spatial growth, as well as mineral deposition [49]. Compared with hydrophobic surfaces, the mineralization was enhanced on hydrophilic surfaces. The effect of surface energy on osteoblasts was also investigated on titanium-zirconium alloy. The results indicated that TiZr with higher surface energy (37.74 mJ m^{-2}) had better cell viability, adhesion, and proliferation than other samples with lower surface energy [50].

1.3.2 Topography

Base membranes, which exist throughout vertebrate body and provide substrata for overlying cellular structures, are composed of extracellular matrix (ECM) proteins which can be exemplified as fibrous collagen, laminin, and fibronectin [51,52]. Pores from nano- to micro-scale, ridges, and other nano-scale features are the main topography of basement membranes. Basement membranes are believed to play a great role in determining cell behaviors. First, ECM proteins of base membranes could provide integrin receptors for cell anchorage and regulate subsequent events [53,54]. Secondly,

mechanical and tensile properties of basement membranes could influence the strength of integrin-cytoskeleton links and determine cell response [55]. Thirdly, complex topography of basement membranes could dramatically affect cell functions [56,57]. To mimic these complex features of basement membranes synthetic substrata with topographic features, such as grooves, pits, pores, wells and nodes, spheres, and ridges, have been developed [58-60]. The topography has been demonstrated to influence cell functions through "contact guidance" and the influence is cell-type dependent [61-63]. Fibroblasts showed higher viability on honeycomb-patterned PCL films prepared using silica microspheres compared with flat PCL films [64]. The adhesion and growth of epidermal keratinocyte and dermal fibroblast cells were also promoted on honeycomb-patterned PCL films (pore size, 3~20 μm) and the pores with size of 3~5 μm showed the best promotion in adhesion and survival [65]. On the other hand, the neural stem cell differentiation on honeycomb-patterned PCL films (pore size, 3~15 μm) was suppressed and the pore edges guided the neurite extension [66]. The chondrocyte cell proliferation on honeycomb-patterned PLA films was inhibited [67]. The major response of cells to microgrooves is cell alignment along groove direction, whereas the cell attachment and proliferation are not significantly influenced [68,69]. When the grooves are deeper and narrower, cells can bridge from ridge to ridge and more effectively react to the microgroove features. Cells may not sense the surface topography via focal adhesions when the groove spacing is larger than 5 μm while the depth is smaller than 1 μm [70].

1.4 Self-Assembled Polymer Structures

1.4.1 Honeycomb Patterns

The formation of honeycomb-patterned polymer films consists of three major steps as shown in Scheme 1.1 [71]. First, the temperature on the surface of polymer solution decreased when the volatile solvent evaporated, which consequently triggered nucleation and growth of water droplets. Secondly, water droplets with similar diameters were arranged into a hexagonal array. The last step was polymer precipitation around the water droplets followed by complete evaporation of organic solvent and water.

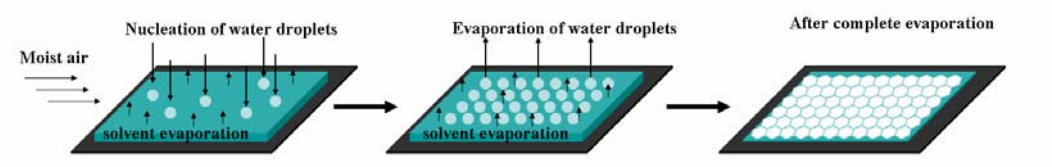

Scheme 1.1 The mechanism of breath-figure method

In the breath-figure method, the pore dimension can be controlled through changing the fabrication parameters such as airflow rate, humidity, concentration, cast volume of polymer solution, and solvent type [71,72-74]. In general, higher airflow rate accelerates the evaporation of solvent and the temperature in the solution is more efficiently decreased, which causes formation of more water droplets available on the solution surface. When the airflow rate is higher, the coalescence of water droplets becomes more difficult. Thus, higher airflow rate generates smaller pores. Higher humidity normally provides more moisture to form more water droplets on the solution surface and the

coalescence tends to occur more easily, which causes formation of bigger pores. The concentration of solution can also influence the pore dimension. Higher concentration provides slower evaporation of solvent and causes formation of fewer pores. When the concentration is high enough, the polymer solution can lose the capability to form porous structure. Bigger cast volume of polymer solution can induce more evaporation of solvent and subsequently causes formation of more water droplets, which induces larger pores through coalescence. When the solvent is denser than water, the water droplets condensed from moisture air tend to form monolayer pores on the solution surface without dropping into the solution. On the other hand, when the solvent is lighter than water, water droplets can drop into the solution and form multilayer pores.

1.4.2 Banded Spherulites

Polymers normally form spherical crystals called spherulites when they crystallize from melts without disturbance at isothermal temperature [75]. A dark Maltese cross of the spherulite can be observed using polarized optical microscopy (POM). The spherulite diameter can range from micro-scale to millimeter-scale, depending on the crystallization parameters, such as crystallization temperature, and the nucleating agent. Spherulites are comprised of layer-shape lamellae. In the center of spherulites, the lamellae are stacked in parallel. From the center to the edge, the lamellae display apart and branched distribution owing to the repulsion of amorphous component between lamellae. The spherulitic growth rate defined as the diameter growth length per unit time was demonstrated to be constant even though the lamellar growth rate for some lamellae initially can grow forward faster than the average spherulitic growth rate. Due to the

regular twisting of the radial crystallite ribbons, some spherulites show alternating dark and bright concentric rings, which is called banded spherulites. Typical semi-crystalline polymers, such as PCL, poly(L-lactide) (PLLA), and poly(3-hydroxybutyrate) (PHB), can form banded spherulites when the crystallization parameters are ideal and the ring dimension, such as spacing and depth, can be varied via tuning crystallization temperature [76-80].

1.4.3 Flat-on and Edge-on Lamellae

Polymer chains can form ordered and regular structure through crystallization and random chain coils transform into perfectly ordered orientation during polymer crystallization. The hierarchy of crystals determines the properties of these polymers. It has been widely accepted that lamellae, the basic unit of polymer spherulites and crystalline domains, are composed of folded polymer chains governed by kinetics. Lamellae have two basal surfaces constituted by chain folds and several lateral surfaces. Normally, anisotropic lamellae are randomly distributed in the bulk. Crystallizing from melts, polymers normally form spherulites from micro- to milli-scale. In case of lamellar twisting along the radial direction in spherulites, banding texture can be observed. Experimentally, there are two major orientation types of lamellae [81]. When the lamellae are perpendicular or parallel to the substrate, they are called edge-on or plat-on lamellae, respectively. When the dimension is confined at the nano-scale which is comparable to lamellae thickness, flat-on lamellae are preferred. As the polymer thickness increases, the edge-on type is more dominant.

1.5 Conclusions

In summary, synthetic polymer systems have been developed for both nerve and bone regeneration. To promote cell functions, polymers with controllable mechanical properties, surface energy, and topography have been fabricated. These synthetic biomaterials show potential to be used for tissue engineering. However, the development of more advanced materials with more powerful functions is still our expectation. Polymers can form self-assembled structures including honeycomb patterns, banded spherulites, and flat-on and edge-on lamellae. To better understand the effect of these special topographies on cell functions, more studies are to be performed, which is also the focus of this thesis.

References

[1] Sikavitsas, V. I.; Temenoff, J. S.; Mikos, A. G. *Biomaterials* ***2001***, 22, 2581.

[2] Song, J.; Saiz, E.; Bertozzi, C. R. *J. Am. Chem. Soc.* **2003**, 125, 1236.

[3] Weiner, S.; Wagner, H. D. *Annu. Mater. Sci.* **1998**, 28, 271.

[4] Yaszemski, M. J.; Payne, R. G.; Hayes, W. C.; Langer, R.; Mikos, A. G. *Biomaterials* **1996**, 17, 175.

[5] Sommerfeldt, D. W.; Rubin, C. T. *Eur. Spine. J.* **2001**, 10, S86.

[6] Teitelbaum, S. L. *Science* **2000**, 289, 1504.

[7] Stains, J. P.; Civitelli, R. *Biochemical and Biophysical Research Communications* **2005**, 328, 721.

[8] Hing, K. A. *Phil. Trans. R. Soc. Lond. A* **2004**, 362, 2821.

[9] Schmidt, C. E.; Leach, J. B. *Annu. Rev. Biomed. Eng.* **2003**, 5, 293.

[10] Millesi, H.; Ganglberger, J.; Berger, A. *Chir. Plast.* **1967**, 3, 47.

[11] Mukhopadhyay, G.; Doherty, P.; Walsh, F. S.; Crocker, P. R.; Filbin, M. T. *Neuron* **1994**, 13, 757.

[12] Chen, M. S.; Huber, A. B.; van der Haar, M. E.; Frank, M.; Schnell, L. *Nature* **2000**, 403, 434.

[13] Morgenstern, D. A.; Asher, R. A.; Fawcett, J. W. *Prog. Brain Res.* **2002**, 137, 313.

[14] Avellino, A. M.; Hart, D.; Dailey, A. T.; Mac-Kinnon, M.; Ellegala, D.; Kliot, M. *Exp. Neurol.* **1995**, 136, 183.

[15] McKeon, R. J.; Schreiber, R. C.; Rudge, J. S.; Silver, J. *J. Neurosci.* **1991**, 11, 3398.

[16] Frerichs, O.; Fansa, H.; Schicht, C.; Wolf, G.; Schnerder, W.; Keihoff, G. *Microsurgery* **2002**, 22, 311.

[17] Ide, C.; Tohyama, K.; Tajima, K.; Endoh, K.; Sano, K.; Tamura, M.; Mizoquchi, A.; Kitada, M.; Morihara, T.; Shirasu, M. *Exp. Neurol.* **1998**, 154, 99.

[18] Sondell, M.; Lundborg, G.; Kanje, M. *Brain Res.* **1998**, 795, 44.

[19] Sondell, M.; Lundborg, G.; Kanje, M. *Brain Res.* **1999**, 846, 219.

[20] Rutishauser, U. *Curr. Opin. Neurobiol.* **1993**, 3, 709.

[21] Grimpe, B.; Silver, J. *Prog. Brain Res.* **2002**, 137, 333.

[22] Chen, Y. S.; Hsieh, C. L.; Tsai, C. C.; Chen, T. H.; Cheng, W. C.; Hu, C. L.; Yao, C. H. *Biomaterials* **2000**, 21, 1541.

[23] Yoshii, S.; Oka, M. *Brain Res.* **2001**, 888, 158.

[24] Yoshii, S.; Oka, M.; Shima, M.; Taniguchi A, Akagi, M. *Brain Res.* **2002**, 949, 202.

[25] Seckel, B. R.; Jones, D.; Hekimian, K. J.; Wang, K. K.; Chakalis, D. P.; Costas, P. D. *J. Neurosci. Res.* **1995**, 40, 318.

[26] Ahmed, Z.; Underwood, S.; Brown, R. A. *Cell Motil. Cytoskelet.* **2000**, 46, 6.

[27] Herbert, C. B.; Nagaswami, C.; Bittner, G. D.; Hubbell, J. A.; Weisel, J. W. *J. Biomed. Mater. Res.* **1998**, 40, 551.

[28] Haipeng, G.; Yinghui, Z.; Jianchun, L.; Yandao, G.; Nanming, Z.; Xiufang, Z. *J. Biomed. Mater. Res.* **2000**, 52, 285.

[29] Mosahebi, A.; Simon, M.; Wiberg, M.; Terenghi, G. *Tissue Eng.* **2001**, 7, 525.

[30] Balgude, A. P.; Yu, X.; Szymanski, A.; Bellamkonda, R. V. *Biomaterials* **2001**, 22, 1077.

[31] Homes, T. C.; de Lacalle, S.; Su, X.; Liu, G.; Rich, A.; Zhang, S. *Proc. Natl. Acad. Sci. USA* **2000**, 97, 6728.

[32] Hashimoto, T.; Suzuki, Y.; Kitada, M.; Kataoka, K.; Wu, S.; Suzuki, K.; Endo, K.; Nishimura, Y.; Ide, C. *Exp. Brain Res.* **2002**, 146, 356.

[33] Molander, H.; Olsson, Y.; Engkvist, O.; Bowald, S.; Eriksson, I. *Muscle Nerve* **1982**, 5, 54.

[34] Nyilas E, Chiu, T. H.; Sidman, R. L.; Henri, E. W.; Brushart, T. M.; Dikkes, P.; Madison, R. *Trans. Am. Soc. Artif. Intern. Organs.* **1983**, 29, 307.

[35] Den Dunnen, W. F.; Meek, M. F.; Grijpma, D. W.; Robinson, P. H.; Schakenraad, J. M. *J. Biomed. Mater. Res.* **2000**, 51, 575.

[36] Nicoli Aldini, N.; Fini, M.; Rocca, M.; Giavaresi, G.; Giardino, R. *Int. Orthop.* **2000**, 24, 121.

[37] Valero-Cabre, A.; Tsironis, K.; Skouras, E.; Perego, G.; Navarro, X.; Neiss, W. F. *J. Neurosci. Res.* **2001**, 63, 214.

[38] Dalton, P. D.; Flynn, L.; Shoichet, M. S. *Biomaterials* **2002**, 23, 3843.

[39] Soldani, G.; Varelli, G.; Minnocci, A.; Dario, P. *Biomaterials* **1998**, 19, 1919.

[40] Young, R. C.; Wiberg, M.; Terenghi, G. *Br. J. Plast. Surg.* **2002**, 55, 235.

[41] Valentini, R. F.; Vargo, T. G.; Gardella, J. A. Jr.; Aebischer, P. *J. Biomater. Sci. Polym. Ed.* **1993**, 5, 13.

[42] Schmidt, C. E.; Shastri, V. R.; Vacanti, J. P.; Langer, R. *Proc. Natl. Acad. Sci. USA* **1997**, 94, 8948.

[43] Cai, L.; Lu, J.; Sheen, V.; Wang, S. *Biomacromolecules* **2012**, 13, 1663.

[44] Cai, L.; Wang, S. *Biomaterials* **2010**, *31*, 7423.

[45] Anselme, K.; Bigerelle, M. *Int. Mater. Rev.* **2011**, *56*, 243.

[46] Dos Santos, E. A.; Farina, M.; Soares, G. A.; Anselme, K. *J Mater Sci: Mater Med* **2008**, 19, 2307.

[47] Hao, L.; Lawrence, *J. Colloid. Surface B* **2004**, 34, 87.

[48] Kennedy, S. B.; Washburn, N. R.; Simon, C. G.; Amis, E. J. *Biomaterials* **2006**, 27, 3817.

[49] Lim, J. Y.; Shaughnessy, M. C.; Zhou, Z.; Noh, H.; Vogler, E. A.; Donahue, H. J. Biomaterials 2008, 29, 1776.

[50] Sista, S.; Wen, C.; Hodgson, P. D.; Pande, G. *J. Biomed. Mater. Res. A* 2011, 97A, 27.

[51] Coopman, P. J.; Bracke, M. E.; Lissitzky, J. C. *J. Cell. Sci.* **1991**, 98, 395.

[52] Flemming, R. G.; Murphy, C. J.; Abrams, G. A.; Goodman, S. L.; Nealey, P. F. *Biomaterials* **1999**, 20, 573.

[53] Ruoslahti, E. *Science* **1997**, 276, 1345.

[54] Clark, E. A.; Brugge, J. S. *Science* **1995**, 268, 233.

[55] Choquet, D.; Felesenfiled, D. P.; Sheetz, M. P. *Cell* **1997**, 88, 39.

[56] Curtis, A. S. G.; Clark, P. *Crit. Rev. Biocompatability* **1990**, 5, 343.

[57] Rosenberg, M. D. *Science* **1963**, 139, 411.

[58] Anselme, K.; Bigerelle, M.; Noel, B.; Iost, A.; Hardouin, P. *J. Biomed. Mater. Res.* **2002**, 60, 529.

[59] Curtis, A.; Wilkinson, C. *Trends Biotechnol.* **2001**, 19, 97.

[60] Wilkinson, C. D. W. *Microelectronic Eng.* **1995**, 27, 61.

[61] Curtis, A. S.; Varde, M. *J. Natl. Cancer. Inst.* **1964**, 33, 15.

[62] Yim, E. K. F.; Reano, R. M.; Pang, S. W.; Yee, A. F.; Chen, C. S.; Leong, K. W. *Biomaterials* **2005**, 26, 5405.

[63] Bettinger, C. J.; Zhang, Z.; Gerecht, S.; Borenstein, J. T.; Langer, R. *Adv. Mater.* **2008**, 20, 99.

[64] Wang, B.; Mao, Z.; Meng, X.; Tong, W.; Gao, C. *Colloid Surf. B-Biointerfaces* **2010**, 76, 38.

[65] Mcmillan, J. R.; Akiyama, M.; Tanaka, M.; Yamamoto, S.; Goto, M.; Abe, R.; Sawamura, D.; Shimomura, M.; Shimizu, H. *Tissue Eng.* **2007**, 13, 789.

[66] Tsuruma, A.; Tanaka, M.; Yamamoto, S.; Shimomura, M. *Colloid Surf. A-Physicochem. Eng. Asp.* **2008**, 313-314, 536.

[67] Fukuhira, Y.; Kaneko, H.; Yamaga, M.; Tanaka, M.; Yamamoto, S.; Shimomura, M. *Colloid Surf. A-Physicochem. Eng. Asp.* **2008**, 313-314, 520.

[68] Wang, J. H. C.; Grood, E. S.; Florer, J.; Wenstrup, R. *J. Biomech.* **2000**, 33, 729.

[69] Kenar, H.; Kose, G. T.; Hasirci, V. *Biomaterials* **2006**, 27, 885.

[70] Wang, K.; Cai, L.; Zhang, L.; Dong, J.; Wang, S. *Adv. Healthcare. Mater.* **2012**, 1, 292.

[71] Bunz, U. H. F. *Adv. Mater.* **2006**, *18*, 973.

[72] Stenzel, M. H.; Barner-Kowollik, C.; Davis, T. P. *J. Polym. Sci. Part A: Polym. Chem.* **2006**, 44, 2363-2375.

[73] Saunders, A. E.; Dickson, J. L.; Shah, P. S.; Lee, M. Y.; Lim, K. T.; Johnston, K. P.; Korgel, B. A. *Phys. Rev.* **2006**, 73, 031608.

[74] Madej, W.; Budkowski, A.; Raczkowska, J.; Rysz, J. *Langmuir* **2008**, 24, 3517-3524.

[75] Jiang, Y.; Luo, Y.; Fan, Z.; Wang, X.; Xu, J.; Guo, B.; Li, L. *Science in China (Series B)* **2003**, *46*, 152.

[76] Wang, K.; Cai, L.; Jesse, S.; Wang, S. *Langmuir* **2012**, 28, 4382.

[77] Nurkhamidah, S.; Woo, E. M. *J. Appl. Polym. Sci.* **2011**, 122, 1976.

[78] Xu, J.; Guo, B. H.; Zhou, J. J.; Li, L.; Wu, J.; Kowalczuk, M. *Polymer* **2005**, 46, 9176.

[79] Wang, Y.; Mano, J. F. *J. Appl. Polym. Sci.* **2007**, 105, 3500.

[80] Hobbs, J. K.; Binger, D. R.; Keller, A.; Barham, P. J. *J. Polym. Sci., Part B: Polym. Phys.* 2000, 38, 1575.

[81] Liu, Y. X.; Chen, E. Q. *Coord Chem Rev*. **2010**, *254*, 1011.

CHAPTER II
BIODEGRADABLE COMB-DENDRITIC TRI-BLOCK COPOLYMERS CONSISTING OF POLY(ETHYLENE GLYCOL) AND POLY(L-LACTIDE) OR POLY(ε-CAPROLACTONE) AND PRE-OSTEOBLASTIC CELLULAR RESPONSE TO THE SPHERULITIC SURFACES

2.1 Introduction

Aliphatic polyesters such as poly(ε-caprolactone) (PCL) and poly(L-lactide) (PLLA) are widely used in tissue-engineering and pharmaceutical applications for their excellent biodegradability and biocompatibility.[1-3] Because PCL and PLLA have poor hydrophilicity, cell affinity is low on them.[4] PLLA can also create local acidity because of the hydrolysis of PLLA chains. Therefore, hydrophilic components have been incorporated into PCL or PLLA. For example, copolymers of PCL or PLLA with PEG have been developed to modulate the physicochemical properties of these aliphatic polyesters because PEG has excellent hydrophilicity, biocompatibility, and non-immunogenicity.[5] These copolymers include linear di- and tri-block copolymers such as PEG-*b*-PCL, PCL-*b*-PEG-*b*-PCL, PEG-*b*-PLLA, and PLLA-*b*-PEG-*b*-PLLA, and also copolymers with branched architectures such as dendrimers,[6,7] graft polymers,[8,9] and star polymers.[10] These amphiphilic polymers can self-assemble into nanometer or micron-scale micelles used for drug delivery.[11-13] Among these branched architectures, dendrimers have attracted much attention because they represent a unique class of macromolecules.[14] The size of nanoparticles based on dendrimers can be adjusted in a

larger range than their linear counterparts to host both hydrophobic and hydrophilic drugs.[15-17]

The demand for dendrimers needs approaches with convenience and efficiency to synthesize such advanced architectures. The typical methods to synthesize dendrimers include convergent growth and divergent growth.[14] In the convergent route, the first step is the synthesis of wedges with desired generations containing a large amount of terminal groups. The second step is the coupling reaction of the wedges with a core to afford the dendritic architecture. In the divergent route, the dendrimer grows radially from a central moiety outward by addition of branched reagent generation by generation. The number of functional end groups increases with the number of generations. Compared with the divergent route, the convergent method has disadvantages such as steric hindrance of the wedges that limits the generation growth.

The synthesis of comb-dendritic tri-block copolymers consisting of PLLA and PEG was reported by the corresponding author of this report and his co-workers using the convergent method and used to regulate HEK-293T cell behavior.[18] HEK-239T cell proliferation was significantly higher on the copolymers with longer PLLA arms because of their porous structures, higher stiffness, and higher protein adsorption.[18] The synthesis and self-assembly of amphiphilic dendrimer consisting of poly(L-lysine) and PLLA dendron-like PCL-*b*-PEG-*b*-PCL tri-block copolymers using the convergent method were also reported.[15,19,20] Recently, acetonide(or acetal)-protected anhydride derivative of 2,2-bis(hydroxymethyl)propionic acid was used to prepared the branched architecture.[14,21-23] Fast and convenient divergent synthesis of PEG dendrimers without PCL or PLLA blocks using this acetonide-protected anhydride was reported.[14]

Here we present a more convenient divergent synthetic route of two series of well-defined comb-dendritic tri-block copolymers, which contained a linear PEG central block and comb-shaped arms of PCL (CoPCL) or PLLA (CoPLLA). The copolymer composition was modulated by controlling the feed ratio of ε-caprolactone or L-lactide to the hydroxyl group in the dendritic PEG to form various lengths of PCL or PLLA arms. After extensive structural characterizations, we studied the effect of the unique chemical structures of comb-dendritic tri-block copolymers on their mechanical properties, crystallization behavior, and hydrophilicity..

Besides observation of the surface morphology of the copolymers using microscopic methods, their crystal structures near the top surface were characterized using Grazing incidence X-ray diffraction (GIXRD). GIXRD studied on polyethylene and isotactic polypropylene thin films showed that the crystallinity, the lattice constants of the orthorhombic unit cell, and the crystallite size varied strongly along the sample thickness and for samples annealed at different temperatures.[24-26] Specifically, the polymer crystallinity was found to be higher in the bulk than on the top surface and the lattice constants and crystallite size were larger for the sample annealed at a higher temperature.[24-26] The GIXRD study on PLLA demonstrated that the crystallinity increased with the annealing time at 70 °C and the crystalline organization in the top 500 nm of the surface was similar to that in the bulk.[27] To date, there are no GIXRD studies on PCL. Here we present the crystallinity, crystallite size, and lattice constants of the copolymers along the thickness from the top surface.

In a previous study, hepatocytes and 3T3 fibroblasts were cultured on PLLA films with different crystallinities and it was found that hepatocytes formed spheroid faster

while the proliferation of 3T3 fibroblasts was slower on the crystalline substrate compared with the amorphous one.[27] The behavior of pre-osteoblastic MC3T3-E1 cells on amorphous poly(D,L-lactic acid) (PDLLA) and PLLA spherulites was also reported previously and the cells had significantly higher proliferation on amorphous PDLLA films than on semi-crystalline PLLA.[28,29] Our research group also MC3T3-E1 cell behavior on PCL spherulites crystallized at different crystallization temperatures and found that the cells did not show clear alignment on both non-banded and banded spherulites but the cell attachment and proliferation were better when the polymer was crystallized at higher temperatures because of the rougher surfaces.[30] After we discuss the synthesis, characterization, and physicochemical properties of the copolymers, distinct MC3T3-E1 responses to the copolymers crystallized at various temperatures and two different copolymer series are presented.

2.2 Experimental Section

2.2.1 Materials

All chemicals in this study were purchased from Sigma-Aldrich unless noted otherwise. Dichloromethane was distilled with calcium hydride prior to use. Tin(II)2-ethylhexanoate [$Sn(Oct)_2$] was distilled under reduced pressure before use. ε-caprolactone was dried over calcium hydride and distilled under reduced pressure. (3s)-*cis*-3,6-Dimethyl-1,4-dioxane-2,5-dione was dried at high vacuum overnight. 2,2-Bis(hydroxymethyl)-propionic acid (bis-MPA), 4-(dimethylamino)pyridine (DMAP), 2,2-dimethoxylpropane, N,N'-dicyclohexylcarbodiimide (DCC, Fluka), *p*-toluenesulfonic

acid, Dowex®50WX2 hydrogen form, methanol, acetone, hexane, and diethyl ether (Acros) were used as received.

2.2.2 Synthesis of Copolymers

Synthesis of Acetonide-2,2-bis(methoxy)propionic Anhydride (2): Acetonide-2,2-bis(methoxy)propionic acid 1 was prepared according to the recipe reported previously (Scheme 2.1). Acetonide-2,2-bis(methoxy)propionic acid **1** was prepared according to the recipe reported previously (Scheme 2.1). **1** (30 g, 172.2 mmol) was stirred in 150 mL of CH_2Cl_2. DCC (19.25 g, 93.65 mmol) was pre-dissolved in 15 mL of CH_2Cl_2 and added to the mixture of **1** in CH_2Cl_2 dropwise. After the stirring was continued for 36 h, the mixture was filtered and the filtrate was evaporated in rotary evaporation under reduced pressure and then high vacuum to remove the solvent completely. Two hundred milliliters of hexane was added to re-dissolve **2** and the solution was filtered again to remove the DCC-urea which was insoluble in CH_2Cl_2. The filtrate was sealed and stored at -20 °C for 24 h to obtain white solid of **2**. The white solid of **2** was collected by filtration and dried completely at room temperature under high vacuum to afford **2** as a white crystal (21.02 g, 74%). ^{1}H NMR ($CDCl_3$): δ 1.22 (s, 6H, -CH_3), 1.37 (s, 6H, -CH_3), 1.43 (s, 6H, -CH_3), 3.65 (d, 4H, J = 12.2 Hz, -CH_2O), 4.18 (d, 4H, J = 12.1 Hz, -CH_2O).

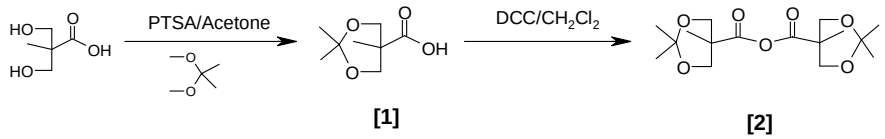

Scheme 2.1 Synthesis of acetonide-2,2-bis(methoxy)propionic anhydride 2

Synthesis of the First Generation Acetonide-protected Dendrimer: Acetonide-[G#1] (3) and General Esterification Procedure by Anhydride Coupling (Scheme 2.2). PEG (20.00 g, 1.38 mmol), Acetonide-2,2-bis(methoxy)propionic anhydride (2) (4.0 g, 12.1 mmol) (4.4 equiv./OH-group) and DMAP (1.04 g, 8.47 mmol) (3.0 equiv./OH-group) were dissolved in 50 mL of CH_2Cl_2. The reaction mixture was stirred at room temperature for 12 h. After completion, excess anhydride was removed by adding 15 mL CH_3OH to the solution, which was stirred for another 12 h. The solution was evaporated under reduced pressure, precipitated in cold diethyl ether (0 °C) and dried completely in vacuum to afford 3 as white crystals (19.15 g, 93%).

Synthesis of the First Generation Hydroxyl-Terminated Dendrimer: [G#1]-$(OH)_4$ (4) and General Procedure for the deprotection of hydroxyl groups. DOWEX50W-X2 (5 g) was added to the solution of acetonide-[G#1] 3 (19.15 g, 1.29 mmol) in 400 mL solvent mixture of methanol and dichloromethane (3:1, v/v). The solution was stirred at room temperature and monitored by ^1H NMR until the disappearance of surface groups (-CH_3) at 1.33-1.42 ppm. When the reaction was complete, the DOWEX50W-X2 was filtered and the solution was evaporated under reduced pressure prior to precipitation in diethyl ether. Finally the product was dried completely in high vacuum to afford 4 as white crystals (18.45 g, 96%).

Acetonide-[G#2] (5): [G#1]-$(OH)_4$ 4 (15.00 g, 1.01 mmol), DMAP (1.48 g, 12.05 mmol), and 2 (5.8 g, 17.5 mmol) were dissolved in 50 mL CH_2Cl_2 and reacted following the general esterification procedure to afford 5 as white crystals (14.48 g, 92%).

[G#2]-$(OH)_8$ (6): Acetonide-[G#2] (13.00 g, 0.838 mmol) and DOWEX50W-X2 (5 g) were added to 400 mL solvent mixture of methanol and dichloromethane (3:1, v/v)

and reacted according to the general procedure for the deprotection of hydroxyl groups to afford 7 as white crystals (12.36 g, 96%).

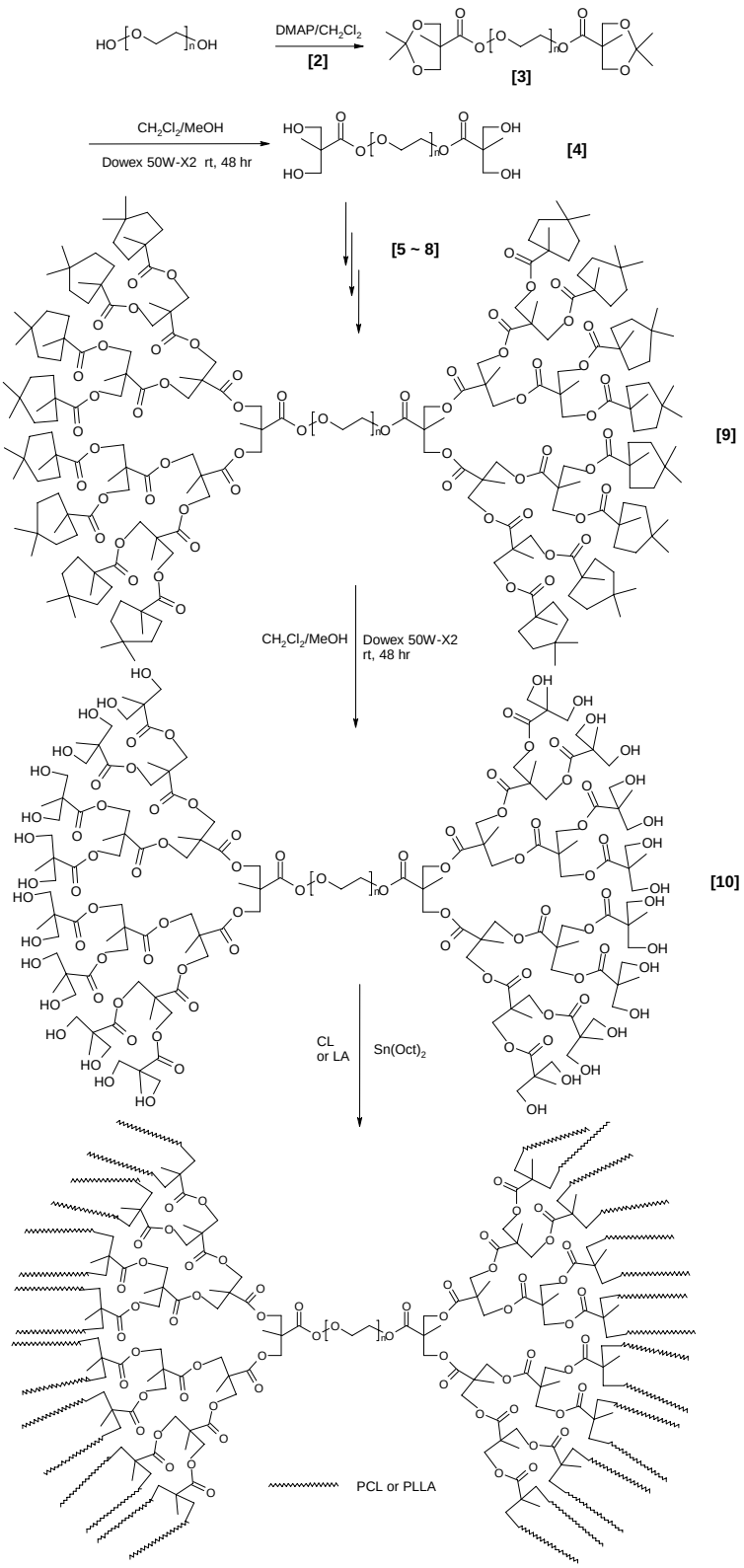

Scheme 2.2 Divergent synthesis of four-generation dendron 10 and copolymers by ROP.

Acetonide-[G#3] (7): [G#2]-(OH)8 6 (12.36 g, 0.81 mmol), DMAP (2.39 g, 19.44 mmol), and 2 (9.45 g, 28.51 mmol) were dissolved in 50 mL CH2Cl2 and reacted following the general esterification procedure to give 7 as white crystals (12.34 g, 91%).

[G#3]-$(OH)_{16}$ (8): Acetonide-[G#3] (12.34 g, 0.74 mmol) and DOWEX50W-X2 (5 g) were added to 400 mL solvent mixture of methanol and dichloromethane (3:1, v/v) and reacted according to the general deprotection procedure to give 8 as white crystals (11.66 g, 96%).

Acetonide-[G#4] (9): [G#3]-$(OH)_{16}$ 8 (11.50 g, 0.70 mmol), DMAP (4.10 g, 33.35 mmol), and 2 (16.33 g, 42.27 mmol) were dissolved in 50 mL CH_2Cl_2 and reacted following the general esterification procedure to afford 9 as white crystals (11.93g, 89%). ^{1}H NMR ($CDCl_3$): δ 1.19 (s, 48H, -CH_3), 1.32-1.35 (m, 42H, -CH_3), 1.38 (s, 48H, -CH_3), 1.43 (s, 48H, -CH_3), 3.65 (m, -CH_2CH_2O-), 3.69 (d, 32H, -CH_2O), 4.21 (d, 32H, -CH_2O), 4.23-4.38 (m, 56H, -CH_2O).

[G#4]-$(OH)_{32}$ (10): Acetonide-[G#4] (11.93 g, 0.62 mmol) and DOWEX50W-X2 (5 g) were added to 400 mL solvent mixture of methanol and dichloromethane (3:1, v/v) and reacted according to the general deprotection procedure to give PEG Dendron 10 as white crystals (10.81 g, 94%). ^{1}H NMR ($CDCl_3$): δ 1.08 (s, 48H, -CH_3), 1.24-1.30 (m, 42H, -CH_3), 2.10 (s, 32H, -OH), 3.64 (m, -CH_2CH_2O-), 3.67 (d, 32H, -CH_2O), 4.19 (d, 32H, -CH_2O), 4.20-4.37 (m, 56H, -CH_2O).

General procedure for the synthesis of dumbbell-shaped tri-block copolymers: Copolymers were synthesized through ring-opening polymerization (ROP) of (3s)-*cis*-3,6-dimethyl-1,4-dioxane-2,5-dione or ε-caprolactone initiated by **10**. As shown in Table 1, the copolymers are named as CoPCL*m* or CoPLLA*m* where *m* denotes the molecular

weight of the PCL or PLLA arm. Here the general synthesis procedure for copolymers is exemplified with the synthesis of CoPLLA28500. (3s)-*cis*-3,6-Dimethyl-1,4-dioxane-2,5-dione (14.79 g, 0.10 mol), **10** (0.3 g, 16.18 μmol), and $Sn(Oct)_2$ (75 μL, 0.0005 mass equiv./monomer) were added to a three-neck flask which was dried completely at 100 °C for 2 h before use. The flask was degassed under high vacuum for 3 h, purged with dry nitrogen and vacuumized for five times and finally filled with dry nitrogen. The mixture was heated to 130 °C and stayed at this temperature for 24 h. Thirty milliliters of CH_2Cl_2 was added to the flask at room temperature to dissolve the polymer and the solution was precipitated in cold diethyl ether (0 °C) and the precipitate was dried at high vacuum to afford CoPLLA28500 as a white crystal (13.45 g, 89%).

Table 2.1 Compositions and molecular weights of PEG dendron 10 and copolymers

samples	PEG in copolymer (wt %)	M_n[a]	M_n[b]	M_n[c]	M_w[c]	M_w/M_n[c]
PEG				14,500	15,100	1.04
PEG dendron				15,900	16,500	1.04
CoPCL1150	30	52,900	50,700	37,900	39,700	1.05
CoPCL4500	10	158,600	155,400	69,900	81,800	1.17
CoPCL17200	2.8	566,300	527,400	273,300	336,100	1.23
CoPCL28500	1.7	927,300	860,500	431,000	516,500	1.20
CoPLLA1150	30	52,900	52,000	32,700	35,900	1.10
CoPLLA4500	10	158,600	156,900	87,300	104,700	1.20
CoPLLA17200	2.8	566,300	534,600	292,100	393,500	1.35
CoPLLA28500	1.7	927,300	881,600	485,000	583,400	1.20

[a]: calculated from feed ratio; [b]: calculated from H-NMR spectrum; [c]: obtained from GPC.

2.2.3 Characterizations

^{1}H NMR spectra were obtained from a Varian Mercury 300 spectrometer with $CDCl_3$ containing tetramethylsilane (TMS) as solvent. All chemical shifts were relative to TMS. Fourier-transform Infrared (FTIR) spectra were recorded on a Perkin Elmer Spectrum Spotlight 300 spectrometer with diamond Attenuated Total Reflectance. Molecular weights, molecular weight distribution, and elution time curves were detected using EcoSEC Gel Permeation Chromatography (GPC) system (Tosoh Bioscience LLC, Montgomeryville, PA) combined with a RI-8320 detector (Tosoh Bioscience LLC), in which linear monodisperse polystyrene (PS) standards were employed to measure molecular weights. Differential Scanning Calorimetrical (DSC) measurements were carried on a Perkin Elmer Diamond differential scanning calorimeter in a N_2 atmosphere. For copolymers with PCL arms, the samples were first heated from 25 to 100 °C at a heating rate of 10 °C/min, then cooled to -80 °C at a cooling rate of 10 °C/min, and heated to 100 °C again at 10 °C/min. For copolymers with PLLA arms, the samples were heated from 25 to 185 °C at a heating rate of 10 °C/min, followed by cooling to -80 °C at 10 °C/min, and heating to 185 °C at 10 °C/min. The tensile properties of the copolymer samples were determined on a dynamic mechanical analyzer (DMTA-5, Rheometric Scientific) at 37 °C. In brief, copolymer strips (~25 × ~1.4 × ~0.4 mm, length × width × thickness) were pulled at a strain rate of 0.0002 s^{-1}. Five specimens were measured and tensile modulus was calculated from the initial slope of the stress-strain curve. The isothermal crystallization of the copolymers was conducted using a Mettler Toledo FP82HT hot stage combined with a FP90 Central Processor. The crystalline

morphologies of the copolymers were observed with a polarized optical microscope (POM; Nikon Eclipse, E600, Japan) and the spherulite growth rate was calculated based on the images. The samples were prepared by spin-coating copolymer solution in dichloromethane (20 mg/mL) on clean glass slides at room temperature at a spinning rate of 1000 rpm for 1 min and further dried by placing samples at room temperature until complete evaporation of the solvent. Atomic force microscopic (AFM) scanning of copolymers was performed on a Nanoscope V control system (Veeco Instruments, Santa Barbara, CA) and the root mean square (rms) roughness (R_{rms}) was measured from the AFM height images. The water contact angles on the copolymer samples were determined using a Ramé-Hart NRC C.A. goniometer (Model 100-00-230, Mountain Lakes, NJ) at room temperature. Twenty microliters of distilled water (pH = 7.0) was injected onto the sample surface and images were taken using a 3.0 megapixel camera (*Moticam 2300*, Motic Inc.) when the water droplet was stable.

2.2.4 Synchrotron-Sourced Grazing-Incidence X-ray Diffraction (GIXRD)

Copolymer films with thickness of >500 μm were prepared by spin-coating copolymer solutions with a concentration of 0.07 g/mL at 1000 rpm on glass slides, followed by complete drying in high vacuum. CoPCL films were annealed at 37 °C overnight. CoPLLA polymer films were melted completely at 200 °C, quenched in ice water, and annealed at 70 °C thoroughly. The crystalline structure near the film surface was investigated by GIXRD (beamline X6B, National Synchrotron Light Source, Brookhaven National Laboratory). The beam size in this study was 0.3 mm (vertical) ×

0.3 mm (horizontal) and the wavelength λ of the incident X-ray was 0.068889 nm. The diffraction pattern was collected using a CCD detector (Princeton Instruments).

2.2.5 Cell Studies

Mouse MC3T3-E1 cells (ATCC, Manassas, VA) were cultured as previously reported.[30-32] Prior to cell culture, copolymer samples were immersed in 70% alcohol solution for 1 h and then rinsed in another clean 70% alcohol solution twice to clean and sterilize samples, followed by complete drying in high vacuum. MC3T3-E1 cells were seeded on copolymer samples at a density of ~13,000 cells/cm^2 and cultured in α-Minimum Essential Media (α-MEM; Gibco, Grand Island, NY) which contains 10% fetal bovine serum (FBS, Gibco) and 1% penicillin/streptomycin (Gibco) for 4 h, 1, 2, and 4 days in a cell incubator at 37 °C with 95% humidity and 5% CO_2. At each time point, the cell number was counted by MTS assay. After the culture medium was removed, the cells were washed with PBS twice to remove dead cells. The attached cells were fixed with 4% paraformaldehyde (PFA) solution for 20 min, rinsed with PBS twice and permeabilized with 0.2% Triton X-100 solution, followed by staining with rhodamine-phalloidin for 1 h at 37 °C and then directly staining with 4',6-diamidino-2-phenylindole (DAPI) at room temperature. The stained cells were photographed using an Axiovert 25 Zeiss light microscope (Carl Zeiss, Germany). Cell area was quantified from 10 fluorescent images of the cells at day 1 using ImageJ software (National Institutes of Health, Bethesda, MD).

2.2.6 Statistical Analysis

Cell studies were conducted in quadruplicates for each group at each cell culture time point. All values were expressed as mean ± standard deviation. The statistical significance ($p < 0.05$ or 0.01) in the differences between groups was determined using the student's *t*-test.

2.3 Results and Discussion

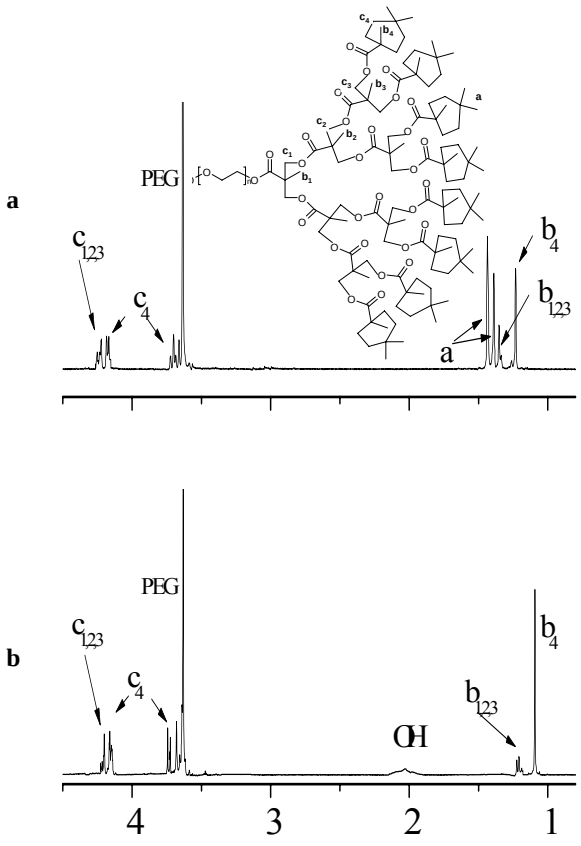

Figure 2.1 ^{1}H NMR spectra of (a) PEG-dendron and (b) PEG-G4-$(OH)_{32}$

The ^{1}H NMR spectra of **9**, **10**, and the copolymers and the assignments of the chemical shifts are shown in Figure 2.1a,b. The major signals (a, δ = 1.38 and 1.43 ppm) corresponding to **9** are the resonances from the methyl groups,[18] from which the ratio of integral area for the hydrogen atoms between PEG and **a** was calculated to be 13.31. This ratio was close to the theoretical ratio of 13.77. After deprotection of **9**, the signals from the methyl groups disappeared and the new resonance (δ = 2.10 ppm) attributed to the replaced hydroxyl groups. Simultaneously the chemical signals shifted towards lower values.

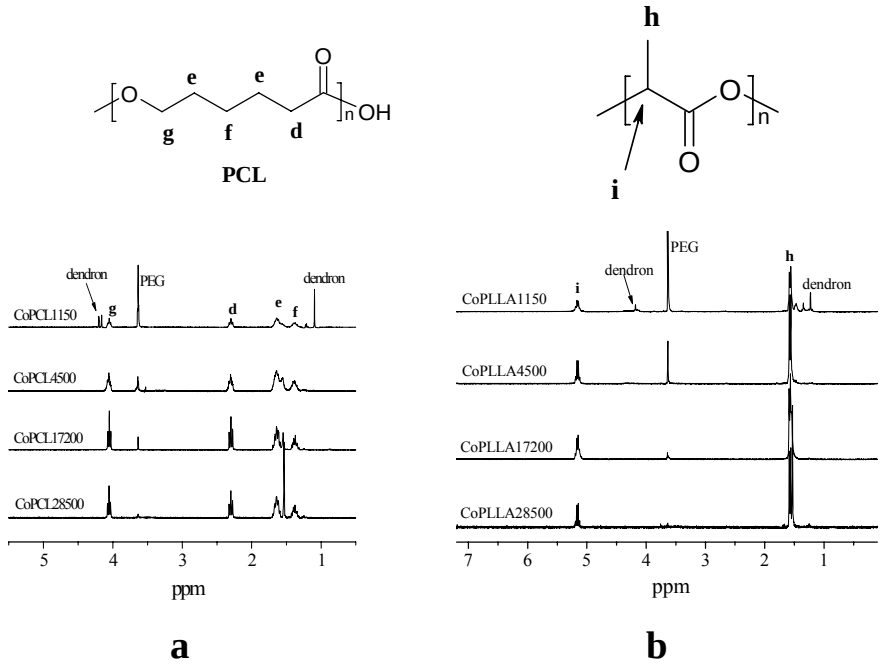

Figure 2.2 ^{1}H NMR spectra of (a) CoPCL series and (b) CoPLLA series.

When **10** was copolymerized with ε-caprolactone or (3s)-*cis*-3,6-dimethyl-1,4-dioxane-2,5-dione (Figure 2.2a,b), the resonance of the hydroxyl groups completely disappeared, indicating that the hydroxyl groups initiated polymerization efficiently. The resonance signals **d-g** and **h-i** are attributed to the arms of PCL and PLLA, respectively.[33,34] Because PCL or PLLA arms in CoPLLA1150 and CoPCL1150 accounted for a small proportion, the resonances from the dendron structure still prominently existed in their ^{1}H NMR spectra. At higher feed ratios of the monomer to the hydroxyl group, the resonances for the dendron structure and the PEG center block were less detectable while those for the PCL or PLLA arms were more prominent.

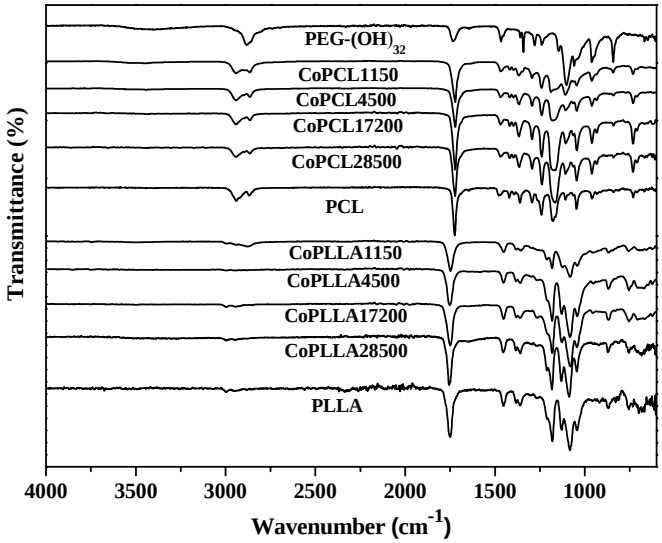

Figure 2.3 FTIR spectra of PEG Dendron 10, CoPCL series, and CoPLLA series.

The FTIR spectra of PEG dendron **10** and the copolymers are shown in Figure 2.3. The broad absorption at 3350–3605 cm^{-1} was ascribed to the hydroxyl group in **10**. In

comparison with the FTIR spectra of **10**, the absorption band for the hydroxyl group disappeared in the copolymers because of the conversion of the hydroxyl groups to ester bonds after the copolymerization. The absorption bands at 2965, 1740, and 1191 cm^{-1} were assigned to the $–CH_2$, –C=O, and C-O-C vibration in CoPCL, respectively. In CoPLLA, the absorption bands at 1760 and 1180-1190 cm^{-1} were ascribed to the –C=O and C-O-C vibration, respectively. The absorption bands at 1378-1389 and 1455-1460 cm^{-1} suggested the presence of $-CH(CH_3)$.

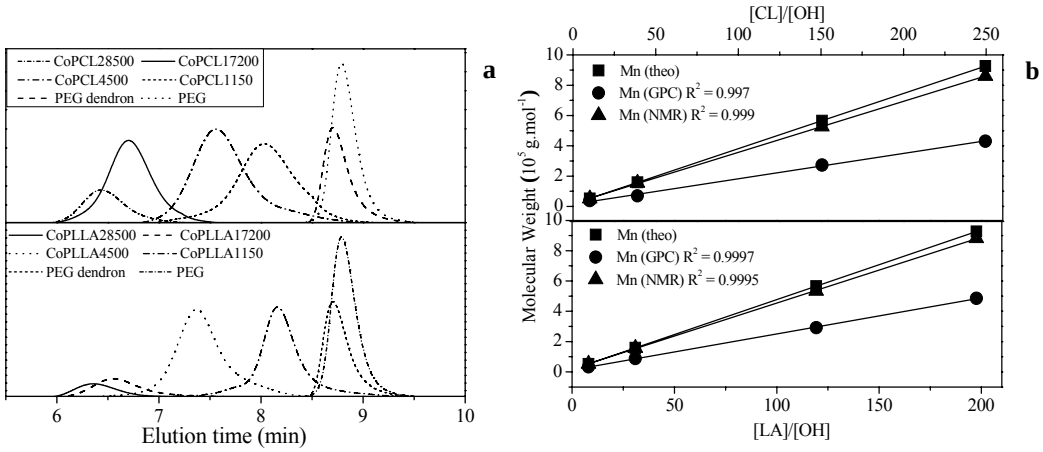

Figure 2.4 (a) GPC traces of PEG, PEG Dendron 10, CoPCL series, and CoPLLA series and (b) MWs as functions of the molar ratio of monomers to the hydroxyl groups in PEG Dendron 10.

The information about the molecular weights and molecular weight distribution in Table 1 was obtained using three methods, GPC, ^1H NMR, and the theoretical prediction. The molecular weights calculated from ^1H NMR were obtained by comparing the signal integral area of the methyl protons between PLLA (δ = 5.18 ppm) or PCL (δ = 4.06 ppm) and the PEG block (δ = 3.64 ppm). The theoretical values were calculated using the feed

ratio of the monomer to the hydroxyl group with assumption that all the terminal hydroxyl groups initiated the monomers in ROP. The average molecular weight of the PLLA or PCL arms was calculated from the ^{1}H NMR molecular weight of the copolymer using the equation of (M_n(PCL/PLLA arm) = (M_n(^{1}H NMR)-M_n(**10**))/32). GPC with the linear monodisperse PS standards was difficult to detect the precise molecular weights of the copolymers with high branched chemical structures. Because in principle polymers with a star structure have smaller hydrodynamic volume than the linear PS with the same molecular weight, the GPC data are lower than the values calculated from ^{1}H NMR and the theoretical prediction. There also existed a discrepancy in the molecular weights calculated by ^{1}H NMR spectra and the theoretical prediction caused by the monomer conversion in ROP, which could be understood from the yield in synthesis. As shown in the elution time curves of the copolymers in Figure 2.4a, the elution curve occurred at earlier time with the increase of molecular weight and all the curves were symmetrical to suggest the high purity of the copolymers. The linear relationship between the molecular weights determined using the three methods and the molar ratio of monomers to hydroxyl groups in ROP reaction, [LA]/[OH] or [CL]/[OH], was shown in Figure 2.4b.

Table 2.2 Thermal properties of PEG, PEG Dendron 10, CoPCL series, and CoPLLA series

samples	T_g (°C)	T_m (°C)	ΔH_m (J/g)	χ_c (%)
PEG	--	63.1	160.1	81.4
PEG dendron	--	52.8	105.6	53.7
CoPCL1150	--	43.7	66.8	49.5
CoPCL4500	--	51.5	67.2	49.8
CoPCL17200	--	53.3	73.2	54.2
CoPCL28500	--	53.7	73.0	54.1
CoPLLA1150	--	72.1	1.1	1.1
CoPLLA4500	39.2	150.3	34.5	36.9
CoPLLA17200	56.1	165.1	36.9	39.5
CoPLLA28500	56.7	168.3	40.2	43.0

The thermal properties of the copolymers were characterized using DSC, as shown in Figure 2.5 and Table 2.2. From the melting peak in the second heating run, the melting temperature (T_m) was determined. After being coupled with acetonide-2,2-bis(methoxy)propionic anhydride, PEG dendron **10** has a much lower T_m than pure PEG. With the increase of the arm molecular weight, the copolymer with a higher molecular weight has a higher T_m. Double melting peaks were previously found in linear PCL-*b*-PEG-*b*-PCL tri-block copolymers because of the co-existence of the crystalline phases of both PEG and PCL.[35,36] In this study, all the copolymers had a single melting peak possibly because the two blocks could not crystallize at the same time. The PCL or PLLA dominated the crystallization for all these copolymers except those two with the lowest arm molecular weight, i.e., CoPCL1150 and CoPLLA1150. For CoPCL1150, the PEG center block dominated its crystallization, as further demonstrated in the later discussion. The DSC curve for CoPLLA1150 indicated that it was amorphous. Meanwhile, the glass transition temperature (T_g) and cold crystallization exothermal peaks appeared in the heating run for CoPLLA4500, CoPLLA17200, and CoPLLA28500. When the

temperature was between T_g and T_m, chain motion could be activated and polymer chains were re-arranged for packing crystallizable chain segments in the copolymers. For CoPLLA1150, no cold crystallization was observed because a high proportion of PEG in CoPLLA1150 confined the crystallization. Pure PLLA has a high T_g of ~65 °C. When the PLLA composition in the copolymers increased, the chain movement of the copolymers controlled by the PLLA arms decreased and needed a higher temperature to facilitate. Thus the T_g was higher for the copolymer with a higher molecular weight. χ_c was calculated by dividing the heat of fusion ΔH_m measured using DSC by the value for 100% crystalline polymer, ΔH_m^0. The ΔH_m^0 values for PLLA, PCL, and PEG are 93.6, 135, and 196.8 J/g, respectively. PEG dendron **10** had a much lower χ_c than pure PEG. The χ_c of CoPCL increased from CoPCL1150 to CoPCL17200 but decreased slightly when the molecular weight increased further to CoPCL28500. Thus the χ_c of CoPCL showed a maximum rather than monotonic increase against the molecular weight at the same T_c.[37] χ_c increased with M_n when it was less than 10000 g/mol and decreased with M_n ranging from 44700 to 64700 g/mol. The reason is that the higher chain entanglement at a higher molecular weight reduces chain mobility and reorganization in crystallization. For CoPLLA, χ_c increased monotonically with increasing the molecular weight, as listed in Table 2. CoPLLA1150 crystallization was strongly confined by the dominant PEG center block and had an extremely low χ_c.

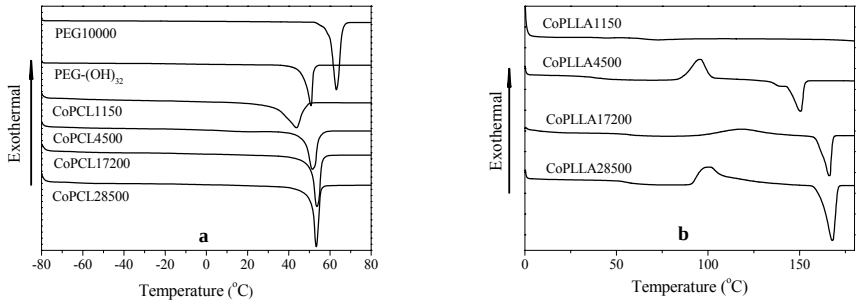

Figure 2.5 DSC curves of (a) PEG, PEG Dendron 10, CoPCL series, and (b) CoPLLA series.

The representative tensile stress-strain curves of the copolymers at 37 °C are shown in Figure 2.6. Because PLLA with a high T_g was glassy in the measurements while a higher molecular weight results in a higher χ_c, CoPLLA4500, CoPLLA17200, and CoPLLA28500 were brittle and higher tensile strength and break strain were found when the molecular weight was higher. In contrast, CoPLLA1150 displayed elastomeric properties with a high strain up to 150%. The tensile modulus for CoPLLA series was determined to be 10.5 ± 1.3, 290.9 ± 24.2, 810.1 ± 31.2, and 920.8 ± 39.8 MPa for CoPLLA1150, CoPLLA4500, CoPLLA17200, and CoPLLA28500, respectively. In a typical tensile test for PCL, the stress-strain curve includes stretching region, necking region in which PCL crystalline domains are strongly aligned, and break region. CoPCL28500 and CoPCL17200 had a prominent necking region because they had high χ_c ensuring the alignment of the crystalline domains. In contrast, CoPCL4500 and CoPCL1150 did not show necking region and were brittle. With the increase of molecular weight, tensile strength was enhanced and strain became larger. The tensile modulus for CoPCL series was measured to be 5.4 ± 0.9, 19.1 ± 6.6, 87.7 ± 17.6, 210.9 ± 16.2 MPa for CoPCL1150, CoPCL4500, CoPCL17200, and CoPCL28500, respectively. Compared

with the CoPLLA with the same molecular weight, CoPCL had a much higher strain value but a lower tensile modulus, because of a much higher T_g for PLLA.

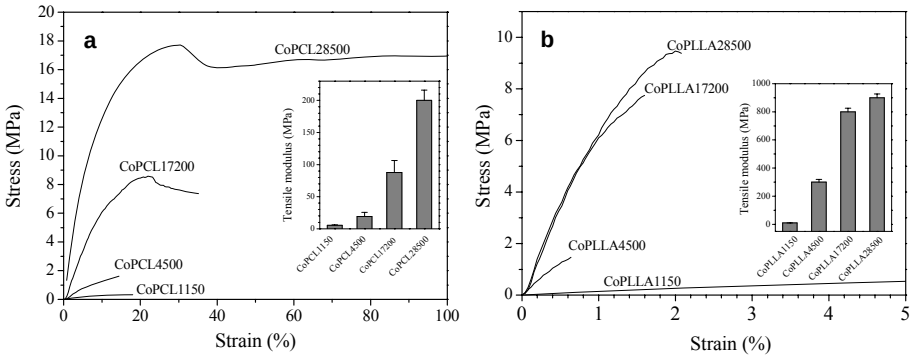

Figure 2.6 Representative stress-strain curves of (a) CoPCL series and (b) CoPLLA series. Insets: tensile modulus of copolymers.

The hydrophilicity of the copolymer flat films was demonstrated using the water contact angles, as shown in Figure 2.7. With the increase of PEG component, the water contact angles decreased sharply. The water contact angles of CoPLLA series were smaller than those of CoPCL series when the PEG compositions were the same. Water contact angles can be affected by two major factors, which are surface chemistry and topography.[38-40] To achieve high hydrophilicity from chemical modification, chemical groups, such as –OH, -COOH, -SO_3H, and -O-, can be incorporated in materials.[41,42] In contrast, fluorinated polymers induce high hydrophobicity because of their low surface evergies.[43] However, chemical modification is not necessary to achieve either good hydrophilicity or good hydrophobicity. Polymer wettability can be altered effectively by roughening the polymer surface.[43] In case of rough surface without formation of air pockets which are air bubble between water droplets and sample surface, Wenzel

demonstrated that the polymers with contact angle of below 90° could become more hydrophilic with the increase of roughness, while hydrophobicity of polymers with contact angle more than 90° could be enhanced by roughness. In case of formation of air pockets on rough surface, Cassie and Baxter suggested that the wettability of polymers depended on the specific topographic features.[38]

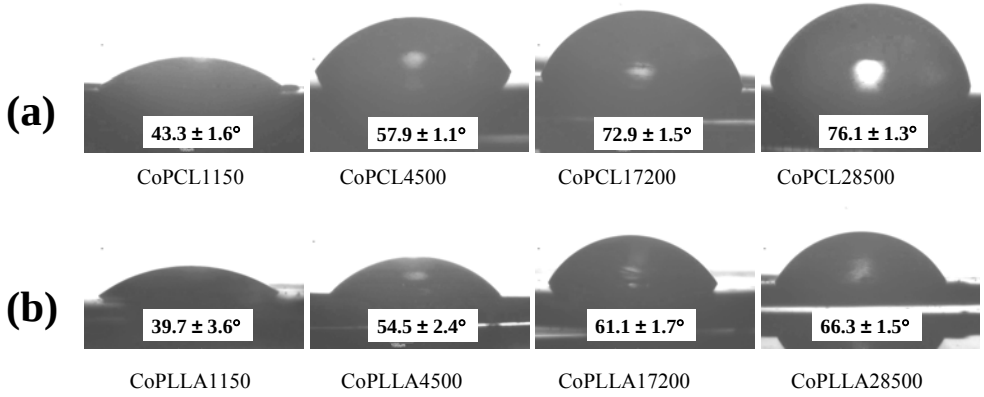

Figure 2.7 Photographs of water droplets on (a) CoPCL series and (b) CoPLLA series. Insets: water contact angles.

In our study, all the films are prepared with flat surface. Consequently, the resolution of water contact angles should be attributed to the chemical components rather than geometric surface structure. PEG has good hydrophilicity because it contains high density of ether bonds.[38] With the increase of PEG component in copolymers, the hydrophilicity could be enhanced. Yuan *et al.* studied the hydrophilicity of linear PCL and its copolymer with PEG and demonstrated that the hydrophilicity was dramatically strengthened with the incorporation of PEG consistent with our present result.[39]

Polymers normally form spherical crystals called spherulites when they crystallize from melts without disturbance at isothermal temperature.[44] The spherulite diameter

can range from micro-scale to millimeter-scale, depending on the crystallization parameters, such as crystallization temperature, and the nucleating agent. Spherulites are comprised of layer-shape lamellae. In the center of spherulites, the lamellae are stacked in parallel. From the center to the edge, the lamellae display apart and branched distribution owing to the repulsion of amorphous component between lamellae. The spherulitic growth rate defined as the diameter growth length per unit time was demonstrated to be constant even though the lamellar growth rate for some lamellae initially can grow forward faster than the average spherulitic growth rate. Figure 2.8a,b shows the T_c dependence of spherulitic growth rate. For CoPCL4500, CoPCL17200, and CoPCL28500, the growth rate increased dramatically with the decrease of T_c because lower isothermal temperature caused rapid formation of nucleation and the stability of segment packing. At the same T_c, CoPCL17200 had the highest growth rate than both CoPCL4500 and CoPCL28500. PEG block in CoPCL4500 might limit the stacking of PCL lamellae and impeded the growth rate of spherulites. For CoPCL28500, the PCL block had a higher molecular weight than CoPCL17200 and slower the chain packing process compared with CoPCL17200. For CoPLLA4500, CoPLLA17200, and CoPLLA28500, CoPLLA17200 had the largest growth rate and CoPLLA4500 had the lowest growth rate at the same T_c for the same reason as CoPCL series. We found that growth rate for CoPLLA4500, CoPLLA17200, and CoPLLA28500 displayed parabolic dependence on T_c. The maximum growth rate could be obtained when T_c located at the critical region ranging from 125 to 130 °C. When T_c was lower and closer to T_g of ~65 °C, chain packing was more difficult and the growth of spherulites was inhibited. In case

that T_c was higher than the critical temperature, chain arrangement would be more difficult and limit the growth rate.[45,46].

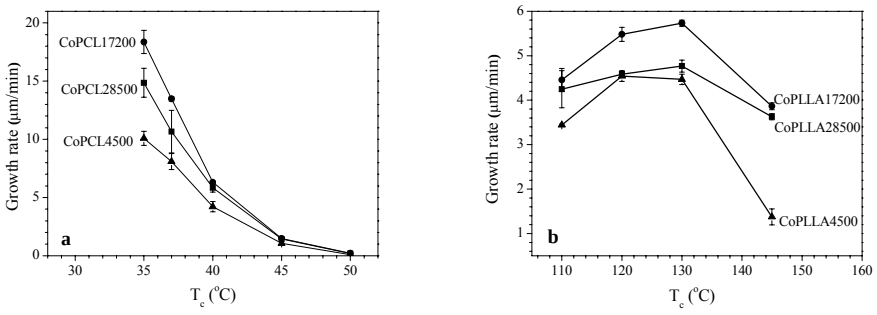

Figure 2.8 (a) T_c dependence of spherulte growth rate for CoPCL series, (b) T_c dependence of spherulte growth rate for CoPLLA series.

The crystalline morphologies of CoPCL series and CoPLLA series crystallized at various T_c were observed by polarized optical micrographs as demonstrated in Figure 2.9a,b. For CoPCL4500, CoPCL17200, and CoPCL28500, typical crystalline spherulites were observed at T_c ranging from 35 to 50 °C. Polymers can also form banded spherulites at certain conditions as the result of periodic twisting of the radial crystallite ribbons growing from spherulite center.[44] For linear PCL-*b*-PEG-*b*-PCL tri-block copolymers, it was reported that when the composition of PCL was higher than 60 wt%, banded spherulites of PCL were formed at T_c of 45 °C.[35] However, CoPCL4500, CoPCL17200, and CoPCL28500 did not form clear banded structure at T_c of both 45 and 50 °C. For CoPCL1150 in which the composition of PEG was much higher than other copolymers, the PCL spherulites were generated firstly and slowly grew with isothermal time. Then PEG formed nucleation and grew rapidly to form the large outer portion of spherulites.

Eventually the huge PEG spherulites were decorated with small PCL spherulites as shown by arrows in Figure 2.9a. This phenomenon was also confirmed by other reports.[47] From the POM images, we found that the spherulite size of CoPCL4500 was larger than CoPCL28500 and CoPCL17200 at the identical T_c. As demonstrated in DSC results, CoPCL17200 has higher T_m than CoPCL4500 but lower than CoPCL28500. Since the T_c was the same, the T_m of CoPCL4500 was closer to T_c than that of CoPCL17200 and CoPCL28500. Therefore, nucleation of CoPCL17200 and CoPCL28500 was easier than CoPCL4500 and this would lead to larger spherulites of CoPCL4500. For CoPLLA series, the spherulite morphologies could be influenced by the molecular MW and T_c. CoPLLA28500 formed huge non-banded spherulites with prominent cracks at T_c of 145 °C, irregular banded spherulites at T_c of 130 °C, and non-banded spherulites at T_c of both 120 and 110 °C. CoPLLA17200 formed similar spherulites with cracks at T_c of 145 °C, non-banded spherulites with few cracks at T_c of 130 °C, clear banded spherulites at T_c of 120 °C, and non-banded spherulites at T_c of 110 °C. CoPLLA4500 formed large banded spherulites with cracks at T_c of 130 °C, non-banded spherulites with many cracks at T_c of 120 °C, and non-banded spherulites at T_c of 110 °C. Rhythmic growth and thermal shrinkage were considered as the main factors causing the formation of PLLA periodic cracks.[48] Circumferential cracks normally are formed in non-banded spherulites of PLLA in the cooling process and the crack spacing decreases with the increase of spherulite radius, which are consistent with our present results. PLLA with low molecular weight was demonstrated to form banded spherulites with both circumferential cracks and radial cracks. CoPLLA17200 crystallized at 120 °C

formed banded spherulites without cracks. On contrary, CoPLLA4500 with lower molecular weight formed prominent banded structure with only circumferential cracks rather than both circumferential and radial cracks. PLLA with higher MW preferred to form banded spherulites and was difficult to form cracks on spherulites when T_c was between 120 and 140 °C.[48] It was also confirmed that PLLA with a lower molecular weight could also generate cracks at lower temperature, which is consistent with our results. The composition dependence of di-block copolymers (PLLA-*b*-PEG) was studied.[49] The findings suggested that when the molecular weight of PLLA was similar to that of PEG, copolymers tended to generate ring-banded spherulites. For example, PEG5000-PLLA6300 in their study formed regular ring-banded spherulites at T_c of 110 °C. However, only CoPLLA17200, in which the molecular weight of PLLA block was nearly 32 times as much as that of the PEG block, formed banded spherulites at 120 °C. This illustrated that the crystallization behavior of comb-dendritic tri-block copolymer was different from that of linear copolymers.

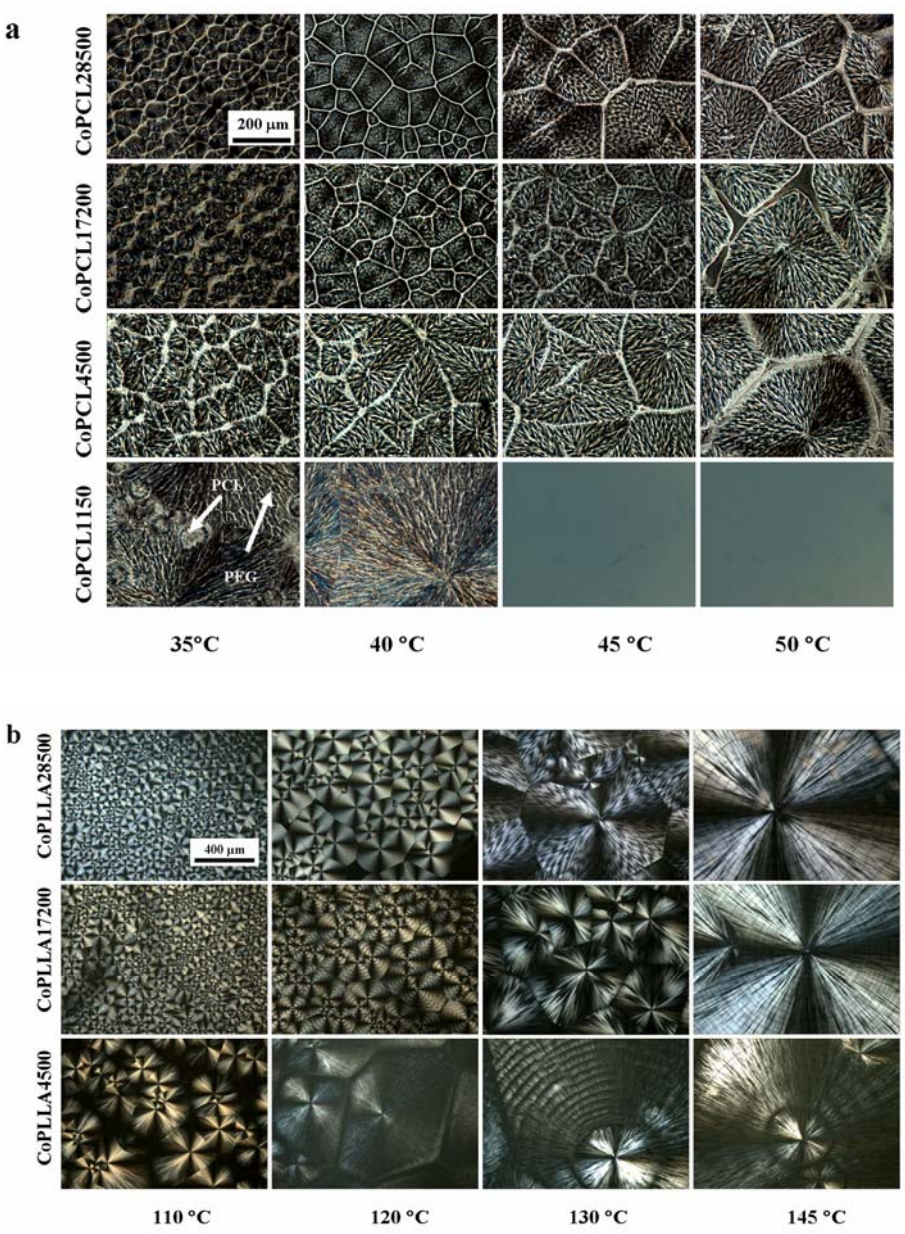

Figure 2.9 (a) POM images of CoPCL series, and (b) POM images of CoPLLA series.

AFM images in Figure 2.10 were used to take further insight into the details of spherulites. Even the scan area applied to this experiment was 100 μm × 100 μm, the scan region for all the samples was almost on a single spherulite. For CoPCL17200 and CoPLLA17200, the surface became rougher with the increase of T_c because higher

temperature induced spherulites with larger scale size. The R_{rms} values of CoPCL17200 crystallized at 35, 40, and 45 °C were 93.5 ± 5.9, 136.7 ± 9.6, and 162.9 ± 12.3 nm, respectively. The R_{rms} values of CoPLLA17200 crystallized at 110, 120, and 145 °C were 28.5 ± 2.3, 52.4 ± 2.5, and 223.2 ± 15.4 nm, respectively. When T_c was 50 °C, CoPCL4500 was rougher than CoPCL17200 and CoPCL28500. The R_{rms} values of CoPCL4500, CoPCL17200, and CoPCL28500 crystallized at 50 °C were 211.5 ± 14.9, 162.8 ± 10.1, and 178.3 ± 11.6, respectively. When the T_c was set up at 130 °C for CoPLLA series, the surface morphology of CoPLLA28500 is similar to CoPLLA17200. On the contrary, CoPLLA4500 had remarkable banded spherulites which confirmed the POM images in Figure 2.11a and the depth profile demonstrated that the width and depth were 41 ± 5 and 1.5 ± 0.3 μm, respectively. Their dimension is much larger than typical banded spherulites [39] and needs further study. The R_{rms} values of CoPLLA4500, CoPLLA17200, and CoPLLA28500 crystallized at 130 °C were 598.6 ± 13.6, 53.6 ± 1.9, and 33.9 ± 4.1 nm, respectively. From the AFM image in Figure 2.11b, the banded spherulites of CoPLLA17200 at T_c of 120 °C did not show perfect banded structure and the depth profile indicated that the width and depth were 55 ± 10 and 215 ± 50 nm, respectively. Polymers could form two kinds of lamellae which were flat-on lamellae and edge-on lamellae.[50,51] When the thickness of polymer films increases, the content of edge-on lamellae increases. In thick films, the growth of lamellae follow the same orientation as the nuclei generated at the interface and edge-on lamellae are formed. In thin films, the formation of edge-on lamellae is confined by the film thickness and flat-on lamellae are preferentially formed. The surface energy of flat-on lamellae is 3-6 times

higher than that of edge-on lamellae for the presence of folding surface. They also suggested that banded spherulites consisted of both flat-on and edge-on lamellae. The ridges in banded spherulites were mainly edge-on lamellae and flat-on lamellae were mainly formed in valleys. Tapping mode AFM scanning can provide insight into the lamellae structure. Because the thickness of all polymer films used for crystallization was determined by AFM to be more than 10 μm. All AFM images demonstrated that edge-on view was recognized in spherulites without banded structure. As shown in Figure 2.11a, CoPLLA4500 crystallized at 130 °C presented edge-on view on ridges. On the contrary, CoPLLA17200 crystallized at 120 °C shown in Figure 2.11b only had obvious edge-on view on both ridges and valleys. The main reason causing this contradiction can be attributed to the fact that CoPLLA17200 crystallized at 120 °C did not form perfect banded structure with significant ridges and valleys.

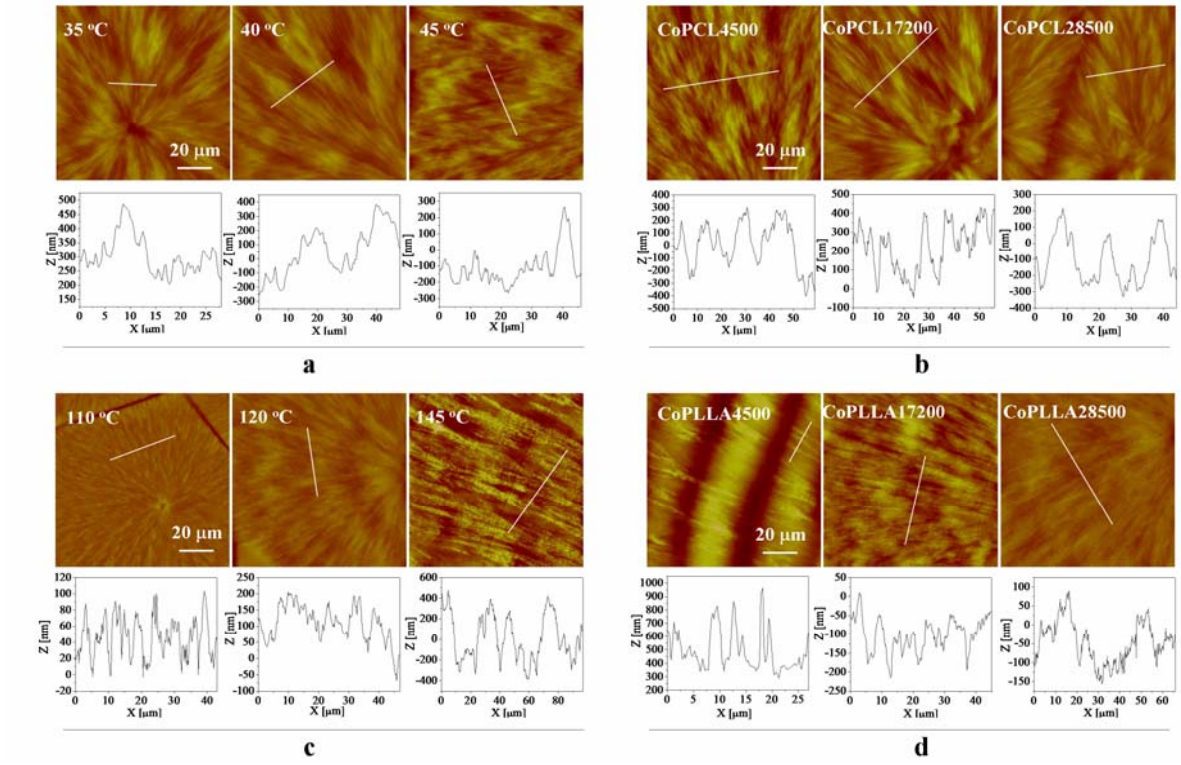

Figure 2.10 AFM height images of (a) CoPCL17200 crystallized at 35, 40, and 45°C, (b) CoPCL4500, CoPCL17200, and CoPCL28500 crystallized at 50 ^{o}C, (c) CoPLLA17200 crystallized at 110, 120, and 145°C, and (d) CoPLLA4500, CoPLLA17200, and CoPLLA28500 crystallized at 130 ^{o}C. Beneath each image is the corresponding depth profile graph.

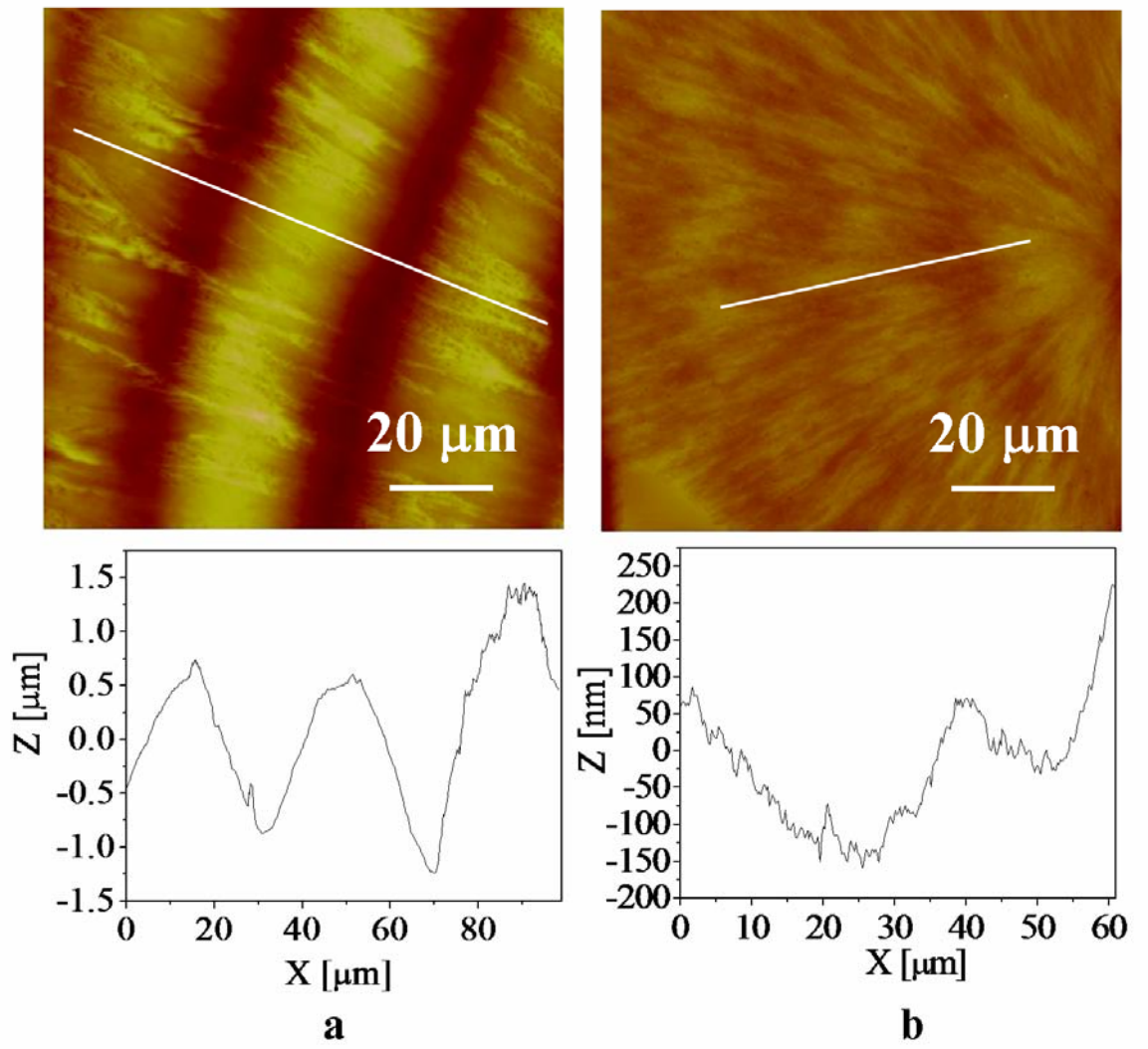

Figure 2.11 AFM height images of (a) Cross-sectional profile of CoPLLA4500 crystallized at 130 °C, and (b) Cross-sectional profile of CoPLLA17200 crystallized at 120 °C.Beneath each image is the corresponding depth profile graph.

When the incident angle α of X-ray is equal to or smaller than the critical angle α_c, the surface can completely reflect the incident X-ray and the X-ray penetrates into the polymers as evanescent waves. α_c is a function of λ and polymer refractive index *n*. α_c can be calculated using the expression shown bellow,[24,25]

$$\alpha_c = (\frac{\lambda^2 r_e N}{\pi})^{1/2} \quad (1)$$

where r_e is the classical electron radius of 2.82×10^{-13} cm and N is the electron density per unit volume of the polymer. The α_c values for CoPCL and CoPLLA in this study were calculated to be 0.073^o and 0.076^o, respectively. The penetration depth, d_p, defined as the depth at which the incident X-ray intensity decreases to e^{-1} can be expressed with the following equations.[25]

$$d_p = \frac{\lambda}{4\pi n(\alpha_c^2 - \alpha^2)^{1/2}} \quad (\alpha < \alpha_c) \quad (2)$$

$$d_c = \frac{\sin\alpha}{\mu} \quad (\alpha > \alpha_c) \quad (3)$$

where μ is a linear absorption coefficient. Using these two equations, α can be converted into d_p and then the X-ray pattern corresponding to specific depth can be obtained. The X-ray patterns of CoPCL17200 and CoPLLA17200 films at various depths in Figure 2.12a,b show that the crystal structure was more ordered at a deeper layer. The X-ray crystallinity was also measured by the method previously proposed. As shown in Figure 2.12c,d, at the same d_p, the crystallinity trend was similar to DSC results. With increasing d_p, crystallinity increased asymptotically to a constant value.

The apparent crystallite size can also be calculated using the following equation,[25]

$$D = \frac{\lambda}{\beta \cdot \cos\theta} \quad (4)$$

where D is the crystallite size, θ is a Brag angle, and β is a corrected integral width obtained from the X-ray pattern. Figure 2.12e,f shows that higher molecular weight had

bigger crystallite size in all plane when d_p was the same and the crystallite size was also increased with d_p. The lattice constants a, b, and c of the orthorhombic unit cell as shown in Figure 2.12g,h calculated from the in plane 2θ angles of the reflection peaks also increased slightly with d_p and molecular weight.

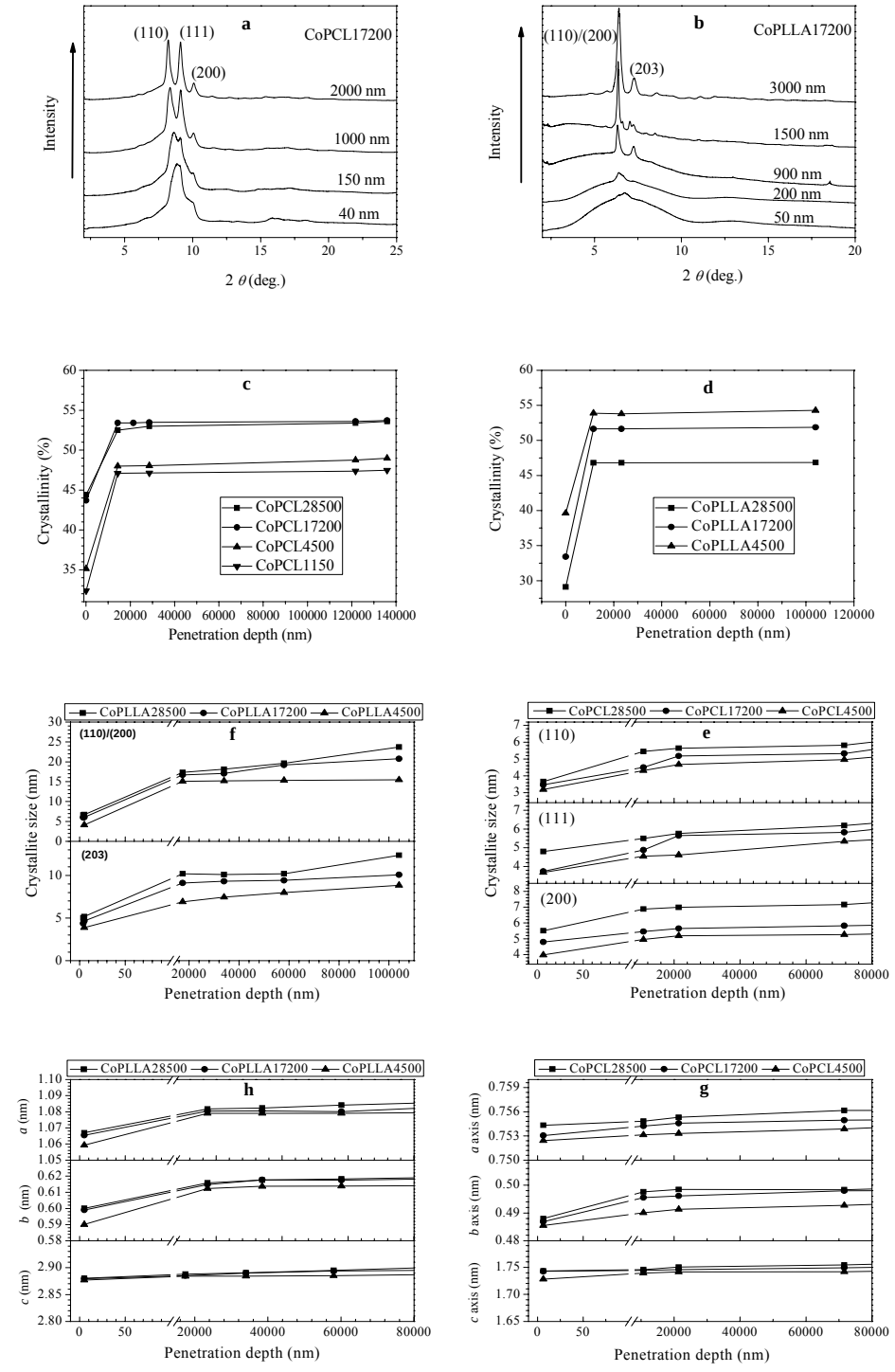

Figure 2.12 GIXRD patterns, crystallinity, crystallite size and lattice constants a, b, c of the orthorhombic unit cell along penetration depth of CoPCL (a, c, e, g) and CoPLLA (b, d, f, h) series.

The effects of molecular weight and crystallization temperature on MC3T3-E1 cell behavior were evaluated for both CoPCL and CoPLLA. As demonstrated in Figure 2.13a, the cell density on CoPCL17200 spherulites crystallized at various temperatures was higher than that on flat films and increased with the increase of crystallization temperature. Figure 2.13b shows that cells proliferated best on CoPCL4500 compared with CoPCL1150, CoPCL17200, and CoPCL28500, while CoPCL1150 had the lowest. Cell morphology on the polymers was also observed in fluorescent images in Figure 2.13c. The images clearly showed that cells on CoPCL17200 spherulites crystallized at various temperatures had better spreading than those on CoPCL17200 flat film and the cells did not display the distortion of both cell cytoplasm and cell nuclei. For CoPCL1150, CoPCL4500, CoPCL17200, and CoPCL28500 films crystallized at 50 °C, cells had poorer spreading on CoPCL1150 films than others. Cells on CoPCL4500 and CoPCL17200 were prominently aligned along the radius direction of the spherulites.

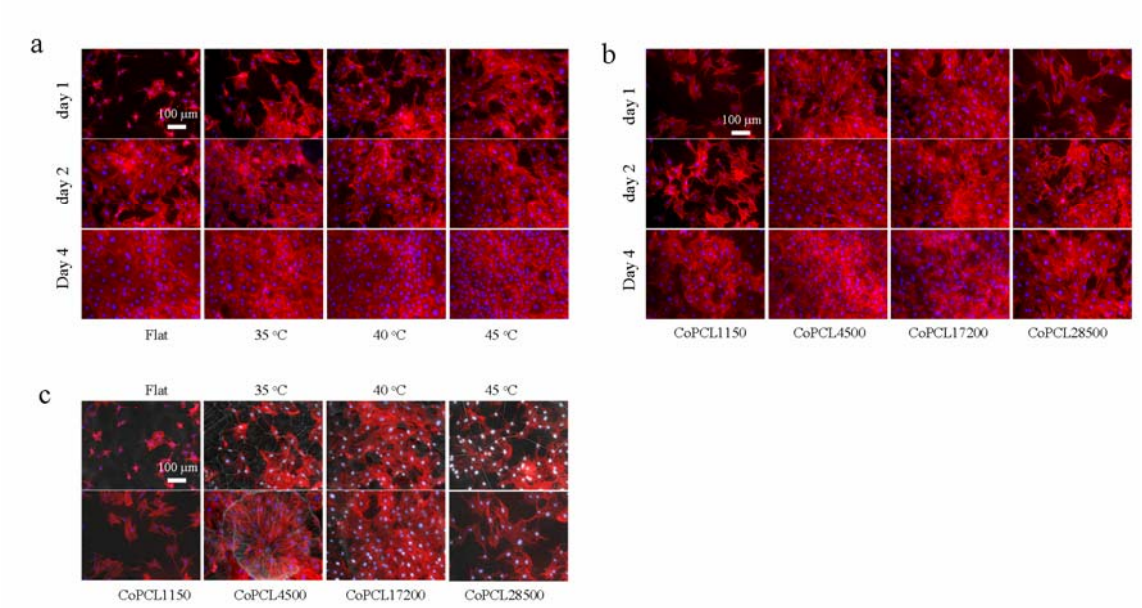

Figure 2.13 (a) Fluorescent images of cells stained with RP (red) and DAPI (blue) at days 1, 2, and 4 on CoPCL17200 flat films and spherulites crystallized at 35°C, 40 °C, and 45 °C. (b) Fluorescent images of cells stained with RP (red) and DAPI (blue) at days 1, 2, and 4 on CoPCL1150, CoPCL4500, CoPCL17200, and CoPCL28500 films crystallized at 50 °C. (c) Fluorescent images combined with backgrounds of CoPCL17200 flat films and spherulites crystallized at 35°C, 40 °C, and 45 °C at day 1 (top row) and CoPCL1150, CoPCL4500, CoPCL17200, and CoPCL28500 spherulites crystallized at 50 °C at day 1 (bottom row) at magnification of × 10.

The MTS results of cell proliferation in Figure 2.14a,b on CoPCL further confirmed the observation in fluorescent images. Cells on CoPCL17200 flat film had a significantly lower cell area than those on CoPCL17200 spherulites crystallized at 35, 40, and 45 °C and the cells on CoPCL1150 films had the smallest area compared with those on CoPCL4500, CoPCL17200, and CoPCL28500 films when they were crystallized at 50 °C. Meanwhile, the shape factor of the cells on CoPCL4500 crystallized at 50 °C was remarkably lower than those of other groups, indicating a strong cell orientation. Cell alignment was quantified using the percentage of aligned cells in the total cells along the

radial direction and cells were considered as aligned when the angle between the long axis and the radial direction of the spherulites was less than 15°. Cells on more than 20 spherulites were counted and analyzed. The percentages of aligned cells along the radial direction were calculated to be 16.5 ± 2% and 24.3 ± 3% for CoPCL17200 films crystallized at 40 and 45 °C, respectively. The percentages of aligned cells along radius direction were 54.6 ± 8%, 33.5 ± 5%, and 23.6 ± 2% for CoPCL4500, CoPCL17200, and CoPCL28500 films crystallized at 50 °C, respectively.

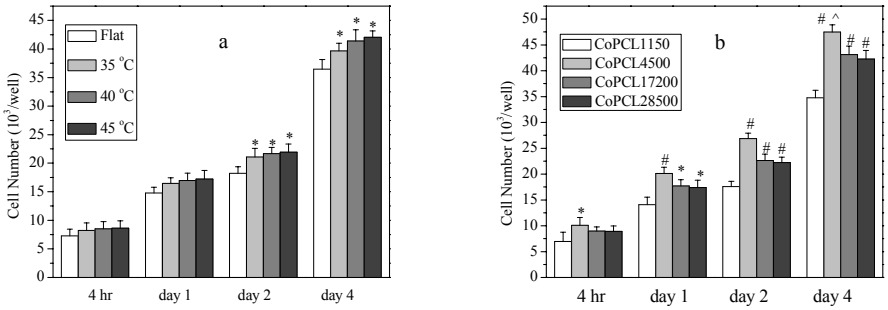

Figure 2.14 (a) Cell proliferation on CoPCL17200 flat films and spherulites crystallized at 35°C, 40 °C, and 45 °C represented by the cell numbers at 4 h, days 1, 2, and 4. *, $p < 0.05$ relative to flat films. (b) Cell proliferation on CoPCL1150, CoPCL4500, CoPCL17200, and CoPCL28500 films crystallized at 50 °C represented by the cell numbers at 4 h, days 1, 2, and 4. *, $p < 0.05$; #, $p < 0.01$ relative to CoPCL1150; ^, $p < 0.01$ relative to CoPCL17200 and CoPCL28500.

Cell proliferation did not show significant difference among CoPLLA17200 flat films and CoPLLA17200 spherulites crystallized at 110, 120, and 145 °C, as demonstrated in Figure 2.15a. On CoPLLA1150, CoPLLA4500, CoPLLA17200, and CoPLLA28500 films crystallized at 130 °C, cell density showed the trend in Figure 2.15b similar to that on CoPCL polymers crystallized at 50 °C. Figure 2.15c shows the fluorescent cell images with the substrate background. Cells on CoPLLA17200

crystallized at 145 °C and CoPLLA4500 crystallized at 130 °C were strongly aligned and those on CoPLLA17200 and CoPLLA28500 films crystallized at 130 °C were also slightly aligned, along the radial direction. However, cells on the other samples did not show clear alignment. Figure 2.15d shows cell distribution on large CoPLLA17200 spherulites crystallized at 145 °C and CoPLLA4500 spherulites crystallized at 130 °C. Clearly, cells were aligned long the radial direction in an individual spherulite and the direction of the long axis of cells was altered at the spherulite boundary. The cell numbers determined using MTS (Figure 2.16a,b) further confirmed the results in the images. Cell spread area did not show significant difference among different samples. Cells on CoPLLA4500, CoPLLA17200, and CoPLLA28500 spherulites crystallized at 130 °C and CoPLLA17200 spherulites crystallized at 145 °C were significantly aligned and those on CoPLLA4500 spherulites crystallized at 130 °C and CoPLLA17200 spherulites crystallized at 145 °C were aligned most prominently.

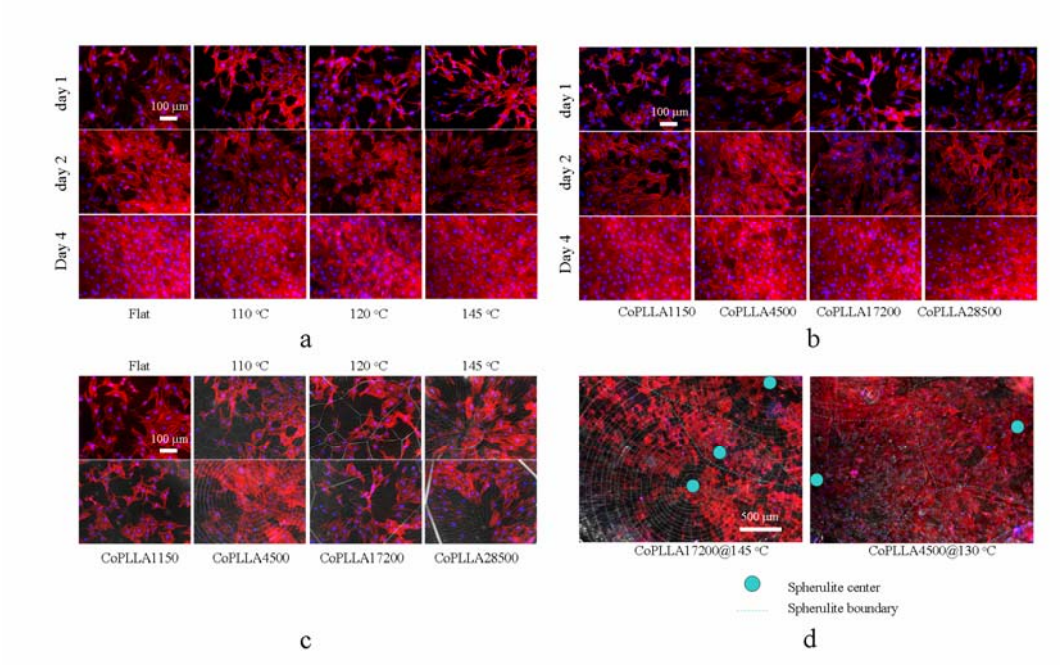

Figure 2.15 (a) Fluorescent images of cells stained with RP (red) and DAPI (blue) at days 1, 2, and 4 on CoLLA17200 flat films and spherulites crystallized at 110^{o}C, 120 ^{o}C, and 145 ^{o}C. (b) Fluorescent images of cells stained with RP (red) and DAPI (blue) at days 1, 2, and 4 on CoPLLA1150, CoPLLA4500, CoPLLA17200, and CoPLLA28500 films crystallized at 130 ^{o}C. (c) Fluorescent images combined with backgrounds of CoPLLA17200 flat film and spherulites crystallized at 110^{o}C, 120 ^{o}C, and 145 ^{o}C at day 1 (top row) and CoPLLA1150, CoPLLA4500, CoPLLA17200, and CoPLLA28500 spherulites crystallized at 130 ^{o}C at day 1 (bottom row) at magnification of × 10. (d) Fluorescent images of cells on CoPLLA17200 crystallized at 145 ^{o}C and CoPLLA4500 crystallized at 130 ^{o}C combined with spherulite backgrounds at magnification of × 20.

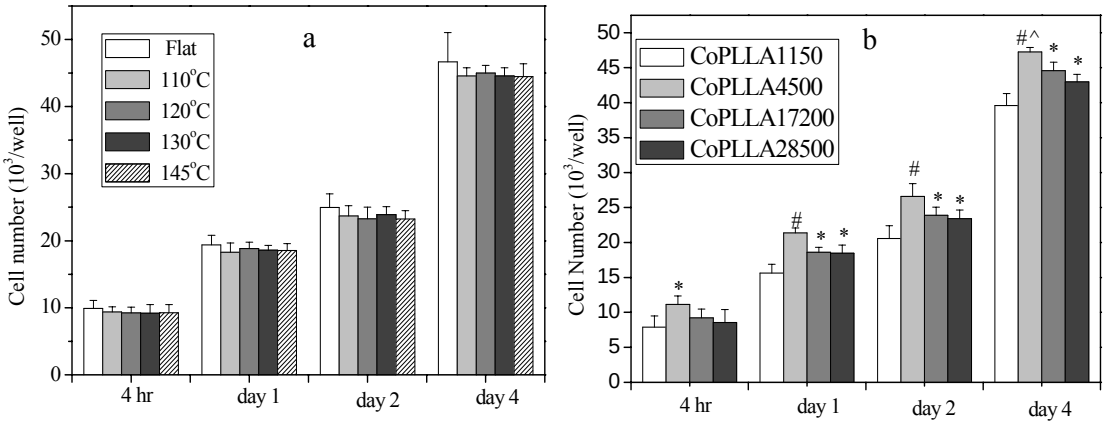

Figure 2.16 (a) Cell proliferation on CoPLLA1150, CoPLLA4500, CoPLLA17200, and CoPLLA28500 films crystallized at 130 °C represented by the cell numbers at 4 h, days 1, 2, and 4. *, $p < 0.05$; #, $p < 0.01$ relative to CoPLLA1150; ^, $p < 0.05$ relative to CoPLLA17200 and CoPLLA28500. (b) Cell proliferation on CoPLLA17200 flat films and spherulites crystallized at 110°C, 120 °C, and 145 °C represented by the cell numbers at 4 h, days 1, 2, and 4. (c) Cell area on the films at day 1.

The fundamental understanding of cell-material interactions provides effective guidance in developing biomedical devices. Both inter and intracellular signals are involved in the response of cells to the underlying substratum. The interface generated between cells and substratum called extra-cellular matrix plays a critical role in early events of cell adhesion, which determines later events such as spreading, migration, proliferation, and differentiation.[31,32] Surface characteristics including topography, chemistry, and mechanics directly determine cell-material interactions and the tissue-engineering applications of biomaterials.[52,53] In this study, the major factors to influence MC3T3-E1 cell behavior were surface roughness, topography, and wettability. Our recent study about the effect of PCL spherulites on MC3T3-E1 cells indicated that higher roughness induced by higher T_c promoted cell attachment and proliferation as a

rougher surface could adsorb more serum proteins.[30] This finding agreed with the present result of cell attachment and proliferation on CoPCL17200 films crystallized at different T_c. Hydrophilicity of biomaterials can regulate cell behavior but not in a monotonic mode. Higher hydrophilicity prevents protein adsorption causing poorer cell adhesion when the water contact angle is <~55^o, while lower hydrophilicity with water contact angle of >~55^o may also inhibit cell adhesion.[30] Our previous study also suggested that there was an optimal PEG composition (5%) at which cell attachment and proliferation maximized.[52] Incorporation of PEG into PCL or PLLA chains can modify the hydrophilicity, as demonstrated by the contact angle results here. As the water contact angles of CoPCL4500 and CoPLLA4500 were close to 55^o and therefore cells on those two samples had the best attachment and proliferation compared with others. CoPCL1150 or CoPLLA1150 had the highest hydrophilicity compared with other polymers and the high density of sparsely distributed PEG chains on the surface might strongly limit the protein adsorption, which in turn suppressed the cell attachment and spreading. Our results of cell proliferation on CoPLLA17200 films crystallized at different T_c were also roughly consistent with a previous finding that MC3T3-E1 cells on rougher PLLA substratum had even lower cell density.[29,54]

However, MC3T3-E1 cell alignment along the radial direction on both CoPCL and CoPLLA spherulites was not found in earlier studies.[27-30] Cells in general strongly respond to substrate topographies, such as micro-scale grooves and ridges, via the “contact guidance” effect.[31,32,55] The closest contact between cells and polymer surface is focal adhesions (FAs) which possess normally rectangular shape with a length of 1-5 μm.[32] The FAs tend to attach grooves or ridges in an oriented manner, especially

when the dimension of grooves or ridges is comparable to or smaller than that of FAs.[32,56,57] Subsequently actin filament or stress fibers can be aligned following the direction of aligned FAs. Cell response to grooves or ridges is cell-type dependent. Cell alignment was reported to occur on grooves with widths and depths as small as 100 and 35 nm, respectively.[58] To obtain thorough understanding about cell alignment on PCL or PLLA spherulites, we should explore the reason from the ridges formed by the lamellae radiating from the spherulite centers or the grooves at the grain boundaries between spherulites. Previous findings suggested that MC3T3-E1 cells were not aligned on both PLLA spherulites with small ridges (~30 nm, height; ~2 μm, width) formed by the lamellae radiating and the grooves at the grain boundaries between PLLA spherulites (~100 nm, depth; ~2 μm, width).[28] Even though human articular chondrocytes showed oriented morphology with a more isolated disposition on big PLLA spherulites (~50 μm, diameter; ~1 μm, depth) crystallized at 120 °C, the cells were not preferentially aligned along the radial direction.[59] The alignment of MC3T3-E1 cells on PCL spherulites crystallized at 25 °C was not observed either.[30] However, our AFM depth profile results in Figure 2.10 demonstrated that CoPCL4500 spherulites crystallized at 50 °C, CoPLLA17200 spherulites crystallized at 145 °C, and CoPLLA4500 spherulites crystallized at 130 °C had much larger depth and width for small ridges, measured to be ~450 nm and ~10 μm, respectively. By comparing our results with the previous studies, we may conclude that the spherulite diameter also exerted a great influence on cell alignment together with the dimension of small ridges formed by the lamellae radiating. In general, the dimension of cells after 1 day culture can reach over 50 μm in length.

Thus the spherulites larger than 50 mm in diameter can effectively guide the alignment of actin filaments. Otherwise, the continuous alignment in an individual spherulite can be interrupted when actin filaments sense neighboring spherulites with totally different directions of small ridges formed by the lamellae radiating.

As demonstrated in AFM results, the groove width and depth of CoPLLA4500 films crystallized at 130 °C were 41 ± 5 and 1.5 ± 0.3 μm, respectively. However, cells were aligned along the radial direction rather than the groove direction. Earlier investigations on cell response to microgrooves indicated that cells were either oriented along grooves or distributed in random direction bridging over multiple grooves.[32,55,60] Our results were different from those studies as the small ridges formed by the lamellae radiating on the top of groove ridges instead of grooves dominated the cell behavior. The small ridges on the top of groove ridges first communicated with cells when cells were exposed to this substrate and the cells respond to the small ridges formed by the lamellae radiating through “contact guidance”. Further the actin filaments were aligned along the small ridges, namely, the radius direction of the spherulites. Cells respond to banded polymer spherulites in a different way from those to traditional grooves. The only topographic feature in traditional grooves is the smooth groove ridge and smooth groove valley. In banded polymer spherulites, the topography is more complicated and can be considered as the combination of traditional grooves and small ridges formed by lamellae radiating, which are located on the top of groove ridges along the radius direction of spherulites. For anchorage-dependent cell type, such as MC3T3-E1, they can easily respond to the small ridges on the top of groove ridges rather than the grooves through “contact guidance”.

2.4 Conclusions

Two series of well-defined comb-dendritic tri-block copolymers have been synthesized via divergent synthesis of dendritic PEG with four generations using acetonide-protected anhydride derivative of 2,2-bis(hydroxymethyl)propionic acid and ring-opening polymerization (ROP) of ε-caprolactone or L-lactide monomers. The composition of copolymers was varied by controlling the feed ratio of monomers to hydroxyl groups to give variable PLLA or PCL arm lengths. The chemical structures were confirmed by ^{1}H NMR, FTIR, and GPC measurements. DSC measurements demonstrated that T_g, T_m, and χ_c increased with the increase of PLLA arm molecular weight. When PCL arm molecular weight increased, the T_m increased. χ_c also increased from CoPCL1150 to CoPCL17200 but decreased for CoPCL28500. DMA confirmed that tensile modulus was strengthened with the increase of molecular weight. Spherulite growth rate was accelerated with the drop of T_c and CoPCL17200 or CoPLLA17200 had the largest growth rate compared with other lengths in CoPCL series and CoPLLA series, respectively. Spherulite size was reduced when T_c dropped. In addition, crystalline cracks, ring-banded structure, and groove-like structure were observed in CoPLLA series. AFM detection demonstrated that the increase of T_c induced larger surface roughness. CoPCL17200 had larger roughness than others in CoPCL series when they were crystallized at 50 °C and CoPLLA4500 had higher roughness than others in CoPLLA series when they were crystallized at 130 °C. Water contact angles measurements showed that hydrophilicity was improved when the incorporation of PEG in copolymers increased. GIXRD study on copolymer films demonstrated that crystallite size, lattice

constants, and the crystallinity of copolymers increased with the penetration depth. Mouse pre-osteoblastic MC3T3-E1 cell attachment and proliferation were regulated by the hydrophilicity of the copolymers. For both CoPCL and CoPLLA, cells had the highest numbers when the arm molecular weight was 4500 g/mol. Cell attachment and proliferation were promoted when CoPCL with an arm molecular weight of 17200 g/mol was crystallized from 35 to 45 °C. There was a significant difference when the crystallization temperature for CoPLLA with an arm molecular weight of 17200 g/mol increased from 110 to 145 °C. Cells on CoPCL with arm molecular weights of 4500 and 17200 g/mol crystallized at 50 °C, as well as CoPLLA with an arm molecular weight of 17200 g/mol crystallized at 145 °C and 4500, 17200, and 28500 g/mol crystallized at 130 °C could sense the small ridges formed by the lamellae radiating and were strongly aligned along radius direction of spherulites.

References

[1] Ouchi, T.; Toyohara, M.; Arimura, H.; Ohya, Y. *Biomacromolecules* **2002**, *3*, 885.

[2] Fujiwara, T.; Miyamoto, M.; Kimura, Y. *Macromolecules* **2001**, *34*, 4043.

[3] Li, S. M.; Liu, L. J.; Garreau, H.; Vert, M. *Biomacromolecules* **2003**, *4*, 372.

[4] Luo, Y. F.; Wang, Y. L.; Niu, X. F.; Shang, J. F. *Eur. Polym. J.* **2008**, *44*, 1390.

[5] Du, Y. J.; Lemstra, P. J.; Nijenhuis, A. J.; Van Aert, H. A. M.; Bastiaansen, C. *Macromolecules* **1995**, *28*, 2124.

[6] Oliveira, J. M.; Salgado, A. J.; Sousa, N.; Mano, J. F.; Reis, R. L. *Prog. Polym. Sci.* **2010**, *35*, 1163.

[7] Malkoch, M.; Carlmark, A.; Woldegiorgis, A.; Hult, A.; Malmstrom, E. E. *Macromolecules* **2004**, *37*, 322.

[8] Teramoto, Y.; Nishi, Y. *Polymer* **2003**, *44*, 2701.

[9] Nouvel, C.; Dubois, P.; Dellacherie, E.; Six, J. L. *J. Polym. Sci. Part A: Polym. Chem.* **2004**, *42*, 2577.

[10] Dong, P. W.; Wang, X. H.; Gu, Y. C.; Wang, Y. J.; Wang, Y. J.; Gong, C. Y.; Luo, F.; Guo, G.; Zhao, X.; Wei, Y. Q.; Qian, Z. Y. *Colloid. Surface. A* **2010**, *358*, 128.

[11] Riess, G. *Prog. Polym. Sci.* **2003**, *28*, 1107.

[12] Fujiwara, T.; Kimura, Y. *Macromol. Biosci.* **2002**, *2*, 11.

[13] Fujiwara, T.; Miyamoto, M.; Kimura, Y. *Macromolecules* **2000**, *33*, 2782.

[14] Malkoch, M.; Malmstrom, E.; Hult, A. *Macromolecules* **2002**, *35*, 8307.

[15] Yang, Y.; Hua, C.; Dong, C. M. *Biomacromolecules* **2009**, *10*, 2310.

[16] Agrawal, P.; Gupta, U.; Jain, N. K. *Biomaterials* **2007**, *28*, 3349.

[17] Bhadra, D.; Bhadra, S.; Jain, N. K. *J. Drug. Del. Sci. Tech.* **2005**, *15*, 65.

[18] Gong, F.; Cheng, X.; Wang, S.; Wang, Y.; Gao, Y.; Cheng, S. *Polymer* **2009**, *50*, 2775.

[19] Li, Y.; Zhu, Y.; Xia, K.; Sheng, R.; Jia, L.; Hou, X.; Xu, Y.; Cao, A. *Biomacromolecules* **2009**, *10*, 2284.

[20] Li, Y.; Li, Q.; Li, F.; Zhang, H.; Jia, L.; Yu, J.; Fang, Q.; Cao, A. *Biomacromolecules* **2006**, *7*, 224.

[21] Hecht, S.; Frechet, J. M. J. *J. Am. Chem. Soc.* **2001**, *123*, 6959.

[22] Ihre, H.; Padilla De Jesus, O. L.; Fréchet, J. M. J. *J. Am. Chem. Soc.* **2001**, *123*, 5908.

[23] Ostmark, E.; Macakova, L.; Auletta, T.; Malkoch, M.; Malmstrom, E.; Blomberg, E. *Langmuir* **2005**, *21*, 4512.

[24] Yakabe, H.; Sasaki, S.; Sakata, O.; Takahara, A.; Kajiyama, T. *Macromolecules* **2003**, 36, 5905.

[25] Nishino, T.; Matsumoto, T.; Nakamae, K. *Polym. Eng. Sci.* **2000**, 40, 336.

[26] Yakabe, H.; Tanaka, K.; Nagamura, T.; Sasaki, S.; Sakata, O.; Takahara, A.; Kajiyama, T. *Polym. Bull.* **2005**, 53, 213.

[27] Park, A.; Cima, L. G. *J. Biomed. Mater. Res.* **1996**, 31, 117.

[28] Simon, C. G. Jr. *J. Microscopy* **2004**, 216,153.

[29] Washburn, N. R.; Yamada, K. M.; Simon, C. G. Jr.; Kennedy, S. B.; Amis, E. J. *Biomaterials* **2004**, 25, 1215.

[30] Wang, K.; Cai, L.; Jesse, S.; Wang, S. *Langmuir* **2012**, 28, 4382.

[31] Wu, X.; Wang, S. *ACS Appl. Mater. Interfaces* **2012**, 4, 4966.

[32] Wang, K.; Cai, L.; Zhang, L.; Dong, J.; Wang, S. *Adv. Healthcare. Mater.* **2012**, 1, 292.

[33] Choi, Y.; Kim, S. Y.; Moon, M. H.; Kim, S. H.; Lee, K. S.; Byun, Y. *Biomaterials* **2001**, *22*, 995.

[34] Cai, L.; Wang, S. *Polymer* **2010**, *51*, 164.

[35] Shiomi, T.; Imai, K.; Takenaka, K.; Takeshita, H.; Hayashi, H.; Tezuka, Y. *Polymer* **2001**, *42*, 3233.

[36] Cerrai, P.; Tricoli, M.; Andruzzi, F.; Paci, M.; Paci, M. *Polymer* **1989**, *30*, 338.

[37] Ou-Yang, W. C.; Li, L. J.; Chen, H. L.; Hwang, J. C. *Polym. J.* **1997**, *29*, 889.

[38] Bhushan, B.; Jung, Y. C. *Ultramicroscopy* **2007**, *107*, 1033.

[39] Yuan, W.; Yuan, J.; Zhang, F.; Xie, X.; Pan, C. *Macromolecules* **2007**, *40*, 9094.

[40] Tao, T.; Gong, A.; Lu, J.; Sue, H. J.; Bergbreiter, D. E. *Macromolecules* **2001**, *34*, 7672.

[41] Ren, Y. J.; Zhang, H.; Huang, H.; Wang, X. M.; Zhou, Z. Y.; Cui, F. Z.; An, Y. H. *Biomaterials* **2009**, *30*, 1036.

[42] Curran, J. M.; Chen, R.; Hunt, J. A. *Biomaterials* **2005**, *26*, 7057.

[43] Ma, M.; Hill, R. M. *Curr. Opin. Colloid Interface Sci.* **2006**, *11*, 193.

[44] Jiang, Y.; Luo, Y.; Fan, Z.; Wang, X.; Xu, J.; Guo, B.; Li, L. *Sci. China Ser. B* **2003**, *46*, 152.

[45] Di Lorenzo, M. L. *Polymer* **2001**, *42*, 9441.

[46] Miyata, T.; Masuko, T. *Polymer* **1998**, *39*, 5515.

[47] He, C.; Sun, J.; Jia, M.; Chen, X.; Jing, X. *Biomacromolecules* **2006**, *7*, 3482.

[48] Nurkhamidah, S.; Woo, E. M. *J. Appl. Polym. Sci.* **2011**, *122*, 1976.

[49] Sun, J. R.; Hong, Z. K.; Yang, L. X.; Tang, Z. H.; Chen, X. S.; Jing, X. B. *Polymer* **2004**, *45*, 5969.

[50] Cheung, Z. L.; Ng, K. M.; Weng, L. T.; Chan, C. M.; Li, L. *Polymer* **2006**, *47*, 3164.

[51] Cheung, Z. L.; Weng, L. T.; Chan, C. M.; Hou, W. M.; Li, L. *Langmuir* **2005**, *21*, 7968.

[52] Cai, L.; Wang, K.; Wang, S. *Biomaterials* **2010**, 31, 4457.

[53] Anselme, K.; Bigerelle, M. *Int Mater Rev.* **2011**, 56, 243.

[54] Degirmenbasi, N.; Ozkan, S.; Kalyon, D. M.; Yu, X. *J. Biomed. Mater. Res., Part A* **2009**, 88, 94.

[55] Bettinger, C. J.; Langer, R.; Borenstein, J. T. *Angew. Chem., Int. Ed.* **2009**, 48, 5406.

[56] Biggs, M. J. P.; Dalby, M. J. *P. I. Mech. Eng. H* **2010**, 224, 1441.

[57] Geiger, B.; Spatz, J. P.; Bershadsky, A. D. *Nat. Rev.* **2009**, 10, 21.

[58] Loesberg, W. A.; te Riet, J.; van Delft, F. C. M. J. M.; Schon, P.; Figdor, C. G.; Speller, S.; van Loon, J. J. W. A.; Walboomers, X. F.; Jansen, J. A. *Biomaterials* **2007**, 28, 3944.

[59] Martinez, E. C.; Escobar Ivirico, J. L.; Munoz Criado, I.; Gomez Ribelles, J. L.; Monleon Pradas, M.; Salmeron Sanchez, M. *J. Mater. Sci. Mater. Med.* **2007**, 18, 1627.

[60] Wang, K.; Cai, L.; Zhang, L.; Dong, J.; Wang, S. *Adv. Healthcare Mater* **2012**, 1, 292.

CHAPTER III
REGULATING MC3T3-E1 CELLS ON DEFORMABLE POLY(ε-CAPROLACTONE) HONEYCOMB FILMS PREPARED USING A SURFACTANT-FREE BREATH FIGURE METHOD IN A WATER-MISCIBLE SOLVENT

3.1 Introduction

It is a great challenge to repair massive defects in bone when the balance between resorption and regeneration is lost in its degeneration caused by aging and disease [1,2]. A variety of synthetic and natural polymers have been developed as filler materials in bone surgery [1,2]. Although they can handle immediate problems, there exist some prominent disadvantages such as mismatch in mechanical properties and lack of sufficient biocompatibility and bioactivity with the surrounding tissue over long-term observation of implants made from these materials [1,2]. Therefore, much attention has been drawn to developing new-generation biomaterials with improved mechanical properties, biocompatibility, and bioactivity using advanced biomimetic approaches.

One biomimetic approach is to mimic basement membrane, which exists throughout vertebrate body and provides substrata for overlying cellular structures. They are composed of extracellular matrix (ECM) proteins such as fibrous collagen, laminin, and fibronectin, which supply integrin receptors for cell anchorage and regulate subsequent events [3,4]. Structural features at the micro- and nanometer scales, the main topography of basement membranes, and their mechanical properties dramatically affect integrin-cytoskeleton links and cell functions [3-5]. To mimic these complex features, synthetic substrates with grooves, pits, pores, wells and nodes, spheres, or ridges, have

been developed [34,6-8]. Many methods such as phase separation, colloidal templating, and lithography have been used to fabricate porous topography with ordered structures [3,4]. Among these methods, the breath-figure method is very simple and economical, in which polymer is dissolved in in a volatile and water-immiscible solvent such as chloroform ($CHCl_3$), benzene, and carbon disulfide (CS_2) and then the solution evaporates quickly in a humid environment [9,10]. The sharp drop of the temperature in polymer solution upon rapid solvent evaporation causes condensation of water vapor in air. Subsequently polymer precipitates and stabilizes water droplets with identical diameters orderly packed in a hexagonal array on the solution/air interface as the result of capillary force and convection currents. Then honeycomb polymer films can be obtained after complete drying.

Poly(ε-caprolactone) (PCL) is a biodegradable semi-crystalline polymer with excellent biocompatibility and biodegradability for biomedical applications and has been fabricated into porous bone tissue engineering scaffolds using different methods [11]. Honeycomb PCL films were prepared using water-immiscible solvents with the assistance of amphiphilic copolymers such as co-carboxyhexyl acrylamide [12-20]. PCL films with multilayers of ordered pores were also prepared using silica microspheres as the template [21]. Honeycomb PCL films with different micropore diameters were further used to regulate adhesion, spreading, and proliferation of endothelial cells, hepatocytes, epidermal keratinocytes, and dermal fibroblasts, and differentiation of neural stem cells [8,14-20]. There lack studies on regulating osteoblastic adhesion, differentiation, and gene expression on honeycomb films of biodegradable polymers with tunable micropores, although porous substrates/scaffolds have been developed for enhancing bone cell

functions [22,23]. In addition, this study was the first time to prepare honeycomb PCL films from solutions in water-miscible tetrahydrofuran (THF) via the breath-figure method without the need of a surfactant. Previously THF was also used as a solvent for poly(L-lactide), poly(methyl methacrylate), cellulose acetate-butyrate, and carboxylate-terminated polystyrene to prepare porous films and fibers [24-27]. Compared with toxic $CHCl_3$ and benzene used in the previous preparation of honeycomb PCL films [12-20], THF is apparently advantageous because it is relatively non-toxic.

In this report, we first present fabrication and characterization of the honeycomb PCL films with tunable pores. Then we discuss the evaluation of these honeycomb films as bone tissue engineering substrates by culturing mouse pre-osteoblastic MC3T3-E1 cells on them and the flat control. Cell adhesion, spreading, proliferation, alkaline phosphatase (ALP) activity, and calcium content were determined and correlated with gene expression of four bone-specific differentiation markers, ALP, collagen type I (COL I), osteocalcin (OCN), and osteopontin (OPN). Honeycomb PCL films were further stretched into groove-like structures, on which MC3T3-E1 cells were cultured for evaluating cell distribution and alignment. This study not only supplies a convenient method to produce large-area porous substrates for biomedical applications, but also demonstrates an appropriate range of micropore dimensions for enhancing pre-osteoblastic cell behavior.

3.2 Experimental Section

3.2.1 Fabrication of PCL Films

PCL (M_n = 97700 g mol^{-1}, M_w = 144200 g mol^{-1}) used in this study was purchased from Aldrich (Milwaukee, WI) and used in our previous studies [28-30]. PCL was dissolved in distilled THF (Aldrich) at a concentration of 50 mg mL^{-1}. Then the PCL solution was cast onto clean glass slides and put in a chamber. At a relative humidity of 75%, honeycomb films with pore diameters of 3.5, 6.0, and 10 μm were fabricated by controlling the airflow rate at 100, 50, and 0 mL min^{-1}, respectively. The PCL films became opaque gradually and evaporation was conducted for 5 min prior to further treatment. For comparison, flat films were also prepared by casting the same PCL solution onto clean glass slides without a humid environment. Stretched PCL films were prepared by stretching all the films at an elongation ratio, i.e., the ratio of the final length to the initial length, of 4.5 at room temperature (23 °C).

3.2.2 Surface Topography

The as-prepared PCL films were fixed on glass slides, dried completely in vacuum, and sputter-coated with a gold-palladium layer (Emscope SC 500, Elexience). The surface morphology of the honeycomb films was observed using Scanning Electron Microscopy (SEM; S-3500, Hitachi Instruments, Tokyo, Japan) at an accelerating voltage of 5 kV.

3.2.3 Water Contact Angle and Protein Adsorption

PCL films were dried completely in vacuum overnight before the measurements. Water contact angles were determined using a Ramé-Hart NRC C. A. goniometer (model 100-00-230) and water droplets were photographed using 3.0 megapixel camera (*Moticam 2300*, Motic) at room temperature. To evaluate serum protein adsorption, flat and honeycomb PCL films were soaked for 4 h at 37 °C in the media used for culturing MC3T3-E1 cells. The films were rinsed with PBS five times to remove unattached proteins, and immersed in 300 μL of 1% sodium dodecyl sulfate (SDS) solution five times with 1 h interval to collect proteins adsorbed on the films. A MicroBCA protein assay kit (Pierce, Rockford, IL) and a micro-plate reader (SpectraMax Plus 384, Molecular Devices, Sunnyvale, CA) were used to determine the concentrations of the proteins in the collected SDS solutions. All data was calibrated using a standard curve constructed from albumin solutions according to the manufacturer's instruction.

3.2.4 Cell Culture

Mouse MC3T3-E1 cells (ATCC, Manassas, VA) were cultured in the same way as reported by us [28-34]. Prior to cell studies, all PCL films were immersed in 70% alcohol solution overnight to remove the residues from sample preparation, further sterilized by 70% alcohol solution for 3 × 30 min, and dried in vacuum. Cells were seeded on the samples at a density of ~15,000 cells/cm^2 in α-Minimum Essential Media (α-MEM, Gibco) containing 10% fetal bovine serum (FBS, Gibco) and 1% penicillin/streptomycin (Gibco). Then the cells were cultured for 4 h, 1, 2, and 4 days in an incubator at 37 °C with humidity of 95% and 5% CO_2.

3.2.5 Immunofluorescence Microscopy and Cell Morphology

MC3T3-E1 cells on the films were fixed with 16% paraformaldehyde (PFA) solution for 30 min. After PFA was removed, cells were rinsed with phosphate buffered saline (PBS) twice and permeabilized with 0.2% (v/v) Triton X-100. Then the cells were washed with PBS and stained with rhodamine-phalloidin (RP) for 2 h at 37 °C, followed by 4',6-diamidino-2-phenylindole (DAPI) staining at room temperature. An Axiovert 25 light microscope (Carl Zeiss, Germany) was used for photographing. Cells were counted using DAPI-stained images and the mean number of nuclei per field (n = 20) was calculated. Average cell area was measured from 20 non-overlapping cells at day 1 using ImageJ software (National Institutes of Health, Bethesda, MD). F-actin cytoskeleton at day 1 was observed using a confocal microscope (SP2, Leica). Focal adhesions (FAs) of cells were stained with mouse monoclonal anti-vinculin antibody (V9264, Sigma-Aldrich) for 1 h at 37 °C followed by five rinses with PBS. Then the FAs were labeled by anti-mouse IgG-FITC antibody (F0257, Sigma) at 37 °C for 5 h and were recorded under a confocal microscope. For SEM imaging, cells cultured for 1 day were fixed in 5% paraformaldehyde (w/v) for 30 min and rinsed with PBS for three times. Then all samples were dehydrated with gradient ethanol solutions (30%, 50%, 70%, 95%, and 100%) for 20 min twice at each concentration and dried in vacuum overnight. After being sputter-coated with one gold-palladium layer, the samples were observed using SEM in the same way for characterizing polymer film topography.

3.2.6 Characterization of Aligned Cells

MC3T3-E1 cells cultured on the stretched PCL films were fixed, stained,

photographed, and analyzed using ImageJ as described above. Cell alignment was characterized with the extent the equimomental ellipse was deformed, defined by dividing the difference between the long-axis length and short-axis length by the short-axis length. The percentage of aligned cells in the entire cell population was also calculated. Cells were considered as aligned when the angle between the long axis and the direction of the underlying polymer microgroove structure was smaller than 15°. For each sample, 200 cells were analyzed to determine these two parameters. Average cell area was measured from 30 cells in the fluorescent images.

3.2.7 ALP Activity and Calcium Content

After 14 days of cell culture, all PCL films were transferred to new plastic tubes and rinsed with PBS twice to remove unattached cells. Then the adherent cells were collected by trypsinization, which was terminated by adding α-MEM. The cell suspension was centrifuged for 4 min at 1000 rpm, rinsed with PBS, and then centrifuged again for 4 min at 1000 rpm. The obtained cell pellet was suspended in 1 mL of 0.2% Nonidet P-40 solution and sonicated in ice water for 2 min. A fluorescence-based ALP detection kit (Sigma, St. Louis, MO) and a QuantiChrom calcium assay kit (BioAssay Systems, Hayward, CA) were used to determine the ALP activity and calcium content of the cell lysate, respectively [32].

3.2.8 Gene Expression

For determining the expression levels of integrin α_1, α_2, and β_3, MC3T3-E1 cells were cultured on PCL films for one day. Then the cellular RNA was isolated from the

cells using an RNeasy Mini Kit (Qiagen, Valencia, CA) and cDNA was synthesized using a cDNA synthesis kit (Thermo Scientific). Expression of integrin subunits of α_1, α_2, β_1, and glyceraldehyde-3-phosphate dehydrogenase (GAPDH) utilized for normalization of the differences in the amount of total RNA was quantified through real-time polymerase chain reaction (PCR) with a Power SYBR® Green PCR Master Mix (Applied Biosystems, Carlsbad, CA) and performed on a thermal cycler with fluorescence detection systems (PTC-200, MJ Research). Expression of ALP, COL I, OCN and OPN was performed after cells were cultured on PCL films for 14 days using the same protocol as described above. All the primers for real-time PCR are shown in Table 3.1.

Table 3.1 Oligonucleotide primer sequences for real-time PCR.

Gene	Primer sequence (5'-3'; F: forward; R: reverse)
COL I	F: TCTCCACTCTTCTAGTTCCT
	R: TTGGGTCATTTCCACATGC
OCN	F: CAAGTCCCACACAGCAGCTT
	R: AAAGCCGAGCTGCCAGAGTT
ALP	F: GCCCTCTCCAAGACATATA
	R: CCATGATCACGTCGATATCC
OPN	F: ACACTTTCACTCCAATCGTCC
	R: TGCCCTTTCCGTTGTTGTCC
Integrin α_1	F: TGAGCCCACCAAGATGAACGA
	R: CCTGGCCGGTGTGATTGT
Integrin α_2	F: ACAAGGCAACTGGCTACTGGT
	R: ACAGGTGGCAGTGGGTAGG
Integrin β_1	F: GGTGTCGTGTTTGTGAATGC
	R: TCCTGTGCACACGTGTCTT
GAPDH	F: ACTTTGTCAAGCTCATTTCC
	R: TGCAGCGAACTTTATTGATG

3.3 Results and Discussion

3.3.1 Morphology and Hydrophilicity of the Honeycomb Films

In the breath-figure method, parameters used to achieve different pore diameters and morphologies include solvent type, air flow rate, humidity, additives, interfacial activity of polymers, and the concentration and amount of polymer solution [9,10]. In this study, the airflow rate was the key factor to regulate the pore diameter of the honeycomb films. When airflow rates of 60, 40, and 0 mL/min were applied in forming honeycomb PCL films, the as-formed average pore diameters were 3.5, 6.0, and 10 μm, respectively (Figure 3.1A). Faster airflow could accelerate the evaporation process and more efficiently decreased the temperature on the polymer solution, condensing a larger amount of water droplets. Owing to the fast evaporation of the solvent, coalescence of water droplets rarely occurred and thus smaller pores on the surface of polymer solution could be formed at a higher airflow rate. Consistent with other honeycomb films prepared from THF solutions, the honeycomb PCL films here also showed a monolayer architecture with a solid bottom although THF is lighter than water [24,25]. As demonstrated in the inset tilted SEM image for 6.0-μm pores, many pores in the honeycomb films were interconnected when the pore diameter was 6.0 or 3.5 μm, similar to honeycomb PCL films prepared with assistance of an amphiphilic copolymer [12,15,18,20]. Figure 1B shows that the distribution of pore diameter was narrow on all the honeycomb films and the 6.0-μm pores were more uniform than the other two. Differential scanning calorimetric tests were performed for the flat and honeycomb PCL films but no differences were found in their melting points and crystallinities, suggesting

that formation of the honeycomb pattern on PCL films did not influence the thermal properties.

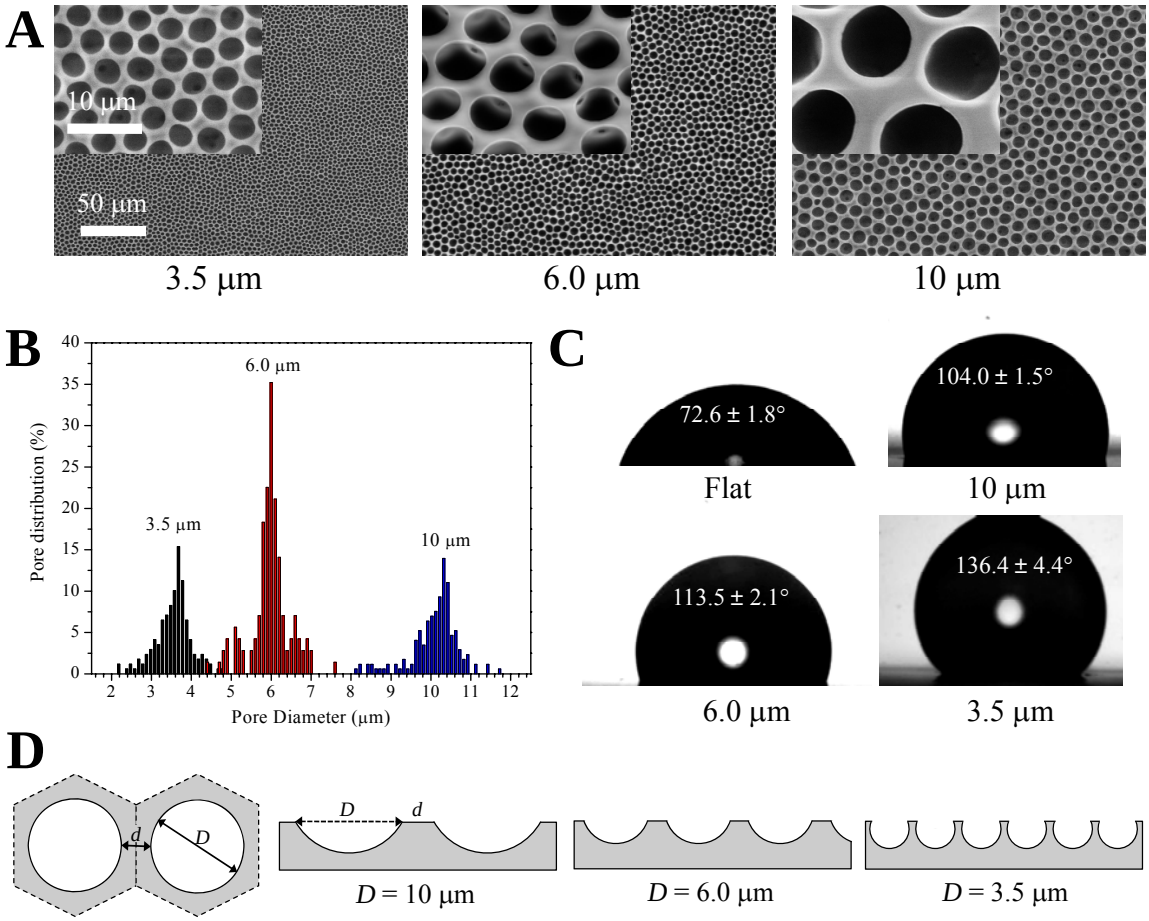

Figure 3.1 (A) SEM images of the honeycomb films with different pore diameters. Scale bar of 50 μm is applicable for the images with the lower magnification (×700). Scale bar of 10 μm is applicable for the insets (magnification: ×5000). (B) Distribution of pore diameter in the honeycomb films. (C) Micrographs of water droplets and contact angles on the flat and honeycomb films. (D) Model of two adjacent hexagonal unit cells containing pores of diameter *D* and rim size *d* (left) and schematic cross-sections of honeycomb films with three different pore diameters.

The wettability of polymer films can be influenced by surface topography [35-37]. As demonstrated in Figure 3.1C, the water contact angles were 72.6 ± 1.8°, 104.0 ± 1.5°,

113.5 ± 2.1° and 136.4 ± 4.4° on the flat film and honeycomb films with pore diameters of 10, 6.0 and 3.5 μm, respectively. Micro- or nano-structured surface such as these honeycomb films are known to be more hydrophobic by producing air pockets between substrate surface and water droplets when water droplets were much larger than the dimension of the structures present on substrate surface. The Cassie and Baxter model in eq. 1 was employed to predict the water contact angles (θ) on these honeycomb films [21,35-37].

$$\cos\theta = (1 - f_o)\cos\theta_s + f_o\cos\theta_o \qquad (1)$$

where f_o is the fractional flat geometrical area of liquid-air interface beneath a water droplet, θ_s is the water contact angle on the smooth PCL surface, i.e., 72.6° here, and θ_o is the water contact angle on the pore filled with air, which is 180°. When the pore diameters (D) were 10, 6.0 and 3.5 μm, the rim sizes (d) measured from the SEM images in Figure 1A were 3.05 ± 0.25, 1.71 ± 0.40, and 0.83 ± 0.04 μm, and then the f_o values were calculated to be 0.528, 0.553, and 0.592, respectively. They were consistent with the values of 0.532, 0.549, and 0.592 estimated from a hexagonal unit cell model with a pore in the center (Figure 3.1D).

The water contact angles calculated from eq. 1 were 112.6°, 114.6°, and 117.9° for the honeycomb films with pore diameters of 10, 6.0, and 3.5 μm, respectively. The prediction was higher than the experimental value for 10-μm pores but lower for 3.5-μm pores. Although the model did not predict the strong dependence of water contact angle on the pore diameter, it still provided reasonable explanation for the increased hydrophobicity on the smaller pores. In another study, the water contact angles were

105.6°, 104.3°, 107.2°, and 105.0° on honeycomb PCL films with pore diameters of 5.3, 9.1, 11.8, and 15.6 μm, and rim sizes of 1.8, 3.1, 3.6, and 7.1 μm, respectively [18]. The reported water contact angle of 74° on flat PCL was close to the θ_o value in our present study. Using these parameters and the model in Figure 1D, we obtained f_o values of 0.505, 0.504, 0.532, and 0.428, in agreement with the porosity data of 0.506, 0.510, 0.547, and 0.426 given in that report [18]. Then we calculated water contact angles of 105.7°, 113.8°, 111.6°, and 111.7° from eq. 1. The comparison between these two studies shows that the hydrophobicity of honeycomb PCL films could be significantly strengthened by smaller pores, which can be stronger than the prediction by the Cassie and Baxter model. In addition, the preparation method here of not using an amphiphilic copolymer could also influence the hydrophilicity of the obtained honeycomb films.

3.3.2 Cell Adhesion

After 1-day culture, MC3T3-E1 cell adhesion was examined using fluorescent cell images, characterization of FAs, which are the closest contacts between cells and the underlying substrate, and integrin expression [38,39]. As shown in Figure 3.2A, all the pores here were subcellular and cells could spread over multiple pores without being aligned along the rim, which was found for cardiac myocytes on overcellular honeycomb PCL films with a pore diameter of 12.5 μm and a rim size of 8.0 μm [19]. Cytoskeleton with F-actin stained red on the flat films had very few stress fibers while the cells on the honeycomb films spread better and had more better-defined stress fibers and protrusions. The cytoskeleton on the honeycomb films with pore diameters of 10 and 6.0 μm was trapped inside the pores. Cells on the honeycomb films with 3.5-μm pores had even

better defined stress fibers while no trapped cytoplasm was found. In a previous report, fibroblasts were found to be sensitive to changes in radius of curvature on quartz surface with microscale round pits to decide they chose to enter the pits or move around this obstacle [40]. In this study, larger pores had larger radius of curvature for both pore edge and inside pores, and consequently less sharp discontinuous region between flat-tops and pores, as illustrated in Figure 3.1D. This may be the reason for MC3T3-E1 cells being trapped by the larger pores.

Vinculin-stained cell images in Figure 3.2A showed significantly more punctate FAs on the honeycomb films, especially when the pores were smaller, in contrast to diffusive vinculin staining on the flat ones. Moreover, the FAs of MC3T3-E1 cells on the honeycomb films were distributed not only on cell periphery but also along the pore edge. As demonstrated in Figure 3.2B, FAs were quantified by using the average area of FAs, FA density, i.e., the average number of FAs per cell, and the circularity of FAs, defined as $4\pi \times \text{area/perimeter}^2$. The first two parameters of FAs on the honeycomb films were markedly larger than those on the flat ones and were further strengthened by decreasing the pore diameter. The circularity of FAs on the flat films was close to 1, a measure for a perfect circle. It was lower on the honeycomb films and further decreased when the pore diameter decreased, indicating that the alignment of FAs expressed as the inverse of circularity was enhanced.

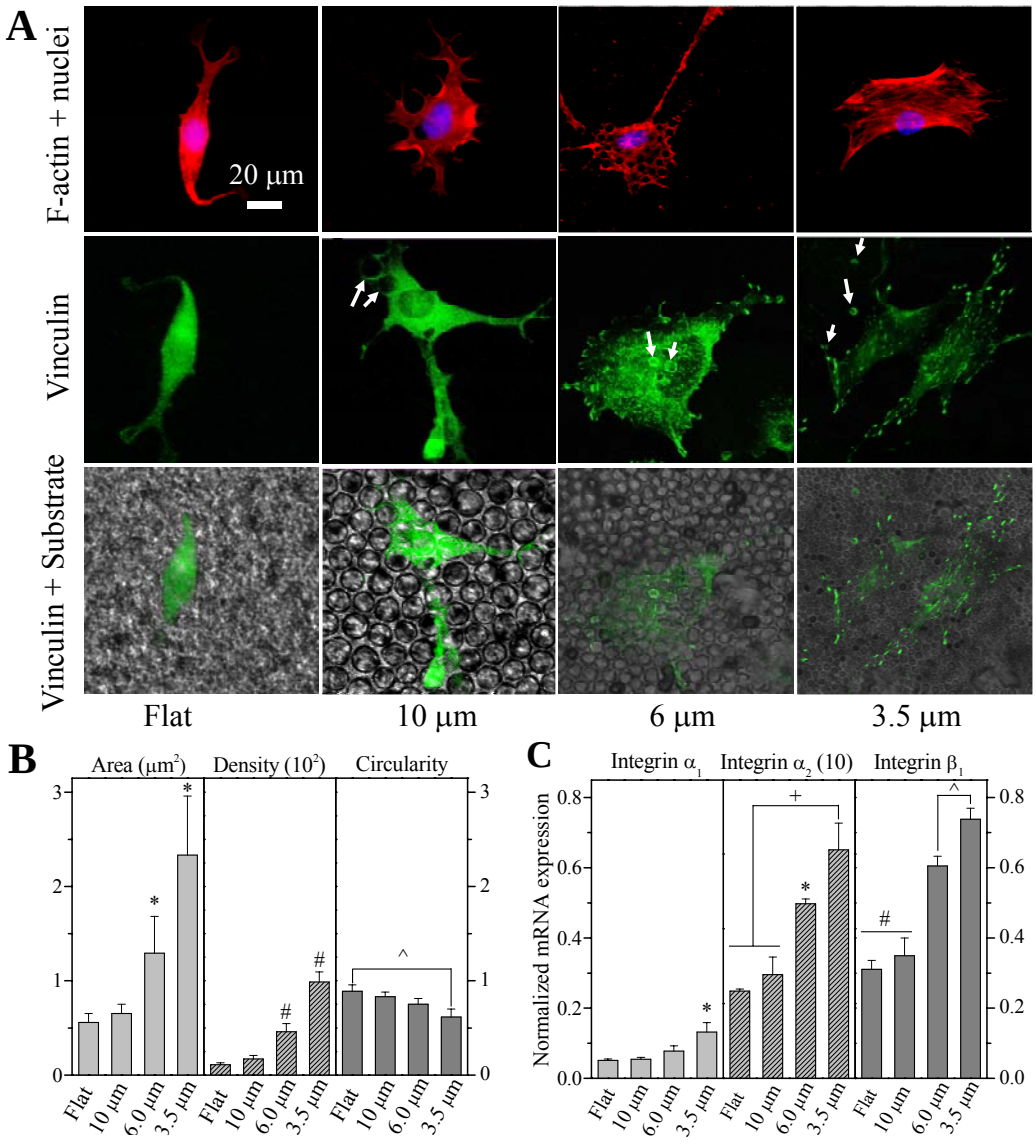

Figure 3.2 (A) Fluorescent images of MC3T3-E1 cells stained with RP (red) and DAPI (blue) (top row), vinculin-stained cell images (middle row) with arrow heads indicating pores of the honeycomb films, and merged images with the underlying substrates at day 1 post-seeding. Scale bar of 20 μm is applicable for all. (B) Area, density, and circularity of FAs. (C) Integrin expression of cells. *: $p < 0.05$; #: $p < 0.01$ relative to others. +: $p < 0.01$. ^: $p < 0.05$.

Cells react to micro/nano-topography mainly through the "contact guidance" effect [3-8]. For example, FAs of fibroblasts were found to appear on the ridges of microgrooved substrates in an oriented manner and the actin filaments would originate

from these adhesion points [6,41]. After FA are aligned, actin filaments or stress fibers in attached cells can also be aligned [6,7,38,39]. Previous findings also suggested that moving or extending cells prefer to be localized at the region of junction or discontinuity, which was the pore edges on the honeycomb films studied here [42]. On the basis of f_o and D, the number of pores and the total length of pore edges in a unit projected area of 1 cm^2 can be estimated. The former parameter increased from 6.8×10^5 to 1.9×10^6 and 6.2×10^6 and the latter increased from 21.3 to 36.6 and 67.7 m when the pore size decreased from 10 to 6.0 and 3.0 μm, respectively. Thus the honeycomb films with small pores generating a large region of junction or discontinuity provide excellent circumstance for cell adhesion and growth.

The FA-ECM interactions involve integrins, which are transmembrane heterodimers of the α-subunit and β-subunit [5,43,44]. Integrins bind different ECM proteins with the external end and cytoskeleton via adapter proteins such as talin, α-actinin, filamin and vinculin, and FAs are based on this integrin-adapter protein–cytoskeleton complex [5,43.44]. ECM proteins, to which osteoblasts can directly react, include fibronectin, COL I, and vitronectin [43,44]. Osteoblasts anchor on substrate surface via integrin receptors which are involved in processes named as "outside-in-signaling" and "inside-out-signaling" between the ECM and the cell. These integrin-involved pathways can regulate subsequent cell adhesion, migration, proliferation, and differentiation. Osteoblasts can express integrin subunits α_1, α_2, α_3, α_4, α_5, α_6, α_v, β_1, β_2, and β_5 [43,45]. As shown in Figure 3.2C, the expression levels of integrin subunits α_1, α_2, and β_1 on the honeycomb films with smaller pores were significantly higher. Binding of

$\alpha_1\beta_1$ and $\alpha_2\beta_1$ to type-I collagen, the most abundant bone matrix protein, is critical in regulating osetoblastic differentiation, whereas subunit β_1 is responsible for attachment to fibronectin or COL I [43-45].

3.3.3 Protein Adsorption

Cell adhesion to a substrate is closely related to proteins adsorbed on the surface, which is dependent on material chemistry and morphology [5]. When the pore diameter in the honeycomb films decreased, the pore edge or the rim also decreased while the entire surface area that included both the flat-tops and inside the pores significantly increased. Figure 3.1D shows three schematic cross-sections of the honeycomb films, in which spherical caps were used to represent the pores left by the water droplets. Using simple geometrical computation, we obtained the entire surface area based on the pore diameters and the heights of spherical caps, which were 2.37, 2.32, and 2.96 μm calculated from the schemes in Figure 3.1D for pore diameters of 3.5, 6.0, and 10 μm, respectively. When the pore diameter was 10 or 6.0 μm, the spherical cap was smaller than a hemisphere. For 3.5-μm pores, the spherical cap was greater than a hemisphere. The ratios (R_s) of the entire surface area to the projected area were 1.00, 1.15 ± 0.11, and 1.25 ± 0.10, and 2.03 ± 0.18 for the flat films and honeycomb ones with pore diameters of 10, 6.0, and 3.5 μm, respectively. Per a unit projected area, the flat-top area of the honeycomb films, calculated using (1 - f_o), decreased from 0.472 to 0.447 and 0.408, while the area inside the pores, calculated using (R_s + f_o - 1), increased from 0.678 to 0.803 and 1.622 when the pore diameter decreased from 10 to 6.0 and 3.5 μm, respectively.

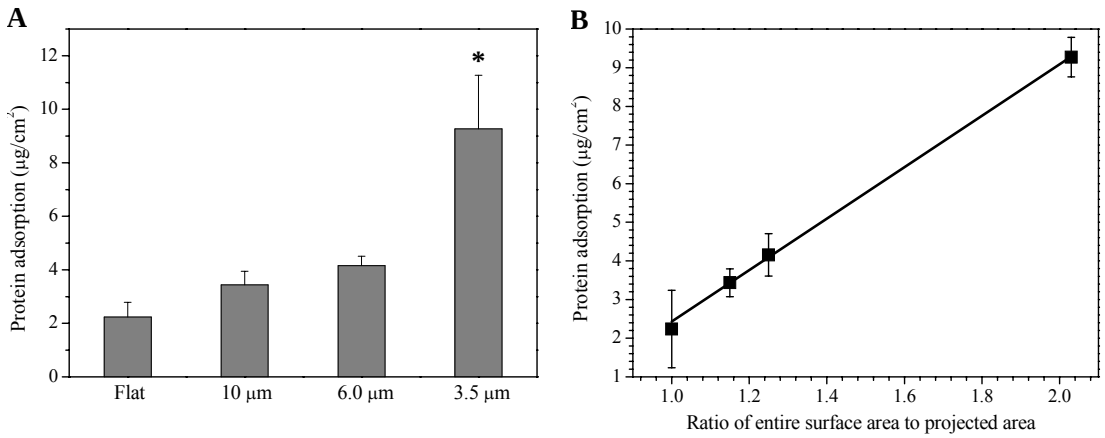

Figure 3.3 (A) Serum protein adsorption of the flat film and honeycomb films with different pore diameters in α-MEM. *: $p < 0.05$ relative to others. (B) Protein adsorption vs. ratio of entire surface area of the films to projected area.

As a result, honeycomb films with larger contract area with the serum proteins in the culture media could promote protein adsorption and it was even higher when pores were smaller. Figure 3.3A indicates that the concentration of the serum proteins adsorbed on the films increased significantly from 2.24 ± 1.00 μg cm^{-2} for the flat one to 9.27 ± 0.51 μg cm^{-2} for the honeycomb films with the pore diameter of 3.5 μm. As shown in Figure 3.3B, protein adsorption followed a linear relationship ($R^2 = 0.9984$) with the ratio of the entire surface area to the projected area, suggesting that it was solely determined by the surface area while the film chemistry did not exert extra effect on the protein adsorption. Although surfaces became more hydrophobic macroscopically, this effect was induced topographically and might not function at the scale of protein size or further influence cell behavior because all the films were rinsed in culture media prior to cell seeding.

MC3T3-E1 cells could sensitively respond to the proteins distributed on the substrates and produce integrin proteins accelerating the formation of FAs and fostering the expression of integrin subunits of α_1, α_2, and β_1 corresponding to osteoblasts, as discussed earlier. However, MC3T3-E1 cells did not spread into most pores, especially when the pore diameter was 3.5 μm, meaning that the proteins adsorbed inside the pores might not contribute much to supporting cell adhesion. In another report, fibroblasts were also seen very occasionally to touch the bottom of the 2-μm grooves while FAs were observed on the wider microgrooves [41]. Assuming that the capability of adsorbing proteins was identical on the surfaces of the flat-tops and inside the pores, we found that the protein concentration on the flat-top area of the honeycomb films with smaller pores would be actually lower. Thus purely the concentration of adsorbed proteins may not be used to interpret the better MC3T3-E1 cell adhesion on the honeycomb films with smaller pores. It should be noted that honeycomb structures could not only enhance protein adsorption but also influence distribution of adsorbed proteins. For example, the fibril-like aggregates of fibronectin were found to locate on the periphery of the pores of honeycomb PCL films, which may further determine the FAs of the cells around these pores [15-18,20]. It is unclear if that was the case in this study but the pore edge itself should be able to stimulate the formation of FAs and then guide and align them, as discussed earlier.

3.3.4 Cell Attachment, Proliferation, and Nuclear Deformation

MC3T3-E1 cell attachment at 4 h and proliferation over 4 days was studied using SEM and fluorescent images (Figure 3.4A). Better cell adhesion on the honeycomb films

with smaller pores as discussed earlier ensured that other adhesion-mediated cell behavior such as cell proliferation, differentiation, and gene expression should also be better [44]. It can be observed from the SEM images that cells could spread and flatten better on the honeycomb films with pore diameters of 3.5 and 6.0 μm than on the flat films. The cytoplasm on the honeycomb films with a pore diameter of 10 μm was partially or completely trapped inside the pores. The honeycomb films with pore diameters of 3.5 and 6.0 μm, especially for the smaller one, had more cells compared with the flat film and the honeycomb film with pore diameter of 10 μm. This result was further confirmed by the fluorescent images, which showed that cell density increased with the culture time and cells reached confluence at day 4. At days 1 and 2, cytoplasm was clearly trapped and deformed on 10- and 6-μm pores. Cell numbers counted from nuclei stained with DAPI in Figure 3.4B also demonstrated that cell proliferation was greatly enhanced on the honeycomb films with pore diameters of 6.0 and 3.5 μm, especially the smaller one. Figure 3.4C shows the average cell area on films, suggesting that cells on films with diameters of 3.5 and 6.0 μm spread and flattened significantly better than those on the flat films.

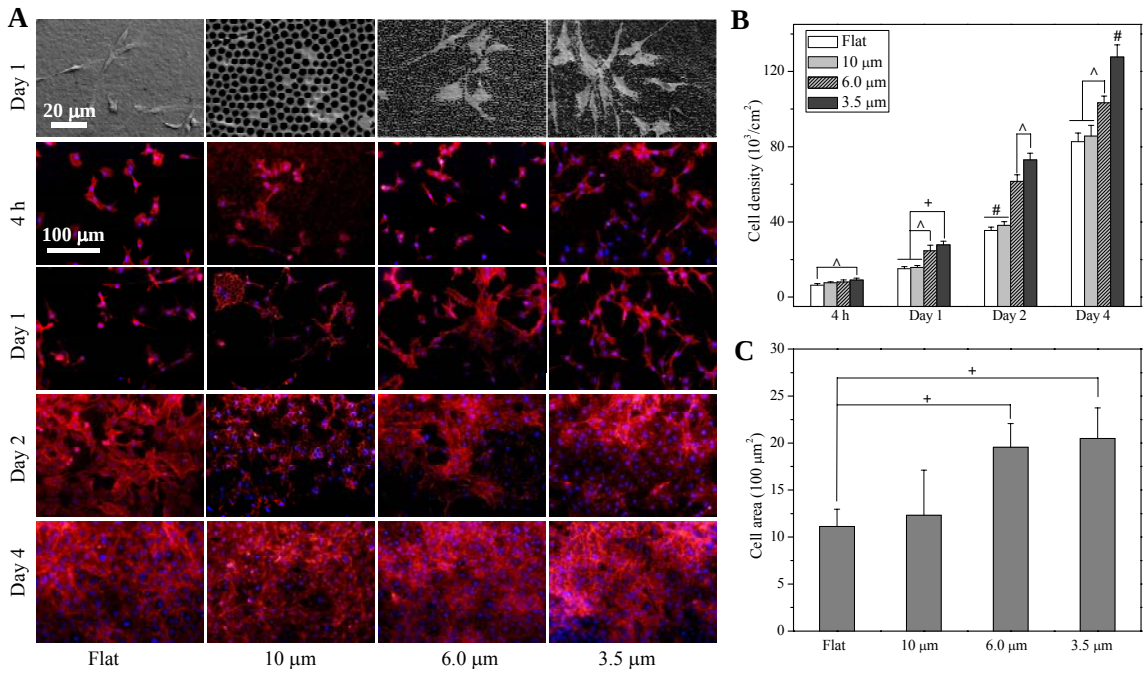

Figure 3.4 (A) SEM images of MC3T3-E1 cells at day 1 (top row) and fluorescent images of cells stained with RP (red) and DAPI (blue) at 4 h, days 1, 2, and 4 on the flat film and honeycomb films with different pore diameters. Scale bar of 20 μm is applicable to all SEM images and scale bar of 100 μm is applicable to all fluorescent images. (B) Cell proliferation on the films represented by the cell numbers at 4 h, days 1, 2, and 4. (C) Cell area on the films at day 1. *: $p < 0.05$; #: $p < 0.01$ relative to others. +: $p < 0.01$. ^: $p < 0.05$.

The effect of pore size in porous substrates on cell behavior has been studied using different materials [16,19,23,46,47]. On honeycomb PCL films with pore diameters of 3-20 μm, keratinocytes and fibroblasts were found to prefer the smallest pores (3-5 μm) in terms of adhesion and proliferation [16]. Smaller pores in this range generated a lager surface area and a longer pore edge whereas overcellular pores could separate cells from communicating with each other, which is detrimental to cell proliferation, signaling, and survival [16]. When the pore diameter was smaller than 1 μm (100-500 nm), MC3T3-E1 cells seeded on porous silica films were elongated on the narrow rims with a much

smaller cell area and slower proliferation [23]. When the pore diameter was even smaller (15-100 nm), surface topography at 15 nm could best support mesenchymal stem cell adhesion, proliferation, migration, and differentiation on TiO_2 nanotube surfaces, as this spacing seems optimal for integrin assembly into FAs [46,47].

MC3T3-E1 cell nuclei stained with DAPI were further analyzed in terms of shape and area, which can be related to gene expression and protein synthesis [48]. As shown in Figure 3.5, cell nuclei became larger on the honeycomb films and were evidently distorted on the 6.0- and 10-μm pores when cytoplasm was trapped inside the pores. Cell nuclear area at day 2 increased from 235 ± 42 μm^2 on the flat films to 294 ± 79 and 367 ± 52 μm^2 on the honeycomb films with pore diameters of 3.5 and 6.0 μm, respectively. Then it decreased to 326 ± 61 μm^2 when the pore diameter was 10 μm. Cell nuclear deformation may induce difference expression of bone-specific gene markers. For example, MC3T3-E1 cell nuclei were found to be aligned in microgrooved substrates of crosslinked PCL triacrylate (PCLTA) with groove width of 7.5 μm and this nuclear alignment was believed to contribute to higher mineralization and OCN expression [29]. As found previously, upregulated OCN expression from constraining primary rat bone cell nuclei, whereas collagen I synthesis reached maximum at an intermediate value of nuclear distension [48]. The nuclei of human osteosarcoma-derived cells (SaOs-2) were found to be severely deformed on micropillars but it had little effect on its viability, proliferation, and ALP activity [49]. It is still unclear if nuclear expansion found here instead of nuclear alignment and distension could result in high MC3T3-E1 differentiation and gene expression.

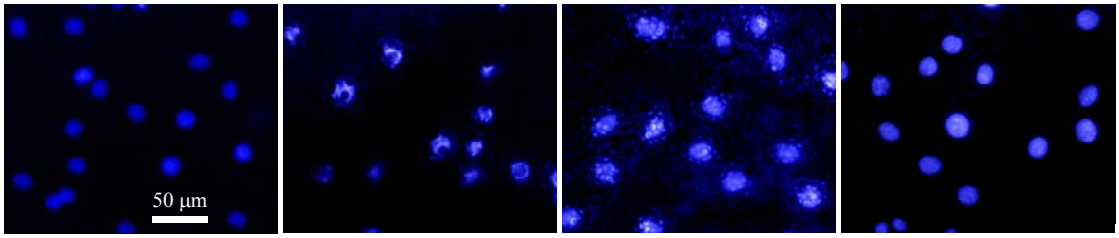

Figure 3.5 MC3T3-E1 cell nuclei stained with DAPI at day 2 post-seeding on the flat film and honeycomb films with different pore diameters.

3.3.5 Cell Behavior on the Stretched Films

Stretched honeycomb PCL films were characterized using SEM and their microgroove-like topography had a notable effect on MC3T3-E1 cells. As shown in Figure 3.6A, after deformation of pores, the surface topography presented majorly elongated hexagons, rectangles, and other irregular structures aligned side by side, which was also observed in another stretched microporous film of PCL [50]. Defects in the honeycomb structure had a remarkable impact on the evolution of pore size and shape during stretching. Overall, the stretched honeycomb films could be considered as microgrooved ones with groove widths of ca. 12, 8, and 5 μm for pore diameters of 10, 6.0, and 3.5 μm, respectively. The groove length and width could be roughly calculated by assuming the pores were perfect circles with uniform dimensions. When the pores were stretched at a stretching ratio of 4.5 along one direction, each groove had a length of 4.5 times as much as the pore diameter. Thus the groove lengths were estimated to be 45, 27, and 15.75 μm for pore diameters of 10, 6.0, and 3.5 μm, in agreement with the values of 40.9 ± 10.3, 30.7 ± 5.2, and 12.6 ± 3.5 μm determined from the SEM images in Figure

6A, respectively. For the rim size or the ridge width, it also increased 4.5 times along the stretching direction but it decreased along the transverse direction. The groove depth should be similar to or lower than the height of spherical cap (2-3 μm) in Figure 3.1D.

Figure 3.6B shows the fluorescent images of MC3T3-E1 cells after culture for 4 h, 1, 2, and 4 days on the stretched flat and honeycomb films. The cell densities on the stretched films were almost equal to those on their unstretched counterparts in Figure 3.4A,B, consistent with our previous finding on microgrooved substrates of crosslinked PCLTA with different groove dimensions [33]. Cell filaments were aligned on the stretched honeycomb films with different groove widths, similar to a previous report when cardiac myocytes were cultured on stretched microporous PCL films [50]. On microgrooved substrates, cells sense forces and adjust shape to obtain optional force equilibrium, inducing aligned cell filaments [51]. Different from that most cells grew on the flat-tops of the unstretched honeycomb films, more than 80% of the cells were trapped inside the grooves on the stretched ones with a slight increase when the pore diameter or groove width decreased, as shown in Figure 3.6C. It was because the surface porosity was larger and the transverse rim size or ridge width was smaller in the stretched honeycomb films.

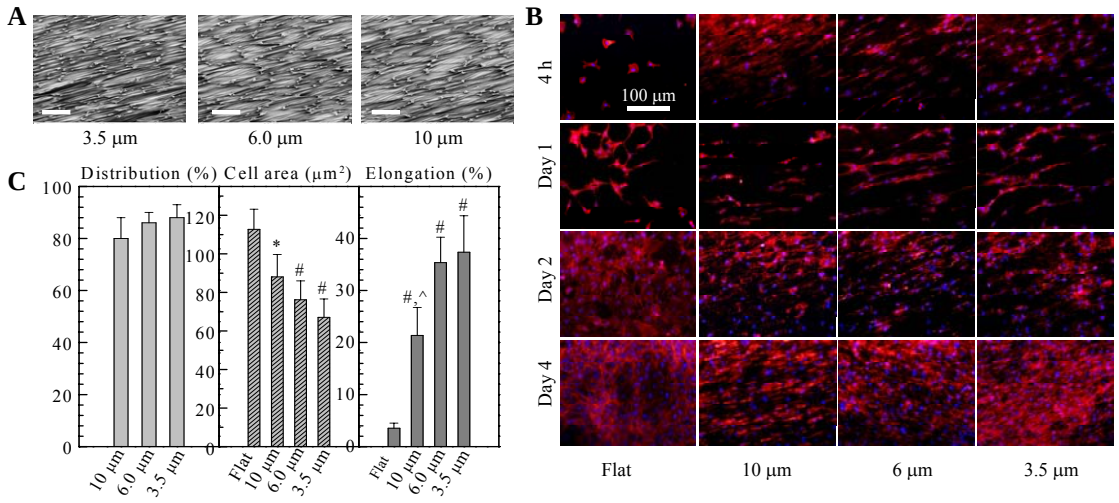

Figure 3.6 (A) SEM images of the stretched honeycomb films with different pore diameters. Scale bar of 20 μm is applicable to all SEM images (magnification: ×1500). (B) Fluorescent images of MC3T3-E1 cells stained with RP (red) and DAPI (blue) at 4 h, days 1, 2, and 4 on the stretched films. Scale bar of 100 μm is applicable to all fluorescent images. (C) Distribution, defined as the percentage of cells trapped inside the grooves of the stretched honeycomb films, cell area and percentage of elongated cells in entire cell population on the stretched films at day 1. *: $p < 0.05$, #: $p < 0.01$ relative to the flat film. ^: $p < 0.05$ relative to films with smaller pores.

Cell area on the stretched flat films was greater than that on the stretched honeycomb films and it was smaller when the groove/ridge width was lower. Cell elongation on the stretched flat films was not observed, compared with much higher percentages of elongated cells on the stretched honeycomb films, especially when the pore diameter or groove width was smaller. Our present results agreed with the conclusions in literature that cell alignment often decreases with increasing groove/ridge width or decreasing the groove depth [4,6,33]. Alignment of cell filaments can also induce nuclear elongation because nuclei are mechanically integrated with the entire cell body and intermediate filaments can transfer the forces sensed by cell filaments to the nucleus via mechanotransduction [6,7,52,53]. Nevertheless, nuclear elongation on the

stretched honeycomb films was not observed here, even though they had strong alignment of cell filaments. In a previous report, NIH3T3 fibroblasts proliferated better on a less stiff biaxially stretched PCL membrane with a lower thickness [54]. However, no difference was found in this study in cell behavior between the flat PCL films before and after stretching, as their thermal and mechanical properties remained the same.

3.3.6 Mineralization and Gene Expression

The honeycomb films not only promoted MC3T3-E1 cell adhesion, spreading, and proliferation, but also enhanced the mineralization process of these cells. As shown in Figure 3.7, the calcium content and ALP activity of MC3T3-E1 cells, two indicators of osteogenesis, on the honeycomb films were both higher than those on the flat one after 14 days of culture. These two parameters were even higher when the pores in the honeycomb films were smaller. These cell results were consistent with each other and indicated that honeycomb PCL films with 3.5-μm pores are potentially useful in bone regeneration and repair and this pore size can be fabricated into other biomaterials to promote adhesion, proliferation, and mineralization of bone cells.

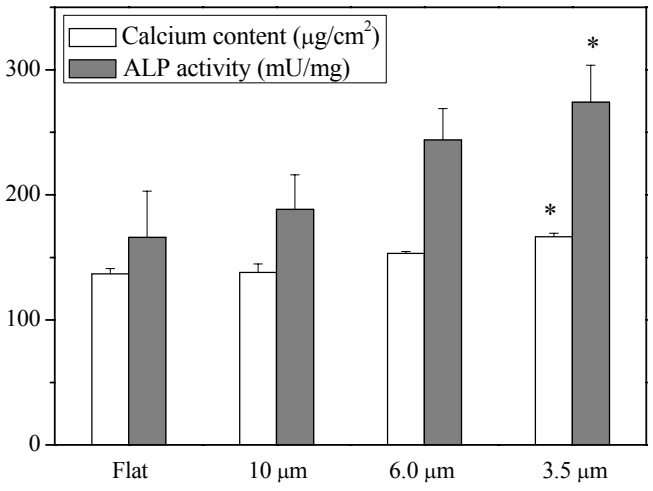

Figure 3.7 ALP activity and calcium content of MC3T3-E1 cells cultured on the flat and honeycomb films with different pore diameters for 14 days. *: $p < 0.05$ relative to the flat film.

To further analyze MC3T3-E1 cell differentiation, real-time PCR was used to assess mRNA expression of bone-specific differentiation markers. The results (Figure 3.8) demonstrated that the expression levels of OCN, COL I, and OPN on the honeycomb films with pore diameters of 6.0 and 3.5 μm were significantly higher than those on the flat films and honeycomb films with 10-μm pores. For ALP, it had a significantly higher expression level on the honeycomb films with 3.5-μm pores than on other films. Cell and tissue development in bone formation have three stages: proliferation, matrix maturation, and mineralization, and different differentiation-related genes reach their maximum expression levels at different stages [43,55]. The gene expression levels of ALP and COL I, which are early-stage markers of osteogenesis, reach peak values in the stage of matrix maturation that occurs after 7 days of culture [55]. In contrast, OCN and OPN reach peak levels or continue to grow in the stage of mineralization [43,55]. Because the present

results were obtained after 14 days of cell culture, which was in the mineralization stage, the relative expression levels of ALP and COL I were lower than those of OCN and OPN. The upregulated gene expression on the honeycomb films can be attributed to easier formation of integrin clusters and FAs, and better cell proliferation stimulated by the pore edges.

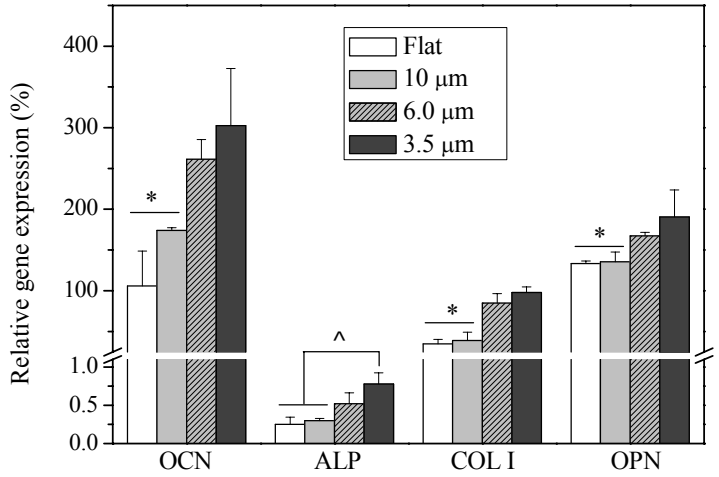

Figure 3.8 Gene expression levels of ALP, OCN, OPN, and COL I relative to GAPDH in MC3T3-E1 cells cultured for 14 days on the flat and honeycomb films with different pore diameters. *: $p < 0.05$ relative to others. ^: $p < 0.05$.

3.4 Conclusions

Honeycomb PCL films with different pore diameters have been fabricated using the breath-figure method in water-miscible THF without assistance of any surfactant. By increasing the airflow rate from 0 to 50 and 100 mL min^{-1}, uniform pores with controllable diameters from 10 to 6.0 and 3.5 μm were achieved, respectively. Compared with the flat control, the honeycomb films significantly promoted mouse MC3T3-E1 cell adhesion, spreading, proliferation, alkaline ALP activity, calcium content, and gene

expression of bone-specific differentiation markers, ALP, COL I, OCN, and OPN, especially when the pores were smaller. The promotion originated from enhanced expression of integrin subunits of α_1, α_2, β_1. Honeycomb PCL films could be stretched into groove-like structures. Compared with stretched flat films, stretched honeycomb films could elongate F-actin filaments of MC3T3-E1 cells significantly and the effect was more prominent when the pore diameter was smaller. These honeycomb PCL films can supply an efficient platform for bone tissue engineering applications.

References

[1] Khan, Y.; Yaszemski, M. J.; Mikos, A. G.; Laurencin, C. T. *J. Bone Joint Surg. Am.* **2008**, 90A, 36.

[2] Hing, K. A. *Philosl. T. Roy. Soc. A* **2004**, 362, 2821.

[3] Bettinger, C. J.; Langer, R.; Borenstein, J. T. *Angew. Chem., Int. Edit.* **2009**, 48, 5406.

[4] Flemming, R. G.; Murphy, C. J.; Abrams, G. A.; Goodman, S. L.; Nealey, P. F. *Biomaterials* **1999**, 20, 573.

[5] Harbers, G. M.; Grainger, D. W. In *Introduction to Biomaterials*; Guelcher, S. A., Hollinger, J. O., Eds.; CRC Press: Boca Raton, 2005; pp 15-45.

[6] Anselme, K.; Bigerelle, M. *Int. Mater. Rev.* **2011**, 56, 243.

[7] Dalby, M. J. *Med. Eng. Phys.* **2005**, 27, 730.

[8] Tanaka, M. *Biochim. Biophys. Acta* **2011**, 1810, 251.

[9] Bunz, U. H. F. *Adv. Mater.* **2006**, 18, 973.

[10] Hernández-Guerrero, M.; Stenzel, M. H. *Polym. Chem.* **2012**, 3, 563.

[11] Woodruff, M. A.; Hutmacher, D. A. *Prog. Polym. Sci.* **2010**, 35, 1217.

[12] Tanaka, M.; Takebayashi, M.; Miyama, M.; Nishida, J.; Shimomura, M. *Bio-Med. Mater. Eng.* **2004**, 14, 439.

[13] Formosa, F.; Sánchez-Vaquero, V.; Rodríguez-Navas, C.; Muñoz-Noval, Á.; Tejera-Sanchez, N.; Silván, M. M.; García-Ruiz, J. P.; Marletta, G. *Plasma Process. Polym.* **2010**, 7, 794.

[14] Tsuruma, A.; Tanaka, M.; Yamamoto, S.; Shimomura, M. *Colloid. Surface. A* **2008**, 313, 536.

[15] Yamamoto, S.; Tanaka, M.; Sunami, H.; Arai, K.; Takayama, A.; Yamashita, S.; Motita, Y.; Shimomura, M. *Surf. Sci.* **2006**, 600, 3785.

[16] McMillan, J. R.; Akiyama, M.; Tanaka, M.; Yamamoto, S.; Goto, M.; Abe, R.; Sawamura, D.; Shimomura, M.; Shimizu, H. *Tissue Eng.* **2007**, 13, 789.

[17] Sunami, H.; Ito, E.; Tanaka, M.; Yamamoto, S.; Shimomura, M. *Colloid. Surface. A* **2006**, 284, 548.

[18] Tanaka, M.; Takayama, A.; Ito, E.; Sunami, H.; Yamamoto, S.; Shimomura, M. *J. Nanosci. Nanotechno.* **2007**, 7, 763.

[19] Arai, K.; Tanaka, M.; Yamamoto, S.; Shimomura, M. *Colloid. Surface. A* **2008**, 313, 530.

[20] Yamamoto, S.; Tanaka, M.; Sunami, H.; Ito, E.; Yamashita, S.; Morita, Y.; M. Shimomura, M. *Langmuir* **2007**, 23, 8114.

[21] Wang, B.; Mao, Z.; Meng, X.; Tong, W.; Gao, C. *Colloid. Surface. B* **2010**, 76, 38.

[22] Lee, S. J.; Choi, J. S.; Park, K. S.; Khang, G.; Lee, Y. M.; Lee, H. B. *Biomaterials* **2004**, 25, 4699.

[23] Orita, T.; Tomita, M.; Kato, K. *Colloid. Surface. B* **2011**, 84, 187.

[24] Zhao, B.; Zhang, J.; Wang, X.; Li, C. *J. Mater. Chem.* **2006**, 16, 509.

[25] Park, M. S.; Kim, J. K. *Langmuir* **2004**, 20, 5347.

[26] Megelski, S.; Stephens, J. S.; Chase, D. B.; Rabolt, J. F. *Macromolecules* **2002**, 35, 8456.

[27] Casper, C. L.; Stephens, J. S.; Tassi, N. G.; Chase, D. B.; Rabolt, J. F. *Macromolecules* **2004**, 37, 573.

[28] Wang, K.; Cai, L.; Hao, F.; Xu, X.; Cui, M.; Wang, S. *Biomacromolecules* **2010**, 11,

2748.

[29] Wang, K.; Cai, L.; Jesse, S.; Wang, S. *Langmuir* **2012**, 28, 4382.

[30] Wang, K.; Jesse, S.; Wang, S. *Macromol. Chem. Phys.* **2012**, 213, 1239.

[31] Cai, L.; Wang, S. *Polymer* **2010**, 51, 164.

[32] Wang, K.; Cai, L.; Wang, S. *Polymer* **2011**, 52, 2827.

[33] Wang, K.; Cai, L.; Zhang, L.; Dong, J.; Wang, S. *Adv. Healthcare Mater*. **2012**, 1, 292.

[34] Cai, L.; Chen, J.; Rondinone, A. J.; Wang, S. *Adv. Func. Mater.* **2012**, 22, 3181.

[35] Cassie, A. B. D.; Baxter, S. *Trans. Faraday Soc.* **1944**, 40, 0546.

[36] Murray, M. D.; Darvell, B. W. *J. Phys. D* **1990**, 23, 1150.

[37] Min, E. H.; Wong, K. H.; Stenzel, M. H. *Adv. Mater.* **2008**, 20, 3550.

[38] Biggs, M. J. P.; Dalby, M. J. *P. I. Mech. Eng. H* **2010**, 224, 1441.

[39] Geiger, B.; Spatz, J. P.; Bershadsky, A. D. *Nature Rev.* **2009**, 10, 21.

[40] Berry, C. C.; Campbell, G.; Spadiccino, A.; Robertson, M.; Curtis, A. S. G. *Biomaterials* **2004**, 25, 5781.

[41] Walboomers, X. F.; Croes, H. J. E.; Ginsel, L. A.; Jansen, J. A. *Biomaterials* **1998**, 19, 1861.

[42] Curtis, A.; Wilkinson, C. *Biomaterials* **1997**, 18, 1573.

[43] Siebers, M. C.; Brugge, P. J.; Walboomers, X. F.; Jansen, J. A. *Biomaterials* **2005**, 26, 137.

[44] Anselme, K. *Biomaterials* **2000**, 21, 667.

[45] Kim, E. J.; Boehm, C. A.; Mata, A.; Fleischman, A. J.; Muschler, G. F.; Roy, S. *Acta Biomater.* **2010**, 6, 160.

[46] Park, J.; Bauer, S.; Schlegel, K. A.; Neukam, F. W.; von der Mark, K.; Schmuki, P. *Small* **2009**, 5, 666.

[47] Park, J.; Bauer, S.; von der Mark, K.; Schmuki, P. *Nano Lett.* **2007**, 7, 1686.

[48] Thomas, C. H.; Collier, J. H.; Sfeir, C. S.; Healy, K. E. *Proc. Natl. Acad. Sci. U.S.A.* **2002**, 99, 1972.

[49] Davidson, P. M.; Özçelik, H.; Hasirci, V.; Reiter, G.; Anselme, K. *Adv. Mater.* **2009**, 21, 3586.

[50] Nishikawa, T.; Nonomura, M.; Arai, K.; Hayashi, J.; Sawadaishi, T.; Nishiura, Y.; Hara, M.; Shimomura, M. *Langmuir* **2003**, 19, 6193.

[51] Ingber, D. E. *J. Cell. Sci.* **1993**, 104, 613.

[52] Maniotis, A. J.; Chen, C. S.; Ingber, D. E. *Proc. Natl. Acad. Sci. U.S.A.* **1997**, 94, 849.

[53] Dalby, M. J.; Riehle, M. O.; Yarwood, S. J.; Wilkinson, C. D. W.; Curtis, A. S. G. *Exp. Cell Res.* **2003**, 284, 274.

[54] Tan, P. S.; Teoh, S. H. *Mater. Sci. Eng C* **2007**, 27, 304.

[55] Stein, G. S.; Lian, J. B.; Owen. T. A. *FASEB J.* **1990**, 4, 3111.

CHAPTER IV
PROMOTING MC3T3-E1 CELL ADHESION, PROLIFERATION, AND DIFFERENTIATION ON PHOTO-CURED POLY(ε-CAPROLACTONE) TRIACRYLATE FILMS WITH PORES TUNED BY BREATH FIGURES

4.1 Introduction

Cells can recognize and respond to surface features via inter- and intracellular signaling events [1-5]. These signaling events are of critical importance for subsequent cell proliferation, differentiation, and development of endogenous extracellular matrix (ECM) [1-5]. Among many topographical features at the micro- and nanoscale to which cells react, substrates with ordered pore/pit distribution have been used to mimic the basement membrane with hierarchical porous structures [1-5]. Unlike methods such as phase separation, colloidal templating, and lithography [1-3], the breath-figure method is very convenient to prepare honeycomb polymer films as condensed water droplets on the surface of polymer solution work as template during the evaporation of volatile solvent in a humid condition [5-9]. For example, honeycomb poly(ε-caprolactone) (PCL) films with pore sizes (diameters) of 3-20 μm were prepared in the presence of a surfactant to regulate cell behavior [5,10-12]. Although great effort has been focused on developing porous substrates/scaffolds for enhancing bone cell functions [1-3,5,13-15], it has not been well studied how to use honeycomb films of biodegradable polymers with tunable micropores to regulate osteoblastic adhesion, differentiation, and gene expression. In addition, the honeycomb polymer films with tunable pores for cell studies here were

fabricated by incorporating photo-curing with the breath figure method without the need of a surfactant.

4.2 Experimental Section

4.2.1 Preparation of Poneycomb Photo-cured PCLTA Films

All chemicals used in this study were purchased from Sigma-Aldrich unless noted otherwise. PCLTA (M_n = 20020 g mol^{-1}, M_w = 22670 g mol^{-1}) synthesized in our lab and photo-initiator, phenyl bis(2,4,6-trimethyl benzoyl) phosphine oxide (BAPO, IRGACURE 819, Ciba Specialty Chemicals) were dissolved in distilled THF at concentrations of 50 and 0.5 mg mL^{-1}, respectively. Then the PCLTA/BAPO solution in THF was cast onto clean glass slides and put in a chamber. At a relative humidity of 60%, honeycomb polymer films with pore sizes of 5.6 and 3.0 μm were fabricated by controlling the airflow rate at 0 and 50 mL min^{-1}, respectively. Polymer films became opaque gradually during solvent evaporation for 5 min, followed by exposure to UV light (λ = 315-380 nm) generated from a Spectroline lamp (SB-100P; intensity: 4800 μw cm^{-2}) for 30 min. For comparison, flat films were prepared by casting the same PCLTA/BAPO solution on glass slides and photo-curing at the same condition.

4.2.2 Physical Characterizations

To obtain their gel fractions, photo-cured PCLTA films with the original weight (W_o) were soaked in excessive methylene chloride for 2 days. Then the films were dried in vacuum for 2 h and weighed as W_d. The gel fraction was then calculated using $W_d/W_o \times 100\%$. The measurement was performed in triplicate. The surface morphology of both

flat and honeycomb films was observed using SEM (S-3500, Hitachi Instruments, Tokyo, Japan) at an accelerating voltage of 10 kV.

4.2.3 Water Contact Angle and Protein Adsorption

Prior to measurements, all photo-cured PCLTA films were dried completely in vacuum overnight. Water contact angles were determined at room temperature using a Ramé-Hart NRC C. A. goniometer (model 100-00-230) and the images of water droplets on the polymer films were taken using a 3.0 megapixel camera (*Moticam 2300*, Motic). For protein adsorption, the polymer films were immersed in the culture media for MC3T3-E1 cells for 4 h at 37 °C. The films were washed with PBS five times to remove unattached proteins and soaked in 300 μL of 1% sodium dodecyl sulfate (SDS) solution 5 times for 1 h each to collect proteins adsorbed on the surface. A microplate reader (SpectraMax Plus 384, Molecular Devices, Sunnyvale, CA) and a MicroBCA protein assay kit (Pierce, Rockford, IL) were used to detect the protein concentrations in the collected SDS solutions. A standard curve for calibration was plotted using albumin in the kit.

4.2.4 Cell Studies

MC3T3-E1 cells (ATCC, Manassas, VA) were cultured as previously reported [15-18]. Prior to cell studies, all polymer films were immersed in a mixture of 70% alcohol solution and acetone (75/25, v/v) overnight to remove excessive unreacted polymer chains and BAPO. The films were dried in vacuum and further sterilized by 70% alcohol solution for 3 × 1 h followed by complete drying in vacuum. MC3T3-E1 cells

were seeded on all the samples at a density of ~15,000 cells per cm^2 and cultured in α-Minimum Essential Media (α-MEM; Gibco, Grand Island, NY) containing 10% fetal bovine serum (FBS, Gibco) and 1% penicillin/streptomycin (Gibco) for 4 h, 1, 2, 4, and 14 days in an incubator at 37 °C with 95% humidity and 5% CO_2. To count cell number and observe F-actin cytoskeleton, the attached cells on the films were fixed with 16% paraformaldehyde (PFA) solution for 20 min. After PFA was removed, cells were washed twice with phosphate buffered saline (PBS), permeabilised with 0.2% Triton X-100, and stained using rhodamine-phalloidin (RP) for more than 1 h at 37 °C and 4',6-diamidino-2-phenylindole (DAPI) at room temperature. Cell images were taken on an Axiovert 25 light microscope (Carl Zeiss, Germany). Cells on each film were counted using DAPI-stained images and the mean number of nuclei per field ($n > 15$) was calculated. Average cell area was obtained from more than 20 non-overlapping cells at day 1 post-seeding using ImageJ software (National Institutes of Health, Bethesda, MD). FAs were stained with mouse monoclonal anti-vinculin antibody (V9264, Sigma-Aldrich) for more than 1 h at 37 °C followed by five rinses with PBS. Then the FAs were labeled by anti-mouse IgG-FITC antibody (F0257, Sigma) at 37 °C for 5 h and observed on a confocal microscope (SP2, Leica). To observe the morphology of both cells and films using SEM, all samples were dehydrated with graded ethanol solutions (25%, 50%, 70%, 95%, and 100%), dried in vacuum overnight, and sputter-coated with gold-palladium.

4.2.5 ALP Activity, Calcium Content, and Gene Expression

After culturing MC3T3-E1 cells on the polymer films for 14 days, all samples were rinsed with PBS twice, trypsinized, washed again, and the cell suspension was

centrifuged for 4 min at 1000 rpm. The obtained cell pellet was re-suspended in 1 mL 0.2% Nonidet P-40 solution and sonicated in ice water for 2 min. Fluorescence-based ALP detection kit (Sigma, St. Louis, MO) and QuantiChrom calcium assay kit (BioAssay Systems, Hayward, CA) were used to determine the ALP activity and calcium content of the cell lysate, respectively [16-18]. After MC3T3-E1 cells were cultured for 14 days, RNA was isolated from the cell pellet using a RNeasy Mini Kit (Qiagen, Valencia, CA), from which cDNA was then synthesized using a cDNA synthesis kit (Thermo Scientific). Expression of ALP, COL I, OCN, OPN, intergrin α_1, α_2, β_1, and glyceraldehyde-3-phosphate dehydrogenase (GAPDH) was quantified using real-time PCR, which was performed on a thermal cycler with a fluorescence detection system (PTC-200, MJ Research, Watham, MA) and a Power SYBR® Green PCR Master Mix (Applied Biosystems, Carlsbad, CA). The oligonucleotide primers used for both RT and real-time PCR were: ALP forward, 5'-GCC CTC TCC AAG ACA TAT A-3'; ALP reverse, 5'-CCA TGA TCA CGT CGA TAT CC-3'; COL I forward, 5'-TCT CCA CTC TTC TAG TTC CT-3'; COL I reverse, 5'-TTG GGT CAT TTC CAC ATG C-3'; OCN forward, 5'-CAA GTC CCA CAC AGC AGC TT-3'; OCN reverse, 5'-AAA GCC GAG CTG CCA GAG TT-3'; OPN forward, 5'-ACA CTT TCA CTC CAA TCG TCC-3'; OPN reverse, 5'-TGC CCT TTC CGT TGT TGT CC-3'; Integrin α_1 forward, 5'-TGA GCC CAC CAA GAT GAA CGA-3'; Integrin α_1 reverse, 5'-CCT GGC CGG TGT GAT TGT-3'; Integrin α_2 forward, 5'-ACA AGG CAA CTG GCT ACT GGT-3'; Integrin α_2 reverse, 5'-ACA GGT GGC AGT GGG TAG G-3'; Integrin β_1 forward, 5'-GGT GTC GTG TTT GTG AAT GC-3'; Integrin β_1 reverse, 5'-TCC TGT GCA CAC GTG TCT T-3'; GAPDH forward, 5'-

ACT TTG TCA AGC TCA TTT CC-3'; GAPDH reverse, 5'-TGC AGC GAA CTT TAT TGA TG-3'. For RT-PCR, cDNA amplification was performed on a Peltier Thermo cycler (PTC-200, MJ Research). DNA products were electrophoresed in 1.5% agarose gel containing Gelgreen (Biotium, Hayward, CA) and visualized using an EpiChemi II darkroom imaging system (UVP, Upland, CA).

4.2.6 Statistical Analysis

Protein adsorption and *in vitro* cell studies were performed in quadruplicates for each group and each time point. The values were expressed as mean ± standard deviation. The statistical significance ($p < 0.05$ or 0.01) in the differences between groups was analyzed by the student's *t*-test.

4.3 Results and Discussion

Photo-curable and biodegradable PCL triacrylate (PCLTA) synthesized using a facile method in our research group has proved to be a promising candidate biomaterial for diverse tissue-engineering applications [16,19]. A semi-crystalline PCLTA network was used in this study because it could better support mouse pre-osteoblastic MC3T3-E1 cell proliferation and mineralization than more compliant amorphous counterparts [16,19]. There were three steps in preparing these honeycomb films. First, the temperature on the polymer solution surface decreased when the moist air was blew over it and the volatile, water-miscible, relatively non-toxic solvent tetrahydrofuran (THF) evaporated, which consequently triggered nucleation and growth of water droplets. Second, water droplets with similar diameters were arranged into a hexagonal array, followed by exposure to UV

light to initiate photo-curing of PCLTA. At last, polymer precipitated around the water droplets and then THF and water were completely removed. As summarized in recent reviews [7,8], photo-cured polymer honeycomb structures with enhanced stability indeed exist but they were not used for regulating cell behavior [20,21]. In this study, we obtained honeycomb films of photo-cured PCLTA and further studied mouse pre-osteoblastic MC3T3-E1 cell adhesion, spreading, proliferation, differentiation, and gene expression on them.

The pore size in the honeycomb polymer films prepared using the breath figure method can be regulated by solvent species, humidity, airflow rate, and solution concentration/volume [6,8,22-24]. In this study, the airflow rate was the key parameter to control the pore size. When the airflow rate was raised from 0 to 50 mL min^{-1}, the average pore size decreased from 5.6 to 3.0 μm, as shown in Figure 4.1. At a lower airflow rate, solvent evaporation was slower and larger water droplets could form, as also found previously [25]. PCLTA networks were confirmed by the high gel fractions of ~80% without a significant difference between the flat and honeycomb films, indicating that photo-curing was still efficient even when water vapor and droplets were present. The melting temperature and crystallinity of the photo-cured PCLTA films slightly decreased from 57.3 °C and 49.7% for the flat one to 55.6 °C and 47.2%, and 54.9 °C and 44.9% for the honeycomb ones with pore sizes of 5.6 and 3.0 mm, respectively. According to the mechanism proposed previously [9,25], the solvent density influences the honeycomb structure directly. When the solvent is chloroform or carbon disulfide with a density higher than that of condensed water droplets, a packed array of honeycomb pores forms as a monolayer on the solution surface because water droplets cannot

penetrate in these dense solvents [9,25]. In contrast, honeycomb films prepared from solutions in benzene or toluene, which has a lower density than water, could form multiple layers [25]. Although the solvent THF used here has a lower density (0.8892 g cm^{-3}) than water, the cross-sections of the honeycomb films (Figure 4.1B,D) showed a monolayer architecture with a solid bottom. This architecture was also found in other honeycomb films prepared from THF solutions and may be due to thin polymer solution coated on glass slides and increasing solution viscosity upon water precipitation [23,24]. The pore size distribution (Figure 4.1F) in both honeycomb films was narrow and the smaller pores were more uniform.

Surface topography can influence the wettability of a polymer substrate [26,27]. As demonstrated in the insets of Figure 4.1A,C,E, the water contact angles were 76.3 ± 1.2°, 111.0 ± 1.4° and 122.0 ± 2.7° on the flat film and honeycomb films with pore sizes of 5.6 and 3.0 μm, respectively. Because air pockets existed between the honeycomb films and water droplets, the Cassie and Baxter model (eq. 1) was used to predict water contact angles (θ) on these films [26,27].

$$\cos\theta = (1 - f_o)\cos\theta_s + f_o\cos\theta_o \qquad (1)$$

where f_o is the fractional flat geometrical area of liquid-air interface beneath a water droplet, θ_s is the water contact angle of 76.3° on the smooth surface of crosslinked PCLTA, and θ_o is the water contact angle of 180° on the pore filled with air. When the pore size (D) decreased from 5.6 to 3.0 μm, the rim size (d) measured using Scanning Electron Microscopic (SEM) images also decreased from 1.65 ± 0.35 to 0.85 ± 0.14 μm and the f_o values obtained by dividing the pore area by the projected area were 0.541 and

0.558, respectively. Consistently, the f_o values estimated on the basis of a hexagonal unit cell with a pore in the center (Figure 4.1G) were 0.541 and 0.551. The water contact angles estimated from eq. 1 were 115.5° and 117.2° for the pore sizes of 5.6 and 3.0 μm, respectively. This estimation was in agreement with the experimental data. Calculated on the basis of f_o and D, the number of pores and total length of pore edges in a unit projected area of 1 cm^2 increased from 2.2×10^6 to 7.8×10^6 and from 38.6 to 73.4 m when the pore size decreased from 5.6 to 3.0 μm, respectively.

Protein adsorption is important for cell adhesion and depends on both substrate chemistry and topography [28]. The entire surface area of the honeycomb films included the areas of the flat-top and the pores. As illustrated in Figure 4.1H, spherical caps used to represent the pores left by the water droplets were smaller than a hemisphere when the pore size was 5.6 μm but greater than a hemisphere for 3.0-μm pores. Then we performed simple geometrical calculation of the entire surface area based on the pore size and the height of the spherical cap, which was measured from the SEM images of the pore cross-sections. The ratios of the entire surface areas for the honeycomb films to their projected areas were 1.37 ± 0.12 and 2.35 ± 0.08 when the pore sizes were 5.6 and 3.0 μm, respectively. For the flat film, the value was 1. Honeycomb structures with larger total surface areas to contact serum proteins in culture media were reported to enhance protein adsorption and regulate distribution of adsorbed proteins by having more on the honeycomb rims [5,10]. The concentration of the proteins adsorbed on the flat films from the culture media was 2.00 ± 0.95 μg cm^{-2}. With statistical significance ($p < 0.01$), it increased to 4.04 ± 1.98 and 9.90 ± 1.08 μg cm^{-2} for the honeycomb films with pore sizes

of 5.6 and 3.0 μm, respectively. These protein concentrations followed a linear relationship ($r = 0.9994$) with the entire surface area of the films, suggesting that the film chemistry did not affect the protein adsorption additionally.

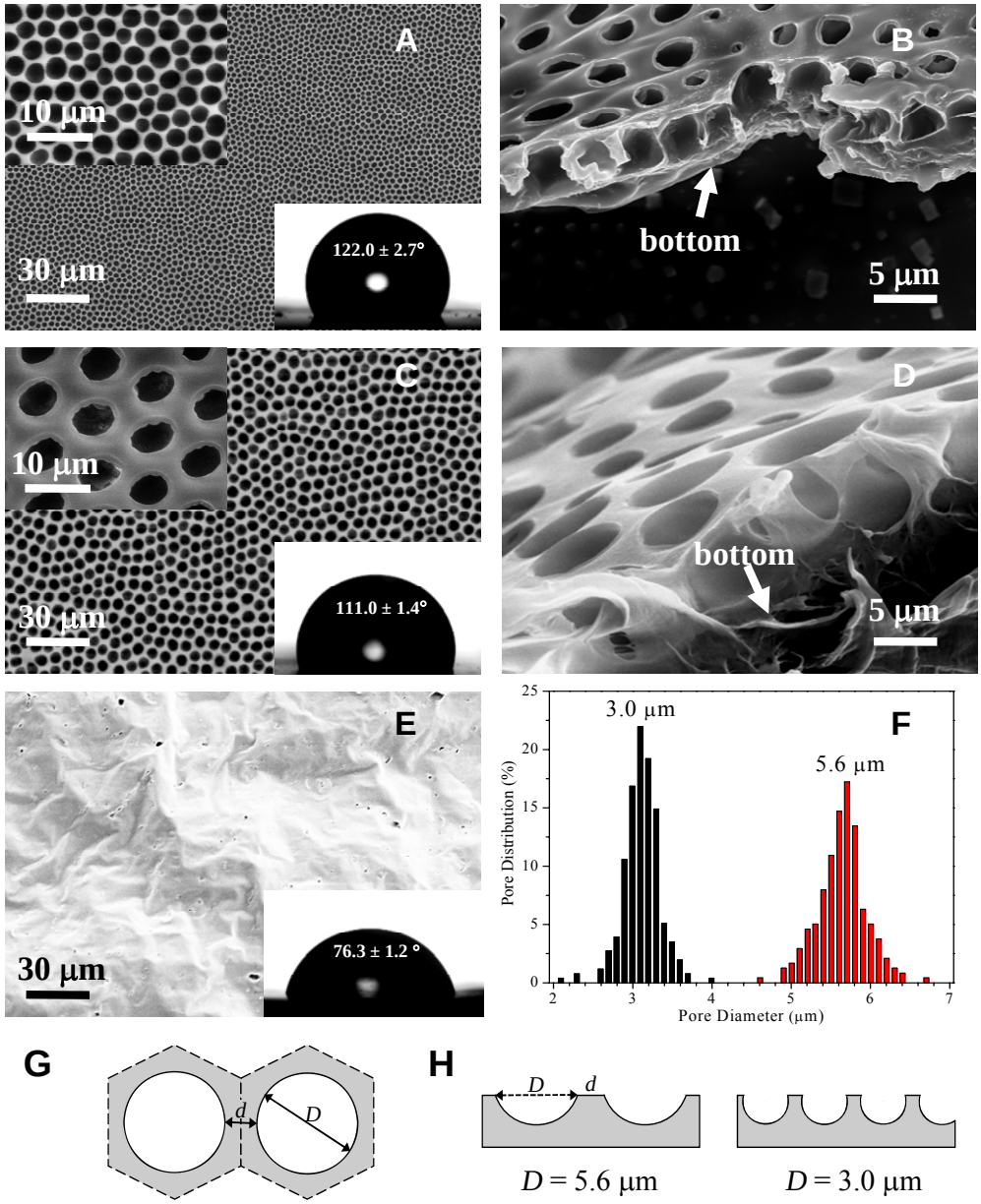

Figure 4.1 SEM images of honeycomb films with pore sizes of (A,B) 3.0 μm and (C,D) 5.6 μm, and (E) a flat film of photo-cured PCLTA. A,C: magnification: × 1000.The cross-sections of the honeycomb films are shown in (B,D) magnification: × 5000. Pore size distribution in the honeycomb films is shown in (F). Insets in (A,C,E): SEM images (left top corners) at a higher magnification × 3000 and micrographs of water droplets (right bottom corners) with the measured water contact angles. (G) Model of two adjacent hexagonal unit cells containing pores with size *D* and rim size *d*. (H) Schematic cross-sections of honeycomb films with two different pore sizes.

Cell-matrix adhesion is a critical step for anchorage-dependent cell proliferation, differentiation, gene expression, and tissue development and organization, and these processes are determined by the chemical, topographical, and mechanical characteristics of the matrix [28,29]. Although the dry honeycomb films demonstrated higher hydrophobicity, this effect did not function as all the films were rinsed in culture media prior to cell seeding. The topographical factor was dominant as PCLTA networks varied little in terms of chemical structure and mechanical properties. Figure 4.2A shows MC3T3-E1 cell images after 1-day culture on both flat and honeycomb films of photo-cured PCLTA. Both pore sizes were subcellular and cells could spread over many pores without showing preferred elongation. The cytoskeletal images on the flat films showed features indicative of motile cells with very few stress fibers, whereas cells were partially trapped in the pores and had more protrusions and better spreading on the honeycomb films with the pore size of 5.6 μm. The smaller pore size of 3.0 μm could induce even more well-defined stress fibers, protrusions, and filopodia. Cell nuclear circularity calculated using the equation of $4\pi \times \text{area/perimeter}^2$, with a measure of 1 indicating a perfect circle, did not change much on different substrates. Nevertheless, as a result of cytoskeletal rearrangements by the underlying pores, cell nuclear area at day 2 increased from 199 ± 26 μm^2 on the flat films to 318 ± 71 and 345 ± 71 μm^2 on the honeycomb films with pore sizes of 5.6 and 3.0 μm, respectively. Nuclear size and shape are important for cell function and thus nuclear expansion found here could enhance mineralization and expression of bone-specific differentiation markers, similar to the effect of geometrical constraint and alignment of nuclei [19,30-32].

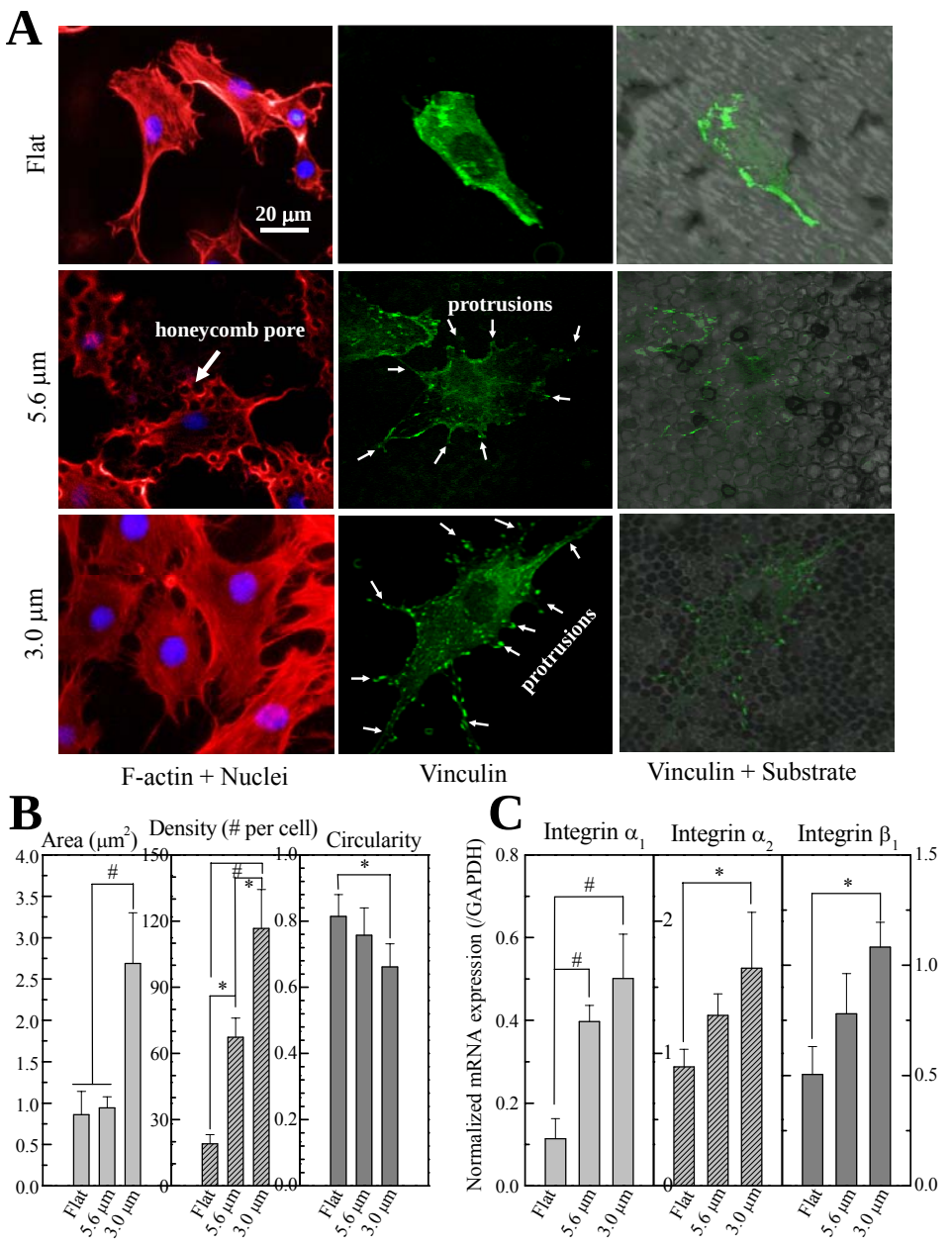

Figure 4.2 (A) Fluorescent images of MC3T3-E1 cells stained with RP (red) and DAPI (blue) (left column), vinculin-stained images (middle column), and merged images with the polymer film background at day 1 post-seeding. Scale bar of 20 μm is applicable for all. (B) Area, density, and circularity of focal adhesions obtained in vinculin-stained cell images in (A). (C) Integrin expression of the cells at day 1. #: $p < 0.01$; *: $p < 0.05$.

Meanwhile, vinculin-stained cell images in Figure 4.2A showed more focal adhesions (FAs) on the honeycomb films compared with the flat ones, and smaller pores could induce even more. FAs on the honeycomb films were distributed not only on cell periphery but also along the pore edges as cells could sense the surface features and detect the proteins distributed on the honeycomb films, consistent with earlier reports [10,12]. The FA area and density (Figure 4.2B), which was defined as the number of FAs per cell, on the honeycomb films were substantially larger than those on the flat films and they further increased with decreasing the pore size from 5.6 to 3.0 μm. Calculated using the same equation for nuclear circularity, the FA circularity values were lower on the honeycomb films, indicating better alignment. FAs, the closest contacts between cells and substrata, have a rectangular shape with a length of 1-5 μm and preferred to attach in an oriented manner along the pore edges [33,34]. After cell adhesion with aligned FAs, actin filaments or stress fibers in cells can also be aligned [33,34].

As discussed in earlier paragraphs, subcellular pores with a smaller size have a larger surface area over which cells can adhere and a higher total length of pore edges per projected area for cells to gain leverage and enhance adhesion by inserting their plasma membrane lamellipodia and filopodial extensions [11]. When the pores were smaller, the radius of curvature was smaller for the pore edge and the spherical cap inside the pores, rendering a sharper discontinuous region between the flat-tops and pores for cells to move around the pores instead of entering [35]. On another side, because direct adjacent cell-cell contact is required for cell growth, signaling, and survival, cell separation by the overcellular pores may be detrimental to these processes [11]. When the pore size was smaller than 1 μm (100-500 nm), MC3T3-E1 cells seeded on porous silica films prepared

using the inverse-opal method were elongated on the narrow rims but the proliferation was inhibited by the pores [14]. When the pore size was in an even lower range of 15-100 nm, a length scale of surface topography at 15 nm was found for best supporting mesenchymal stem cell adhesion, proliferation, migration, and differentiation on TiO_2 nanotube surfaces, as this spacing seems optimal for integrin assembly into FAs [36,37].

Osteoblasts could recognize ECM ligands, such as collagen, laminin, fibronectin, and vitronectin, and anchor on substrate surface via integrin receptors, which mediate subsequent cell adhesion, migration, proliferation, and differentiation [28]. Osteoblasts generally express integrin subunits β_1, β_3, β_5, α_1, α_2, α_3, α_4, α_5, α_6, and α_v [38,39]. To correlate with the cell adhesion results, integrin expression was performed on the subunits α_1, α_2, and β_1, which are closely related to formation of FAs. Figure 4.2C showed that the honeycomb films could foster the expression levels of all these three integrin subunits, especially when the pore size was 3.0 μm. Binding of $\alpha_1\beta_1$ and $\alpha_2\beta_1$ to type-I collagen (COL I), which is the most abundant bone matrix protein, is known to regulate osetoblastic differentiation, whereas subunit β_1 is responsible for attachment to fibronectin or COL I [29,39].

As consequences of cell adhesion, MC3T3-E1 cell spreading, proliferation, differentiation, and gene expression were all influenced by the honeycomb pattern and pore size. Cell proliferation was characterized using SEM micrographs and fluorescent images of the cells (Figure 4.3A) and cell densities (Figure 4.3B), which were counted directly from nuclei at different culture time periods up to 4 days. Cells on the honeycomb films exhibited greater spreading and flattening with a higher density than

those on the flat ones. The trend was more significant on the films with smaller pores, in agreement with the earlier reports that the highest cell proliferation occurred when the pore size was the smallest (3-5 μm) among the studied ranges [10,11]. The average cell area at day 1 was 1660 ± 380 μm^2 on the flat film and it increased significantly ($p < 0.05$) to 2460 ± 690 and 2730 ± 630 μm^2 for the honeycomb films with pore sizes of 5.6 and 3.0 μm, respectively. MC3T3-E1 cell proliferation over 4 days on the honeycomb films was faster than that on the flat films. Significantly faster cell proliferation on the honeycomb films with the smaller pores (3.0 μm) was observed after day 2. Similar to the present result, the fastest fibroblast proliferation was reported on quartz surfaces with 7-μm pores, which were the smallest in that study [35]. However, OCT-1 osteoblast-like cell proliferation over 2 days on micropit polystyrene surfaces was reported not to be significantly enhanced compared with the smooth surface [15]. This discrepancy might be due to differences in cell type, surface porosity, and cell density, which decided if cells could be greatly influenced by the pores instead of only staying largely undisturbed on the flat-top area. After 14-day culture, the alkaline phosphatase (ALP) activity and calcium content of MC3T3-E1 cells (Figure 4.3C) as two indicators of osteogenesis were higher on the honeycomb films than those on the flat films, especially for the smaller pores.

The results from both real-time polymerase chain reaction (PCR; Figure 4.3D) and reverse transcriptase (RT)-PCR (Figure 3E) showed that expression of ALP, osteocalcin (OCN), osteopontin (OPN), and COL I on the honeycomb films was upregulated compared with those on the flat films, especially for ALP and OCN. In cell

and tissue development in bone formation, different differentiation-related genes reach their highest expression levels in different subsequent periods: proliferation, matrix maturation, and mineralization [38,40]. ALP and COL I are two early-stage markers of osteogenesis and they express best in matrix maturation which occurs after 7-day culture, whereas the expression of OCN maximizes during mineralization [40]. Because the present results were obtained at day 14 post-seeding, the relative expression levels of ALP and COL I were significantly lower than those of OCN and OPN. The upregulated gene expression on honeycomb films can be attributed to enhanced formation of integrin clusters and FAs, and enlarged cell nuclei via direct cell mechanotransduction induced topographically [3,4].

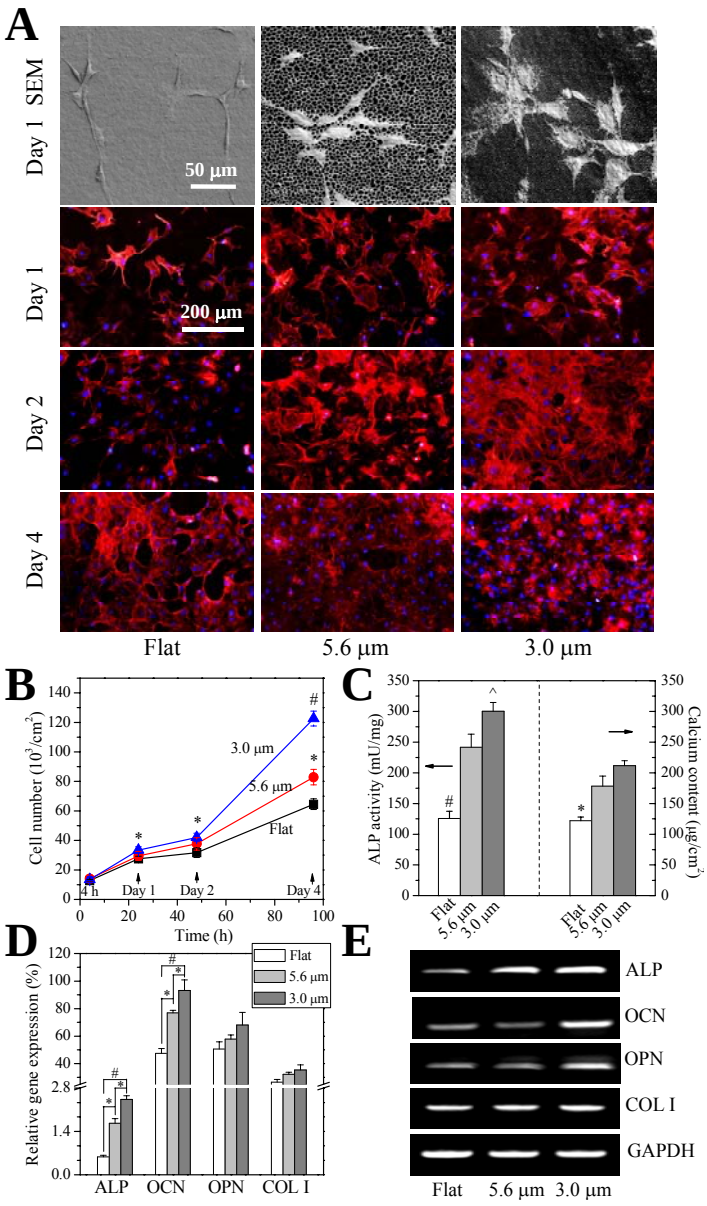

Figure 4.3 (A) SEM images at day 1 and fluorescent images of MC3T3-E1 cells with cytoplasm stained with RP (red) and nuclei stained with DAPI (blue) at days 1, 2, and 4 post-seeding. The scale bar of 50 μm is applicable to all SEM images (magnification: × 1000) and the scale bar of 200 μm is applicable to all fluorescent images. (B) Proliferation of MC3T3-E1 cells cultured on flat and honeycomb film represented by the cell numbers at 4 h, days 1, 2, and 4. #: $p < 0.01$ relative to others, *: $p < 0.05$ relative to the flat film at the same time. (C) ALP activity and calcium content of the cells after 14-day culture. #: $p < 0.01$, *: $p < 0.05$ relative to other films, ^: $p < 0.05$ relative to the honeycomb film with pore size of 5.6 μm. (D,E) Relative gene expression levels of ALP, OCN, OPN, and COL I to GAPDH using real-time PCR (D) and RT-PCR (E). #: $p < 0.01$; *: $p < 0.05$.

4.4 Conclusions

Honeycomb films of photo-cured PCLTA with different pore sizes have been fabricated by incorporating the breath-figure method with photo-curing. It is a facile method for generating substrates to mimic bone topography and enhance bone growth. In addition, this method can be further extended to large-area stereolithographic production. Two different pore sizes of 5.6 and 3.0 μm were achieved by modulating the airflow rate: the faster airflow resulted in the smaller pores. The honeycomb films, especially those with smaller pores, could significantly promote MC3T3-E1 cell adhesion, spreading, proliferation, ALP activity, mineralization, and gene expression of osteoblastic markers, via fostering expression of integrin subunits.

References

[1] Bettinger, C. J.; Langer, R.; Borenstein, J. T. *Angew. Chem., Int. Ed.* **2009**, *48*, 5406.

[2] Flemming, R. G.; Murphy, C. J.; Abrams, G. A.; Goodman, S. L.; Nealey, P. F. *Biomaterials* **1999**, *20*, 573.

[3] Anselme, K.; Bigerelle, M. *Int. Mater. Rev.* **2011**, *56*, 243.

[4] Dalby, M. J. *Med. Eng. Phys.* **2005**, *27*, 730.

[5] Tanaka, M. *Biochim. Biophys. Acta* **2011**, *1810*, 251.

[6] Bunz, U. H. F. *Adv. Mater.* **2006**, *18*, 973.

[7] Ma, H.; Hao, J. *Chem. Soc. Rev.* **2011**, *40*, 5457.

[8] Hernández-Guerrero, M.; Stenzel, M. H. *Polym. Chem.* **2012**, *3*, 563.

[9] Francois, B.; Pitois, O.; Francois, J. *Adv. Mater.* **1995**, *7*, 1041

[10] Tanaka, M.; Takayama, A.; Ito, E.; Sunami, H.; Yamamoto, S.; Shimomura, M. *J. Nanosci. Nanotechnol*. **2007**, *7*, 763.

[11] McMillan, J. R.; Akiyama, M.; Tanaka, M.; Yamamoto, S.; Goto, M.; Abe, R.; Sawamura, D.; Shimomura, M.; Shimizu, H. *Tissue Eng.* **2007**, *13*, 789.

[12] Arai, K.; Tanaka, M.; Yamamoto, S.; Shimomura, M. *Colloid. Surf. A* **2008**, *313-314*, 530.

[13] Lee, S. J.; Choi, J. S.; Park, K. S.; Khang, G.; Lee, Y. M.; Lee, H. B. *Biomaterials* **2004**, *25*, 4699.

[14] Orita, T.; Tomita, M.; Kato, K. *Colloid. Surface. B* **2011**, *84*, 187.

[15] Wan, Y.; Wang, Y.; Liu, Z.; Qu, X.; Han, B.; Bei, J.; Wang, S. *Biomaterials* **2005**, *26*, 4453.

[16] Cai, L.; Wang, S. *Polymer* **2010**, *51*, 164.

[17] Wang, K.; Cai, L.; Zhang, L.; Dong, J.; Wang, S. *Adv. Healthcare Mater*. **2012**, *1*, 292.

[18] Yabu, H.; Kojima, M.; Tsubouchi, M.; Onoue, S.; Sugitani, M.; Shimomura, M. *Colloid. Surface. A* **2006**, *284-285*, 254.

[19] Karikari, A. S.; Williams, S. R.; Heisey, C. L.; Rawlett, A. M.; Long, T. E. *Langmuir* **2006**, *22*, 9687.

[20] Tanaka, M.; Takebayashi, M.; Miyama, M.; Nishida, J.; Shimomura, M. *Bio-Med. Mater. Eng.* **2004**, *14*, 439.

[21] Zhao, B.; Zhang, J.; Wang, X.; Li, C. *J. Mater. Chem.* **2006**, *16*, 509.

[22] Park, M. S.; Kim, J. K. *Langmuir* **2004**, *20*, 5347.

[23] Srinivasarao, M.; Collings, D.; Philips, A.; Patel, S. *Science* **2001**, *292*, 79.

[24] Cassie, A. B. D.; Baxter, S. *Trans. Faraday Soc.* **1944**, *40*, 546.

[25] Min, E. H.; Wong, K. H.; Stenzel, M. H. *Adv. Mater.* **2008**, *20*, 3550.

[26] Harbers, G. M.; Grainger, D. W. in *An introduction to biomaterials* (Eds.: S. A. Guelcher, J. O. Hollinger), CRC Press Taylor & Francis Group, Boca Raton, FL, USA **2006** pp. 15.

[27] Anselme, K. *Biomaterials* **2000**, *21*, 667.

[28] Ingber, D. E.; Madri, J. A.; Folkman, J. *In Vitro Cell. Dev. Biol.* **1987**, *23*, 387.

[29] Webster, M.; Witkin, K. L.; Cohen-Fix, O. *J. Cell. Sci.* **2009**, *122*, 1477.

[30] Thomas, C. H.; Collier, J. H.; Sfeir, C. S.; Healy, K. E. *Proc. Natl. Acad. Sci. U.S.A.* **2002**, *99*, 1972.

[31] Biggs, M. J. P.; Dalby, M. J. *P. I. Mech. Eng. H* **2010**, *224*, 1141.

[32] Geiger, B.; Spatz, J. P.; Bershadsky, A. D. *Nat. Rev.* **2009**, *10*, 21.

[33] Berry, C. C.; Campbell, G.; Spadiccino, A.; Robertson, M.; Curtis, A. S. G. *Biomaterials* **2004**, *25*, 5781.

[34] Park, J.; Bauer, S.; Schlegel, K. A.; Neukam, F. W.; von der Mark, K.; Schmuki, P. *Small* **2009**, *5*, 666.

[35] Park, J.; Bauer, S.; von der Mark, K.; Schmuki, P. *Nano Lett.* **2007**, *7*, 1686.

[36] Kim, E. J.; Boehm, C. A.; Mata, A.; Fleischman, A. J.; Muschler, G. F.; Roy, S. *Acta Biomater.* **2010**, *6*, 160.

[37] Siebers, M. C.; ter Brugge, P. J.; Walboomers, X. F.; Jansen, J. A. *Biomaterials* **2005**, *26*, 137.

[38] Stein, G. S.; Lian, J. B.; Owen, T. A. *FASEB J.* **1990**, *4*, 3111.

[39] Wang, K.; Cai, L.; Wang, S. *Polymer* **2011**, *52*, 2827.

[40] Cai, L.; Chen, J.; Rondinone, A. J.; Wang, S. *Adv. Func. Mater.* **2012**, *22*, 3181.

CHAPTER V
PHOTOCROSSLINKED HONEYCOMB-PATTERNED FILMS WITH SUBMICRON PORES FABRICATED USING MONODISPERSE SILICA NANOPARTICLES AS TEMPLATES FOR REGULATING MC3T3-E1 CELL FUNCTIONS

5.1 Introduction

Understanding the interactions between cells and substrates is critical to developing advanced biomaterials for tissue engineering applications. When cells are exposed to an implant, they can sense the surrounding physicochemical characteristics such as topography, chemistry, and mechanics, which are associated with cell adhesion, migration, proliferation, and differentiation, especially for anchorage-dependent cell lineages.[1-3] In vertebrate body, widely existing basement membranes composed of various extracellular matrix (ECM) proteins, such as laminin, fibronectin, and fibrous collagen, supply integrin receptors to determine cell fate.[4,5] Micrometric or nanometric topographies such as pores, ridges, pillars, and spheres are the dominant structural features of basement membranes and they contribute to cell-matrix interactions via contact guidance. Substrates with grooves, pores, pillars, or spheres have been fabricated to mimic the topography of basement membranes in regulating cell behavior.[6-8]

Honeycomb-patterned poly(ε-caprolactone) (PCL) films with various pore diameters have been fabricated via the breath-figure method from water-immiscible solvents with assistance of amphiphilic copolymers.[9-12] The adhesion, spreading, and proliferation of various cell lineages on these honeycomb-patterned PCL films were also studied. Adhesion of cardiac myocytes and endothelial cells on honeycomb-patterned

PCL films was regulated by the porous structures through the distribution of fibronectin adsorption.[9] The adhesion and growth of epidermal keratinocytes and dermal fibroblasts were enhanced on honeycomb-patterned PCL films (pore size, 3~20 μm) and the best promotion was found when the pores were 3~5 μm.[10] Neural stem cell differentiation on honeycomb-patterned PCL films (pore size, 3~15 μm) was suppressed by the pores and the pore edges guided neurite extension.[11] Chondrocyte proliferation was inhibited on honeycomb-patterned poly(lactic acid) (PLA) films prepared via the breath-figure method with assistance of a surfactant.[13] Fibroblasts showed higher viability on honeycomb-patterned PCL films (pore size, 4 μm or 1 μm) prepared using silica microspheres as the template compared with the flat one.[12] Mouse pre-osteoblastic MC3T3-E1 cell adhesion, attachment, proliferation, mineralization, and the expression of osteoblastic differentiation-related gene markers were found by us to be enhanced on honeycomb-patterned PCL films (pore size, 3~12 μm) prepared using the breath-figure method from a water-miscible solvent, tetrahydrofuran (THF), in particular, films with smaller pores.[6] Despite the extensive studies discussed above, they only focused on the micron-sized pores, except the study on the effect of macroporous hydroxyapatite (HA) and alumina films (pore size, 100~1000 nm) on MC3T3-E1 cell functions, which were inhibited when the pores ranged from 100 to 1000 nm compared with non-porous films.[14] Thus there is a straightforward but elusive question about whether or not there exists a range of pore size to achieve the best promoted MC3T3-E1 cell functions on.

In this report, we present a method to fabricate honeycomb-patterned photo-crosslinked PCLTA films with pore diameters of 43, 93, 322, and 725 nm using monodisperse silica nanoparticles as the templates. Then these films were used to study how the pore size affectsMC3T3-E1 cell adhesion, proliferation, mineralization, and gene expression.

5.2 Experimental Section

5.2.1 Reagents

Chemicals used here were purchased from Sigma-Aldrich unless noted otherwise. Pure ethanol 200 Proof was purchased from Decon Labs Inc.

5.2.2 Fabrication of Monodisperse Silica Nanoparticles

Monodisperse silica nanoparticles with diameters of 43, 93, 322, and 725 nm were prepared using an adapted Stober seed-growth method as described in a previous report.[15] Briefly, ethanol (80 mL), distilled water (4.85 mL) and 28.0-30.0% ammonium hydroxide solution (3.21 mL) were added to a 250 mL flask and gradually heated to a temperature (discussed below) with continuous stirring at 500 rpm. Then a mixture of tetraethyl orthosilicate (TEOS) (3.1 mL) and enthanol (8 mL) was added to the solution and maintained with the same stirring and temperature for 5 h to obtain a suspension of silica nanoparticles. Monodisperse silica nanoparticles with diameters of 43 and 93 nm were prepared at temperatures of 55 and 45 °C, respectively. The 93 nm silica nanoparticles were further used as the seeds for preparing the ones with diameters of 322 and 725 nm. For preparation of the 322 nm silica nanoparticles via seed-growth,

ethanol (70 mL), pure water (13 mL), and ammonium hydroxide solution (6.7 mL) were added to the suspension of the 93 nm silica nanoparticles (10 mL) in a 250 mL flask at 45 °C. Then 1 mL of TEOS was slowly added to the reaction mixture in the presence of continuous stirring. TEOS was added again every hour until the expected size of silica nanoparticles was achieved. The total volume of TEOS used in the reaction was 9 and 14 mL for synthesizing 322 and 725 nm silica nanoparticles, respectively. After the reaction, the suspension of silica nanoparticles was centrifuged at 10000 rpm for 5 min and re-suspended in ethanol for further use.

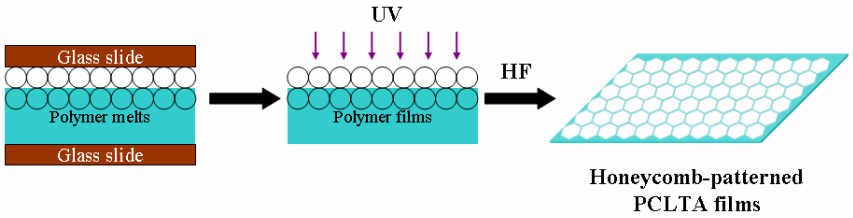

Scheme 5.1 Schematic representation of the fabricating method for honeycomb-patterned PCLTA films. The PCLTA polymer film was melted on glass slide at 60 °C and covered by glass slide with nanoparticles. After the films were cooled down to room temperature, the photocrosslinking reaction was triggered by UV light (λ = 315-380 nm) for 30 min. Then the embedded silica nanoparticles in photo-crosslinked PCLTA films were etched out in 0.5 M hydrofluoric acid (HF) to obtain honeycomb-patterned PCLTA films.

5.2.3 Preparation of Photo-crosslinkable Honeycomb-patterned PCLTA Films

PCLTA (M_n = 20,020 g mol^{-1}, M_w = 22,670 g mol^{-1}) was synthesized in our lab according to a previous report.[16] Photo-initiator phenyl bis(2,4,6-trimethyl benzoyl) phosphine oxide (BAPO, IRGACURE 819) was supplied as a gift by Ciba Specialty Chemicals (Tarrytown, NY). PCLTA and BAPO were dissolved in distilled THF at 50 and 0.5 mg mL^{-1}, respectively. The PCLTA/BAPO solution was cast on a clean glass

slide and covered with another glass slide to prepare thin PCLTA films (thickness, ~ 1 mm) with flat surfaces, followed by gradual drying in air. Silica nanoparticle suspension in ethanol was dip-cast on a clean glass slide and ethanol was slowly evaporated in air and then completely dried in vacuum to obtain silica nanoparticle layers. An as-prepared PCLTA film was melted at 60 °C with the film top covered with the dried silica nanoparticle layers on a glass slide. After the films were cooled down to room temperature, they were exposed to UV light (λ = 315-380 nm) for 30 min. Then the embedded silica nanoparticles in photo-crosslinked PCLTA films were etched by immersing in 0.5 M hydrofluoric acid (HF) overnight and cleaned with ethanol three times, followed by drying in vacuum. The representative procedure was simply shown in scheme 1.

5.2.4 Physical Characterizations

The as-prepared silica nanoparticle layers on glass slides and the as-fabricated photo-crosslinked PCLTA films were sputter-coated with a gold-palladium layer (Emscope SC 500, Elexience) before the surface topography was observed using Scanning Electron Microscopy (SEM; S-3500, Hitachi Instruments, Tokyo, Japan) at an accelerating voltage of 2 kV. The PCLTA network was confirmed by measuring the gel fraction. The polymer films with the original weight of W_0 were immersed in excessive CH_2Cl_2 for 2 days and then dried completely in vacuum before they were weighed as W_d. The gel fraction was calculated using $W_d/W_0 \times 100\%$.

5.2.5 Water Contact Angle and Protein Adsorption

Prior to determination of water contact angle and protein adsorption, the polymer films were dried thoroughly in vacuum. Water contact angles were measured after the water droplets were stable on the polymer films using a Ramé-Hart NRC C.A. goniometer (model 100-00-230) at room temperature. For determining protein adsorption, the polymer films were immersed in the culture medium for MC3T3-E1 cells or fibronectin/phosphate buffered saline (PBS) solution (10 μg mL^{-1}) for 4 h at 37 °C. Then the films were rinsed with PBS several times to remove unattached proteins and subsequently immersed in 300 mL of 1% sodium dodecyl sulfate (SDS) solution 5 times with 1 h interval each time to collect proteins. The protein concentrations in the SDS solutions were measured using a MicroBCA protein assay kit (Pierce, Rockford, IL) on a microplate reader (SpectraMax Pus 384, Molecular Devices, Sunnyvale, CA). A standard calibration curve was plotted using eight albumin solutions with known concentrations. Albumin was from the MicroBCA kit and the procedure was according to the manufacturer's instruction. .

5.2.6 In vitro Cell Attachment and Proliferation

Mouse MC3T3-E1 cells (ATCC, Manassas, VA) were cultured as described previously.[6,17] The polymer films were immersed in 70% alcohol solution for 2 × 30 min to first clean the surfaces and then sterilized in 70% alcohol solution again for 2 × 20 min, followed by complete drying in high vacuum overnight. Cells were seeded on the polymer films at a density of ~12000 cells/cm^2 and cultured in α-Minimum Essential Media (α-MEM, Gibco) that contained 10% fetal bovine serum (FBS, Gibco) and 1%

penicillin/streptomycin (Gibco) in an incubator with humidity of 95% and 5% CO_2 at 37 °C. At each time point, cell numbers on the polymer films were determined using a colormetric cell metabolic assay (CellTiter 96 Aqueous One Solution, Promega, Madison, WI), as elaborated in a previous report.[18]

5.2.7 Immunofluorescence Microscopy and Cell Morphology

MC3T3-E1 cells on the polymer films were fixed in 4% paraformadehyde (PFA) solution for ~20 min and rinsed with PBS twice after the removal of PFA solution. The fixed cells were further permeabilized with 0.2% (v/v) Triton X-100, washed with PBS twice, and stained with rhodamine-phalloidin (RP) for 1.5 h at 37 °C and 4',6-diamidino-2-phenylindole (DAPI) at room temperature. An Axiovert 25 light microscope (Carl Zeiss, Germany) was used to photograph the cytoskeleton and nuclei. For observation of focal adhesions (FAs), cells were stained via incubation with mouse monoclonal anti-vinculin antibody (V9246, Sigma-Aldrich) for 1 h and then stored at 4 °C overnight. Afterwards, cells were rinsed with PBS more than 10 times. The FAs in the cells were labeled by incubating the cells with anti-mouse IgG-FITC antibody (F0257, Sigma) for 4 h. The cells were also stained with RP using the procedure described above. The FAs and cytoskeleton in the cells were photographed using a confocal microscope (SP2, Leica). For SEM observation, cells cultured on the polymer films for 1 day were fixed with PFA and rinsed with PBS twice. The samples were further dehydrated with gradient ethanol solutions (30%, 50%, 60%, 70%, 80%, 90%, 95%, and 100%) for 10 min at each concentration. Then the cells were dehydrated in a mixture (1:1, v/v) of ethanol and hexamethyldisilazane (Electron Microscopy Science, Hatfield, PA) and subsequently in

100% hemamethyldisilazane. The samples were completely dried in air overnight and sputter-coated with a gold-palladium layer before SEM imaging.

5.2.8 In vitro Cell Mineralization

After 14-day culture, the polymer films with cells were rinsed with PBS to remove unattached cells. Then the attached cells were trypsinized and collected using centrifugation at 1000 rpm for 4 min. The cell pellet was re-suspended in PBS and centrifuged again at the same condition. Then the collected cell pellet was suspended in 1 mL of 0.2% Nonidet P-40 solution and sonicated in ice water for 2 min. The alkaline phosphatase (ALP) activity and calcium content of the cells were determined using an ALP detection kit (Sigma, St. Louis, MO) and a QuantiChrom calcium assay kit (BioAssay Systems, Hayward, CA), respectively.

5.2.9 Gene Expression

RNA was isolated from the cells cultured on the polymer films for 14 days using an RNeasy Mini Kit (Qiagen, Valencia, CA) and then cDNA was synthesized from the RNA using a cDNA synthesis kit (Thermo Scientific) according to the manufacturer's instruction. The expression of integrin subunits (α_1, α_2, and β_1) and glyceraldehyde-3-phosphate dehydrogenase (GAPDH) in the cells cultured on the polymer films for 1 day, and the expression of three osteoblastic differentiation markers, i.e., ALP, osteocalcin (OCN), and osteopontin (OPN), in the cells cultured on the polymer films for 14 days was quantified using real-time polymerase chain reaction (PCR) with a Power SYBR Green PCR Master Mix (Applied Biosystems, Carlsbad, CA) and recorded on a thermal

cycler with fluorescence detection systems (PTC-200, MJ Research). The oligonucleotide primers for real-time PCR reaction were listed in Table 3.1.

5.2.10 Statistical Analysis

Cell studies were conducted in quadruplicates for each group at each time point. All values were written as mean ± standard deviation. The measurement of cell area and the quantification of FAs were conducted on ~20 images (~200 cells) using ImageJ software (National Institues of Health, Bethesda, MD). The statistical significant differences ($p < 0.05$ and $p < 0.01$) between groups were determined using student's *t*-test.

5.3 Results and Discussion

The morphologies of the silica nanoparticles and honeycomb polymer films with different pore diameters fabricated using the nanoparticles as the templates are demonstrated in SEM images in Figure 5.1. The smallest the nanoparticles had a diameter of 47 ± 5 nm. When more TEOS was added to the reaction solution, the diameter of the nanoparticles increased to 103 ± 9, 335 ± 28, and 756 ± 71 nm, as shown in Figure 1a. The pores in the honeycomb films in Figure 1b were fairly monodisperse and their structure and size were close to those of the template nanoparticles. The smaller pore diameters of 725 ± 63, 322 ± 53, 93 ± 7, and 43 ± 4 nm in the honeycomb polymer films compared with their corresponding nanoparticles was because that the pores appeared on the top surface were not exactly from hemispheres. There were structural defects, i.e., a few small regions without pores, on the honeycomb surface because some fully embeded nanoparticles might not be etched away by HF acid. The gel fractions of the flat, solid

photo-crosslinked PCLTA film and the honeycomb-patterned ones were ~83% without significant differences among them, indicating that they all were well crosslinked.

The topography can influence the wettability of polymer films.[19-21] As demonstrated in Figure 1b, the water contact angles were 128.3 ± 4.5°, 126.2 ± 3.3°, 125.7 ± 5.1°, and 123.5 ± 3.7° when the pore diameter was 725, 322, 93, and 43 nm, respectively. Pores on the film surface can efficiently generate air pockets between the water droplet and the surface when the water droplet contacting the porous film is larger than the pore. Air pockets can increase the hydrophobicity of a polymer film. The water contact angle (θ) on a honeycomb polymer film can be predicted using the Cassie and Baxter model in eq. 1.[13,19-21]

$$\cos\theta = (1 - f_o)\cos\theta_s + f_o\cos\theta_o \qquad (1)$$

where f_o is the fractional flat geometrical area of liquid-air interface beneath a water droplet, θ_s is the water contact angle on the smooth surface of photo-crosslinked PCLTA, which was determined to be 75.8 ± 2.9°, and θ_o is the water contact angle of 180° on the pore filled with air. When the pore diameters were 725, 322, 93, and 43 nm, the rim sizes measured from the SEM images in Figure 1b were 65 ± 15, 45 ± 8, 15 ± 2, and 7 ± 2 μm, and the f_o values were calculated to be 0.601, 0.600, 0.590, and 0.585, then the water contact angles predicted using eq. 1 were 120.2°, 119.8°, 119.1°, and 118.3°, respectively. Although the predicted values were smaller than the experimental data, it showed higher hydrophobicity on the larger pores. In our earlier study on honeycomb PCL films, the water contact angle increased from 72.6 ± 1.8° on the smooth film to 104.0 ± 1.4°, 113.5 ± 2.1°, and 136.4 ± 4.4° on the films with 10, 6.0, and 3.5-μm pores, respectively.[14] In

that study, f_o increased from 0.528 to 0.553 and 0.592 when the pore diameter decreased from 10 to 6.0 and 3.5 μm, respectively. In contrast, in this study, f_o and the water contact angles decreased with decreasing the pore diameter.

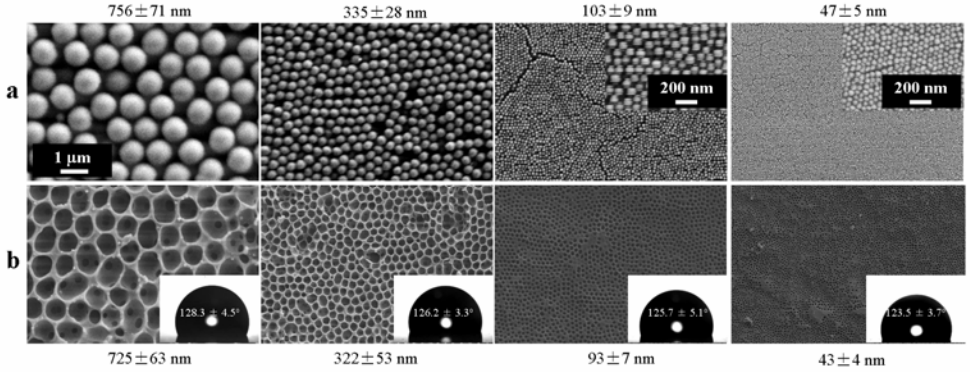

Figure 5.1 SEM images of (a) silica nanoparticles with different diameters and (b) honeycomb-patterned photo-crosslinked PCLTA films fabricated using nanoparticles as templates. Magnification: × 20000. Insets in (a): magnification of × 50000. Insets in (b): micrographs of water droplets on the films marked with the water contact angles.

For anchorage-dependent cells, e.g., MC3T3-E1 cells, ECM proteins such as fibronectin, vitronectin, and type-I collagen are critical to early-stage cell adhesion when a substrate is exposed to cells for interaction and ECM protein adsorption can be influenced by substrate chemistry and morphology.[3] Our earlier study showed that the surface area was larger when the pores were smaller as the result of a higher f_o and consequently the amount of proteins adsorbed on honeycomb PCL films with smaller pores was higher.[6] In this study, f_o decreased with decreasing the pore diameter because of the formation of larger flat-top area fraction caused by the rim size. Based on the rough assumption that the pores were hemispheres and their diameters, the ratios (R_s) of the entire surface area to the projected area were calculated to be 1.0, 1.81 ± 0.16, 1.62 ±

0.13, 1.55 ± 0.11, and 1.52 ± 0.14 on the solid film and honeycomb films with pore diameters of 725, 322, 93, and 43 nm, respectively. As the result, the honeycomb film with larger pores has a greater contact area with serum proteins in the culture media. As shown in Figure 5.2, both serum proteins and fibronectin were adsorbed more on the honeycomb films than on the solid one. The protein adsorption was slightly higher on the films with smaller pores but without significant difference. The serum protein adsorbed was 2.2 ± 0.6, 10.8 ± 1.4, 9.8 ± 1.3, 9.6 ± 1.7, and 9.5 ± 1.4 μg/cm^2 while the fibronectin adsorbed was 1.2 ± 0.3, 5.9 ± 0.8, 5.5 ± 0.7, 5.2 ± 0.4, and 5.3 ± 0.3 μg/cm^2 on the solid film and honeycomb films with pore diameters of 725, 322, 93, and 43 nm, respectively.

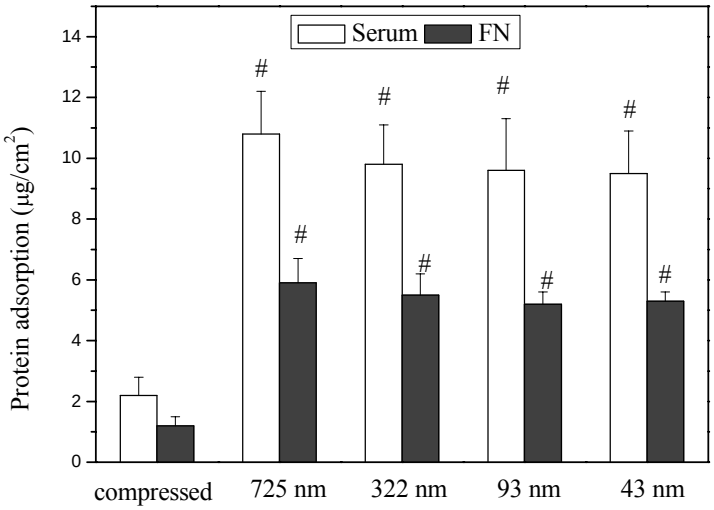

Figure 5.2 Adsorption of serum proteins and fibronectin onto the solid film and the honeycomb ones with different pore diameters. #: $p < 0.01$ relative to the solid film.

MC3T3-E1 adhesion at day 1 was evaluated using vinculin/RP-stained fluorescent images, characterization of FAs, which are the closest contacts between cells

and the underlying substrate, and integrin expression.[22,23] As shown in the images in Figure 5.3a, the cells had significantly more FAs on the honeycomb films, especially when the pore diameter was smaller, compared with cells on the solid film. The FA length was estimated to be 2-8 μm and was much larger than the pores. Thus, the FAs on the honeycomb films did not show preferable alignment along the pore rims, which was present in MC3T3-E1 cells cultured on honeycomb PCL films with pore diameters of 3.5~10 μm.[6] As demonstrated in the RP-stained images, cytoskeleton on the solid film had few stress fibers and protrusions while it had prominently better stress fibers and protrusions projecting from the cell bodies on the honeycomb ones. Unlike our previous finding that MC3T3-E1 cells were trapped in 10 or 6 μm pores on honeycomb PCL films,[6] it was not observed in this study because the pores were much smaller than the cytoskeleton. The vinculin-stained images at a higher magnification in Figure 5.3a indicated that the FAs on the honeycomb films were longer and more aligned than those on the solid film, especially when the pores were smaller.

Determined from the vanculin-stained images, the average area of the FAs, the FA density defined as the average number of FAs per cell, and the circularity of FAs defined as $4\pi \times \text{area/perimeter}^2$ are shown in Figure 5.3b. The average area and density of FAs on the honeycomb films were much larger than those on the solid one, especially when the pores were smaller. The circularity of FAs decreased significantly with decreasing the pore diameter, indicating that FAs were better aligned on smaller pores. The FA-ECM interaction involves integrins, i.e., transmembrane heterodimers of an α-subunit and a β-subunit, to bridge osteoblasts and ECM proteins such as fibronectin,

vitronectin, and type-I collagen through "outside-in-signaling" and "inside-out-signaling".[24,25] Thus integrins play a key role in determining cell adhesion, proliferation, and differentiation. Here we determined the expression levels of integrin subunits α_1, α_2, and β_1 using real-time RT-PCR, as shown in Figure 5.3c. The expression levels of all these three integrin subunits on the honeycomb films were significantly higher than on the solid, especially when the pores were smaller.

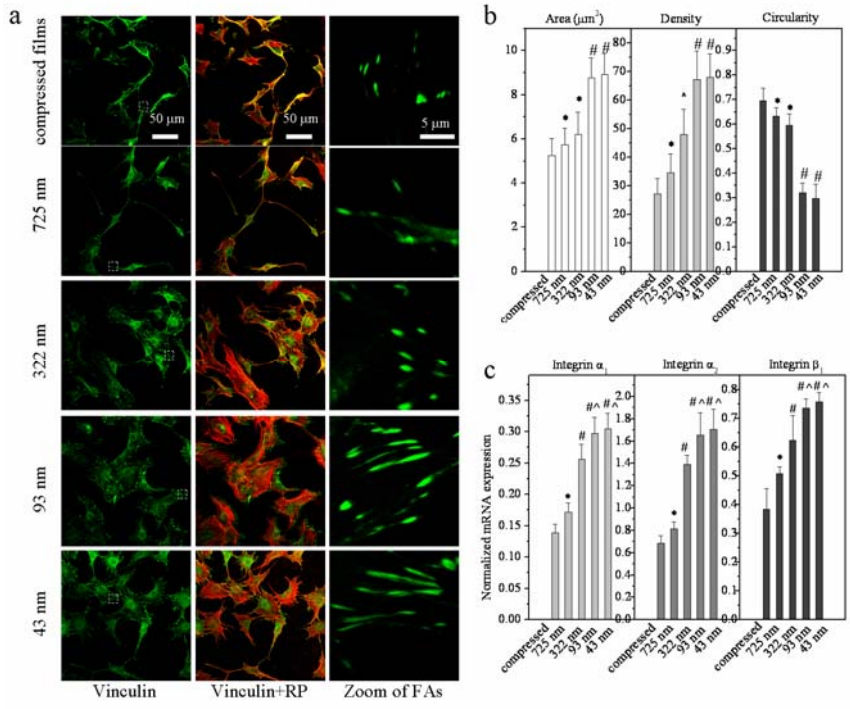

Figure 5.3 (a) Fluorescent images of vinculin-stained MC3T3-E1 cells on the polymer films at day 1 (left and right columns, green) and merged ones (middle column) with the cells stained using RP. The images in the right column are magnified views of the dotted areas in the left column. The scale bars in the first row are applicable to the images in the same columns. (b) Area, density, and circularity of FAs in the cells cultured on the polymer films for 1 day. *: $p < 0.05$ relative to the solid film; #: $p < 0.01$ relative to the solid film and the honeycomb films with pores of 725 and 322 nm; ^: $p < 0.05$ relative to the solid film and the honeycomb films with pores of 725 nm. (c) Expression of integrin subunits α_1, α_2, and β_1 in the cells cultured on the polymer films for 1 day. *: $p < 0.05$ relative to the solid film; #: $p < 0.01$ relative to the solid film and the honeycomb film with pores of 725 nm; ^: $p < 0.05$ relative to the honeycomb film with pores of 322 nm.

MC3T3-E1 cell adhesion was also demonstrated using SEM images in Figure 5.4. More cells were observed on the honeycomb films, especially when the pores were smaller. Cells on the solid film were still spreading with a large thickness and few filopodia, whereas the cells on the honeycomb ones, especially with smaller pores, spread

much better with a smaller thickness and many filopodia projecting from the cell membrane.

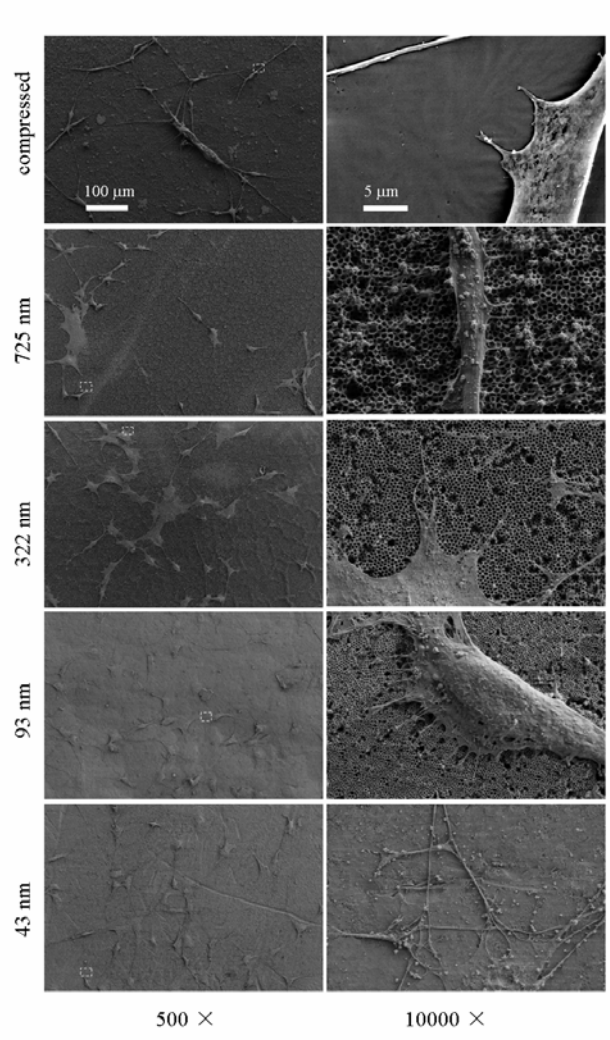

Figure 5.4 SEM images of MC3T3-E1 cells at day 1 on the solid film and the honeycomb films with different pore diameters. The images in right column are magnified images of the dotted areas in the left column. Magnification: × 500 (left column) and × 10000 (right column).

Cells interact with micro/nano-topographic features on the underlying substrate via "contact guidance".[4,5,7,8] Although the honeycomb films had higher surface area

and higher protein adsorption, which might enhance cell adhesion, MC3T3-E1 cell adhesion was even lower on the films with larger pores that adsorbed more serum proteins. Since cells were not trapped inside the pores, mainly the proteins adsorbed on the flat-tops influenced cell adhesion. Assuming that the surfaces of the flat-tops and inside the pores had the same capability of adsorbing proteins, we calculated the proteins adsorbed on the flat-tops as a fraction $(1- f_o)/R_s$ of the total amount of adsorbed proteins. Then the amounts of serum proteins adsorbed on the flat-tops were 2.38 ± 0.15, 2.45 ± 0.12, 2.54 ± 0.11, and 2.60 ± 0.13 μg/cm^2 while the amounts of adsorbed fibronectin were 1.30 ± 0.06, 1.34 ± 0.05, 1.38 ± 0.04, and 1.42 ± 0.05 on the honeycomb films with pores of 725, 322, 93, and 43 nm, respectively. These data showed that protein adsorption was slightly better on the flat-tops of the honeycomb films than on the solid one. In our previous study, smaller pores resulted in lower protein adsorption on the flat-tops of honeycomb PCL films with pores diameters of 3.5 and 6.0 μm but MC3T3-E1 cells showed much better adhesion on the films with smaller pores.[6] Fibril-like fibronectin aggregates were observed around the periphery of the pores in honeycomb-patterned PCL films to determine the distribution of FAs in the cells.[9,10,26-28] Nevertheless, the pores in the previous studies were at micrometer scale. It is unclear if the submicron pores in the present study influenced the distribution of ECM proteins. In addition, only the proteins adsorbed and could not be rinsed away on the films were counted but the entire films were immersed in the culture media in cell studies. The pores might hold unattached ECM proteins inside, which might be released gradually to support cell adhesion when cells spread over these pores.

Better cell adhesion on the honeycomb films with smaller pores subsequently resulted in enhanced cell proliferation.[24] Cell attachment at 4 h and proliferation over 4 days were investigated using both fluorescent images and MTS assay, as shown in Figure 5.5a,b. Consistent with the SEM images in Figure 5.4, more cells were found on the honeycomb films than on the solid one, especially when the pores were smaller. Cells at day 4 were confluent over the films without being trapped inside the pores of the honeycomb films. As shown in Figure 5.5b, cell attachment and proliferation were higher on the honeycomb films than on the solid one., Cell spread area in Figure 5.5c was measured from the fluorescent images at day 1 using ImageJ and the values on the honeycomb films, especially the ones with smaller pores were higher.

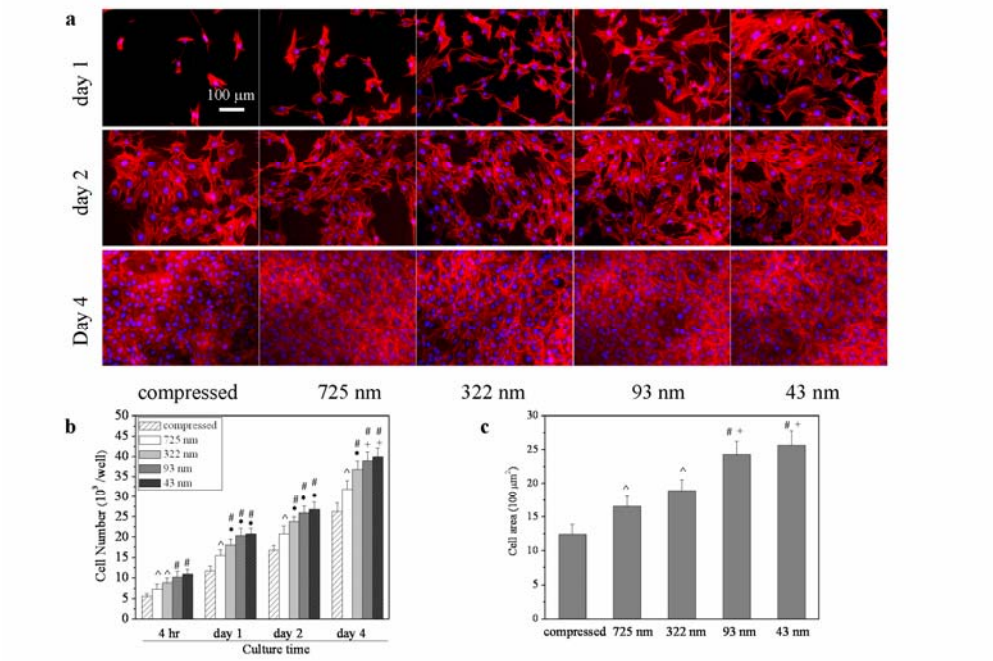

Figure 5.5 (a) Fluorescent images of MC3T3-E1 cells stained with RP (red) and DAPI (blue) at days 1, 2, and 4 on the solid film and the honeycomb films with different pore diameters. Scale bar of 100 mm is applicable to all. (b) MC3T3-E1 cell attachment and proliferation on the films represented by cell numbers at 4 h, days 1, 2, and 4. ^: $p < 0.05$ relative to the solid film; #: $p < 0.01$ relative to the solid film; *: $p < 0.05$ relative to the honeycomb film with pores of 725 nm; +: $p < 0.01$ relative to the honeycomb film with pores of 725 nm. (c) Cell spread area on the films at day 1. ^: $p < 0.05$ relative to the solid film; #: $p < 0.01$ relative to the solid film; +: $p < 0.01$ relative to the solid film and the honeycomb films with pores of 725 and 322 nm.

MC3T3-E1 cell nuclei stained with DAPI were analyzed using ImageJ in terms of circularity and area. As shown in Figure 5.6, cell nuclei on all the films showed a nearly round shape with a circularity of ~0.9, indicating that there was no preferential alignment along a specific direction. However, the nuclei on the honeycomb films were larger, especially when the pores were smaller. The value increased continuously from 215 ± 21 μm^2 on the solid film to 257 ± 32, 276 ± 51, 293 ± 48, and 325 ± 73 μm^2 on the honeycomb films with pores of 725, 322, 93, and 43 nm, respectively. This nuclear

expansion was caused by the expansion in cytoskeleton through mechanotransduction as cytoskeleton spread much better on the honeycomb films with smaller pores discussed earlier.[7,8,29,30] In mechanotransduction, the stress in the actin structure immediately transferred to intermediate filaments and further to cell nuclei.

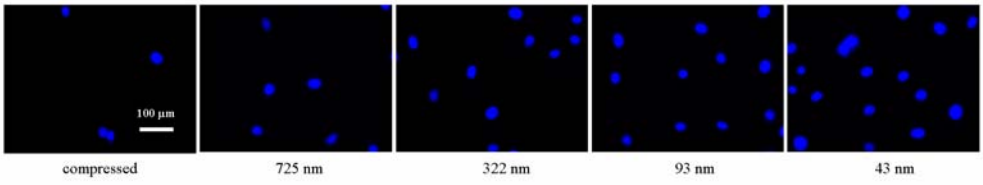

Figure 5.6 MC3T3-E1 cell nuclei stained with DAPI at day 1 on the solid film and the honeycomb ones with different pore diameters. Scale bar of 100 μm is applicable to all the images.

The higher cell adhesion on the honeycomb films, especially those with smaller pores also promoted MC3T3-E1 cell mineralization. As shown in Figure 5.7a, the ALP activity and calcium content of MC3T3-E1 cells cultured for 14 days, two indicators of osteogenesis, were significantly higher on the honeycomb films than on the solid one and the values increased with decreasing the pore diameter. The expression levels of three bone-specific differentiation markers, ALP, OCN, and OPN, are shown in Figure 5.7b. Consistent with the ALP activity and calcium content, the expression levels of ALP, OCN, and OPN on the honeycomb films were higher than on the solid one, especially when the pores were smaller. The low expression level of ALP at day 14 was because ALP is an early-stage marker of osteogenesis and reaches maximum in the matrix maturation stage at day 7.[25,31] In contrast, the much higher expression levels of OCN and OPN were because they are mature bone-specific markers and reach maximum or

continue to grow in the mineralization stage that happen at day 14. [21,31] The above results in MC3T3-E1 cell differentiation and mineralization can be attributed to two reasons. The first reason was that MC3T3-E1cell adhesion was promoted by the honeycomb films, especially those with smaller pores, and such promotion was extended to cell proliferation, which resulted in a higher cell population for beginning cell differentiation and mineralization earlier on the small-pore films. The second reason was that expansion of MC3T3-E1 cell nuclei on the honeycomb films could upregulate the expression of bone-specific gene markers.[17,32-34] In our previous studies, MC3T3-E1 cell skeleton and their nuclei were deformed (either expansion or aligned) and correlated with enhanced mineralization on $CaCO_3$ grooves and honeycomb PCL films compared with flat $CaCO_3$ and solid PCL films, respectively. [6,17]

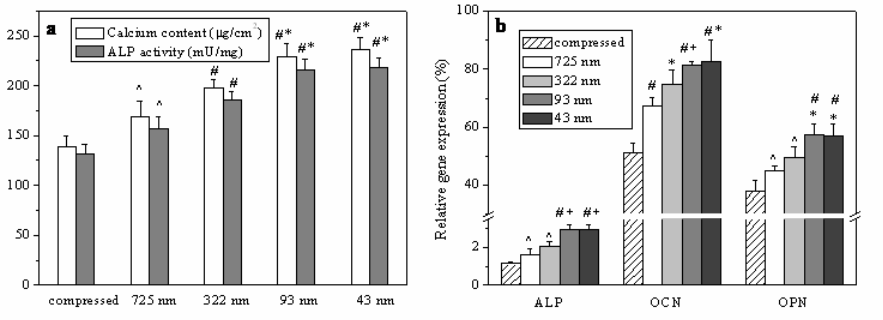

Figure 5.7 (a) ALP activity and calcium content of MC3T3-E1 cells cultured for 14 days on the solid film and the honeycomb films with different pore diameters. ^: $p < 0.05$ relative to the solid film; #: $p < 0.01$ relative to the solid film; *: $p < 0.05$ relative to the honeycomb films with pores of 725 nm; (b) Gene expression levels of ALP, OCN, and OPN relative to GAPDH in MC3T3-E1 cells cultured for 14 days on the films. ^: $p < 0.05$ relative to the solid film; #: $p < 0.01$ relative to the solid film; *: $p < 0.05$ relative to the honeycomb films with pores of 725 nm; +: $p < 0.01$ relative to the honeycomb films with pores of 725 nm.

5.4 Further Discussion

For different cell types, their responses to honeycomb substrates can be different. For example, epidermal keratinocyte and dermal fibroblast cell adhesion and proliferation were higher on honeycomb PCL films with pores of 3 and 5 μm than on the flat film and films with 15 or 20 μm pores.[10] Diferrently, chondrocyte proliferation was slower on honeycomb PLA films with pores of 5 μm than on the flat film.[12]

For MC3T3-E1 cells, we reported that the cells preferred to adhere and proliferate on honeycomb PCL films than on the solid one, especially when the pores were smaller in the range of 3-10 mm.[6] This trend was found in the present study to be extended to the range of 43 to 725 nm. Ordered macroporous silica films with pore of 100-1000 nm were used as the underlying substrates for culturing MC3T3-E1 cells and the porous

structures inhibited cell adhesion and proliferation, especially when the pores were smaller.[14]

The cellular responses to honeycomb films should be understood by incorporating pore dimension, rim size, and material properties. When the pores are larger than 6 μm, cell filaments and protrusions can enter the pore or be partly trapped inside pores to cause distortion of both cytoskeleton and cell nuclei. The pore size also determines the total length of the pore edges per unit area, which provides leverage to support cell adhesion and are "discontinuities" on the surface. Besides affecting the cell body directly, micron-scale honeycomb pores also influence the cell adhesion through the distribution of adsorbed proteins on the surface because the protein distribution has an important role in formation of FAs during cell-substrate interactions.[9,10,26-28] When the pores are at the nanometer scale, both FA and cytoskeleton are much larger and then the substrate topography influence cell-substrate interactions through ECM protein adsorption and distribution of integrins. For example, pores with a diameter of 15 nm best promoted mesenchymal stem cell functions compared with larger or smaller pores in TiO_2 porous substrates as this pore size was optimal for integrin assembly into FAs.[35,36]

Besides the pore size, other structural parameters such as rim size and f_o in honeycomb films are also important in regulating MC3T3-E1 cell behavior. In our previous study using micron-pore honeycomb PCL films as the substrates for MC3T3-E1 cells, f_o increased from 0.528 to 0.592 with decreasing the pore size from 10 to 3.5 μm because rim size also decreased from 3.05 ± 0.25 to 0.83 ± 0.04 μm.[6] Therefore, the total surface area of the honeycomb film increased to gather more adsorbed proteins when the pore size decreased.[6] However, this trend did not happen in the present study, in which f_o

and the total surface area also decreased when the pore diameter decreased from 725 to 43 nm because of the slower decrease of rim size. Consequently, protein adsorption was higher on the films with larger pores instead, though the protein adsorption on the flat-tops of the honeycomb films was slightly better on those with smaller pores.

Note that different materials from which honeycomb films are made also affect the cellular responses to these films. For example, the honeycomb films made from photocrosslinked PCLTA in this study could promote MC3T3-E1 cell functions but macroporous silica films with similar pore diameters were reported to inhibit MC3T3-E1 cell functions.[14] Given the variations in structural parameters and material properties, which oftentimes were not sufficed in literature, it is still difficult to generalize how honeycomb films in regulating cell fate.

5.5 Conclusion

Honeycomb-patterned photocrosslinked PCLTA films with pore diameters of 43, 93, 322, and 725 nm were fabricated using monodisperse silica nanoparticles as templates. Compared with the solid film of photocrosslinked PCLTA, these honeycomb films promoted pre-osteoblastic MC3T3-E1cell adhesion, spreading, proliferation, and differentiation and this promotion was more prominent on the films with smaller pores. These honeycomb films with submicron pores serve as excellent platform for investigating cell-material interactions and also promising materials for bone tissue engineering applications.

References

[1] Discher, D. E.; Janmey, P.; Wang, Y. *Science* **2005**, 310, 1139.

[2] Yu, L. M. Y.; Leipzig, N. D.; Shoichet, M. S. *Mater. Today* 2008, 11, 36.

[3] Harbers, G. M.; Grainger, D. W. Cell-matetial interactions: fundamental design issues for tissue engineering and clinical considerations. In Introduction to Biomaterials; Guelcher, S. A., Hollinger, J. O., Eds.; CRC Press: Boca Raton, FL, 2005; pp 15-45.

[4] Bettinger, C. J.; Langer, R.; Borenstein, J. T. *Angew. Chem. Int. Ed.* **2009**, 48, 5406.

[5] Flemming, R. G.; Murphy, C. J.; Abrams, G. A.; Goodman, S. L.; Nealey, P. F. *Biomaterials* **1999**, 20, 573.

[6] Wu, X.; Wang, S. *ACS Appl. Mater. Interfaces* **2012**, 4, 4966.

[7] Anselme, K.; Bigerelle, M. *Int. Mater. Rev.* **2011**, 56, 243.

[8] Dalby, M. J. *Med. Eng. Phys.* **2005**, 27, 730.

[9] Yamamoto, S.; Tanaka, M.; Sunami, H.; Arai, K.; Takayama, A.; Yamashita, S.; Morita, Y.; Shimomura, M. *Surf. Sci.* **2006**, 600, 3785.

[10] Mcmillan, J. R.; Akiyama, M.; Tanaka, M.; Yamamoto, S.; Goto, M.; Abe, R.; Sawamura, D.; Shimomura, M.; Shimizu, H. Tissue Eng. 2007, 13, 789.

[11] Tsuruma, A.; Tanaka, M.; Yamamoto, S.; Shimomura, M. *Colloids Surf A* **2008**, 313-314, 536.

[12] Fukuhira, Y.; Kaneko, H.; Yamaga, M.; Tanaka, M.; Yamamoto, S.; Shimomura, M. *Colloids Surf A* **2008**, 313-314, 520.

[13] Wang, B.; Mao, Z.; Meng, X.; Tong, W.; Gao, C. *Colloids Surf B* **2010**, 76, 38.

[14] Orita, T.; Tomita, M.; Kato, K. *Colloids Surf B* **2011**, 84, 187.

[15] Chen, C.; Li, Y.; Liu, S. *J. Electroanal. Chem.* **2009**, 632, 14.

[16] Cai, L.; Wang, S. *Polymer* **2010**, 51, 164.

[17] Wu, X.; Wang, S. *Adv. Healthcare. Mater.* **2013**, 2, 326.

[18] Wang, S.; Kempen, D. H.; Simha, N. K.; Lewis, J. L.; Windebank, A. J.; Yaszemski, M. J.; Lu, L. *Biomacromolecules* **2008**, 9, 1229.

[19] Cassie, A. B. D.; Baxter, S. *Trans. Faraday Soc.* **1944**, 40, 0546.

[20] Murray, M. D.; Darvell, B. W. *J. Phys. D* **1990**, 23, 1150.

[21] Min, E.; Wong, K. H.; Stenzel, M. H. *Adv. Mater.* **2008**, 20, 3550.

[22] Biggs, M. J. P.; Dalby, M. J. *P. I. Mech. Eng. H* **2010**, 224, 1441.

[23] Geiger, B.; Spatz, J. P.; Bershadsky, A. D. *Nature Rev.* **2009**, 10, 21-33.

[24] Anselme, K. *Biomaterials* **2000**, 21, 667.

[25] Siebers, M. C.; ter Brugge, P. J.; Walboomers, X. F.; Jansen, J. A. *Biomaterials* **2005**, 26, 137.

[26] Sunami, H.; Ito, E.; Tanaka, M.; Yamamoto, S.; Shimomura, M. *Colloids Surf A* **2006**, 284-285, 548.

[27] Tanaka, M.; Takayama, A.; Ito, E.; Sunami, H.; Yamamoto, S.; Shimomura, M. *J. Nanosci. Nanotechnol.* **2007**, 7, 763.

[28] Yamamoto, S.; Tanaka, M.; Sunami, H.; Ito, E.; Yamashita, S.; Morita, Y.; Shimomura, M. Langmuir 2007, 23, 8114.

[29] Dalby, M. J.; Reihle, M. O.; Yarwood, S. J.; Wilkinson, C. D. W.; Curtis, A. S. G. *Exp. Cell Res.* **2003**, 284, 274.

[30] Maniotis, A. J.; Chen, C. S.; Ingber, D. E. *Proc. Natl. Acad. Sci. USA.* **1997**, 94, 849.

[31] Stein, G. S.; Lian, J. B.; Owen, T. A. *Faseb J.* **1990**, 4, 3111.

[32] Thomas, C. H.; Collier, J. H.; Sfeir, C. S.; Healy, K. E. *PNAS* **2002**, 99, 1972

[33] Relan, N. K.; Yang, Y.; Beqaj, S.; Miner, J. H.; Schuger, L. J. Cell Biol. 1999, 147, 1341.

[34] Itano, N.; Okamoto, S.; Zhang, D.; Lipton, S. A.; Ruoslahti, E. *PNAS* **2003**, 100, 5181.

[35] Park, J.; Bauer, S.; Schlegel, K. A.; Neukam, F. W.; von der Mark, K.; Schmuki, P. *Small* **2009**, 5, 666.

[36] Park, J.; Bauer, S.; von der Mark, K.; Schmuki, P. *Nano. Lett.* **2007**, 7, 1686.

CHAPTER VI
HONEYCOMB PATTERNS AND MICROGROOVES SYNERGISTICALLY REGULATE MC3T3-E1 CELL FUNCTIONS

6.1 Introduction

Biomimetic materials can mimic basement membranes throughout vertebrate body with surface features such as wells, pores, grooves, and pillars at the nanometer and micron scale. These surface features include microgrooves, pores, pillars, and posts,[1,2] among which the former two have been used and studied more often. Adherent cells sense and respond to the substrate topography via contact guidance and these responses are cell-type dependent.[1-3]

Endothelial and cardiac myocyte adhesions on honeycomb-patterned poly(ε-caprolactone) (PCL) films were regulated by pores as the pores influenced the distribution of fibronectin adsorption.[4] Both adhesion and proliferation of dermal fibroblasts and epidermal keratinocytes were promoted on honeycomb-patterned PCL films with diameters of 3~20 μm, especially when the pores were smaller.[5] The viability of fibroblasts on honeycomb-patterned PCL samples fabricated using silica microspheres as the template was higher than that on flat PCL films.[6] Pre-osteoblastic MC3T3-E1 cell adhesion, attachment, proliferation, and mineralization were promoted on honeycomb-patterned PCL samples with diameters of 3~10 μm prepared using breath-figure method and smaller pores had a stronger effect.[3] On the other hand, neural stem cell differentiation was suppressed on honeycomb-patterned PCL films with diameters of 3-15 μm, whereas the pore edges showed clear guidance for neurite extension.[7] In

another study, chondrocyte proliferation was inhibited on honeycomb-patterned poly(lactic acid) (PLA) samples.[8] The main response of cells to microgrooves is cell alignment along the groove direction, especially when the grooves are deeper and narrower, whereas cell attachment and proliferation are not significantly influenced.[9,10] It is believed that cells may not sense the surface topography via focal adhesions when the groove spacing is > 5 μm and, meanwhile, the depth is < 1 μm.[11]

Although advancement of microfabrication methods fosters cell studies on numerous surface features, many complicated structures are still challenging to produce. For example, how cells respond to substrates with both microgrooves and honeycomb patterns is yet to be understood. Polydimethylsiloxane (PDMS)-based honeycomb-patterned samples with hierarchal surface features have been achieved on transmission electron microscopy template grids with various morphologies via the breath-figure method.[12-14]

In this study, we used a tri-block amphiphilic copolymer synthesized recently by us and incorporated the breath figure method with replica molding to fabricate complicated substrate structures for regulating MC3T3-E1 cells. This copolymer named as CoPLLA17200 consisted of a linear poly(ethylene glycol) (PEG) center block and poly(L-lactide) (PLLA) dendrons with a PLLA arm molecular weight of 17200 g/mol. Previously our research group reported that MC3T3-E1 cells spread and proliferated better on honeycomb-patterned films than on the solid one,[3] while the cell spreading was limited along the groove direction on polymer microgrooved substrates although the alignment and differentiation was stimulated. Thus we performed this study to elucidate the roles of two kinds of surface features in regulating MC3T3-E1 cells.

6.2 Experimental Section

6.2.1 Materials

CoPLLA17200 was synthesized in our research group as described previously. All chemicals used here were purchased from Sigma-Aldrich Co. (Milwaukee, WI) unless otherwise noted. Silicon wafers with parallel microgrooves with groove widths of ~5, ~15, and ~45 μm and groove depth of 10 μm were fabricated as templates using standard stereolithography.

6.2.2 Fabrication of CoPLLA17200 Microgrooves with Honeycomb-Patterned Feature

CoPLLA17200 was dissolved in methylene chloride (CH_2Cl_2) at a concentration of 0.015 g/mL and the solution was cast on the silicon wafers in a closed chamber with a constant relative humidity of 80% and moist airflow over the solution cast on the silicon wafers at a flow rate of 50 mL/min. As CH_2Cl_2 evaporated gradually, the solution on the wafers became opaque. Honeycomb-patterned copolymer films on flat glass slides were prepared as the control group using the same procedure. After drying, the copolymer films were peeled off and further dried in vacuum. Microgrooved copolymer substrates without honeycomb patterns were prepared in absence of humidity. In the following sections, microgrooved substrates with honeycomb patterns, microgrooved substrates without honeycomb patterns, and honeycomb films are named as H-grooves, F-grooves, and H-films, respectively. The number attached to H- or F- denotes the groove width of the silicaon wafter used to fabricate the polymer sample.

6.2.3 Surface Feature

The as-prepared copolymer films were fixed on flat glass slides and sputter-coated with a gold-palladium layer (Emscope SC500, Elexience) before their topography was observed using Scanning Electron Microscopy (SEM; S-3500, Hitachi Instruments, Tokyo, Japan) at an accelerating voltage of 5.0 kV.

6.2.4 In vitro Cell Attachment and Proliferation

Mouse MC3T3-E1 cells (ATCC, Manassas, VA) were cultured using the procedure reported previously by our research group.[3,15] The polymer samples were immersed and cleaned in phosphate buffered saline (PBS) solution overnight, sterilized in 70% ethanol solution for 25 min twice, and completely dried in vacuum. Prior to cell studies, the samples were exposed to UV light for 20 min and rinsed with PBS solution thoroughly. After removal of PBS solution, MC3T3-E1 cells were seeded on the polymer samples at a density of ~15000 cells/cm^2 and cultured in α-Minimum Essential Media (α-MEM, Gibco) containing 10% fetal bovine serum (FBS, Gibco) and 1% penicillin/streptomycin (Gibco) in cell incubator with relative humidity of 95% and 5% CO_2 at 37 °C. Cell attachment at 4 h and proliferation over 4 days represented by the cell numbers were measured using a colormetric cell metabolic assay (CellTiter 96 Aqueous One Solution, Promega, Madison, WI).

6.2.5 Immunofluorescence Microscopy and Cell Morphology

After the cells were cultured for 4 h, 1, 2, and 4 days, they were fixed in 4% paraformadehyde (PFA) solution for ~30 min and rinsed with PBS twice. Then the cells

were permeabilized with 0.2% (v/v) Triton X-100, rinsed with PBS for three times, and stained with rhodamine-phalloidin (RP) for 1 h in an incubator. After cell nuclei were stained with 4',6-diamidino-2-phenylindole (DAPI) at room temperature, an Axiovert 25 light microscope (Carl Zeiss, Germany) was used to photograph the cytoplasm and nuclei. Focal adhesions (FAs) were evaluated using vinculin staining. Briefly, cells were first stained with mouse monoclonal anti-vinculin antibody (V9246, Sigma-Aldrich) for ~1 h in an incubator and then rinsed with PBS for ~10 times. The cells were further incubated with anti-mouse IgG-FITC antibody (F0257, Sigma) for 4 h and stained with RP. Photographing of F-actin in cytoskeleton and FAs was conducted on a confocal microscope (SP2, Leica). The cell area were measured from the RP-stained cell images at day 1 and quantifying FAs from the vinculin-stained cell images were conducted using ImageJ software (National Institutes of Health, Bethesda, MD) on ~20 images for each group. To observe cell morphology using SEM, the fixed cells were rinsed with PBS twice after cultured for 1 day. Further dehydration of cells was performed in gradient ethanol solutions (50%, 60%, 70%, 80%, 90%, 95%, and 100%) for 15 min at each concentration. Then a mixture (1:1, v/v) of ethanol and hexamethyldisilazane (Electron Microscopy Science, Hatfield, PA) and pure hemamethyldisilazane were used for completely dehydrating the cells. The samples were completely dried in air and sputter-coated with a gold-palladium layer prior to SEM observation at an accelerating voltage of 5 kV.

6.2.6 Characterization of Cell Alignment and Spreading

A cell was considered as aligned when the angle between the long axis of the cell and the groove direction beneath the cell body was smaller than 15°. To quantify cell alignment, three parameters were determined using ImageJ over 150 cells for each sample, i.e., cell area, percentage of cells trapped inside the grooves in the total cell population, and the percentage of aligned cells in the total cell population.

6.2.7 ALP Activity and Calcium Content

After MC3T3-E1 cells were cultured on the samples for 14 days, they were transferred into new plastic tubes and rinsed with PBS to remove unattached cells. Then the cells were trypsinized and the as-obtained cell suspension was centrifuged at 1000 rpm for 5 min. After removal of the supernatant, the cells was re-suspended in PBS and centrifuged again. The obtained cell pellet was suspended in 1 mL of 0.2% Nonidet P-40 solution and subsequently sonicated in ice-water bath for 2 min. The ALP activity and calcium content of the cells were measured using an ALP detection kit (Sigma, St. Louis, MO) and a QuantiChrom calcium assay kit (BioAssay Systems, Hayward, CA), respectively. The details about the measurements can be found in our previous report.

6.2.8 Gene Expression

MC3T3-E1 cells cultured on the samples for days 1 and 14 were transferred into new plastic tubes and the cellular RNA was isolated from the cells using an RNeasy Mini Kit (Qiagen, Valencia, CA) according to the manufacturer's instructions. The concentration of RNA was determined using a Nanodrop1000 spectrophotometer (Thermo Scientific, Wilmington, DE). cDNA was then synthesized using a cDNA

synthesis kit (Thermo Scientific) according to the manufacturer's instructions. Expression of integrin subunits including α_1, α_2, and β_1 and glyceraldehyde-3-phosphate dehydrogenase (GAPDH) at day 1 was quantified through real-time polymerase chain reaction (PCR) with a Power SYBR Green PCR Master Mix (Applied Biosystems, Carlsbad, CA) and determined on a thermal cycler with fluorescence detection systems (PTC-200, MJ Research). Expression of gene markers for osteogenesis, such as ALP, OCN, and OPN, in the cells cultured for 14 days was also measured according to the same recipe for integrin subunits. Table 1 shows the oligonucleotide primers used in real-time PCR reaction.

6.2.9 Statistical Analysis

Four samples for each group were used for the cell culture at each time point. All experimental results are presented as mean ± standard deviation. The significant difference ($p < 0.05$ or $p < 0.01$) between groups was analyzed using student's *t*-test.

6.3 Results and Discussion

The surface topography of samples was shown in the SEM images in Figure 6.1. F-grooves presented typical microgrooves with flat features. The groove widths for F-grooves fabricated from the silicon wafers with designed groove/ridge width of 5, 15, and 45 μm were measured to be 4.8 ± 0.3, 14.6 ± 0.5, and 44.2 ± 0.6 μm, respectively. In general, the surface of microgrooved substrates contacting the silicon wafer was used for cell culture and the feature dimension was close to that of the silicon wafers. In this study, the microgrooved substrates were the backside of the substrates that did not contact the

silicon wafers in replica molding. Therefore, the feature dimension of the F-grooves was not perfectly consistent with that of the silicon wafers. The H-groove samples showed microgrooves with similar dimensions. At a higher magnification of × 10000, the SEM images of the H-groove samples demonstrated that both the ridges and valleys were fully honeycomb-patterned. The pore diameters on the ridges of the H-grooves were measured to be 1.9 ± 0.2 μm while the values in the valleys were larger and measured to be 2.1 ± 0.2, 2.0 ± 0.3, and 2.3 ± 0.4 μm for H-5, H-15, and H-45 substrates, respectively. In the breath-figure method, the pore size can be influenced by the flow rate of moisture air, the solvent for the polymer solution, the volume of the polymer solution, and humidity.[16-19] As the CoPLLA17200/CH_2Cl_2 solution was cast on the silicon wafers, the solution on the ridges was dried first and the solution in the valley was dried later. In this situation, the valleys were considered to be covered with a larger volume of the polymer solution than the ridges and the larger volume of solution induced stronger coalescence of water droplets on the solution surface before it evaporated and resulted in larger pores. In H-films, the pore size was identical to that on the ridges of H-grooves.

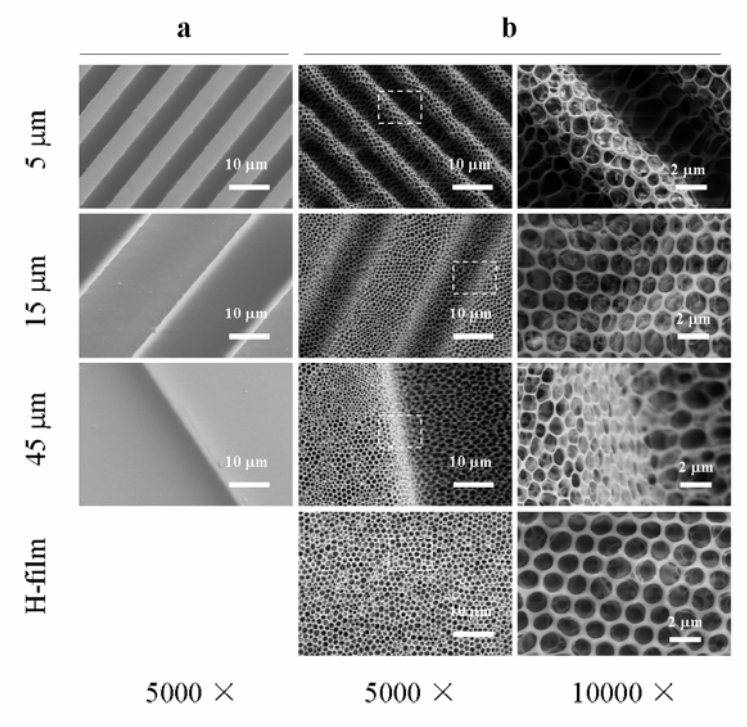

Figure 6.1 SEM images of (a) F-grooves. Magnification: × 5000. (b) H-grooves and H-films. Magnification: × 5000 (left column) and × 10000 (right column).

MC3T3-E1 MC3T3-E1 cell adhesion was evaluated using vinculin-staining images, characterization of FAs, and integrin expression, as shown in Figure 6.2. FAs are the closest contacts between cells and substrates. The cells on the H-grooves displayed FAs with a higher density than on the F-grooves with the same groove width. The FAs on F-5 and especially H-5 samples showed significantly aligned morphology along the groove direction and this phenomenon became less clear when the groove was wider. More punctuate FAs on the H-films were observed than on the F-grooves and H-grooves. A previous study on the MC3T3-E1 cell adhesion on honeycomb-patterned PCL films with pores of 3-10 μm showed that the FAs were distributed not only on cell periphery but also along the pore edge.[3] However, our present vinculin-staining images did not

show FAs along the pore edge. The FAs were analyzed using the average area of FAs, FA density defined as the average number of FAs per cell, and circularity of FAs defined as $4\pi \times \text{area/perimeter}^2$. The density of FAs on the H-grooves was significantly higher than that on the F-grooves with the same groove width and cells had a much higher density on the H-films than on the others. The average area of FAs on the H-grooves was slightly larger than that on the F-grooves with the same groove width. The significant difference between H-45 or F-45 and H-5 or F-5 was observed and the average area of FAs on H-films was measured to be significantly higher than that on the others. In a good agreement with vinculin-staining images, the FAs showed a much lower circularity on the H-grooves than on the F-grooves with the same groove width. Meanwhile, the circularity of FAs was smaller on the narrower grooves. The previous study demonstrated that the circularity of FAs was smaller on honeycomb-patterned PCL films, especially on films with smaller pores, than on flat PCL films.[3] Our present results showed that the FAs on F-5 had an even smaller circularity to indicate stronger alignment than that on the H-films.

Cells respond to surface topography through the "contact guidance" effect, in which the FAs play a critical role.[1,2,20-22] FAs have a rectangular shape with a length of 1-10 μm and preferentially attach on the groove ridges in an oriented manner when the groove dimension was smaller than FAs.[23,24] The aligned FAs further induced the alignment of actin filaments. For anchorage-dependent cells, such as MC3T3-E1 cells here, surface topography can influence the distribution of FAs on microgrooves to regulate cell functions through affecting the composition and conformation of ECM proteins.[25] Once ECM protein adsorption is distinct along the groove ridges, the

preferably formed FAs on these sites would orient actin filaments. Consequently, when the groove width was smaller and more comparable to the FA size, FAs were aligned more significantly, as shown in Figure 6.2. These aligned FAs further induced the orientation of cell bodies along the same direction. In contrast with the F-grooves, the H-grooves with the same groove width induced more prominent FA alignment, which triggered better aligned cells along the grooves. Previously MC3T3-E1 cells cultured on honeycomb-patterned PCL films were found distorted because the cells were preferably localized at the region of junction or discontinuity formed by the pore edges and the formation of FAs was also promoted compared with flat PCL films.[3] Accordingly, the formation of FAs in terms of FA density and FA area was enhanced on the H-films than on the F-grooves, whereas the FA alignment was more prominent on F-5 than on the H-films because narrower microgrooves with a width comparable to the size of FA fostered the FA alignment along the groove direction. The promoted FAs on the H-films further helped cell spreading. In case of the H-grooves with both microgrooves and honeycomb patterns, these two topographies synergistically aligned the FAs along the groove direction, which subsequently enhanced the alignment of cell bodies along the same direction.

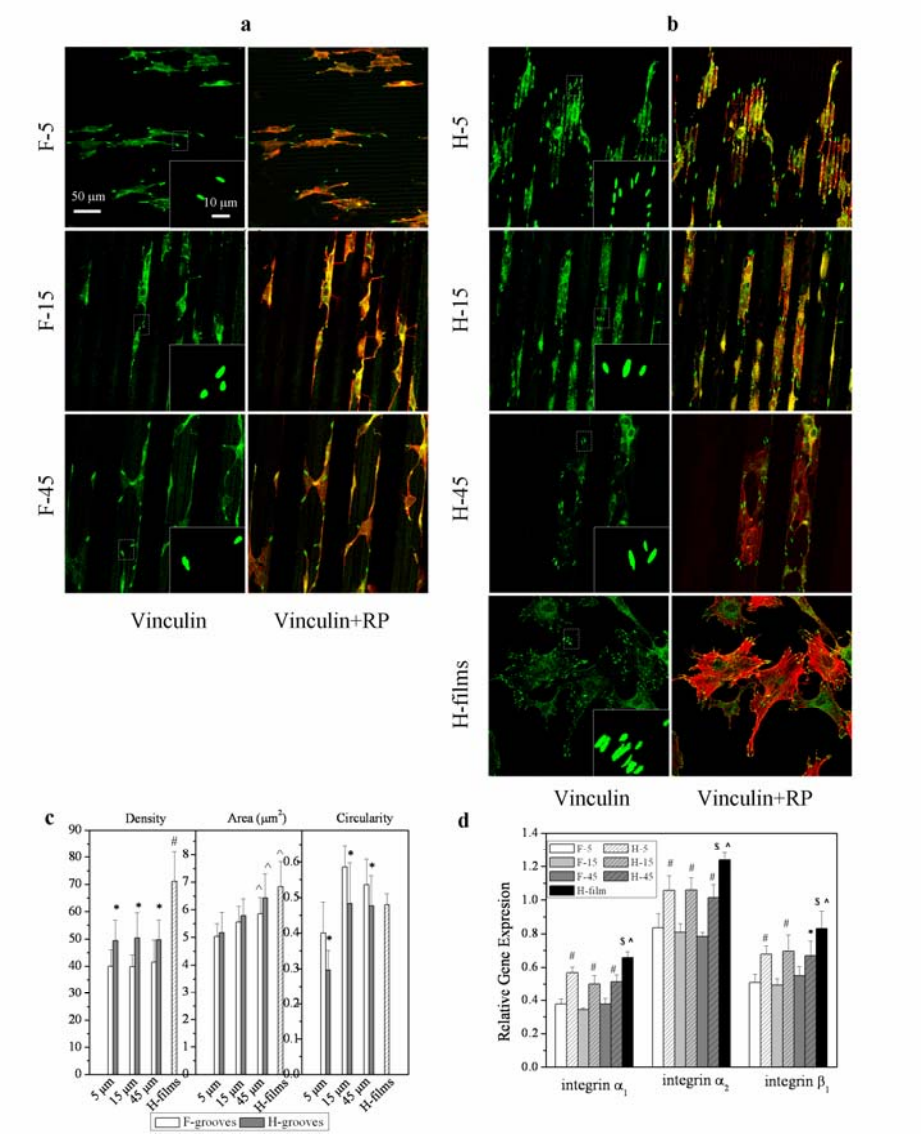

Figure 6.2 Fluorescent images of cells stained with RP (red) and vinculin (green) at day 1 on (a) F-grooves and (b) H-grooves and H-films. Insets indicate images at higher magnification. (c) Density, area, and circularity of FAs. *: $p < 0.05$ relative to F-grooves with the same width; #: $p < 0.01$ relative to others; ^: $p < 0.05$ relative to F-groove and H-groove with width of 5 μm. (d) Integrin expression of cells. #: $p < 0.01$ relative to F-grooves with the same width; ^: $p < 0.01$ relative to F-grooves; $: $p < 0.05$ relative to H-grooves

The transmembrane Integrins are transmembrane heterodimers of an α-subunit and a β-subunit to control the FA-ECM interactions, in which integrins bind the

cytoskeleton with adapter proteins (e.g., α-actinin, filamin, talin, and vinculin) and the ECM proteins with the external end.[26,27] The major ECM proteins that influence anchorage-dependent MC3T3-E1 cells are fibronectin, vitronectin, and type I collagen, which interact with the cells via integrin receptors via "outside-in-signaling" and "inside-out-signaling".[26,27] The expression levels of three representative integrin subunits, α_1, α_2, and β_1, are shown in Figure 2d. Consistent with the results on FAs, the expression levels of subunits, α_1, α_2, and β_1, were significantly higher on the H-grooves than on the F-grooves and they were even better on the H-films than on the H-grooves.

The cytoskeleton and nuclei of MC3T3-E1 cells cultured on the polymer samples for 1 day were also demonstrated in the fluorescent cell images in Figure 6.3. Like the results in Figure 6.2, narrower grooves induced more significant cell alignment and the alignment was more evident on the H-grooves. MC3T3-E1 cell spreading on the H-films was random without a preferential direction. The cell area was 1023 ± 122, 1281 ± 143, and 1437 ± 186 μm^2 on F-5, F-15, and F-45, respectively. The value increased from 962 ± 116 μm^2 on H-5 to 1354 ± 198, 1621 ± 231, and 2016 ± 265 μm^2 on H-15, H-45, and H-film, respectively. The percentage of aligned cells was 99 ± 2%, 88 ± 5%, and 58 ± 3% on F-5, F-15, and F-45, respectively. It decreased from 99 ± 3%, on H-5 to 92 ± 4% on H-15 and 63% ± 5% on H-45. The shape of cell nuclei was also influenced strongly by the surface topography. The alignment of nuclei was more evident on narrower grooves. Interestingly, the alignment of nuclei was enhanced on the H-grooves than on the F-grooves with the same groove width. The nuclei on the H-films displayed a round shape with better spreading in random direction compared with the nuclei on the F-grooves and

H-grooves. Our present findings agreed with previous conclusions that cell alignment increases with decreasing the groove dimension. The FAs on the H-grooves stimulated by the honeycomb pores were localized on the groove ridges and aligned in the groove direction, which further aligned cell filaments along the same direction. This shape alignment triggered the change of intermediate filaments which transferred the forces from cell filaments to the nucleus and also caused the nuclear alignment along the groove direction through mechanotransduction.[1,2,28,29] Alignment of both cytoplasm and nuclei was more prominent on the H-grooves than on the F-grooves with the same groove width. Because of the free spreading of cells on the H-films without being confined in grooves, the nuclei on the H-films had a larger area compared with those on the F-grooves and H-grooves. The circularity and area of the cell nuclei were characterized using ImageJ. The nuclear circularities were 0.56 ± 0.08, 0.69 ± 0.09, and 0.81 ± 0.12 on F-5, F-15, and F-45, and 0.43 ± 0.06, 0.54 ± 0.07, 0.75 ± 0.07, and 0.89 ± 0.14 on H-5, H-15, H-45, and H-film, respectively. The nuclear area increased from 183 ± 24 μm^2 on F-5 to 216 ± 28 μm^2 on F-15 and 228 ± 39 μm^2 on F-45, and increased from 175 ± 21 μm^2 on H-5 to 220 ± 32, 253 ± 46, and 279 ± 41μm^2 on H-15, H-45, and H-film, respectively.

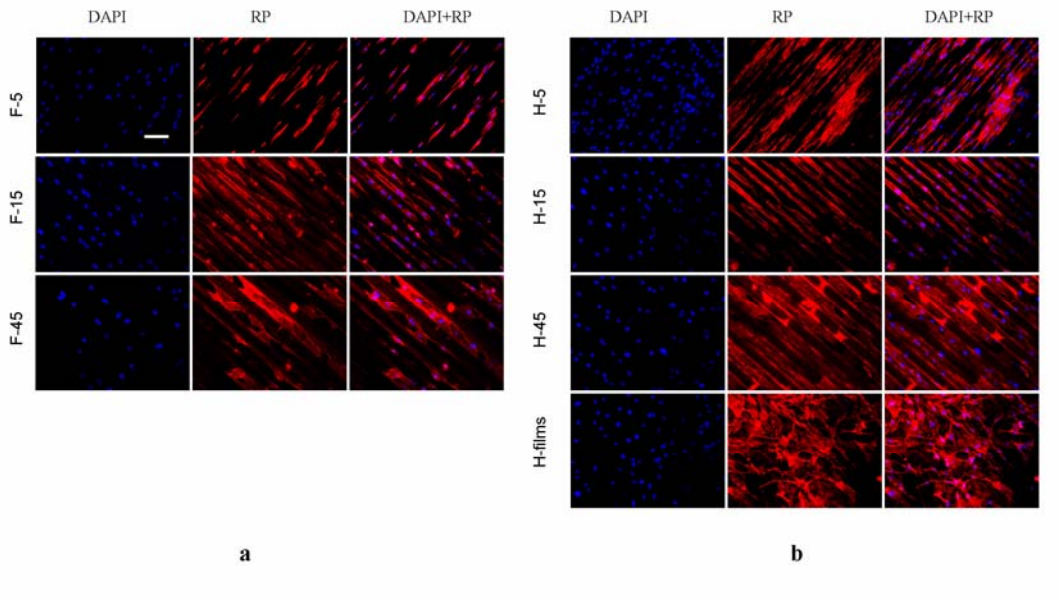

Figure 6.3 Fluorescent images of cells stained with RP (red) and DAPI (blue) at day 1 on (a) F-grooves. (b) H-grooves and H-films. Scale bar of 100 μm is applicable to all images.

The MC3T3-E1 cell morphology on all the samples at day 1 was also observed using SEM, as shown in the images in Figure 6.4. Consistently, cell filaments and nuclei on the F-grooves and H-grooves were aligned along the groove direction on the ridge or in the valley, and the alignment was more significant on the narrower grooves. Clearly, the cells on the H-grooves had better spreading and alignment compared with those on the F-grooves. Although some cells on F-films could spread and flatten well, most cells were still spreading with a high thickness and few filopodia. In contrast, cells on the H-grooves spread better with more and longer filopodia, some of them along the groove direction. Compared with cells on the F-grooves and H-grooves, they spread even much better on the H-film with much more filopodia projecting from cell bodies. Meanwhile, cell nuclei could also be observed in SEM images. The percentage of nuclei in the grooves analyzed from the SEM images was 85 ± 6%, 67 ± 7%, and 53 ± 9% on F-5, F-

15, and F-45, and 63 ± 10%, 35 ± 5%, and 32 ± 4% on H-5, H-15, and H-45, respectively. A previous study in our research group on MC3T3-E1 cell functions on photo-cured PCL triacrylate (PCLTA) substrates with concentric microgrooves demonstrated that the percentage of cells trapped in the grooves was more than 50% on microgrooves with groove width of 91.2 μm and increased up to 95% with decreasing the groove width to 7.5 μm, which was in agreement with literature.[11] Similarly, our present results showed that the percentage of cells in the grooves increased with decreasing the groove width. However, more cells were localized on the ridges rather than in the grooves, especially when the groove width increased on the H-grooves. Honeycomb pores could also enhance protein adsorption dramatically on the substrates. When H-15 and H-45 were exposed to MC3T3-E1 cells with α-MEM medium, those pores on the ridge first contacted ECM proteins such as fibronectin and absorbed them into the pores, which more possibly served as cell anchorage sites and induced better formation of FAs on the ridges. Therefore, honeycomb pores not only promoted cell alignment in the grooves but also influenced cell distribution on the surface.

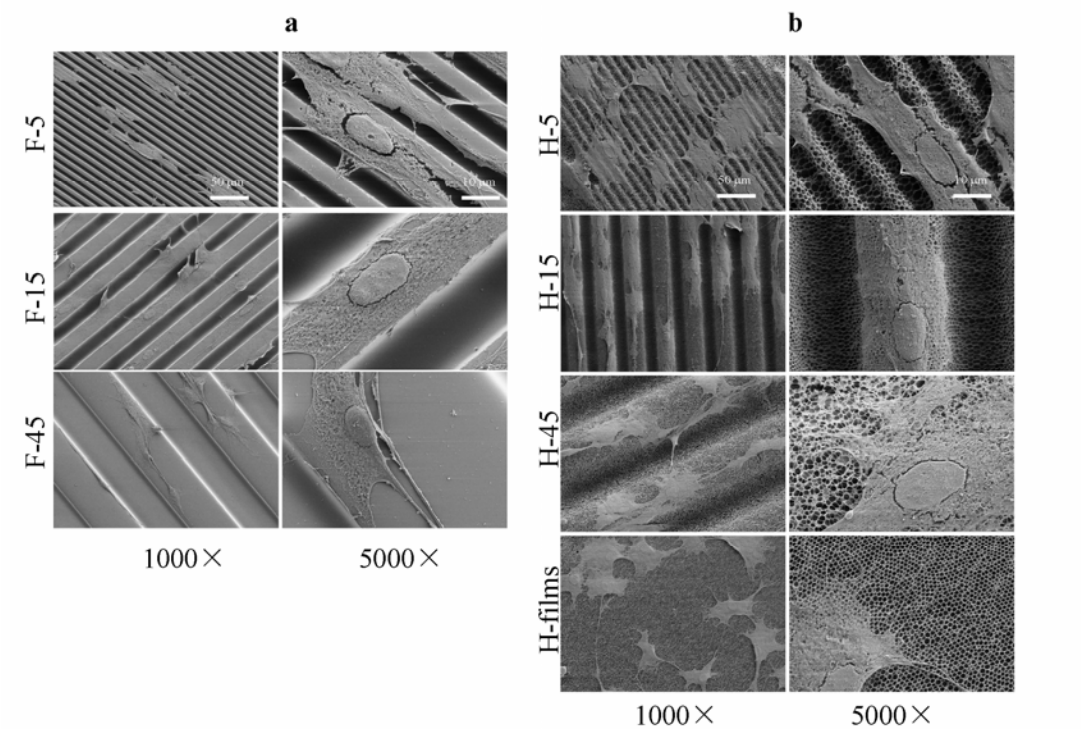

Figure 6.4 SEM images of cells at day 1 on (a) F-grooves and (b) H-grooves and H-films. Magnification: Magnification: × 1000 (left column) and × 5000 (right column).

MC3T3-E1 cell attachment at 4 h and proliferation over 4 days on the polymer samples are shown in Figure 6.5. For anchorage-dependent cells, cell proliferation and differentiation were strongly affected by the early stage cell adhesion. Cell attachment on the H-grooves was slightly better than on the F-grooves with the same groove width but without significant difference. The cell numbers on the F-grooves or H-grooves with different groove widths did not show difference. The cell number on the H-films was significantly higher than on the other samples. At days 1, 2, and 4, the cell numbers on the H-film were significantly higher than those on the H-grooves and the numbers were significantly lower on the F-grooves than on the H-grooves. A previous study in our research group also showed that the groove width could not influence MC3T3-E1 cell proliferation significantly on microgrooved substrates of photo-cured PCLTA with

groove widths of 7.5, 16.1, 44.2, and 91.2 μm and a groove depth of 10 μm.[11] MC3T3-E1 cell proliferation on silicone microgrooved substrates was not significantly different from that on the flat control.[30] However, in our present study the cell proliferation on the microgrooves was significantly inhibited compared with the H-film. As reported by us, MC3T3-E1 cell adhesion, proliferation, and differentiation were strongly promoted on honeycomb-patterned PCL films compared with flat PCL films.[3] As expected, the H-film here supported MC3T3-E1 cell proliferation better than the F-grooves. Intriguingly, the H-films supported cell proliferation better than the H-grooves. As demonstrated in the SEM images, the pore size was similar (~2 μm) in the H-grooves and H-films and the only difference was the microgrooves. A possible explanation is that the honeycomb pores strongly promoted MC3T3-E1 cell proliferation to reach cell confluence, which might suppress proliferation especially when the cells were localized on the ridges of the H-grooves. In contrast, MC3T3-E1 cells on the H-films that were not confined in the grooves during their proliferation could spread over the entire surface.

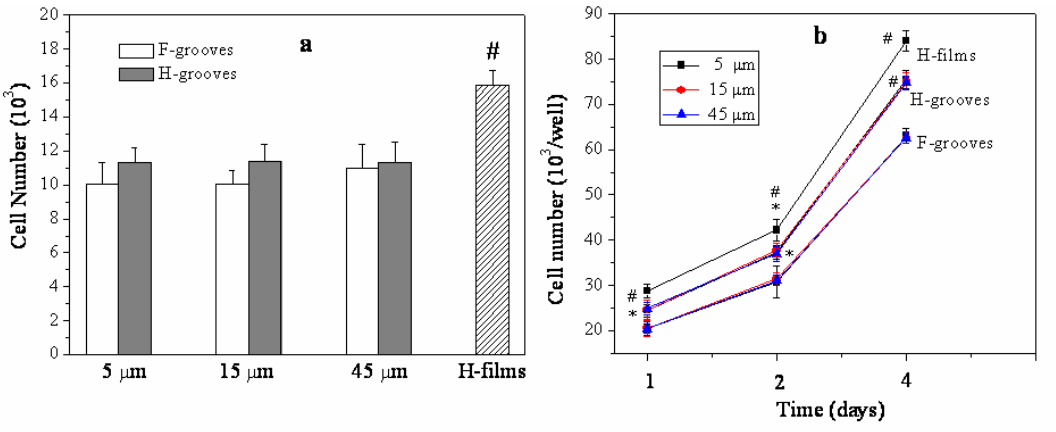

Figure 6.5 (a) Cell attachment at 4 h and (b) Cell proliferation at day 1, 2, and 4 represented by the cell numbers. *: $p < 0.05$ relative to F-grooves; #: $p < 0.01$ relative to F-grooves.

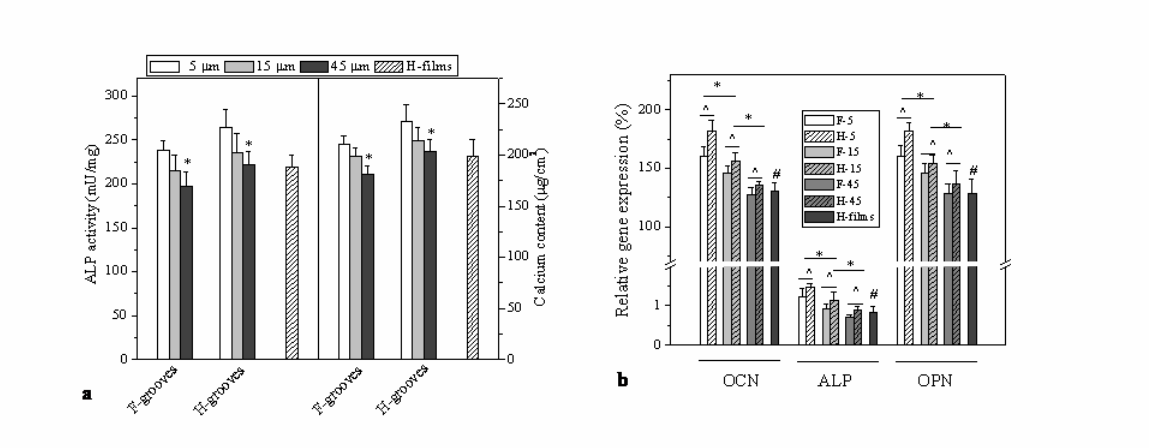

Figure 6.6 (a) ALP activity and calcium content of cells cultured on F-grooves, H-grooves, and H-films for 14 days. *: $p < 0.05$ relative to 5 μm grooves. (b) Gene expression levels of OCN, ALP, and OPN relative to GAPDH in MC3T3-E1 cells cultured for 14 days on F-grooves, H-grooves, and H-films. * and ^: $p < 0.05$; #: $p < 0.01$ relative to others.

The honeycomb-patterned microgrooves not only promoted MC3T3-E1 cell alignment but also supported better mineralization after the cells were cultured for 14

days. As shown in Figure 6.6a, the ALP activity and calcium content of MC3T3-E1 cells was both higher on the H-grooves than on the F-grooves, especially when the grooves were narrower. The two parameters on the H-films were similar to those on H-45 but significantly lower than the values on F-5 and H-5.

To understand MC3T3-E1 cell mineralization at the gene level, the mRNA expression of bone-specific differentiation markers, such as OCN, ALP, and OPN, was assessed using real-time PCR, as shown in Figure 6.6b. Following a similar trend as observed in ALP activity and calcium content, these three gene markers all had much higher expression levels on the H-grooves than on the F-grooves, and narrower grooves could promote them even further. In general, these gene markers were expressed better on microgrooved substrates with groove widths of 5 and 15 μm than on the H-film. This finding agreed with the results on microgrooved substrates of photo-cured PCLTA .[11]

The results can be interpreted using several factors. First, the H-grooves induced better cell adhesion than the F-grooves and this early-stage advancement could promote later cell proliferation and differentiation. However, the best cell adhesion on the H-film did not result in the highest differentiation results. Thus alignment of MC3T3-E1 cell body and nuclei was critical in fostering their differentiation because they trigger the release of calcium ions from the perinuclear space via the mechanotransduction pathway and the released calcium ions are known to upregulate MC3T3-E1 cell mineralization and mRNA expression of bone-specific gene markers.[15,31-33] The microgrooves also provided a microenvironment to condense some regulatory factors that are important in osteogenesis to reach the critical concentrations for promoting the formation of calcified tissue.

6.4 Conclusions

Honeycomb-patterned copolymer microgrooves with various groove widths of ~5, ~15, and ~45 μm and depth of ~8 μm and honeycomb-patterned films were fabricated from microfabricated silicon wafers using the breath-figure method. Mouse pre-osteoblastic MC3T3-E1 cells cultured on these samples demonstrated that honeycomb-patterned microgrooves promoted the alignment of cell filaments and nuclei, ALP activity and calcium content of the cells, and expression of ALP, OCN, and OPN compared with the solid microgrooved substrate without pores. Furthermore, the smaller groove width induced better results. However, the cell proliferation on honeycomb-patterned microgrooves was inhibited compared with honeycomb-patterned films without microgrooves.

References

[1] Anselme, K.; Bigerelle, M. *Int. Mater.Rev.* **2011**, 56, 243.

[2] Dalby, M. J. *Med. Eng. Phys.* **2005**, 27, 730.

[3] Wu, X.; Wang, S. *ACS Appl. Mater. Interfaces* **2012**, 4, 4966.

[4] Yamamoto, S.; Tanaka, M.; Sunami, H.; Arai, K.; Takayama, A.; Yamashita, S.; Morita, Y.; Shimomura, M. *Surf.Sci.***2006**, 600, 3785.

[5] Mcmillan, J. R.; Akiyama, M.; Tanaka, M.; Yamamoto, S.; Goto, M.; Abe, R.; Sawamura, D.; Shimomura, M.; Shimizu, H. *Tissue Eng.* **2007**, 13, 789.

[6] Wang, B.; Mao, Z.; Meng, X.; Tong, W.; Gao, C. *Colloids Surf., B* **2010**, 76, 38.

[7] Tsuruma, A.; Tanaka, M.; Yamamoto, S.; Shimomura, M. *Colloids Surf., A* **2008**, 313-314, 536.

[8] Fukuhira, Y.; Kaneko, H.; Yamaga, M.; Tanaka, M.; Yamamoto, S.; Shimomura, M. *Colloids Surf., A* **2008**, 313-314, 520.

[9] Wang, J. H.-C.; Grood, E. S.; Florer, J.; Wenstrup, R. *J. Biom.* **2000**, 33, 729.

[10] Kenar, H.; Kose, G. T.; Hasirci, V. *Biomaterials* **2006**, 27, 885.

[11] Wang, K.; Cai, L.; Zhang, L.; Dong, J.; Wang, S. *Adv. Healthcare Mater.* **2012**, 1, 292.

[12] Connal, L. A.; Vestberg, R.; Gurr, P. A.; Hawker, C. J.; Qiao, G. G. *Langmuir* **2008**, 24, 556.

[13] Connal, L. A. *Aust. J. Chem.* **2007**, 60, 794.

[14] Connal, L. A.; Qiao, G. G. *Soft Mater* **2007**, 3, 837.

[15] Wu, X.; Wang, S. *Adv. Healthcare Mater.* **2013**, 2, 326.

[16] Bunz, U. H. F. *Adv. Mater.* **2006**, 18, 973.

[17] Stenzel, M. H.; Barner-Kowollik, C.; Davis, T. P. *J. Polymer Sci. Polymer Chem.* **2006**, 44, 2363.

[18] Saunders, A. E.; Dickson, J. L.; Shah, P. S.; Lee, M. Y.; Lim, K. T.; Johnston, K. P.; Korgel, B. A. *Phys. Rev. E* **2006**, 73, 031608.

[19] Madej, W.; Budkowski, A.; Raczkowska, J.; Rysz, J. *Langmuir* **2008**, 24, 3517.

[20] Bettinger, C. J.; Langer, R.; Borenstein, J. T. *Angew. Chem. Int. Ed.* **2009**, 48, 5406.

[21] Flemming, R. G.; Murphy, C. J.; Abrams, G. A.; Goodman, S. L.; Nealey, P. F. *Biomaterials* **1999**, 20, 573.

[22] Tanaka, M. *Biochim.Biophys. Acta* **2011**, 1810, 251.

[23] Biggs, M. J. P.; Dalby, M. J. *Proc. Int. Mech. Eng. H.* **2010**, 224, 1441.

[24] Geiger, B.; Spatz, J. P.; Bershadsky, A. D. *Nat. Rev.* **2009**, 10, 21.

[25] Curtis, A.; Wilkinson, C. *Biomaterials* **1997**, 18, 1573.

[26] Siebers, M. C.; ter Brugge, P. J.; Walboomers, X. F.; Jansen, J. A. *Biomaterials* **2005**, 26, 137.

[27] Anselme, K. *Biomaterials* **2000**, 21, 667.

[28] Maniotis, A. J.; Chen, C. S.; Ingber, D. E. *Proc. Natl. Acad. Sci. USA* **1997**, 94, 849.

[29] Dalby, M. J.; Riehle, M. O.; Yarwood, S. J.; Wilkinson, C. D. W.; Curtis, A. S. G. *Exp. Cell Res.* **2003**, 284, 274.

[31] Thomas, C. H.; Collier, J. H.; Sfeir, C. S.; Healy, K. E. *PNAS* **2002**, 99, 1972.

[32] Relan, N. K.; Yang, Y.; Beqaj, S.; Miner, J. H.; Schuger, L. *J. Cell Biol.* **1999**, 147, 1341.

[33] Itano, N.; Okamoto, S.; Zhang, D.; Lipton, S. A.; Ruoslahti, E. *PNAS* **2003**, 100, 5181.

CHAPTER VII
EDGE-ON OR FLAT-ON, IT MAKES A DIFFERENCE IN CELL RESPONSES TO POLYMER LAMELLAE

7.1 Introduction

Polymer chains can form ordered and regular structure through crystallization and random chain coils transform into perfectly ordered orientation during polymer crystallization. The hierarchy of crystals determines the properties of these polymers. It has been widely accepted that lamellae, the basic unit of polymer spherulites and crystalline domains, are composed of folded polymer chains governed by kinetics. Lamellae have two basal surfaces constituted by chain folds and several lateral surfaces. Normally, anisotropic lamellae are randomly distributed in the bulk. Crystallizing from melts, polymers normally form spherulites from micro- to milli-scale. In case of lamellar twisting along the radial direction in spherulites, banding texture can be observed. Experimentally, there are two major orientation types of lamellae [1-3]. When the lamellae are perpendicular or parallel to the substrate, they are called edge-on or plat-on lamellae, respectively. When the dimension is confined at the nanoscale which is comparable to lamellae thickness, flat-on lamellae are preferred. As the polymer thickness increases, the edge-on type is more dominant. Poly(ε-caprolactone) (PCL) was found to form flat-on lamellae preferentially when the film was thiner than 200 nm, while it was more likely to form edge-on lamellae in thicker films [4]. In banded spherulites crystallized from a blend of poly(ε-caprolactone) and poly(vinyl chloride), the ridges and valleys were mainly composed of edge-on and flat-on lamellae,

respectively [5,6]. PCL films with thickness of 110 nm showed edge-on lamellae directly after spin-coating, whereas flat-on lamellae were observed after they were melted at 75 °C and recrystallized at 45 °C [7]. Because the surface energy of the folded surface is much larger than that of the lateral surface in lamellae, flat-on lamellae are predicted to haves three times higher surface energy than edge-on lamellae.

Cell-substratum interactions are important to fundamental understanding of biological issues and design of biomedical devices. When cells are exposed to biomaterials, they first respond to the surface of materials via inter or intracellular signals and then produce interface with substratum to provide extracellular signals. These initial processes determine subsequent cell adhesion, proliferation, and differentiation. Surface chemistry, topography, and stiffness are three major categories of factors to directly affect cell-substratum interactions [8].

PCL and poly(L-lactide acid) (PLLA) as two important semi-crystalline biodegradable polyesters have been widely studied. Using these two polymers, the effects of surface spherulitic topography on cell attachment and proliferation have been reported [9-12]. However, the effect of lamellae orientation on cell functions is still unknown. In this study, we prepared PCL films composed of either edge-on or flat-on lamellae for regulating surface energy, fibronectin and serum protein adsorption, and MC3T3-E1 cell adhesion, proliferation, mineralization, and gene expression.

7.2 Experimental Section

7.2.1 Materials

PCL with M_w of 142,658 g mol^{-1} and M_n of 77,352 g mol^{-1}) was synthesized through ring opening polymerization of ε-caprolactone (Aldrich, St. Louis, MO), initiated by pure water.

7.2.2 Preparation of Samples

The flat-on and edge-on samples were prepared according to the method reported previously [7]. Briefly, PCL was dissolved in dichloromethane at 0.01 g mL^{-1} and spin-coated on clean microscope slides (Fisher Scientific, Pittsburgh, PA) at a spinning rate of 4000 rpm for 30 s. The thickness was determined by AFM scanning to be ~100 nm. To prepare PCL films with thickness of ~1 μm as comparison, the PCL was dissolved in dichloromethane at 0.04 g mL^{-1} and spin-coated on clean glass slide at 1000 rpm for 30 s. All samples were melted at 85 °C completely for 5 min. Then the melted samples were quickly transferred to a hot stage for crystallization at 45 °C for 100 h. Hot-compressed samples were also prepared as control group by compressing melted PCL between two clean microscope slides. Then the hot-compressed samples were crystallized at room temperature.

7.2.3 AFM Scanning

AFM scanning of the samples was performed on a Nanoscope V control system (Veeco Instruments, Santa Barbara, CA) with the tapping mode. The root mean square roughness (R_{rms}) and depth profile were determined from height images.

7.2.4 Determination of Surface Free Energy

Three fluids including pure water, diiodomethane, and ethylene glycol were used to determine the surface free energy according to the reported method [13-15]. Contact angles were measured with a Ramé-Hart NRC C. A. goniometer (model 100-00-230) at room temperature. The contact angles were not recorded until the fluid droplet was stable for more than 30 s. The van Oss-Chaudhury-Good (vOCG) equation (eq. 1) was used to determine the apolar γs^{LW}, acidic γs^{+}, and basic γs^{-} components of polymers.

$$(1+\cos\theta)\gamma_L = 2(\sqrt{\gamma s^{LW}\gamma L^{LW}} + \sqrt{\gamma s^{+}\gamma L^{-}} + \sqrt{\gamma s^{-}\gamma L^{+}}) \quad (1)$$

where γ_L is the liquid surface tension. γL^{LW} is the total apolar component of the liquid. γL^{-} and γL^{+} are the electron donor and electron acceptor contributions to the polar component of the liquid. The acido-basic component γs^{AB} is given in eq.2 [16],

$$\gamma s^{AB} = 2(\gamma s^{-}\gamma s^{+})^{1/2} \quad (2)$$

The total SFE of polymers γ^{tot} is the sum of acido-basic γs^{AB} and apolar γs^{LW} components of polymers.

7.2.5 Protein Adsorption

Protein adsorption in both serum media used for MC3T3 cells and fibronectin/PBS solution (10 μg mL^{-1}) were evaluated. Samples with precise area were immersed in serum media or fibronectin solution for 4 h at 37 °C. The samples were rinsed with PBS five times to remove unattached proteins and subsequently immersed in 300 μL of 1% sodium dodecyl sulfate (SDS) solution four times with 30 min interval to collect proteins adsorbed on samples. The concentrations of proteins in the collected SDS

solutions were determined using A micro-plate reader (SpectraMax Plus 384, Molecular Devices, Sunnyvale, CA) and a MicroBCA protein assay kit (Pierce, Rockford, IL).

7.2.6 In vitro Cell Attachment and Proliferation

Mouse MC3T3-E1 cells (ATCC, Manassas, VA) were cultured as reported [9,17]. All samples were sterilized in 70% alcohol solution for 30 min. Prior to cell culture, all sterilized samples were dried completely in vacuum at room temperature. MC3T3-E1 cells were seeded on samples at a density of ~16000 cells per cm^2 in a 24-well plate with α-Minimum Essential Medium (α-MEM, Gibco) which contains 1% penicillin/streptomycin (Gibco) and 10% fetal bovine serum (FBS, Gibco). Wells without samples but seeded with cells at the same density served as positive control. Then the cells were cultured at 37 °C with 95% humidity and 5% CO_2 for designated time. At each time point, the cell number was quantified using a colorimetric cell metabolic assay (CellTiter 96 Aqueous One Solution, Promega, Madison, WI).

7.2.7 Immunofluorescence Microscopy and SEM

After cultured for one day, attached MC3T3-E1 cells on the samples were fixed with 4% paraformaldehyde solution for 30 min at room temperature and rinsed with phosphate buffered saline (PBS) twice. The cells were further permeabilized with 0.2% (v/v) Triton X-100 and rinsed with PBS twice. Then the cells were stained using rhodamine-phalloidin (RP) for 1.5 h at 37 °C and 4',6-diamidino-2-phenylindole (DAPI) at room temperature. The observation of cytoplasm and nuclei was performed using an Axiovert 25 light microscope (Carl Zeiss, Germany). Cell area was also measured by using ImageJ software (National Institutes of Health, Bethesda, MD) from RP-stained

cell images. To observe FAs, cells were first stained with mouse monoclonal anti-vinculin antibody (V9264, Sigma-Aldrich) for 1.5 h at 37 °C and then rinsed with PBS for 10 times. FAs were further labeled by anti-mouse IgG-FITC antibody (F0257, Sigma) at 37 °C for 5 h and photographed by using a confocal microscope (SP2, Leica). To observe cell morphology using SEM, each sample after fixation with 4% paraformaldehyde (w/v) for 30 min and rinse with PBS for three times was dehydrated with gradient ethanol solution (25%, 50%, 70%, 95%, and 100%). The samples were dehydrated twice at each concentration of ethanol solution for 10 min before higher concentration. Then the final dehydration was conducted in hexamethyldisilazane (Electron Microscopy Sciences, Hatfield, PA), followed by drying in air overnight. After dry, all samples were sputter-coated with one gold-palladium layer before observed with SEM (S-3500, Hitachi Instruments Inc., Tokyo, Japan) at an accelerating voltage of 10 keV.

7.2.8 ALP Activity and Calcification Assay

The measurement of ALP activity and calcium content were conducted as reported previously [17]. After cultured for 14 days, cells were rinsed with PBS, trypsinized, and washed again, followed by centrifugation for 4 min at 1000 rpm. The cell pellet was re-suspended in 1 mL 0.2% Nonidet P-40 solution and further sonicated in ice water for 2 min. The ALP activity and calcium content of the cell lysate were determined by fluorescence-based ALP detection kit (Sigma, St. Louis, MO) and QuantiChrom calcium assay kit (BioAssay Systems, Hayward, CA), respectively.

7.2.9 Gene Expression

After cells were cultured for 14 days, a RNeasy Mini Kit (Qiagen, Valencia, CA) was employed to isolate RNA from the cell pellet and then cDNA was synthesized using a cDNA synthesis kit (Thermo Scientific). Expression of OCN, COL I, ALP, OPN, and glyceraldehyde-3-phosphate dehydrogenase (GAPDH) was quantified through real time PCR and performed on a thermal cycler with fluorescence detection systems (PTC-200, MJ Research) using a Power SYBR® Green PCR Master Mix (Applied Biosystems, Carlsbad, CA).

7.3 Results and Discussion

We prepared PCL films with thickness of ~100 nm of edge-on or flat-on lamellae as well as hot-compressed ones. Edge-on films with thickness of 100 nm were obtained directly from spin-coating without further recrystallization. When polymer coating is very thin on the substrate, cells can sense the stiffness of the substrate. Thus, thicker edge-on samples (~1 μm) were also prepared to compare with the 100-nm-thick ones in affecting the cell behavior; however, no difference was found between them. For simplicity, the discussion on edge-on films with thickness of ~1 μm is omitted here. The surface topography of hot-compressed, edge-on and flat-on samples was examined using Atomic Force Microscopy (AFM), as shown in Figure 7.1A. The hot-compressed samples showed random feature with very fine details. The edge-on samples displayed clear edge-on lamellae with fibrous morphology. The bright fine lines with branches were the crystalline layers separated by amorphous layers. The fold length of the PCL chains was measured from the width of crystalline layers to be 9.7 ± 0.5 nm, consistent with the

reported value [7]. After this 100 nm-thick film were melted at 85 °C and recrystallized at 45 °C for 100 h, flat-on lamellae were clearly observed. The fold length was also indicated by the height of these domains, which was 9.9 ± 0.7 nm. From AFM height images, we could obtain the height profiles for specific regions, as shown in Figure 7.1B. Hot-compressed samples had very smooth surface and flat-on surface was also quite smooth in one individual crystalline terrace. However, the height profile of edge-on surface presented regular pattern corresponding to the fibrous fine lines. Obtained from height images, the surface root-mean-square roughness (R_{rms}) values of hot-compressed, edge-on, and flat-on samples were 4.9 ± 0.4, 10.5 ± 0.7, and 8.4 ± 0.5 nm, respectively.

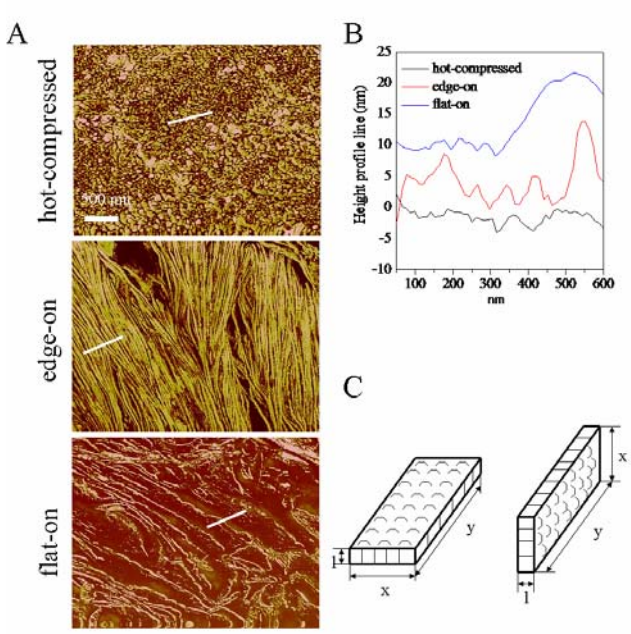

Figure 7.1 AFM phase images (A) and height profiles (B) of the hot-compressed, edge-on, and flat-on samples and (C) Schemetic flat-on and edge-on lamellae.

The surface free energy and its apolar, and polar components for each group were calculated from contact angles of water, diiodomethane, and ethylene glycol on the

samples, as shown in Table 7.1. The surface free energies of hot-compressed and edge-on samples were similar to each other and the values were consistent with a previous report [5]. The surface free energy of flat-on samples had much higher value than both hot-compressed and edge-on samples. To date, the surface free energy of flat-on PCL has not been reported despite the prediction of 3-6 times as high as that of edge-on PCL [5]. Our experimental surface free energy of the flat-on samples was much lower than the predicted values although it was significantly higher than that of edge-on samples. Meanwhile, our results showed that the basic component for the flat-on samples was lower while the acidic component for the flat-on samples was much higher compared with hot-compressed and edge-on samples, indicating that flat-on surface was more positively charged. Table 1 also shows the protein adsorption of the samples immersed in culture media and fibronectin solutions. Protein adsorption is determined by surface properties such as ionic bonding, van der Waals interaction, electrostatic force, and hydrophilicity of the materials [18]. In both culture media and fibronectin solutions, edge-on samples could adsorb more proteins than hot-compressed samples, although without significant difference. This can be explained by the rougher surface in the edge-on samples [9]. The flat-on samples with slightly lower roughness showed remarkably higher protein adsorption than the edge-on ones in both cases. Note that fibronection with a molecular weight of 220-250 kg mol^{-1} has an acidic isoelectric point of 5.5-6.0 and prefers hydrophobic surface to hydrophilic one. However, the flat-on samples had a higher surface free energy and were more hydrophilic than edge-on samples. Therefore, both roughness and hydrophilicity cannot be used to interpret the results on protein adsorption. The flat-on samples were more positively charged, indicated by the lower

basic component and higher acidic component compared with the edge-on and hot-compressed samples. Most serum proteins and fibronectin have low acidic isoelectric points of less than 6 when the pH value was 7.4, showing that these proteins bear negative charges. Consequently, the flat-on sample could absorb more proteins than others because of the electrostatic interaction between proteins and the PCL samples.

Table 7.1 Surface free energies and concentrations of adsorbed proteins of different PCL samples.

samples	γ_s^{LW}	γ_s^+	γ_s^-	γ_s^{AB}	γ^{tot}	Protein adsorption ($\mu g\ cm^{-2}$)	
			($mJ\ m^{-2}$)			Serum	FN
Hot-compressed	39.2	0.3	6.8	2.8	42.1±1.5	6.9±1.4	3.3±0.7
edge-on	39.6	0.4	6.3	3.2	42.8±2.0	7.7±0.8	4.2±1.0
flat-on	48.0	1.3	4.7	4.6	52.6±1.9	10.8±1.3	6.2±0.9

MC3T3-E1 cell adhesion of at day 1 post-seeding was evaluated via vinculin staining and gene expression of integrin subunitsα_1, α_2, and β_1. As demonstrated in Figure 7.2A, focal adhesions (FAs) on the flat-on samples had much larger size and density than those on the edge-on and hot-compressed ones, on which most of FAs had round shape. In contrast, FAs on the flat-on samples were dramatically aligned. The quantification of FAs in Figure 7.2B was consistent with the above observation. FAs on flat-on samples had significantly higher density (defined as the number of FAs per cell), area, and elongation (defined as the reciprocal of circularity, $4\pi\times$ area/perimeter^2,) than those on the hot-compressed samples. FAs are located in the cytoskeletal components, such as vinculin, paxilin, and actin microfilaments, and provide sites for activating intracellular signaling molecules, such as focal adhesion kinase (FAK) and extracellular signal-regulated kinase (ERK½) [19,20]. For anchorage-dependent MC3T3-E1 cells,

adsorption of adhesion-related ECM proteins from the culture media plays an important role in mediating cell adhesion and spreading. ECM proteins related to attachment of osteoblasts mainly include fibronectin, vitronectin, and collagen type I [21,22]. The better adsorption of ECM proteins on the flat-on samples might enhance cell adhesion. The formation of FAs is regulated by transmembrane integrins composed of α and β subunits. Integrins can pass information in the communications between ECM proteins and cell nucleus [22]. These signaling pathways determine cell adhesion, proliferation, and differentiation. Integrin subunit β_1 is believed to be responsible for attachment of osteoblasts to fibronectin and collagen type I, whereas integrin subunits α_1 and α_2 are important for their attachment to collagens [21,22]. Figure 7.2C shows that cells on the flat-on samples had significantly better expression of integrin subunits α_1, α_2, and β_1 than those on the edge-on samples, whereas cells on the hot-compressed samples had the lowest integrin expression. These results suggested that ECM proteins, namely, fibronectin, should play a critical role in the signaling pathway.

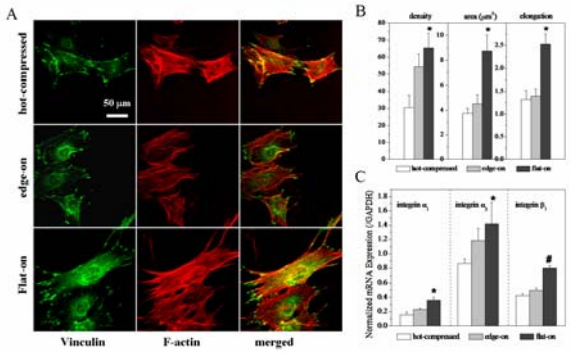

Figure 7.2 MC3T3-E1 cell adhesion on the hot-compressed, edge-on, and flat-on samples. (A) Vinculin-stained images (left column), fluorescent images stained with rhodamine-phalloidin (red, middle column), and merged images of the cells at day 1 post-seeding. Scale bar of 50 μm is applicable to all. (B) Density, area, and elongation of FAs. (C) Relative expression of integrin subunits of α_1, α_2, and β_1 at day 1. *: $p < 0.05$; #: $p < 0.01$ relative to the hot-compressed samples.

Cell morphology was demonstrated by fluorescent and SEM images in Figure 7.3. Cells on the flat-on samples had notably better spreading and a higher density than those on the flat-on and hot-compressed samples (Figure 7.3A). There was no significant difference in cell spreading and density between the flat-on and hot-compressed samples. SEM images in Figure 7.3B show the same trend. At magnification of 10000×, it was evident that cells on the flat-on samples were much thinner and more filopodia extended from cytoplasm than those on the hot-compressed and edge-on samples, indicating better cell adhesion. Cell area determined from cytoplasm-stained images at day 1 showed that cells on the flat-on samples were much larger than other groups (Figure 7.3D). Cell attachment at 4 h and proliferation over 4 days were quantified by using the cell numbers (Figure 7.3C). Cells on the flat-on samples attached and proliferated better than other groups. In this study, surface topography, roughness, and surface free energy were all

involved in regulating cell behavior. The roughnesses of all samples were in a small range of 4.9-10.5 nm. Rougher surfaces can enhance cell adhesion and subsequent processes [8,9,23]. It may be the reason why the edge-on samples could better support MC3T3-E1 cell adhesion and proliferation than the hot-compressed ones. However, it cannot explain why the less rough flat-on samples had much better cell adhesion and spreading than the edge-on ones. The difference in cell adhesion and proliferation between the flat-on and edge-on samples can be ascribed to the topography or surface energy rather than roughness. Typical surface topography in micro- or nano-scale which cells respond to include gratings and arrays of posts or pits [24,25]. The edge-on samples could be considered as nanogratings or nanogrooves with the ridge width of ~10 nm and depth of ~10 nm, whereas the flat-on ones could be considered as smooth surfaces with irregular boundaries. Nanogrooves generally enhance cell adhesion via rearranging the distribution of FAs, expedite migration along the groove direction, and lower the proliferation rate.[19] Cell alignment is cell-type dependent when cells are cultured on grooves with certain dimension [24]. This morphological response can be observed on grooves with widths and depths as small as 100 and 35 nm, respectively [24,25,26]. In general, the increased depth strengthens the alignment effect sharply. In this study, the groove-like edge-on lamellae have very small dimensions in terms of both groove width and depth. Consequently, no morphological response was observed on the edge-on samples. If only topography played the role, cells on the edge-on samples should have better adhesion than those on the flat-on and hot-compressed ones. However, it was just opposite to the findings here and groove-like edge-on lamellae had no prominent effect on cell behavior. After ruling out the effects of topography and roughness on cell adhesion and

proliferation on edge-on and flat-on samples, we speculate that the reason is surface energy, whose role in regulating osteoblast cell adhesion is still in debate [27]. Kennedy *et al.* prepared the surface energy gradient by ozonolysis to convert the CH_3 group into OH and COOH layers and further coated the surface gradient with fibronectin layer.[22] Because the surface with lower surface energy had higher protein adsorption, conformational changes in the proteins, and irreversible protein adsorption, the gradient fibronectin layer was formed before cell study [27]. Osteoblasts showed the best spreading when the water contact angle was ~60° and lower surface energy supported better cell adhesion and proliferation. Lim *et al.* prepared samples with different surface energies using plasma-discharge-treatment of quartz for studying human fetal obsteoblastic (hFOB) cell behavior [28]. They found that hydrophilic surfaces resulted in homogeneous spatial growth and mineral deposition, which were enhanced from hydrophobic surfaces [28]. Pande *et al.* found that titanium-zirconium alloy with a higher surface energy (37.74 mJ m^{-2}) had better osteoblast viability, adhesion, and proliferation than samples with lower surface energies [29]. Our results are consistent with these conclusions [28,29]. However, these studies were on the surfaces treated chemically and cannot rule out the effects of functional groups. The PCL samples in this study were prepared through crystallization without chemical treatment and thus had identical chemistry and surface free energy was solely determined by surface topography and organization of lamellae.

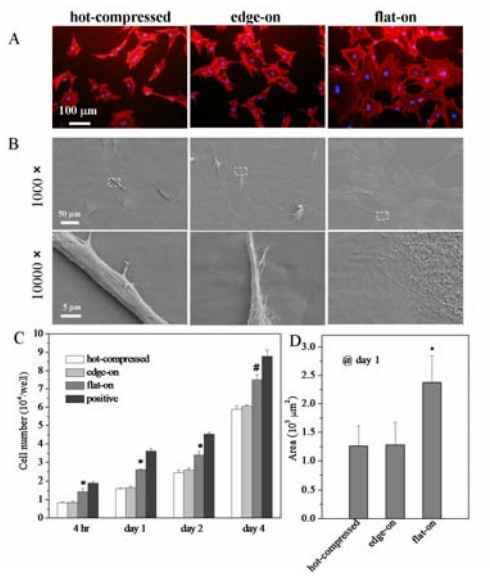

Figure 7.3 MC3T3-E1 cell phenotype, attachment, proliferation, and spreading on the hot-compressed, edge-on, and flat-on samples. (A) Fluorescent cell images with cytoplasm stained with rhodamine-phalloidin (red) and nuclei stained with DAPI (blue) at day 1 post-seeding. The scale bar of 100 m is applicable to all fluorescent images. (B) SEM images (day 1) at magnifications of 1000× and 10000×. (C) Cell attachment and proliferation represented by the cell numbers at 4 h, days 1, 2, and 4. (D) Cell area at day 1. *: $p < 0.05$ relative to hot-compressed and edge-on samples; #: $p < 0.01$ relative to hot-compressed and edge-on samples.

MC3T3-E1 cell mineralization that included calcium content and ALP activity, and relative gene expression of OCN, OPN, COL I, and ALP were examined after 14-day cell culture, as shown in Figure 4. Calcium content and ALP activity had the same trend for all samples. Cells on the edge-on samples had slightly better mineralization but without significant difference. In contrast, cells on the flat-on samples had notably higher mineralization than the edge-on samples. Relative gene expression results further confirmed the trend for mineralization at the gene level. Normally, ALP and COL I reached their maximum expression levels in the period of matrix maturation after one week post-seeding [30]. COL I, an early stage marker, was synthesized mainly to support

matrix formation and its value dramatically decreased after matrix maturation. OCN, OPN, and ALP that are related to mineralization had remarkably upregulated expression on the flat-on samples compared with other groups. COL I, even though after the period of matrix maturation, still had a better expression level on the flat-on samples.

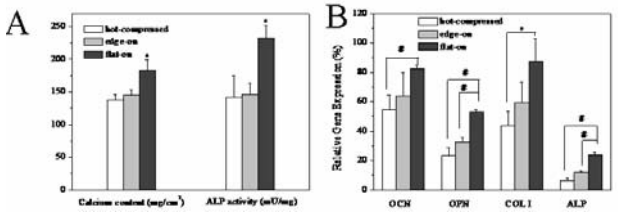

Figure 7.4 (A) Calcium content and ALP activity of MC3T3-E1 cells after 14-day culture; *: $p < 0.05$; #: $p < 0.01$ relative to the hot-compressed and edge-on samples. (B) Relative gene expression levels of OCN, OPN, COL I, and ALP to GAPDH using real time PCR. *: $p < 0.05$; #: $p < 0.01$. The relative expression value of ALP was multiplied by 10.

7.4 Conclusion

Hot-compressed, edge-on, and flat-on PCL films were prepared and the surface morphology was observed by AFM scanning. Flat-0n surface had higher surface free energy compared with hot-compressed and edge-on surface. MC3T3 attachment, adhesion, spreading, proliferation, mineralization, and gene expression were evaluated systemtically. The flat-on samples with a much higher surface free energy could dramatically promote MC3T3-E1 cell adhesion and subsequent spreading, proliferation, mineralization, and expression of gene markers related to osteogenesis.

References

[1] Liu, Y. X.; Chen, E. Q. *Coord. Chem. Rev.*. **2010**, *254*, 1011.

[2] Muthukumar, M. *Adv. Chem. Phys.* **2004**, *128*, 1.

[3] Ramanathan, M.; Darling, S. B. *Prog. Polym. Sci.* **2011**, *36*, 793.

[4] Wang, Z.; Xie, X. M.; Yang, R.; Wang, X. F. *Chemical J. Chinese Univ.-Chinese edition.* **2006**, *27*, 161.

[5] Cheung, Z. L.; Weng, L. T.; Chan, C. M. *Langmuir* **2005**, *21*, 7968.

[6] Jiang, Y.; Luo, Y. H.; Fan, Z. F.; Wang, X. Y.; Xu, J.; Guo, B. H. *Science in China (Series B)* **2003**, *46*, 152.

[7] Demirel, A. L.; Yurteri, S.; Cianga, I.; Yagci, Y. *Macromolecules* **2005**, *38*, 6402.

[8] Anselme, K.; Bigerelle, M. *Int. Mater. Rev.* **2011**, *56*, 243.

[9] Wang, K.; Cai, L.; Jesse, S.; Wang, S. *Langmuir* **2012**, *28*, 4382.

[10] Simon Jr, C. G.; Eidelman, N.; Kennedy, S. B.; Sehgal, A.; Khatri, C. A.; Washburn, N. R. *Biomaterials* **2005**, *26*, 6906.

[11] Simon Jr, C. G. *J Microscopy* **2004**, *216*, 153.

[12] Park, A.; Cima, L. G. *J. Biomed. Mater. Res.* **1996**, *31*, 117.

[13] O'Connel, C.; Sherlock, R.; Ball, M. D.; Aszalos-Kiss, B.; Prendergast, U.; Glynn, T. J. *Appl. Surf. Sci.* **2009**, *255*, 4405.

[14] Lampin, M.; Warocquier-Clerout, R.; Legris, C.; Degrange, M.; Sigot-Luizard, M. F. *J Biomed Mater Res.* **1997**, *36*, 99.

[15] Harnett, E. M.; Alderman, J.; Wood, T. *Colloids and Surfaces B: Biointerfaces* **2007**, *55*, 90.

[16] Van Oss, C. J.; Good, R. J.; Chaudhury, M. K. *Langmuir* **1988**, *4*, 884.

[17] Wang, K.; Cai, L.; Wang, S. *Polymer* **2011**, *52*, 2827.

[18] Misra, R. D. K.; Thein-Han, W. W.; Pesacreta, T. C.; Hasenstein, K. H.; Somani, M. C.; Karjalainen, L. P. *Acta Biomater.* **2009**, *5*, 1455.

[19] Kim, M. H.; Kino-oka, M.; Taya, M. *Biotechnology Advances* **2010**, *28*, 7.

[20] Dalby, M. J. *Med. Eng. Phys.* **2005**, *27*, 730.

[21] Anselme, K. *Biomaterials* **2000**, *21*, 667.

[22] Siebers, M. C.; Walboomers, X. F.; van den Dolder, J.; Leeuwenburgh, S. C. G.; Wolke, J. G. C.; Jansen, J. A. *J. Mater. Sci: Mater Med.* **2008**, 19, 861.

[23] Boyan, B. D.; Hummert, T. W.; Dean, D. D.; Schwartz, Z. *Biomaterials* **1996**, *17*, 137.

[24] Bettinger, C. J.; Langer, R.; Borenstein, J. T. *Angew. Chem. Int. Ed.* **2009**, *48*, 5406.

[25] Anselme, K.; Davidson, P.; Popa, A. M.; Giazzon, M.; Liley, M.; Ploux, L. *Acta Biomater.* **2010**, *6*, 3824.

[26] Loesberg, W. A.; te Riet, J.; van Delft, F. C. M. J. M.; Schon, P.; Figdor, C. G.; Speller, S.; van Loon, J. J. W. A.; Walboomers, X. F.; Jansen, J. A. *Biomaterials* **2007**, *28*, 3944.

[27] Kennedy, S. B.; Washburn, N. R.; Simon Jr, C. G.; Amis, E. J. *Biomaterials* **2006**, 27, 3817.

[28] Lim, J. Y.; Shaughnessy, M. C.; Zhou, Z.; Noh, H.; Vogler, E. A.; Donahue, H. J. *Biomaterials* **2008**, *29*, 1776.

[29] Sista, S.; Wen, C.; Hodgson, P. D.; Pande, G. *J. Biomed. Mater. Res. A* **2011**, *97A*, 27.

[30] Kim, E. J.; Boehm, C. A.; Mata, A.; Fleischman, A. J.; Muschler, G. F.; Roy, S. *Acta Biomater.* **2010**, *6*, 160.

CHAPTER VIII
PROMOTING MC3T3-E1 CELL FUNCTIONS ON BIOMIMETIC CALCIUM CARBONATE CONCENTRIC MICROGROOVES WITH TUNABLE WIDTH

8.1 Introduction

Bone consists of a mineral moiety of hydroxyapatite (HA) and amorphous calcium phosphate deposited on the organic collagen matrix [1]. Osteoblasts adhere to and communicate with each other mainly through adherens junctions, which require calcium-dependent cell-cell adhesion via cadherins [2,3]. The interaction between the organic matrix and calcium-containing components is thus critical in bone regeneration and ceramic bone implants have been developed from calcium carbonate ($CaCO_3$), HA, and calcium phosphate [4]. However, long-term observation of these materials showed mismatch of mechanical properties and poor interaction with the surrounding tissue [5]. Facile, biomimetic synthetic approaches are needed in developing biomaterials with improved mechanical properties, biocompatibility, and bioactivity.

One inspiration is to mimic basement membranes that widely exist in vertebrate body and work as substrata for overlying cellular structures [6]. They have complex topography and consist of extracellular matrix (ECM) proteins such as fibrous collagen, laminin, and fibronectin [6]. The components, mechanical properties and topography of both basement membranes and bioinspired substrates and scaffolds can modulate cellular functions through activation of transmembrane integrin receptors and the strength of integrin-cytoskeleton links [7]. To mimic these complex topographical features and study

their impact on cell functions, micro-patterned surfaces with grooves and ridges, pits, pores, wells and nodes, and spheres have been fabricated using various biomaterials [6,8-12]. Photo-crosslinked poly(ε-caprolactone) triacrylate (PCLTA) substrates with concentric microgrooves were also developed recently in our research group through replica molding from microfabricated silicon wafers to mimic natural self-assembled structures such as banded spherulites and osteons for regulating mouse pre-osteoblastic MC3T3-E1 cell behaviors [13].

In this study, we focus on biomimetic substrates made from $CaCO_3$, which is abundant in nature, e.g. coral skeletons and sea urchin spines, and has been widely studied in biomineralization and biomimetic chemistry [14,15]. Amorphous $CaCO_3$ films were evaluated for bone replacement using rat bone marrow stromal cells [16]. $CaCO_3$ concentric microgrooved morphology was achieved by spontaneous two-step crystal growth on hydrogel matrices made from poly(vinyl alcohol) (PVA), poly(vinyl alcohol-*co*-vinyl acetate), or cholesterol-bearing pullulan matrices, in the presence of poly(acrylic acid) (PAA) [17-21]. The first step is *in situ* formation of disk-like flat thin film of calcite with a thickness of ~100 nm through the cooperation of the hydrogel matrix and PAA [17,19]. On the calcite disk, the *c* axes out of the disk plane are alternately aligned perpendicularly and parallel to the radial direction of the disk because of diffusion-controlled crystal growth [17,19]. The second step is formation of 3D relief structures consisting of needlelike calcite crystals, which grow into elongated shape along their *c* axes with increasing incubation time [17,19]. On the basis of these previous findings, here we report $CaCO_3$ substrates with tunable groove width through a facile means, and

the effect of these microgrooves on adhesion, proliferation, distribution, alignment, and differentiation of MC3T3-E1 cells.

8.2 Experimental Section

8.2.1 Materials

PVA (87-89% hydrolyzed, M_w: 124000-186000 g/mol), PAA (M_w: 1800 g/mol), calcium chloride ($CaCl_2$), and ammonium carbonate [$(NH4)_2CO_3$] were purchased from Sigma-Aldrich (Milwaukee, WI).

8.2.2 Preparation of Patterned $CaCO_3$ Films

The procedures were based on the previous reports [17,19]. PVA was dissolved in dimethylsulfoxide (2 wt%). Then the PVA solution (70 μL) was spin-coated on microscope slides (Fisher Scientific, Pittsburgh, PA) at a spinning rate of 3000 rpm for 30 s at room temperature. The as-coated slide was subsequently annealed at 185 °C for 30 min to crosslink PVA on the surface and slowly cooled down to room temperature. Pure water from Millipore system was used to prepare $CaCl_2$ aqueous solution ([Ca^{2+}] = 10 mM) containing PAA (2.4×10^{-3} wt%). The annealed slide immersed in $CaCl_2$ aqueous solution was placed in a closed desiccator with $(NH4)_2CO_3$ aqueous solution in pure water. 5.0-μm-wide $CaCO_3$ grooves were fabricated at room temperature when the molar ratio of $(NH4)_2CO_3$ to $CaCl_2$ was 18 and the incubation time was 17 h. 10-μm-wide grooves were fabricated in the same way at 37 °C. Flat $CaCO_3$ substrates as the control group were fabricated using the same procedure for 5.0-μm-wide grooves but without PAA.

8.2.3 Characterizations

Optical micrographs were taken with an optical microscope (Nikon, Japan). SEM (S-3500, Hitachi Instruments, Japan) was employed to observe the surface and cross-section structures of $CaCO_3$ microgrooves at an accelerating voltage of 5 kV. Prior to observation, samples were dried completely in high vacuum and sputter-coated with a gold-palladium layer (Emscope SC 500, Elexience).

8.2.4 Cell Culture

Mouse MC3T3-E1 cells (ATCC, Manassas, VA) were cultured using the method previously reported [22,23]. All $CaCO_3$ substrates were first rinsed with 70% alcohol solution twice and then sterilized twice in excessive 70% alcohol solution for 1 h, followed by complete drying in vacuum. MC3T3-E1 cells were seeded on all $CaCO_3$ substrates at a density of ~11000 cells/cm^2 with α-Minimum Essential Medium (α-MEM, Gibco) containing 10% fetal bovine serum (FBS, Gibco) and 1% penicillin/streptomycin (Gibco). The cells were cultured in an incubator at 37 °C with 95% humidity and 5% CO_2.

8.2.5 Immunofluorescence Microscopy and SEM

To observe actin cytoskeleton and nuclei and measure cell density, attached MC3T3-E1 cells on the substrates were fixed with 16% paraformaldehyde (PFA) solution for 20 min at room temperature followed by two rinses with phosphate buffered saline (PBS). Then the cells were permeabilized with 0.2% (v/v) Triton X-100 followed by three rinses with PBS. Then the cells were stained with RP for 1 h at 37 °C, followed by DAPI staining at room temperature. An Axiovert 25 light microscope (Carl Zeiss,

Germany) was used for photographing. Cells on substrates were counted from DAPI-stained images and the average number of nuclei per field in 15-20 fields was calculated for each sample. Average cell area was calculated from over 20 non-overlapping cells at day 1 post-seeding using ImageJ software (National Institutes of Health, Bethesda, MD). Additionally, individual cytoskeleton at day 1 was observed using a confocal microscope (SP2, Leica). FAs in MC3T3-E1 cells were stained first with mouse monoclonal anti-vinculin antibody (V9264, Sigma-Aldrich) for 1 h at 37 °C and rinsed with PBS five times. Then FAs were labeled by anti-mouse IgG-FITC antibody (F0257, Sigma) at 37 °C for 5 h and observed using the Leica confocal microscope. For characterization of cells attached on the substrates at day 1 post-seeding, each sample was fixed in 5% paraformaldehyde (w/v) for 20 min and rinsed with PBS for three times. All the samples were dehydrated with graded ethanol solution (25%, 50%, 70%, 95%, and 100%) and dried in vacuum overnight before the same procedure for observation using SEM.

8.2.6 ALP Activity and Calcium Assay

MC3T3-E1 cells cultured for 2 weeks were fixed with 16% PFA solution for 30 min and subsequently rinsed with PBS twice. The ALP activity was determined using a Leukocyte Alkaline Phosphatase Kit (Sigma-Aldrich). Cell nuclei were stained with red violet color and a higher stain intensity indicated a higher ALP activity. The calcium deposition of MC3T3-E1 cells on the substrates was determined by immersing them in alizarin red S solution (Ricca Chemical, Arlington, TX) for 30 min and photographed on the Nikon optical microscope after four thorough 20-min rinses with deionized water.

8.3 Results and Discussion

$CaCO_3$ groove width was tuned by modulating incubation temperature. Two different groove widths of 10 and 5.0 μm were obtained at 37 °C and room temperature (~20 °C), respectively. Estimated from the reported images, the groove width was ~8.8 μm for $CaCO_3$ concentric microgrooves prepared using the same method at 30 °C [17]. Controlling the groove width was inspired by the larger band width in polymer banded spherulites when the crystallization is slower at a higher crystallization temperature [13,24]. The diffusion-controlled crystal growth in formation of flat calcite thin films and the periodic orientation were influenced by the incubation temperature in a similar manner. The morphology of these two microgrooves was examined using optical microscopy and scanning electron microscopy (SEM), as shown in Figure 8.1. From the optical images, closely connected $CaCO_3$ concentric microgrooves were observed and the diameter of a ringed structure could extend to ca. 250 μm with ~10 successive concentric rings. The 5.0- and 10-μm-wide $CaCO_3$ grooves had a similar height of ~5.0 μm, consistent with the reported value [17]. The groove height and width were constant along the radius except on the edge of a ringed structure. Although the annealing time of the substrate polymer and the molecular weight of PAA were also used to tune the morphology of the $CaCO_3$ films [20,21], this is the first time to report tunability of the groove width in its concentric ringed morphology.

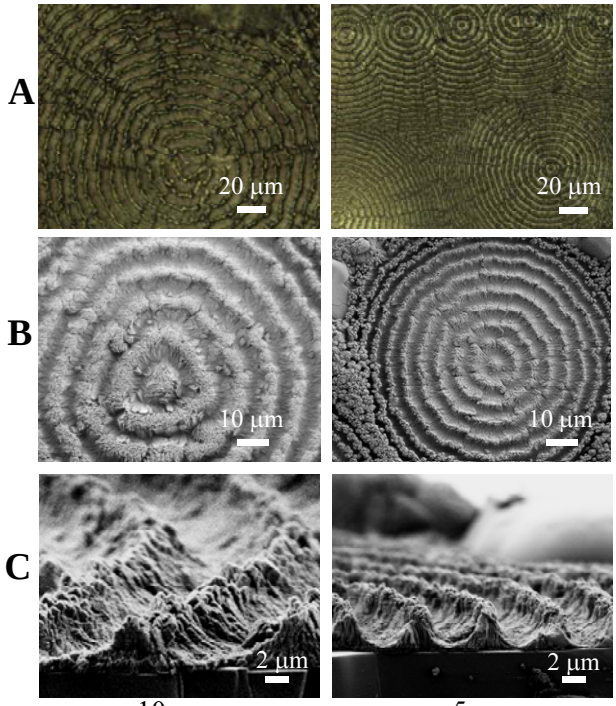

Figure 8.1 $CaCO_3$ concentric microgrooves grown on PVA matrix. (A) Optical microscopic images; (B) SEM images of the surfaces (× 3000, top view); (C) SEM images of the cross-sections (× 10000, side view).

Cell adhesion is a determining step for cell proliferation, differentiation, gene expression, and tissue development and organization [25]. Figure 8.2A shows MC3T3-E1 cell images and focal adhesions (FAs) in the cells after 1-day culture on both flat substrates and concentric microgrooves of $CaCO_3$. The F-actin-stained cytoskeletal images indicated that cells on flat $CaCO_3$ substrates were motile with very few stress fibers. In contrast, the cells on the $CaCO_3$ microgrooves were well spread with more well-defined stress fibers, protrusions, and filopodia. In addition, the effect of microgrooves was more prominent when the groove width was smaller (5.0 μm). Cell protrusions on $CaCO_3$ microgrooves preferred to be aligned along the direction of ridges. Vinculin-stained cells consistently had much more FAs on the microgrooves compared

with those on the flat substrates. Again, the narrower microgrooves could induce more FAs. The FA density, defined as the number of FAs per cell on $CaCO_3$ microgrooves, and the average area of FAs were larger than these on the flat substrates, and the values increased with decreasing the groove width from 10 to 5.0 μm (Figure 8.2B). FA circularity was also calculated using the equation of $4\pi \times \text{area/perimeter}^2$, with a measure of 1 indicating a perfect circle. The lower circularity values on $CaCO_3$ microgrooves meant that FAs were more aligned. In addition, FAs on $CaCO_3$ microgrooves were mainly distributed on the ridges. Similar to F-actin-stained cytoskeletal images, vinculin-stained images also showed that MC3T3-E1 cells tended to grow along the groove direction, especially when the groove width was 5.0 μm.

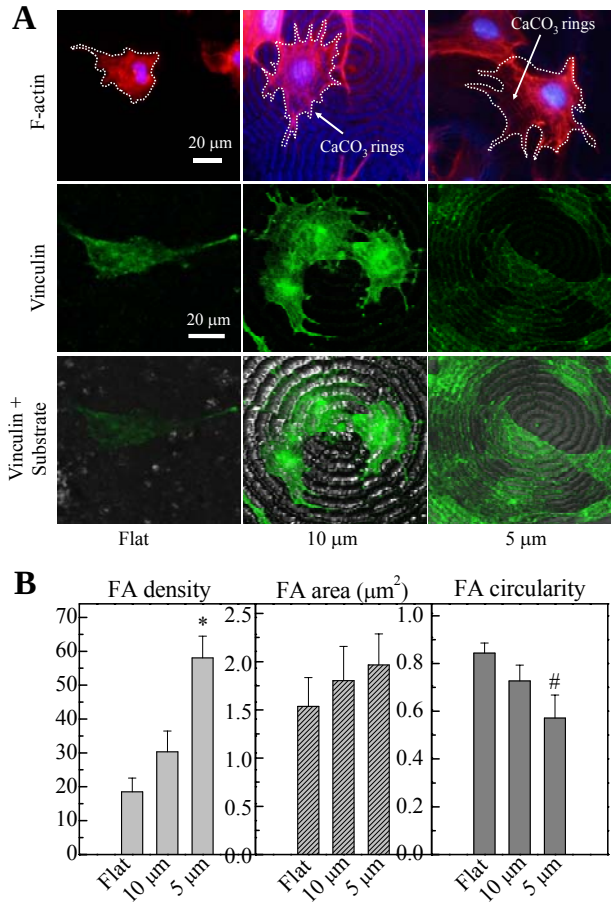

Figure 8.2 (A) Fluorescent images of MC3T3-E1 cells stained with rhodamine-phalloidin (RP, red) and 4',6-diamidino-2-phenylindole (DAPI, blue) (top row), vinculin-stained images (middle row), and merged images with the background of $CaCO_3$ microgrooves (bottom row) at day 1 post-seeding. Scale bar of 20 μm is applicable for all. (B) Density, area, and circularity of FAs measured from vinculin-stained cell images in (A). *: $p < 0.05$, #: $p < 0.01$: relative to flat $CaCO_3$ substrates.

Substrates with micro-scale grooves and ridges can align cells along the groove direction through the "contact guidance" effect [6,8-12]. FAs, the closest contacts between cells and substrata, have a rectangular shape with a length of 1-5 μm and preferred to attach in an oriented manner on the ridges when the grooves were smaller than FAs [26,27]. After cell adhesion with aligned FAs, actin filaments or stress fibers in

cells can also be aligned. Surface topography can regulate cell behavior through influencing the composition and conformation of ECM proteins that serve as anchorage sites for cells [8]. Once protein adsorption shows distinction along the ridges of concentric microgrooves, oriented cell shape will appear as the result of preferably formed FAs at these sites. As discussed earlier, FAs on $CaCO_3$ microgrooves were oriented along the ridges and it was more apparent on 5.0-μm-wide ones because the diameter of FAs (1-2 μm) was closer to the groove width. Accordingly, the actin filaments on 5.0-μm-wide $CaCO_3$ grooves were also more significantly aligned along the ridge direction than those on 10-μm-wide and flat ones. According to the mechanical mechanism proposed for cell alignment on microgrooves, cells tend to seek a state to balance their internal and external forces [28,29]. On microgrooved substrata, cells could sense the forces from the microenvironment and reach equilibrium that induced an aligned cell shape. Unlike straight parallel ones, concentric $CaCO_3$ microgrooves with larger curvatures produced extra tension and inhibited MC3T3-E1 cells from efficiently migrating and growing along the ridges. Therefore, the actin filaments in cells could not be aligned completely along the ridges.

MC3T3-E1 cell proliferation was also enhanced by $CaCO_3$ concentric microgrooves, as indicated by the fluorescent cell images (Figure 8.3A) and cell densities (Figure 8.3B) counted from the nuclei over 4-day cell culture. It should be noted that only substrates with full coverage of $CaCO_3$ were used here. Consistently in both images and data, the cell densities were higher on the microgrooved substrates than that on the flat ones, especially on the 5.0-μm-wide grooves after day 2. Figure 8.3C shows that cells on

$CaCO_3$ microgrooves had larger areas than those on flat $CaCO_3$ substrates, and substrates with the narrower grooves (5.0 μm) could help cells spread better compared with the wider ones (10 μm). As discussed earlier, MC3T3-E1 cell adhesion regulated by surface topography was the reason for the differences in later adhesion-mediated events such as proliferation and differentiation [30].

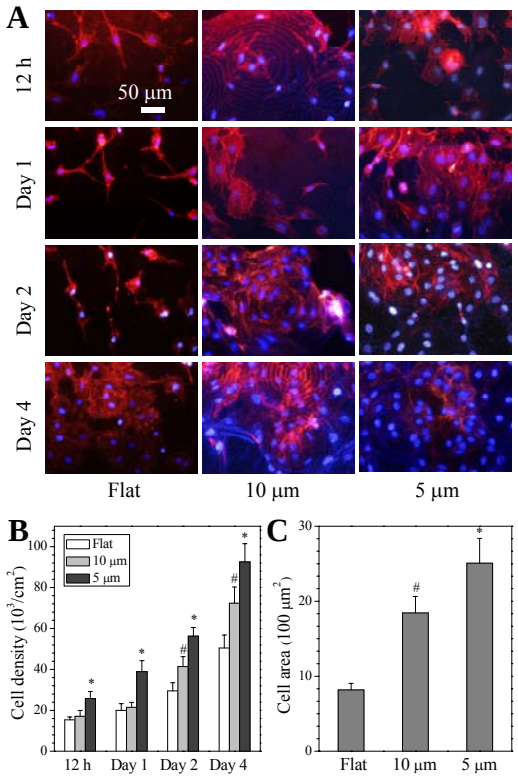

Figure 8.3 (A) Fluorescent images of MC3T3-E1 cells with cytoplasm stained with RP (red) and nuclei stained with DAPI (blue) at 12 h, days 1, 2, and 4 post-seeding. Scale bar of 50 μm is applicable to all. (B) Cell proliferation on flat and microgrooved substrates of $CaCO_3$, represented by the cell numbers at 12 h, days 1, 2, and 4. (C) Cell area at day 1. *: $p < 0.01$ relative to flat $CaCO_3$ substrates; #: $p < 0.05$ relative to flat and 5.0-μm-wide $CaCO_3$ grooves.

MC3T3-E1 cell adhesion and proliferation were also characterized using SEM images (Figure 8.4). More cells were observed on $CaCO_3$ microgrooves than on the flat

ones and this trend was more evident on the narrower grooves (Figure 8.4A), in agreement with the cell images in Figure 8.3A. With a higher magnification (Figure 8.4B), cells on the flat $CaCO_3$ substrates were still spreading with high thicknesses and very few filopodia. In contrast, cells cultured on the microgrooves were more spread with more filopodia. Cells on the 5.0-μm-wide $CaCO_3$ grooves had remarkably larger spread areas with much lower cell thicknesses and more filopodia projecting from cell membranes. The SEM result was consistent with the quantification of cell area in Figure 8.3C, suggesting that $CaCO_3$ microgrooves, especially 5.0-μm-wide ones, could promote cell spreading. We also compared MC3T3-E1 cells on the PVA matrix for $CaCO_3$ crystallization with those on $CaCO_3$ microgrooves and flat surfaces, and found cells preferred to grow and proliferate on the $CaCO_3$ substrates, in particular, 5-μm-wide grooves (Figure 8.5). This result was expected because PVA matrix was essentially a hydrogel layer that is known to resist protein adsorption and cell adhesion [7].

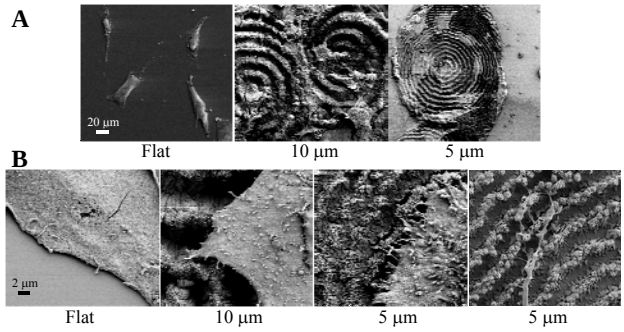

Figure 8.4 SEM images of MC3T3-E1 cells cultured on $CaCO_3$ substrates for 1 day. A: × 1000; B: × 10000.

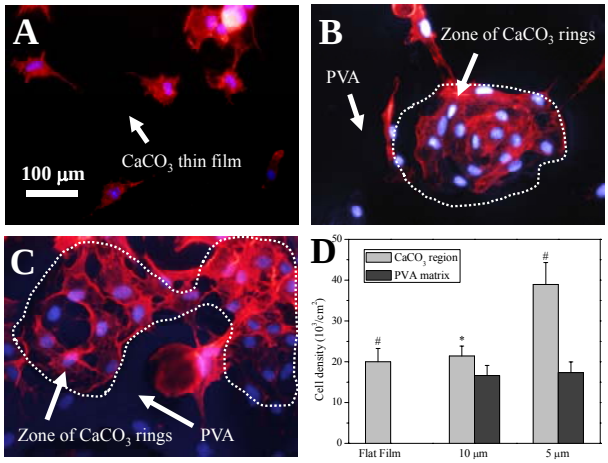

Figure 8.5 Fluorescent images of MC3T3-E1 cells with cytoplasm stained with RP (red) and nuclei stained with DAPI (blue) at day 1 post-seeding on (A) flat substrates, (B) 10-μm-wide, and (C) 5.0-μm-wide grooves of $CaCO_3$. Scale bar of 100 μm is applicable for A-C. (D) Cell number on different substrates. *: $p < 0.05$ and #: $p < 0.01$: relative to the PVA matrix.

MC3T3-E1 cell nuclear dimensions and distribution were also regulated by the $CaCO_3$ microgrooves. As shown in Figure 8.6A, nuclei were randomly distributed and had a round shape at all time points on flat substrates and 5.0-μm-wide grooves of $CaCO_3$. At day 4, the nuclear area of MC3T3-E1 cells was 130 ± 10 μm^2 and the diameter was 12.3 ± 0.9 μm on flat $CaCO_3$ substrates. These two values increased to 201 ± 18 μm^2 and 15.7 ± 1.0 μm on 5.0-μm-wide $CaCO_3$ grooves, respectively. In clear contrast, when the groove width was 10 μm, cell nuclei could be trapped inside the microgrooves and aligned along the groove direction after day 2 with an area as small as 115 ± 6 μm^2. Nuclear distribution was defined as the percentage of cell nuclei trapped inside the microgrooves in the entire number of nuclei. Unlike those on flat substrates or 5-μm-wide grooves, the nuclear circularity on 10-μm-wide grooves decreased with increasing the culture time, indicating more alignment (Figure 8.6B). Meanwhile, cell nuclei were

more likely trapped in the 10-μm-wide grooves (Figure 8.6C). As discussed in Figure 2, actin cytoskeleton of the cells on $CaCO_3$ microgrooves could be circularly oriented. This distortion in the pattern of actin structure would immediately affect intermediate filaments, which effectively transfer the force from membrane distortion to nuclei [31-33]. In other words, molecular connections between actin filaments, intermediate filaments, and nuclei can produce a pathway for mechanical signal transfer through the cells when they respond to changes in ECM adhesivity or mechanics [31-33]. Cell nuclei could be oriented in the same direction as that of actin cytoskeleton distortion. Though distortion of actin cytoskeleton was found on all $CaCO_3$ microgrooves, nuclear alignment was not evident on 5.0-μm-wide ones. This observation can be interpreted using the comparison in the dimensions between cell nuclei and the grooves underlying them. When the groove width was 5.0 μm, nuclei with a larger dimension could span over several grooves and ridges. To reach mechanical equilibrium, the nuclei bridging ridges would be stretched to a larger content because of the distortion of actin cytoskeleton and the stress applied by the ridges. Consequently, cell nuclei on 5.0-μm-wide $CaCO_3$ grooves could spread over a bigger area whereas those on 10-μm-wide ones showed opposite. Nevertheless, cell nuclei were distorted in both scenarios when compared with the flat substrates.

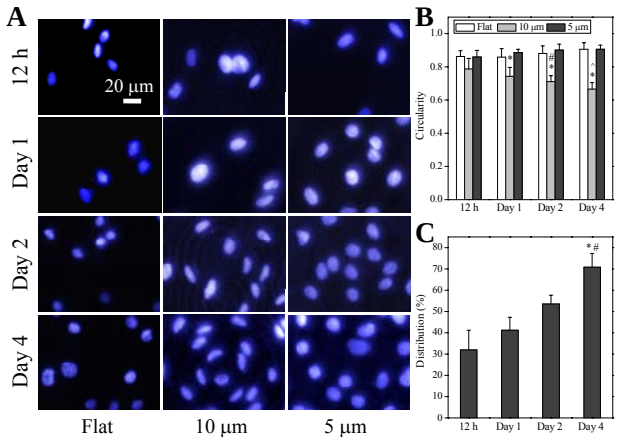

Figure 8.6 (A) Fluorescent images of MC3T3-E1 cells with nuclei stained with DAPI (blue) at day 1 post-seeding; (B) Nuclear circularity; *: $p < 0.01$ relative to flat $CaCO_3$ substrates and 5.0-μm-wide $CaCO_3$ grooves at the same time; #: $p < 0.05$ relative to flat $CaCO_3$ substrates at 12 h; ^: $p < 0.01$ relative to flat $CaCO_3$ substrates at 12 h; (C) Distribution of MC3T3-E1 cells on 10-μm-wide $CaCO_3$ crystals. *: $p < 0.01$ relative to 12 h; #: $p < 0.05$ relative to day 1.

MC3T3-E1 cell differentiation was also promoted by the $CaCO_3$ microgrooves. After 14-day cell culture, the alkaline phosphatase (ALP) activity and calcium content of the cells (Figure 8.7A,B), two indicators of early-stage osteoblastic differentiation, on all substrates were semi-quantified by staining with fast blue RR and alizarin red S solutions, respectively. Both parameters were greatly enhanced on $CaCO_3$ microgrooves. Compared with 10-μm-wide grooves, 5.0-μm ones were darker, suggesting a better mineralization level. This discrepancy between flat and microgrooved substrates of $CaCO_3$ in MC3T3-E1 cell differentiation should be ascribed to the following aspects, which were well explored in literature [9,13,37]. First, $CaCO_3$ grooves induced stronger cell adhesion and thus strengthened cell communications, proliferation, and differentiation. Secondly, both flat and microgrooved substrates of $CaCO_3$ could gradually release calcium ion (Ca^{2+}) and promote the formation of cadherins to enhance differentiation. Thirdly, alignment and

distortion of actin filaments and nuclei induced release of Ca^{2+} from the perinuclear space through the mechanotransduction pathway and the released Ca^{2+} in turn upregulated MC3T3-E1 cell differentiation and gene expression [34-36]. The fourth reason was that the cell-material interaction depends on the restricted distribution of regulatory factors. $CaCO_3$ microgrooves could provide a microenvironment for achieving critical concentrations of regulatory factors and leads to the calcified tissue formation [37]. These factors worked collectively in regulating MC3T3-E1 cell functions.

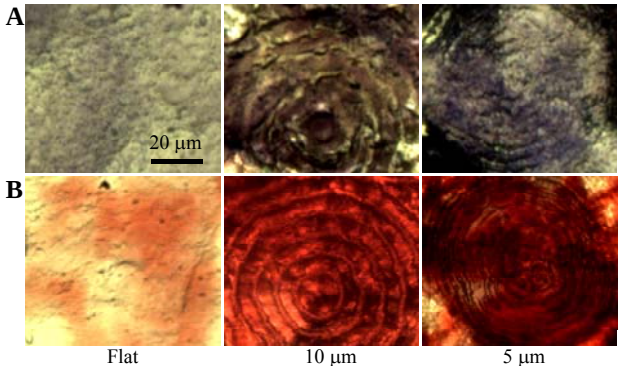

Figure 8.7 (A) ALP activity of MC3T3-E1 cells stained with fast blue RR/naphthol solution (violet); (B) Calcification of MC3T3-E1 cells stained with alizarin red S solution (red). Scale bar of 20 μm is applicable to all.

The present results can be compared with our recent reports on two groups of substrates with concentric microgrooves [13,38]. Consistently, photo-crosslinked PCLTA substrates with highly uniform 7.5-μm-wide and 10-μm-deep concentric grooves enhanced MC3T3-E1 cell alignment and mineralization; however, different microgroove dimensions did not influence cell attachment and proliferation in that study and no groove width smaller than 7.5 μm was used [13]. Cell alignment was less significant when the aspect ratio of grooves, defined by dividing the groove depth by the width, was

smaller, because cells cannot sense the shallow surface topography efficiently [39]. For MC3T3-E1 cells seeded on poly(ε-caprolactone) (PCL) banded spherulites with the groove depth of ~350 nm and the groove width of ~30 μm, cell attachment and proliferation were better than those on flat hot-compressed disks but no cell alignment was observed because of the low aspect ratio of grooves [38]. In this study, we found increased cell numbers, strongly aligned cytoplasm and nuclei along the ridge direction, and better mineralization on $CaCO_3$ microgrooves.

8.4 Conclusions

$CaCO_3$ concentric microgrooves with groove widths of 5.0 and 10 μm were fabricated through modulating incubation temperature. MC3T3-E1 cells cultured on flat and microgrooved substrates of $CaCO_3$ demonstrated that the microgrooves could dramatically enhance their adhesion, spreading, proliferation, and differentiation, especially on the narrower ones. In addition, cell nuclear distortion, either being aligned or stretched, and distribution were also studied and more aligned cell nuclei were trapped in 10-μm-wide $CaCO_3$ grooves because of their comparable dimensions. This study showed the great promise of using biomimetic $CaCO_3$ concentric microgrooved topography in bone tissue engineering applications.

References

[1] Kartsogiannis, V.; Ng, K. W. *Mol. Cell. Endocrinol.* **2004**, *228*, 79.

[2] Sommerfeldt, D. W.; Rubin, C. T. *Eur. Spine. J.* **2001**, *10*, S86.

[3] Stains, J. P.; Civitelli, R. *Biochem. Biophys. Res. Comm.* **2005**, *328*, 721.

[4] Hing, K. A. *Phil. Trans. R. Soc. Lond. A* **2004**, *362*, 2821.

[5] Song, J.; Saiz, E.; Bertozzi, C. R. *J. Am. Chem. Soc.* **2003**, *125*, 1236.

[6] Flemming, R. G.; Murphy, C. J.; Abrams, G. A.; Goodman, S. L.; Nealey, P. F. *Biomaterials* **1999**, *20*, 573.

[7] Harbers, G. M.; Grainger, D. W. In *Introduction to Biomaterials*, (Eds: S. A. Guelcher, J. O. Hollinger), CRC Press: Boca Raton, FL, USA, **2005**, pp. 15-45.

[8] Curtis, A.; Wilkinson, C. *Biomaterials* **1997**, *18*, 1573.

[9] Curtis, A.; Wilkinson, C. *J. Biomater. Sci., Polym. Ed.* **1998**, *9*, 1313.

[10] Lim, J. Y.; Donahue, H. J. *Tissue Eng.* **2007**, *13*, 1879.

[11] Anselme, K.; Bigerelle, M. *Int. Mater. Rev.* **2011**, *56*, 243.

[12] Bettinger, C. J.; Langer, R.; Borenstein, J. T. *Angew. Chem. Int. Ed.* **2009**, *48*, 5406.

[13] Wang, K.; Cai, L.; Zhang, L.; Dong, J.; Wang, S. *Adv. Healthcare Mater.* **2012**, *1*, 292.

[14] Meldrum, F. C. *Int. Mater. Rev.* **2003**, *48*, 187.

[15] Meldrum, F. C.; Cölfen, H. *Chem. Rev.* **2008**, *108*, 4332.

[16] Popescu, D. C.; van Leeuwen, E. N. M.; Rossi, N. A. A.; Holder, S. J.; Jansen, J. A.; Sommerdijk, N. A. J. M. *Angew. Chem. Int. Ed.* **2006**, *45*, 1762.

[17] Sakamoto, T.; Oichi, A.; Oaki, Y.; Nishimura, T.; Sugawara, A.; Kato, T. *Cryst. Growth Des.* **2009**, *9*, 622.

[18] Sugawara, A.; Ishii, T.; Kato, T. *Angew. Chem. Int. Ed.* **2003**, *42*, 5299.

[19] Kato, T.; Sakamoto, T.; Nishimura, T. *MRS Bulletin* **2010**, *35*, 127.

[20] Sakamoto, T.; Oichi, A.; Sugawara, A.; Kato, T. *Chem. Lett.* **2006**, *35*, 310.

[21] Sakamoto, T.; Oichi, A.; Nishimura, T.; Sugawara, A.; Kato, T. *Polym. J.* **2009**, *41*, 522.

[22] Cai, L.; Wang, S. *Polymer* **2010**, *51*, 164.

[23] Wang, K.; Cai, L.; Hao, F.; Xu, X.; Cui, M.; Wang, S. *Biomacromolecules* **2010**, *11*, 2748.

[24] Wang, K.; Jesse, S.; Wang, S. *Macromol. Chem. Phys.* **2012**, Doi: 10.1002/macp.201200004.

[25] Gumbiner, B. M. *Cell* **1996**, *84*, 345.

[26] Biggs, M. J. P.; Dalby, M. J. *P. I. Mech. Eng.* H **2010**, *224*, 1141.

[27] Geiger, B.; Spatz, J. P.; Bershadsky, A. D. *Nature Rev.* **2009**, *10*, 21.

[28] Ingber, D. E. *J. Cell. Sci.* **1993**, *104*, 613.

[29] Ingber, D. E. *Curr. Opin. Cell. Biol.* **1991**, *3*, 841.

[30] Anselme, K. *Biomaterials* **2000**, *21*, 667.

[31] Maniotis, A. J.; Chen, C. S.; Ingber, D. E. *Proc. Natl. Acad. Sci. U.S.A.* **1997**, *94*, 849.

[32] Helmke, B. P.; Thakker, D. B.; Goldman, R. D.; Davis, P. F. *Biophys. J.* **2001**, *80*, 184.

[33] Dalby, M. J.; Riehle, M. O.; Yarwood, S. J.; Wilkinson, C. D. W.; Curtis, A. S. G. *Exp. Cell Res.* **2003**, *284*, 274.

[34] Relan, N. K.; Yang, Y.; Beqaj, S.; Miner, J. H.; Schuger, L. *J. Cell. Biol.* **1999**, *147*, 1341.

[35] Itano, N.; Okamoto, S.; Zhang, D.; Lipton, S. A.; Ruoslahti, E. *Proc. Natl. Sci. U.S.A.* **2003**, *100*, 5181.

[36] Thomas, C. H.; Collier, J. H.; Sfeir, C. S.; Healy, K. E. *Proc. Natl. Sci. U.S.A.* **2002**, *99*, 1972.

[37] Chehroudi, B.; Ratkay, J.; Brunette, D. M. *Cells and Materials* **1992**, *2*, 89.

[38] Wang, K.; Cai, L.; Jesse, S.; Wang, S. *Langmuir* **2012**, *28*, 4382.

[39] Crouch, A. S.; Miller, D.; Luebke, K. J.; Hu, W. *Biomaterials* **2009**, *30*, 1560.

CHAPTER IX
MC3T3-E1 CELL FUNCTIONS REGULATED BY UNIAXIALLY AND BIAXIALLY STRETCHED POLY(ε-CAPROLACTONE) FILMS

9.1 Introduction

Novel biomaterials with desirable properties have been developed to satisfy the imperative clinical needs. When implants made from these biomaterials are exposed to *in vivo* environment, cells generate extra-cellular matrix (ECM) proteins to cover the implant surface. Cells sense and respond to the implant surface via focal adhesions (FAs), which are mediated by integrin receptors on the cell membrane to transduce signals out of and into the living cells. The factors exerting a paramount impact on the formation of the interface between the implant and cells include surface chemistry, topography, and mechanical properties [1]. The roles of these factors in regulating cell behavior have been investigated in the last several decades [2].

Cells normally survive and proliferate on solid substrates that are able to resist force disturbance and this is called anchorage dependence. Cell anchorage on substrates occurs with myosin-based contractility and transcellullar adhesions involving adhesion molecules such as integrins and cadherins. Cells not only apply forces but also respond to the resistance from substrate, tissue matrix, or adjacent cells sensed through cytoskeleton organization. For anchorage-dependent cells, the contractile forces produced in the cross-bridging interactions of actin and myosin filaments can be transmitted to the substrate, which in turn resist the mechanical impact and adjust cell adhesion and cytoskeleton

organization. Cells were found to prefer a substrate with mechanical properties similar to those of the corresponding tissue.

Most studies on how substrate stiffness affects cell functions were performed on polymer networks such as hydrogels because their mechanical properties can be readily tuned via the cross-linking density [3]. In our research group, poly(ε-caprolactone) (PCL) acrylates are used to form networks with physicochemical properties controlled through both crosslinking density and crystallinity for regulating cell fate [4]. MC3T3-E1 cells were found to attach and proliferate better on stiffer PCL with a molecular weight of 80,000 g/mol than on the softer substrate of this PCL blended with PCL with a lower molecular weight of 2000 g/mol [5]. Biaxially stretched PCL membranes were found to have different mechanical properties [6-10]. The film stiffness was lower when the stretch ratio was larger [8]. 3T3 fibroblast cell proliferation was promoted on the film with a higher stretching ratio but this result contradicted with the other results that 3T3 fibroblasts preferred stiffer substrates [8]. The effect of both uniaxial and biaxial stretching on the mechanical properties and surface topography of PCL films and how these substrate characteristics influence cell behavior have not been systematically investigated. Here we report the different mechanical properties of uniaxially and biaxially stretched PCL films and distinct MC3T3-E1 cell adhesion, attachment, proliferation, mineralization, and gene expression on these films.

9.2 Experimental Section

9.2.1 Materials

PCL (M_w: 142,658 g mol^{-1}, M_n: 77,352 g mol^{-1}) was synthesized through ring opening polymerization of ε-caprolactone (Aldrich, St. Louis, MO) with pure water as the initiator.

9.2.2 Sample Preparation

PCL was melted at 85 °C, compressed into thin films (thickness: ~2 mm) between two clean glass slides, and cooled down at room temperature. Then the as-compressed films were stretched using a film stretcher (T. M. Long Co. Somerville, NJ) according to the instruction manual. For uniaxial stretching, two strain levels of 600% and 1000% were applied and the resulted films were named as S600 and S1000, respectively. For biaxial stretching, the films were stretched at an elongation ratio of 4.0, beyond which the films were liable to break.

9.2.3 Characterizations

The mechanical properties of the PCL specimens were measured using a dynamic mechanical analyzer (DMTA-5, Rheometric Scientific) at 37 °C. Briefly, PCL strips (~20 × ~1.5 × ~0.5 mm, length × width × thickness) were elongated at a strain rate of 0.0005 s^{-1}. For each group, five specimens were studied and the tensile modulus was the initial slope of the stress-strain curve. The thermal properties of the PCL samples were determined using a Perkin Elmer Diamond differential scanning calorimeter (DSC) in a N_2 atmosphere. The PCL samples were heated from 25 to 100 °C at a heating rate of 10

°C/min and the heat flow was recorded. To observe the surface features, all the samples were dried completely in high vacuum and sputter-coated with one gold-palladium layer prior to observation via SEM (S-3500, Hitachi Instruments Inc., Tokyo, Japan) at an accelerating voltage of 5 keV. AFM scanning of the sample surface was performed on a Nanoscope V control system (Veeco Instruments, Santa Barbara, CA) using the tapping mode. The root mean square roughness (R_{rms}) was determined from the height images.

9.2.4 In vitro Cell Attachment and Proliferation

Mouse MC3T3-E1 cells (ATCC, Manassas, VA) were cultured using the procedure reported previously [11,12]. Prior to cell culture, all the PCL samples were immersed in 70% alcohol solution for 20 min to clean the surface, sterilized in 70% alcohol solution, and dried completely in high vacuum at room temperature. MC3T3-E1 cells were seeded on the samples at a density of ~ 15000 cells/cm^2 in a 24-well tissue culture plate and cultured in α-Minimum Essential Medium (α-MEM, Gibco) containing 10% fetal bovine serum (FBS, Gibco) and 1% penicillin/streptomycin (Gibco). Then the samples seeded with cells were placed in a cell incubator with 95% humidity, 5% CO_2, and a temperature of 37 °C. At cell culture time points of days 1, 2, and 4, cell number was quantified using a colorimetric cell metabolic assay (CellTiter 96 Aqueous One Solution, Promega, Madison, WI).

9.2.5 Immunofluorescence Microscopy and SEM

At each time point, cells were fixed with 4% (w/v) paraformaldehyde (PFA) solution (Electron Microscopy Science, PA) for ~20 min at room temperature, rinsed

with phosphate buffered saline (PBS) three times, and subsequently permeabilized with 0.2% (v/v) Triton X-100. After being rinsed with PBS twice, the cells were stained with rhodamine-phalloidin (RP) for 1 h at 37 °C and 4',6-diamidino-2-phenylindole (DAPI) at room temperature. An Axiovert 25 light microscope (Carl Zeiss, Germany) was used to visualize the cytoplasm and nuclei. Cell area was measured using ImageJ software (National Institutes of Health, Bethesda, MD) from over 50 non-overlapping RP- stained cells.

Cell adhesion was studied using both vinculin staining and SEM. Vinculin staining was performed as follows. The cells fixed with 4% PFA solution were stained with mouse monoclonal anti-vinculin antibody (V9264, Sigma-Aldrich) for ~1 h at 37 °C and then rinsed with PBS thoroughly. Then the cells were stained with anti-mouse IgG-FITC antibody (F0257, Sigma) in an incubator for more than 4 h. The focal adhesions were photographed using a confocal microscope (SP2, Leica). Quantification of focal adhesions was conducted using ImageJ from more than 50 vinculin-stained cells. Prior to SEM observation, the cells fixed with 4% PFA and rinsed with PBS three times were dehydrated with gradient alcohol solutions (30%, 50%, 60%, 70%, 80%, 90%, 95%, and 100%). Dehydration was performed twice at each alcohol concentration and the dehydration time was 10 min each. Then the cells were dehydrated in a mixture (1:1, v/v) of alcohol and hexamethyldisilazane (Electron Microscopy Science, Hatfield, PA) and further in hexamethyldisilazane. After complete drying in air, the cells were sputter-coated with a gold-palladium layer and observed using SEM (S-3500, Hitachi Instruments Inc., Tokyo, Japan) at an accelerating voltage of 10 keV.

9.2.6 ALP Activity and Calcification Assay

The ALP activity and calcium content of MC3T3 cells cultured for 14 days were measured as described previously [11]. Briefly, the cells were rinsed with PBS to remove unattached cells and other residues, trypsinized, and rinsed again with PBS. Then cell suspension in PBS was centrifuged at 1000 rpm for 5 min to obtain cell pellet. Then the cell pellet was re-suspended in 1 mL 0.2% Nonidet P-40 solution after removing the supernatant and sonicated in ice water for 2 min. A fluorescent-based ALP detection kit (Sigma, St. Louis, MO) and a Quantichrom calcium assay kit (BioAssay System, Hayward, CA) were used to determine the ALP activity and calcium content, respectively.

9.2.7 Gene Expression

MC3T3-E1 cells cultured on the samples for 14 days were rinsed with PBS twice and the RNA was isolated from cells using an RNeasy Mini Kit (Oiagen, Valencia, CA), followed by cDNA synthesis using a cDNA synthesis kit (Thermo Scientific). The expression levels of integrin subunits, α_1, α_2, and β_1 in cells cultured for 1 day and OCN, ALP, and OPN in cells cultured for 14 days, as well as the house-keeping gene glyceraldehyde 3-phosphate dehydrogenase (GAPDH), were quantified through real time polymerase chain reaction (PCR) and determined on a thermal cycler with fluorescence detection systems (PTC-200, MJ Research) using a Power SYBR® Green PCR Master Mix (Applied Biosystems, Carlsbad, CA)**.**

9.2.8 Statistical Analysis

Cell culture was conducted in quadruplicates for each group and each time point. All values were expressed as mean ± standard deviation. The statistical significance ($p < 0.05$ or < 0.01) in the differences between groups was determined using student's *t*-test.

9.3 Results and Discussion

In general, the stress-strain curve of a semi-crystalline polymer has three typical regions, i.e., elastic region before the yield point, cold-drawing region in which polymer chains are highly aligned, and strain-hardening region. As shown in Figure 9.1a, the original PCL sample presented this typical stress-strain curve and the cold-drawing stage followed a yield point at the strain of ~40% and ended at the strain of ~800%. The strain-hardening stage appeared before polymer fracture at the strain of ~1000%. For the original PCL, the Young's modulus, tensile stress, and elongation at break were determined to be 323 ± 19 MPa, 24 ± 4 MPa, and 1007 ± 59%, respectively. The 600% uniaxially stretched PCL films, i.e., S600, showed a higher Young's modulus of 547 ± 34 MPa and a higher tensile stress of 98 ± 8 MPa, but a much lower elongation at break of 39 ± 6%. Because of the highly aligned polymer chains along the drawing direction, S1000 samples displayed highly improved Young's modulus of 1287 ± 85 MPa and tensile stress of 175 ± 17 MPa, but an even lower elongation at break of 8 ± 2%. Polymer chains in biaxially stretched (BS) films were aligned in multiple directions and thus they had to go through realignment in single-direction tensile testing and did not show significantly improved tensile strength, as shown in Figure 9.1a. The Young's modulus, tensile stress, and elongation at break of the BS sample were measured to be 359 ± 42

MPa, 43 ± 5 MPa, and 98 ± 13%, respectively. Figure 9.1b shows the enlarged region at strain of 0-30% in the representative stress-strain curves of original, S600, S1000, and BS samples to indicate the distinct Young's moduli among these samples.

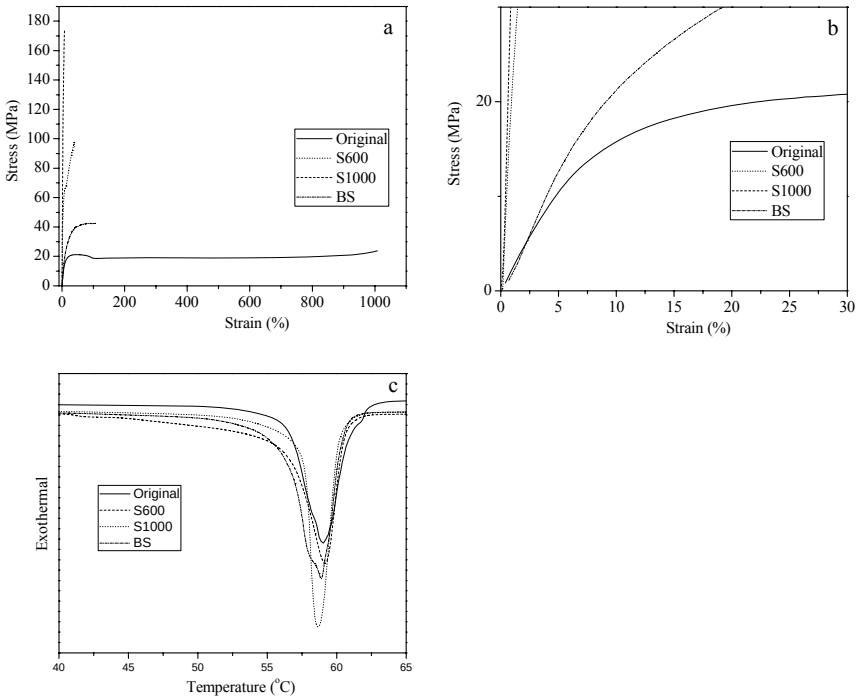

Figure 9.1 (a) Representative stress-strain curves of PCL samples. (b) Representative stress-strain curves of PCL samples at low strain region. (c) DSC curves of PCL samples

The DSC curves of the PCL samples used to determine their thermal properties are demonstrated in Figure 9.1c. The melting points of original, S600, S1000, and BS samples were measured to be 59.2, 58.7, 58.3, and 58.9 °C, respectively. On the basis of the heat of fusion (ΔH_m) obtained from the DSC curves, the crystallinity was calculated by dividing ΔH_m by ΔH_m^0, which is the value of 135 J/g for 100% crystalline PCL. The crystallinities of original, S600, S1000, and BS samples were calculated to be 68%, 62%, 61%, and 62%, respectively. These results indicated that stretching did not significantly

alter the crystallinity and melting point of PCL. Melting of a semi-crystalline polymer is a first-order phase transition, which is discontinuous. In melting, polymer chains well folded in crystallites gradually appear in the disordered state. The whole process absorbs heat energy to obtain the freely extended chains in the melt. Polymer stretching lowers the folding extent of those polymer chains and aligns them in a specific direction, which may in turn decrease ΔH_m slightly. However, the crystallinities of the stretched PCL samples did not change significantly compared with original samples, as also found in a previous report [7]. The effect of drawing on the melting point for orthorhombic unit cell crystal structures, for example, those for PCL and ultra-high-molecular-weight polyethylene (UHMWPE), was studied and larger and thicker lamellas formed in drawing to induce higher melting points [7,13]. In contrast, we found that the drawing decreased the melting point of PCL slightly. The discrepancy might be caused by the difference in the drawing extent between the previous studies and ours. For example, the biaxially drawing ratio of 3 × 3 applied to PCL in the previous study was lower than our present value of 4 × 4. A higher drawing ratio causes polymer chain alignment instead of formation of larger and thicker lamellas and thus it may decrease the melting point of the polymer. In the literature study, biaxially stretched PCL and UHMWPE also showed a broader melting peak, suggesting that the lamellas were broken and the lamellar size distribution widened. Our DSC curves of S600 and BS showed the same trend but S1000 had an even narrower melting peak compared with original PCL because the highly aligned polymer chains might have extremely narrow chain arrangement rather than wider lamella size distribution.

Biaxially stretched PCL films fabricated at a drawing ratio of 2.5 × 2.5 were reported to show fibril morphology aligned along the drawing direction[9]. Consistently, the S600 PCL sample here also displayed oriented fibril-like view along the stretching direction, as demonstrated in the SEM images in Figure 9.2. In contrast, the original and BS PCL films showed a regular, smooth surface while the S1000 sample displayed fine fibril-like view.

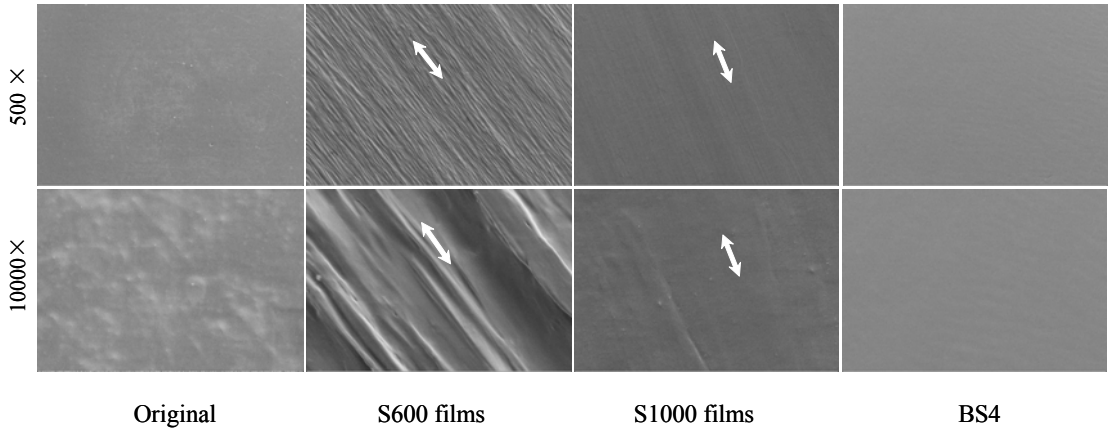

Figure 9.2 SEM images of PCL samples. Top row: ×500; bottom row: ×10000

The polymer lamellae attach the substrates in two ways which are flat-on and edge-on [14, 15]. In case of flat-on arrangement, the chain folds of the lamellae cover the substrate surface, whereas the lateral surface of the lamellae covers the substrate surface in edge-on arrangement. Chain folds are normally considered as amorphous or quasi-amorphous state and the lateral surface is believed to be crystalline state. Thus, polymer lamellae are anisotropic units. However, the lamellae do not show preference in orientation in bulk or films with large thickness. Consequently, the bulk and thick films illustrate isotropic arrangement of polymer lamellae. The feasible method to control the

arrangement of polymer lamellae on substrates is to tune the film thickness in which polymer lamellae are formed. When the film thickness is comparable to the lamellar thickness, the free rotation of lamellae is inhibited and the lamellae exist with the surface of chain folds parallel to the substrate, namely, the flat-on lamellae are formed. In the other situation in which the film thickness is much larger than lamellar thickness, the surface of the lateral surface parallel to the substrate surface is induced, namely, edge-on lamellae. Normally, the larger the film thickness is, the higher the component of edge-on lamellae.

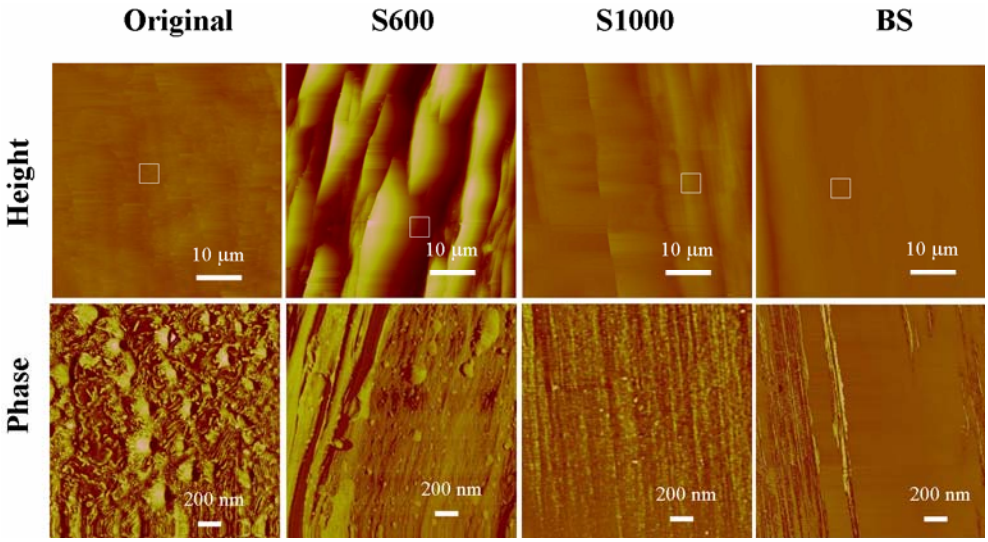

Figure 9.3 AFM images of PCL samples. Top row: height images; bottom row: phase images corresponding to the square in the top row.

As shown in the AFM phase image in Figure 9.3, the surface of the original PCL sample was covered with both flat-on and edge-on lamellae. The fibril-like structure was the feature of edge-on lamellae, while the rest part was flat-on lamellae. As observed in SEM images, the AFM images of the S600 film also showed that drawing generated

groove-like structure on the surface and the groove depth determined from the height profile was ~1.5 μm and the widths of both the valleys and ridges were irregular in the range of 5~10 μm. Also consistent with the SEM images, the AFM images of S1000 films showed a fine fibril-like structure aligned by drawing. The AFM images of the BS film also showed slight fibril-like topography, similar to a previous report [9]. Overall, the edge-on lamellar view disappeared due to the alignment in S600, S1000, and BS films.

MC3T3-E1 cell adhesion was evaluated using three different methods, characterization of FAs, SEM, and integrin expression [16,17]. FAs are the closest contacts between cells and substrates, shown as green spots in Figure 9.4a. FAs were larger and denser on the S1000 and BS films than on the original and S600 ones. The FAs on the S1000 and BS films were strongly oriented, whereas those on the original and S600 films were almost round. MC3T3-E1 cell morphology was also highly influenced by the underlying substrates. Cells on the S600 film were prominently aligned along the stretching direction, while those on the original and S1000 films spread randomly without showing a preferential direction. The cells on S1000 films had a much larger spread area and much better stress fibers compared with those on the original and S600 films, and the cells on the BS film were between them. The SEM images in Figure 9.4b further provided insight into the interaction between the cells and the substrates. The cells on the original and S600 films were thicker and had fewer filopodia extending from cell body. However, in comparison with the cells on original films, the cells on the S600 film were clearly aligned along the stretching direction either in the valley or on the ridges, as also found in Figure 9.4a. The cells on the S1000 and BS films were much thinner, indicating much better spreading, than those on the original and S600 films. In addition to good

spreading, cells on the S1000 film also showed more filopodia compared with those on BS films.

The FAs were also quantified from vinculin-stained cells in Figure 9.4a using ImageJ and the results are shown in Figure 9.4c. FAs on the S1000 film had a significantly larger area than those on the original and S600 films, while those on the BS film were also larger than the latter two but the difference was not significant. The density of FAs, which is defined as the number of FAs per cell, was significantly higher on the S1000 and BS films than on the original and S600 films, and the value on the S1000 film was even higher than on the BS film. The circularity, defined using the equation of $4\pi \times \text{area/perimeter}^2$, of FAs on the S1000 film was significantly smaller than on the other films, showing better alignment of FAs. FAs provide sites to activate intracellular signaling molecules, for example, focal adhesion kinase (FAK) and extracellular signal-regulated kinase (ERK1/2), and they are regulated by transmembrane integrins, which are critical in the communications between ECM proteins and the nucleus [18,19]. Hence, cell adhesion can be characterized by the integrin expression. Figure 4d shows the expression levels of integrin subunits α_1, α_2, and β_1 relative to that of GAPDH. The relative expression levels for all these three subunits were significantly larger on the S1000 and BS films than on the original and S600 films, and they were much better on the S1000 film than on the BS film.

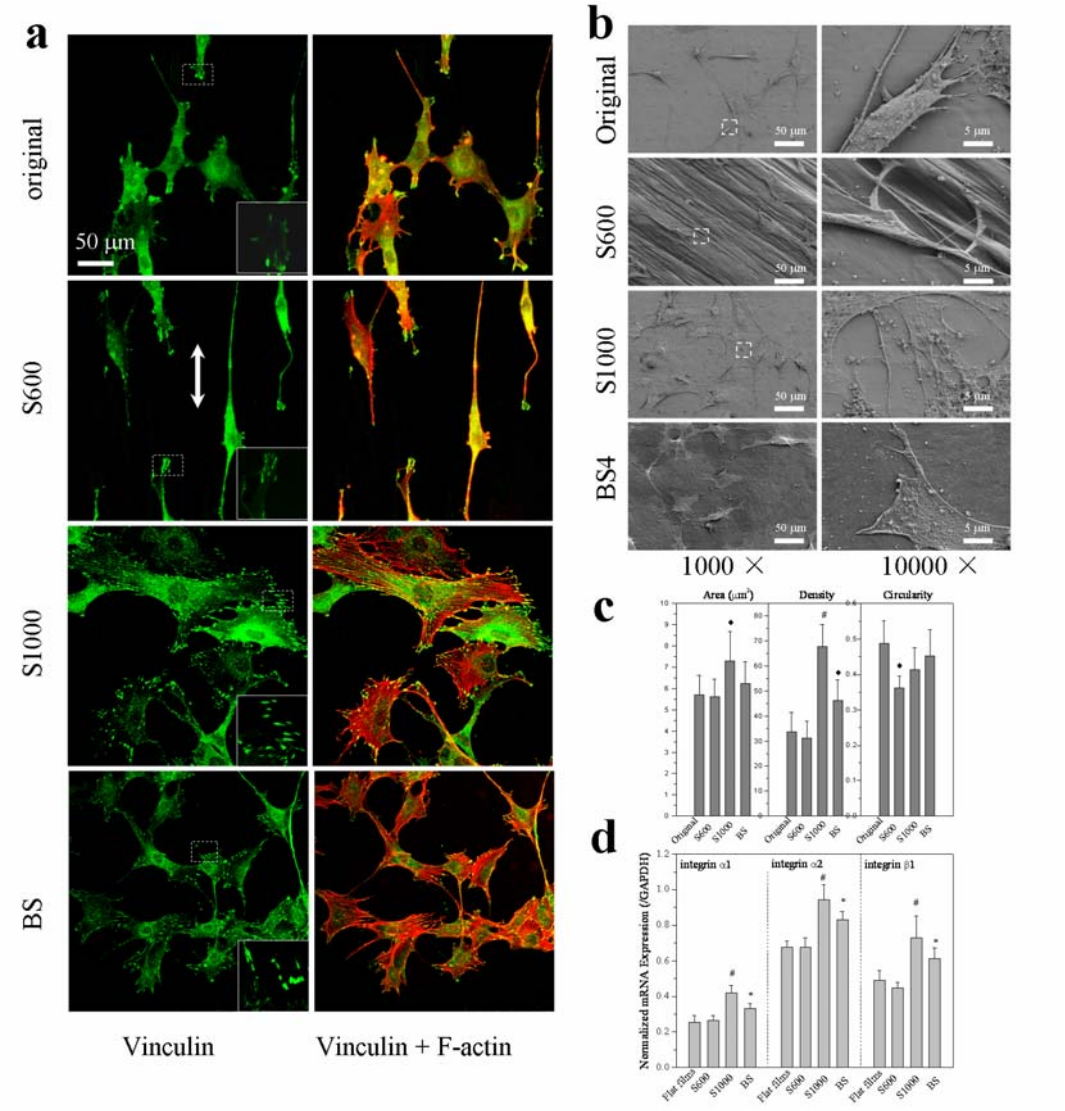

Figure 9.4 MC3T3-E1 cell adhesion on the original, S600, S1000, and BS PCL samples. (a) Vinculin-stained images (green, left column) and merged images of cells stained with rhodamine-phalloidin (red) and vinculin (right column). White arrow indicates the stretching direction. (b) SEM images (day 1) at magnifications of ×1000 (left column) and ×10000 (right column). (c) Density, area, and elongation of FAs. (d) Relative expression of integrin subunits of α_1, α_2, and β_1 at day 1. *: $p < 0.05$; #: $p < 0.01$ relative to the original samples.

The optimal environment for MC3T3-E1 cell attachment, proliferation, and mineralization should be similar to the *in vivo* bone tissue that provides appropriate topographical, chemical, and mechanical factors. During the interaction between cells

and substrates, the contractile forces generated by the cross-bridging interactions of actin and myosin filaments can be transmitted to the substrates and exert mechanical impact on the substrate. The substrate, in turn, is resistant to this impact, which leads to the adjustment of cells in adhesions and cytoskeleton. Stretching enhanced the mechanical strength of the PCL film and thus the stretched PCL films with increased stiffnesses, in particular, the S1000 and BS films, promoted MC3T3-E1 cell functions.

In addition to substrate stiffness, substrate topography was also involved in affecting MC3T3-E1 cell adhesion, attachment, spreading, proliferation, and differentiation via "contact guidance" in this study [1,20-23], as the fibril-like structure on the S600 and S1000 films were like grooves. In contact guidance, micron-sized FAs bridge cells and substrates closely and can be aligned on groove ridges when the grooves are comparable to or smaller than FAs, and subsequently the cell actin filaments are also aligned. [16,17]. On the other hand, ECM protein absorption is also influenced by grooves and such preferred ECM protein distribution was found to affect FA distribution and cell alignment [24]. Our previous research showed that MC3T3-E1 cells were aligned on photocured polymer substrates with 7.5 μm-wide and 1 or 10 μm-deep microgrooves, while they could not sense the surface roughness and topography when the grooves were wider than 5 μm and shallower than 1 μm [25]. Consistent with the previous report, Figures 9.4a,b showed that the cytoplasm was strongly aligned along the stretching direction on the S600 film, which had a groove-like structure with the groove depth of ~1.5 μm and width of 5~10 μm.

The effect of groove dimension on osteoblasts can occur when the groove size is at the nanometer scale. Osteoblastic cytoplasm and F-actin filaments were found to be

aligned when the groove width was 75-150 nm and depth was as small as 33 nm, which were comparable to the dimension of bone ECM [20,26,27]. FAs were also reported to be oriented along the groove direction [28]. In this study, the S1000 and BS films were similar to nanoscale grooves with a width of ~50 nm and a depth of ~10 nm. However, cells on the S1000 and BS films did not show clear alignment of cytoplasm and FAs along the stretching direction, which can be explained by the irregular and discontinuous ridges and valleys and low aspect ratio of the grooves defined by the ratio of depth to width.

MC3T3-E1 cell attachment and proliferation on the PCL films were also studied using MTS assay and fluorescence images, as shown in Figure 9.5. The fluorescence images demonstrated that cells had higher densities on the S1000 and BS films than on the S600 and original films and the value on the S1000 film was the highest. Cells were aligned along the stretching direction on the S600 film, as also shown in Figure 9.4a,b. As shown in Figure 9.5b, cell attachment represented using the cell numbers obtained at 4 h post-seeding was significantly higher on the S1000 film than on the other films and it was slightly higher on the BS film than on the original and S600 films. Figure 9.5c shows that cells proliferated much better on the S1000 film than on the others at all time points and the difference became larger when the culture time was longer. At days 1 and 2, there were no significant differences observed among the original, S600, and BS films, although cells on the BS film showed slightly better proliferation and eventually had a significantly higher number at day 4. As discussed earlier, the cell attachment and proliferation results should be ascribed to the consequences of cell adhesion [29].

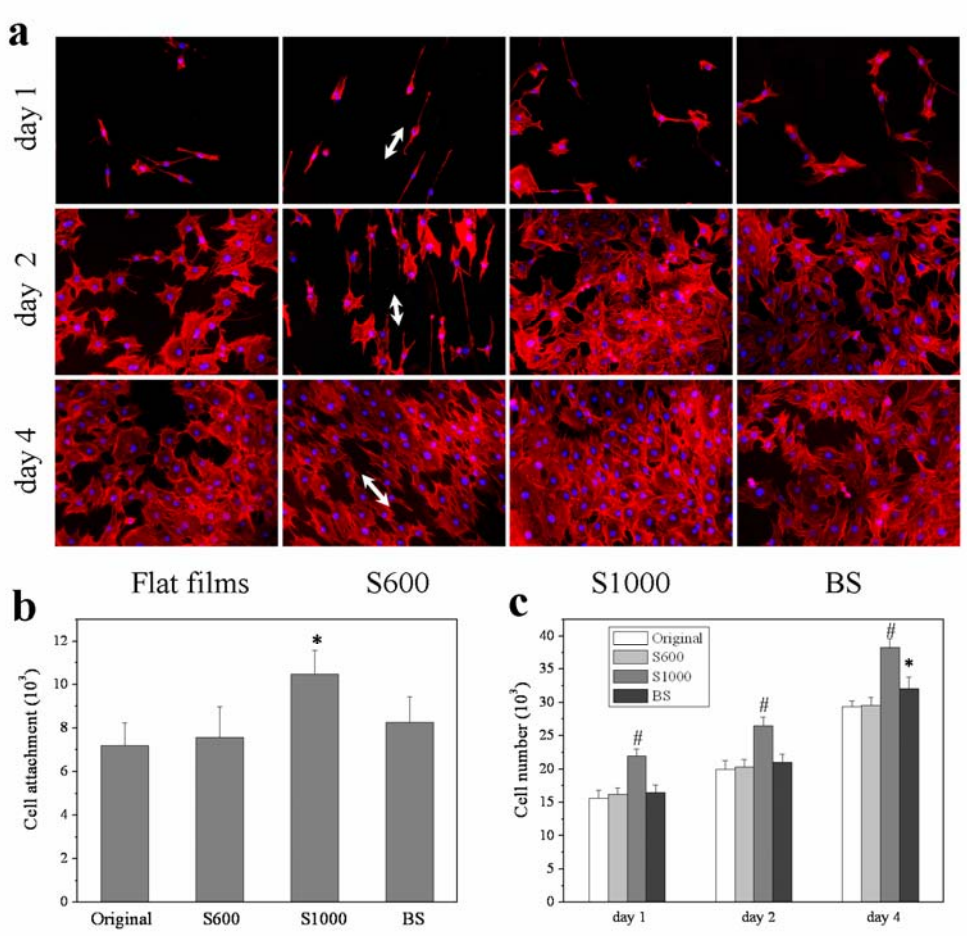

Figure 9.5 (a) Fluorescence images of MC3T3-E1 cells stained with rhodamine-phalloidin (red) and DAPI (blue) at day 1, 2, and 4. The white arrow indicates the stretching direction. (b) Cell attachment represented by the cell number determined by MTS assay at 4 h. (c) Cell proliferation represented by the cell numbers at day 1, 2, and 4. *: $p < 0.05$ relative to original and S600 samples; #: $p < 0.01$ relative to original, S600, and BS samples.

DAPI-stained MC3T3-E1 cell nuclei at day 1 post-seeding were analyzed in terms of shape and area using ImageJ, as shown in Figure 9.6. Cell nuclei on the original, S1000, and BS films had a regular round shape, whereas those on the S600 film were evidently aligned along the stretching direction. In addition, cell nuclei on the S1000 and BS films were distorted and had a larger size compared with those on the original one.

The cell nuclear area decreased from 171 ± 20 μm^2 on the original film to 119 ± 21 μm^2 on the S600 film. The value increased to 248 ± 36 and 260 ± 27 μm^2 on the S1000 and BS films, respectively. The nuclear circularity was determined to be 0.92 ± 0.03, 0.80 ± 0.05, 0.91 ± 0.02, and 0.92 ± 0.02 on the original, S600, S1000, and BS films, respectively. As the cytoskeleton and actin was aligned along the stretching direction for the S600 film (Figure 9.5a), the intermediate filaments sensed the force from the alignment and further transferred the force to deform nuclei through the mechanical signal transfer pathway [30-32]. Following the similar mechanism, better cell spreading on the S1000 and BS films induced nuclear expansion.

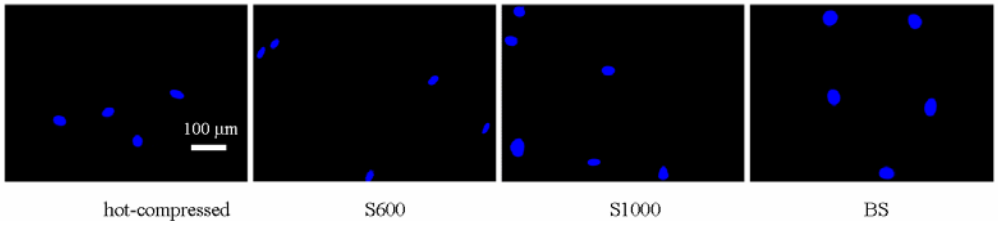

Figure 9.6 MC3T3-E1 cell nuclei stained with DAPI at day 1 post-seeding on the hot-compressed and stretched films.

MC3T3-E1 cell mineralization was evaluated at day 14 using ALP activity, calcium content, and expression levels of three osteoblastic gene markers, i.e., ALP, OCN, and OPN. As shown in Figure 9.7a, the ALP activity and calcium content of the cells on the S1000 and S600 films were significantly better than on the original and BS films, and the values on the S1000 film were the highest. Figure 9.7b shows that the cells on the S1000 film had much higher expression levels for ALP, OCN, and OPN than others, and in turn, cells on the S600 and BS films had significantly higher values than on

the original film. Because the S1000 film supported cell adhesion and proliferation better than other samples, it should also support better mineralization. Intriguingly, the cell adhesion and proliferation on the S600 film were similar to those on the original film and even poorer than on the BS film, but the S600 film resulted in better mineralization of the cells than the other two. This result can be interpreted using the effect of microgrooves on MC3T3-E1 cell functions. First, the distortion of actin filaments and nuclei could induce release of calcium ions from perinuclear space via the mechanotransduction pathway and the calcium ions further promoted MC3T3-E1 cell mineralization and gene expression [33-35]. The microgrooves also provide a microenvironment to condense regulatory factors to reach the critical concentrations, beyond which calcified tissue formation can be fostered [36]. The ALP activity and calcification of MC3T3-E1 cells were promoted on microgrooved $CaCO_3$ substrates of than on the flat one, and the 5 μm-wide microgrooves induced better differentiation than the 10 μm-wide ones [12]. In another report, photocured polymer microgrooved substrates with a fixed depth of 10 μm and different groove widths of 7.5, 16.1, 44.2, and 91.2 μm were used to regulate MC3T3-E1 cell functions and higher mineral deposition and better OCN expression were observed,[25] consistent with the results in the present study.

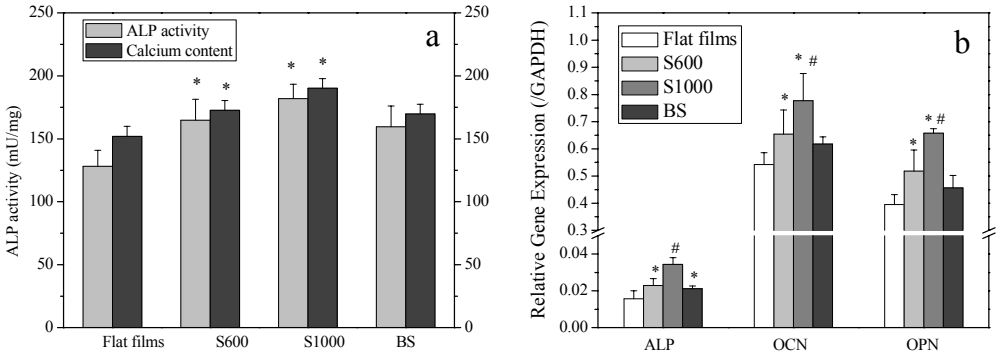

Figure 9.7 (a) ALP activity and Calcium content of MC3T3-E1 cells at day 14. *: $p < 0.05$ relative to the original and BS samples. (b) Relative gene expression levels of ALP, OCN, and OPN to GAPDH determined by real time PCR. *: $p < 0.05$ relative to original samples; #: $p < 0.01$

9.4 Conclusions

Uniaxially and biaxially stretched PCL films were prepared. The S600 film showed an evident groove-like view along the stretching direction while the S1000 and BS films showed a fibril-like view. Stretching enhanced the substrate stiffness dramatically, especially for the S1000 film, but did not alter their thermal properties significantly. The S1000 and BS films, especially the S1000 one, promoted mouse MC3T3-E1 cell adhesion, attachment, proliferation, and mineralization, than the original film. The S600 film did not promote MC3T3-E1 cell attachment and proliferation but enhanced its differentiation because of the groove-like topography compared with the original film.

References

[1] Anselme, K.; Bigerelle, M. *Int. Mater. Rev.* **2011**, *56*, 243.

[2] Bukoreshtliev, N. V.; Haase, K.; Pelling, A. E. *Cell Tissue Res.* **2013**, *352*, 77.

[3] Wong, J. Y.; Leach, J. B.; Brown, X. Q. *Surf. Sci.* **2004**, *570*, 119.

[4] Cai, L.; Wang, S. *Polymer* **2010**, *51*, 164.

[5] Wang, K.; Cai, L.; Jesse, S.; Wang, S. *Langmuir* **2012**, *28*, 4382.

[6] Cheng, Z.; Teoh, S. H. *Biomaterials* **2004**, *25*, 1991.

[7] Ng, C. S.; Teoh, S. H.; Chung, T. S.; Hutmacher, D. W. *Polymer* **2000**, *41*, 5855.

[8] Tan, P. S.; Teoh, S. H. *Mater. Sci. Eng. C* **2007**, *27*, 304.

[9] Ang, L. P. K.; Cheng, Z. Y.; Beuerman, R. W.; Teoh, S. H.; Zhu, X.; Tan, D. T. H. *Invest. Ophth. Vis. Sci.* **2006**, *47*, 105.

[10] Tiaw, K. S.; Teoh, S. H.; Chen, R.; Hong, M. H. *Biomacromolecules* **2007**, *8*, 807.

[11] Wu, X.; Wang, S. *ACS Appl. Mater. Interfaces* **2012**, *4*, 4966.

[12] Wu, X.; Wang, S. *Adv. Healthcare Mater.* **2013**, *2*, 326.

[13] Sakai, Y.; Miyasaka, K. *Polymer* **1990**, *31*, 51.

[14] Cheung, Z. L.; Ng, K. M.; Weng, L. T.; Chan, C. M.; Li, L. *Polymer* **2006**, *47*, 3164.

[15] Cheung, Z. L.; Weng, L. T.; Chan, C. M.; Hou, W. M.; Li, L. *Langmuir* **2005**, *21*, 7968.

[16] Biggs, M. J. P.; Dalby, M. J. *P. I. Mech. Eng. H* **2010**, *224*, 1441.

[17] Geiger, B.; Spatz, J. P.; Bershadsky, A. D. *Nature Rev.* **2009**, *10*, 21.

[18] Kim, M. H.; Kino-oka, M.; Taya, M. *Biotechnol. Adv.* **2010**, *28*, 7.

[19] Dalby, M. J. *Med. Eng. Phys.* **2005**, *27*, 730.

[20] Bettinger, C. J.; Langer, R.; Borenstein, J. T. *Angew. Chem., Int. Ed.* **2009**, *48*, 5406.

[21] Flemming, R. G.; Murphy, C. J.; Abrams, G. A.; Goodman, S. L.; Nealey, P. F. *Biomaterials* **1999**, *20*, 573.

[22] Dalby, M. J. *Med. Eng. Phys.* **2005**, *27*, 730.

[23] Tanaka, M. *Biochim. Biophys. Acta* **2011**, *1810*, 251.

[24] Curtis, A.; Wilkinson, C. *Biomaterials* **1997**, *18*, 1573.

[25] Wang, K.; Cai, L.; Zhang, L.; Dong, J. Y.; Wang, S. F. *Adv. Healthcare Mater.* **2012**, *1*, 292.

[26] Anselme, K.; Davidson, P.; Popa, A. M.; Giazzon, M.; Liley, M.; Ploux, L. *Acta Biomater.* **2010**, *6*, 3824.

[27] Loesberg, W. A.; te Riet, J.; van Delft, F. C. M. J. M.; Schon, P.; Figdor, C. G.; Speller, S.; van Loon, J. J. W. A.; Walboomers, X. F.; Jansen, J. A. *Biomaterials* **2007**, *28*, 3944.

[28] Lamers, E.; Walboomers, X. F.; Domanski, M.; te Riet, J.; van Delft, F. C. M. J. M.; Luttge, R.; Winnubst, L. A. J. A.; Gardeniers, H. J. G. E.; Jansen, J. A. *Biomaterials* **2010**, *31*, 3307.

[29] Anselme, K. *Biomaterials* **2000**, *21*, 667.

[30] Maniotis, A. J.; Chen, C. S.; Ingber, D. E. *Proc. Natl. Acad. Sci. U.S.A.* **1997**, *94*, 849.

[31] Helmke, B. P.; Thakker, D. B.; Goldman, R. D.; Davis, P. F. *Biophys. J.* **2001**, *80*, 184.

[32] Dalby, M. J.; Riehle, M. O.; Yarwood, S. J.; Wilkinson, C. D. W.; Curtis, A. S. G. *Exp. Cell. Res.* **2003**, *284*, 274.

[33] Relan, N. K.; Yang, Y.; Beqaj, S.; Miner, J. H.; Schuger, J. *Cell. Biol.* **1999**, *147*, 1341.

[34] Itano, N.; Okamoto, S.; Zhang, D.; Lipton, S. A.; Ruoslahti, E. *Proc. Natl. Sci. U.S.A.* **2003**, *100*, 5181.

[35] Thomas, C. H.; Collier, J. H.; Sfeir, C. S.; Healy, K. E. *Proc. Natl. Sci. U.S.A.* **2002**, *99*, 1972.

[36] Chehroudi, B.; Ratkay, J.; Brunette, D. M. *Cell. Mater.* **1992**, *2*, 89.

CHAPTER X
BANDED SPHERULITES OF POLY(ε-CAPROLACTONE) AND POLY(3-HYDROXYBUTYRATE) FOR REGULATING PC12 CELL ATTACHMENT, PROLIFERATION, AND DIFFERENTIATION

10.1 Introduction

To facilitate peripheral and center nerve regeneration, researchers have been developing novel and advanced nerve guides to promote nerve cell growth, guide the growth of axons, and provide neurotrophic or cellular support *in vivo*. Understanding nerve cell-material interactions is critical in design novel biomaterials for fabricating these nerve guides. Cells can respond to the surface chemistry, topography, and mechanical properties of the underlying substrates and implants.[1-3] Thus a desirable nerve guide should combine optimized physicochemical and structural factors together to obtain the best regenerative capacity.

In cell-material interactions, focal adhesions (FAs) in cells are critical as they are protein complexes to connect the internal cytoskeleton to the extracellular matrix (ECM).[4-7] FAs also play an essential role in neuronal differentiation because neurite initiation and extension depend on the formation and stabilization of FAs.[8-10] FAs can sense the topography of a substrate or implant and coordinate morphometric changes to induce cell polarity, long cellular protrusions, and neuronal differentiation.[10,11] The emerging neuritis from neuronal cells grow and extend towards specific direction, which is known as neurite pathfinding.[12] This topographical guidance is a means to regulate nerve cell migration and polarization. Thus biomaterial substrates or nerve guides with

specific topographical features, such as nanogratings,[8,13] nanoparticles,[14] and nanowires,[15] have been developed for fostering nerve regeneration.

Because of the reversible adoption of neuronal characteristics upon exposure to nerve growth factor (NGF), PC12 cells are widely used to study nerve cell communication, differentiation, and neurite outgrowth *in vitro*.[16] Previously our research group reported fabrication of microgrooved substrates made from photocrosslinked poly(ε-caprolactone) triacrylates (PCLTAs) with various microgroove dimensions (depths of 0.4-12 μm, widths of 5-90 μm) via replica molding from silicon wafers with parallel microgrooves.[17] PC12 cells cultured on these microgrooved polymer substrates were aligned strongly in all microgrooves and the cells exposed to NGF had more prominent neurite outgrowth along groove direction. Meanwhile, PC12 cells were highly sensitive to the groove features and neurite outgrowth was enhanced on microgrooved substrates than on the flat one, especially when the grooves were narrower and shallower. PC12 cell differentiation was performed on nanogratings (linewidths of 500-750 nm, depths of 200-250 nm) prepared using nanoimprint lithography and nanogratings were found to efficiently induce bipolar cells with decreased migration speed and neurite length.[8]

Poly(ε-caprolactone) (PCL) is a well studied biodegradable, semi-crystalline polymer with a low glass transition temperature (T_g) of ~-60 °C and a melting temperature (T_m) of 20-60 °C, depending on its molecular weight.[18] Our research group reported that mouse pre-osteoblastic MC3T3-E1 cell attachment and proliferation were higher on the rougher surface of PCL banded spherulites, compared with those on non-banded and hot-compressed PCL films.[19] In contrast, MC3T3-E1 cell attachment

and proliferation were lower on rougher spherulitic surfaces of poly(L-lactide) (PLLA) than on the amorphous one prepared from quenching the melt.[20,21] Because PLLA has a higher T_g of ~60 °C than that of PCL, we speculated that the different MC3T3-E1 responses to PLLA and PCL spherulitc surfaces might be attributed to their flexibility and chain mobility at the cell culture temperature of 37 °C. PC12 cells were reported to respond to different substrate stiffnesses by having greater neurite extension on a softer one.[22,23] To obtain a good understanding about how polymer crystalline surfaces affect cell behavior, we deliberately selected two semi-crystalline biomaterials that can readily form banded and non-banded spherulites but with distinct thermal and mechanical properties to conduct PC12 cell study. One of them is PCL as a relatively softer substrate while the other one, poly(3-hydroxybutyrate) (PHB), a bioderived and biodegradable polyester with a T_g of ~0 °C and a high T_m of 175 °C, was used as a relatively more rigid one. In addition, how PC12 cells respond to circular microgrooves has not been reported to date. In this report, we address these issues by conducting PC12 cell studies on PCL and PHB substrates, including banded and non-banded spherulitic surfaces and hot-compressed smooth surfaces.

10.2 Experimental Section

10.2.1 Materials

PCL was synthesized through ring-opening polymerization of ε-caprolactone in the presence of initiator water in our lab. Using gel permeation chromatography (GPC, PL-GPC120, Polymer Laboratories) with polystyrene standard samples (Polymer

Laboratories) for calibration and THF as the eluent, the number-average molecular weight and weight-average molecular weight of PCL were determined to be 77350 and 142660 g mol^{-1}, respectively. PHB was purchased from Sigma-Aldrich (Milwaukee, WI) and used as received.

10.2.2 Sample Preparation

PCL was dissolved in methylene chloride (CH_2Cl_2) at 0.1 g mL^{-1}. Three hundred microlitters of PCL solution was spin-coated onto a round glass coverslip (15 mm, diameter) using a single-wafer spin processor (Laurell Technologies, North Wales, PA) at a spin rate of 1000 rpm for 30 s at room temperature. After the PCL films on coverslips were dried completely in vacuum, they were melted at 80 °C for 10 min and then transferred to a hot stage with a preset crystallization temperature. PHB films were prepared by drop-casting 60 μL PHB solution in chloroform ($CHCl_3$) (0.1 g mL^{-1}) directly on round glass coverslips. After being completely dried in vacuum, PHB films were melted at 190 °C for 10 min and then quickly transferred to a hot stage with a preset crystallization temperature. Flat films of PCL and PHB as the control groups were prepared by compressing their melts between two glass slides and cooled down to room temperature.

10.2.3 Surface Characterizations

The crystalline structures of the polymer films were observed using -polarized optical microscopy (POM). The surface morphologies of the polymer films were detected using a multimode atomic force microscope (AFM) with a Nanoscope V control system (Veeco Instruments, Santa Barbara, CA). A tapping mode over a scan area of 100 μm

×100 μm and 50 μm ×50 μm was used for PCL and PHB films, respectively. Root-mean-square roughness (R_{rms}) was measured from the height AFM images using the WSxM 4.0 software (Nanotec. Electronica S.L.).

10.2.4 In vitro PC12 Cell Attachment, Proliferation, and Differentiation

Prior to cell studies, the polymer films were immersed in 70% alcohol solution for 30 min for cleaning, rinsed in 70% alcohol solution again for 10 min twice for sterilization, and completely dried in vacuum. Rat PC12 cells (CRL-1721, ATCC, Manassas, VA) were cultured in a growth medium composed of F-12K media (Gibco, Grand Island, NY), 5% fetal bovine serum (FBS, Gibco), 15% horse serum, and 1% penicillin/streptomycin (Gibco) in a cell incubator with 5% CO_2 and 95% relative humidity at 37 °C. PC12 cells were seeded on the sterilized PCL and PHB films at a density of ~14000 cells per cm^2 and cultured in incubator for 4 h and 1, 4, and 7 days. Cell numbers were quantified using a colorimetric cell metabolic assay (CellTiter 96 Aqueous One Solution, Promega, Madison, WI), on the basis of a standard curve that correlated the number of viable cells to the UV absorbance at 490 nm measured using a microplate reader (SpectraMax Plus 384, Molecular Devices, Sunnyvale, CA). To conduct PC12 cell differentiation, they were cultured in a growth medium replenished with 50 ng mL^{-1} NGF for 7 days. After cell culture, the medium was removed and PBS was used twice to remove unattached cells and medium residue. The attached cells were fixed using 4% paraformaldehyde (PFA) solution for 30 min, rinsed with PBS twice, and permeabilized with 0.2% Triton X-100 solution. The fixed cells were stained with rhodamine-phalloidin (RP) for 1 h at 37 °C in a cell incubator and then diamidino-2-

phenylindole (DAPI) at room temperature. The stained cells were photographed using an Axiovert 25 Zeiss light microscope (Carl Zeiss, Germany). The number of neurites per cell, neurite length, and percentage of differentiation (percentage of cells bearing neurites in entire attached cells) were analyzed from more than 200 non-overlapping cells.

10.2.5 Statistical Analysis

Cell studies were performed in quadruplicates for each group at each time point. All values were expressed as mean ± standard deviation. The statistical significance ($p < 0.05$ or 0.01) in the difference between two groups was obtained using student's *t*-test.

10.3 Results and Discussion

When crystallized from solution or melts, semi-crystalline polymers such as PLLA, PCL, and PHB can form non-banded spherulites, which normally present dark Maltese crosses under a polarized optical microscopy (POM).[24] These three semi-crystalline polymers can also form banded spherulites with alternating dark and bright concentric rings as the result of lamellar twisting during crystal growth when they are isothermally crystallized at a proper temperature.[19,25,26] The concentric rings are ridge-valley structures with a ridge-to-ridge width or spacing that can be influenced by the crystallization temperature and the polymer type.[24] Figure 10.1 shows the POM images of the hot-compressed smooth films, non-banded spherulites, and banded spherulites for both PCL and PHB. The hot-compressed sample of PHB still showed spherulites on the surface while the hot-compressed PCL sample was much smoother. PHB crystallized at 65 °C and PCL crystallized at 37 °C showed typical non-banded

spherulites with small surface features. Banded spherulites were clearly observed on PHB and PCL samples when they were crystallized at higher temperatures of 80 and 53 °C, respectively. The diameter of the banded spherulites was ~150 μm and the ridge-to-ridge widths were 8.5 ± 0.8 and 7.5 ± 0.5 μm for PCL and PHB, respectively.

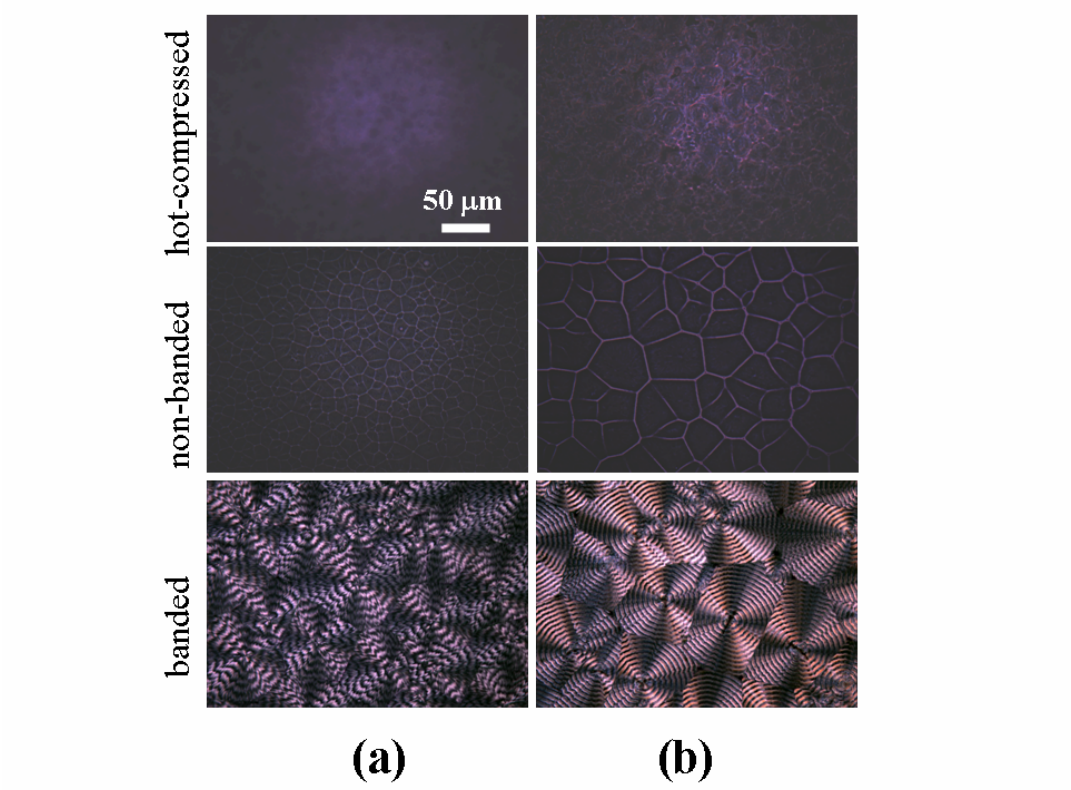

Figure 10.1 POM images of the hot-compressed films, non-banded spherulites, and banded spherulites. (a) PCL and (b) PHB.

The topographies of the polymer samples were also characterized using AFM images, as shown in Figure 2. Hot-compressed PCL and PHB samples had fairly flat surfaces with similar R_{rms} values of 19.4 ± 2.5 and 20.6 ± 2.5 nm, respectively. Non-banded spherulites of both polymers displayed typical lamellar organization radiating

from the center and their R_{rms} values were 43.5 ± 3.4 and 34.5 ± 5.1 nm for PCL and PHB, respectively. Consistent with POM observation, the AFM images of PCL and PHB banded spherulites showed alternating concentric rings along the radial direction. The corresponding depth profiles indicated that the banded spherulites had ridge-to-valley depths of ~200 and ~80 nm for PCL and PHB, respectively. The surfaces of the banded spherulites were rougher and the R_{rms} values were 167.5 ± 8.7 and 68.5 ± 4.3 nm for PCL and PHB, respectively. The increase in R_{rms} was lower for PHB than for PCL was because their shallower valleys.

In general, polymer lamellae are bounded with two types of surfaces: one is the surface covered by chain folds in amorphous or quasi-amorphous state and the other is the lateral surface which is considered as crystalline.[27,28] Although polymer lamellae have anisotropic structures, they are normally randomly distributed in polymer bulk or thick films as isotropic organization. When the polymer film thickness is comparable to lamellar thickness, lamellae in confinement cannot freely rotate and distribute isotropically. The surface of chain folds is parallel to the substrate in ultrathin polymer films and this type of lamellar orientation is called “flat-on”. The other type of lamellar orientation “edge-on” is that the surface of chain folds is perpendicular to the substrate. The surface of regular spherulites with thickness (> 2 μm) much larger than lamellar thickness is generally covered with edge-on lamellae. The AFM phase images of the non-banded spherulites in Figure 10.2 showed that the lamellae were mostly edge-on as the fibril-like structure dominated the whole surface. For banded spherulites, the ridges and valleys alternated periodically with varied thicknesses in these two regions and thus the ridge was sufficiently thick to have random distribution of lamellae and the edge-on

morphology but the thinner valley was composed of the flat-on lamellae. Similar to the literature report,[28] PCL banded spherulites had edge-on lamellae in the ridges and flat-on in the valleys, as shown in Figure 10.2b. Different from the situation in PCL and the previous finding that PHB banded spherulites consisted of circular ridges of edge-on lamellae and valleys of flat-on crystals,[29] PHB banded spherulites in this study only showed fibril-like edge-on lamellae radiating from the spherulite center on both the ridges and the valleys. This discrepancy might be because the valleys in our PHB banded spherulites were not sufficiently thin to generate flat-on lamellae, as evidenced by the very shallow valleys.

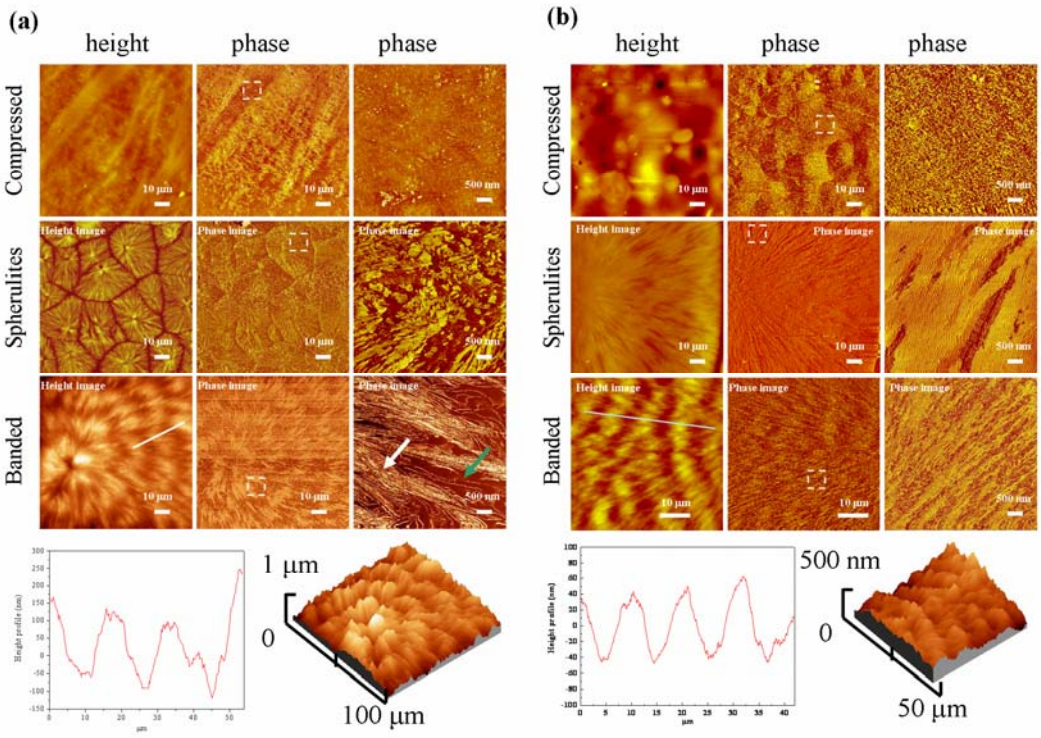

Figure 10.2 AFM height and phase images of the hot-compressed films, non-banded spherulites, and banded spherulites. (a) PCL and (b) PHB.

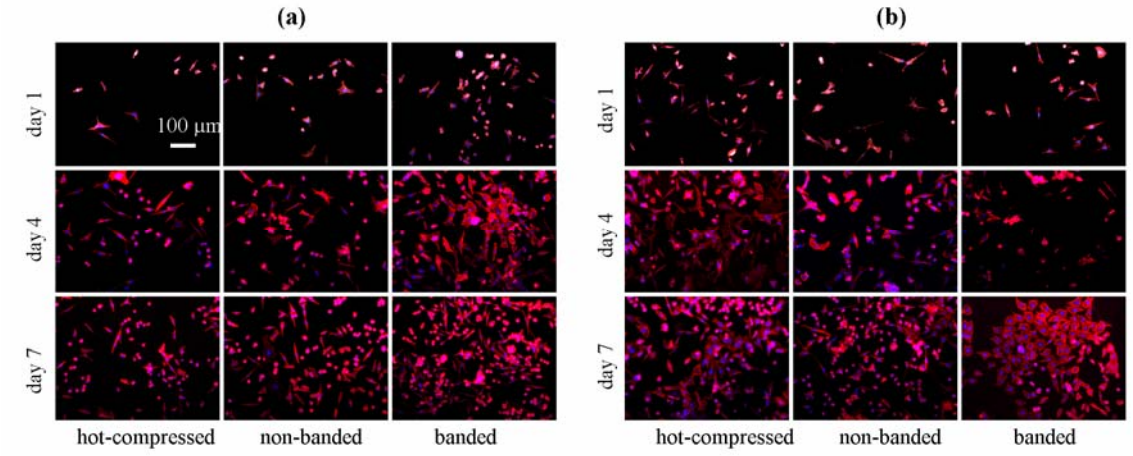

Figure 10.3 Fluorescent images of PC12 cells stained with RP (red) and DAPI (blue) on the hot-compressed films, non-banded spherulites, and banded spherulites at days 1, 2, and 4 post-seeding. (a) PCL and (b) PHB. Scale bar of 100 μm is applicable to all images.

PC12 cells were cultured on the hot-compressed films, banded and non-banded spherulites of PCL and PHB to investigate their response to both materials and topographies. As shown in Figure 10.3a, PC12 cells had a lower density on hot-compressed PCL than on the spherulites and the highest value was found on the banded spherulites at all time points. The opposite trend was found for PHB as PC12 cells preferred to grow on the hot-compressed spherulites while the slowest proliferation occurred on the banded spherulites. This finding agreed with our previous report that MC3T3 cell proliferation was enhanced on rougher spherulites of PCL because the higher surface roughness resultedin higher protein adsorption.[16] As discussed in Introduction, MC3T3-E1 cell proliferation was reported to be lower on the rougher spherulitic surfaces of PLLA compared with its quenched amorphous counterpart.[20,21] The distinct thermal properties such as T_g in PCL and PLLA might be the origin for the different cell responses to their crystalline surfaces. Although PCL is a tough semi-crystalline polymer

with a T_m of 60 °C, it's T_g is as low as ~-60 °C and thus the chain flexibility and mobility are higher at the cell culture condition than those of PLLA with a much higher T_g of ~60 °C.[19] In this study, the T_g (~0 °C), T_m (175 °C) for PHB were both much higher than the values for PCL and thus PHB here could be considered to be equivalent to PLLA in terms of regulating cell behavior using crystalline surfaces, i.e., cell proliferation was also inhibited on the rougher surface. The observation from cell images was further confirmed by the cell numbers at 4 h, days 1, 4, and 7, as shown in Figure 10.4.

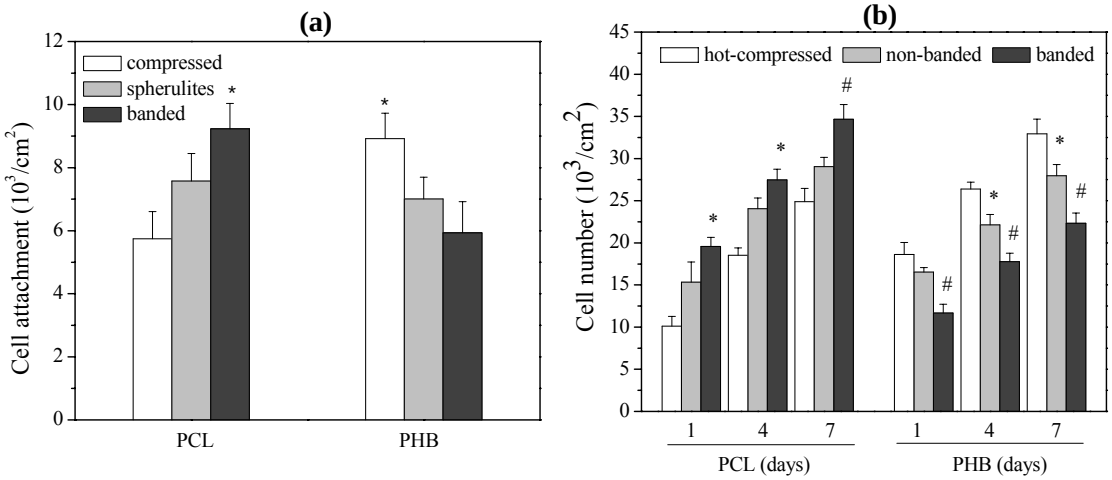

Figure 10.4 (a) PC12 cell attachment indicated by the cell density at 4 h post-seeding on the hotcompressed films, non-banded spherulites, and banded spherulites of PCL and PHB. *: $p < 0.05$ relative to ???. (b) PC12 cell proliferation indicated by cell numbers at days 1, 2, and 4 post-seeding on the hot-compressed films, non-banded spherulites, and banded spherulites of PCL and PHB. *: $p < 0.05$ relative to the banded spherulites and hot-compressed films; #: $p < 0.01$ relative to the banded spherulites.

To demonstrate the effect of banded spherulites on PC12 cell morphology, fluorescent images of the cells at day 1 post-seeding were taken with the background, as shown in Figure 10.5a. PC12 cells did not show alignment on the banded spherulites,

either PCL or PHB. In Figure 10.5b, PC12 cell nuclei did not show evident alignment along any specific direction on the banded spherulites but they indeed preferred to stay in the valleys. The percentages of cell nuclei located in the valleys of the banded spherulites were ~65% and ~70% for PCL and PHB, respectively. According to the literature reports, aligned cytoskeleton can cause distortion of cell nuclei through mechanotransduction as the alignment of actin structure sensitively influences intermediate filaments transferring the applied force from actin struction to nuclei.[9,14,30,31] Because the cytoskeleton spread randomly on the banded spherulites, no clear mechanical signal was transduced to PC12 cell nuclei to generate deformation.

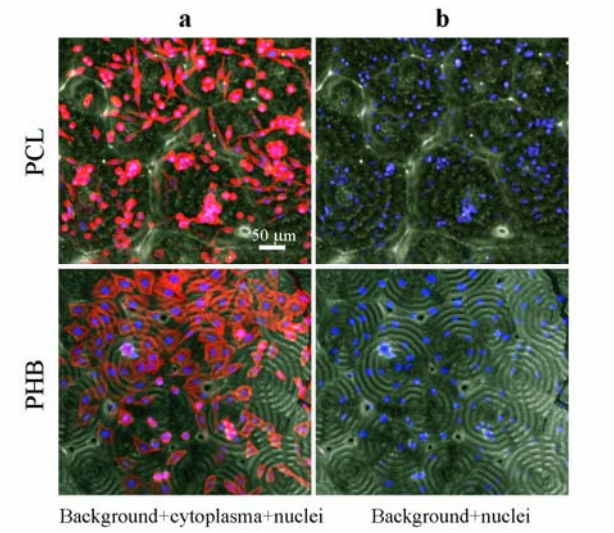

Figure 10.5 PC12 cells (a) stained with RP (red) and DAPI (blue) and their nuclei (b) stained with DAPI (blue) at day 1 post-seeding on the banded spherulites of PCL and PHB.

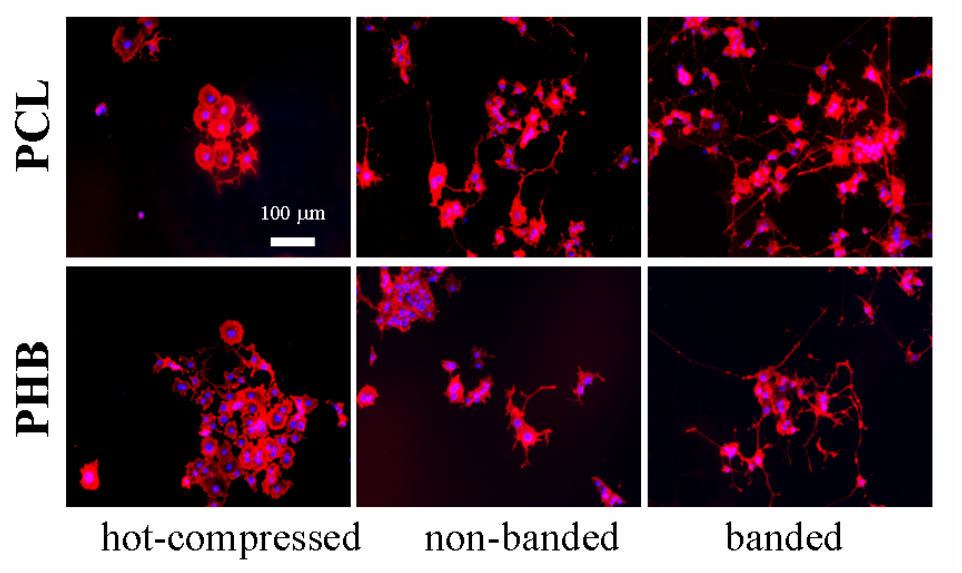

Figure 10.6 Fluorescence images of PC12 cell neurite extension stained with RP (red) and DAPI (blue) after exposure to NGF for 7 days on the hot-compressed samples, non-banded spherulites, and banded spherulites of PCL and PHB. Magnification: × 10. Scale bar of 100 μm is applicable to all the images.

PC12 cell differentiation or neurite extension after the cells were cultured in the presence of NGF for 7 days on the PCL and PHB substrates was investigated using fluorescent images in Figure 10.6. NGF-induced neurite growth was evident on all the samples. The neurites on the hot-compressed samples were few and short. Neurite growth was significantly promoted on the spherulites, in particular, on the banded ones. As demonstrated in the magnified images in Figure 10.7a, PC12 cell neurites on the banded spherulites were dendrites and preferentially followed the ridge or groove direction. The PC12 cell neurites on the samples were analyzed using ImageJ in terms of the number of neurites per cell, the percentage of cells bearing neurites, and the average length per cell, as shown in Figure 10.7b. These three parameters were significantly higher on the spherulites than on the hot-compressed samples, and the best results were on the banded spherulites.

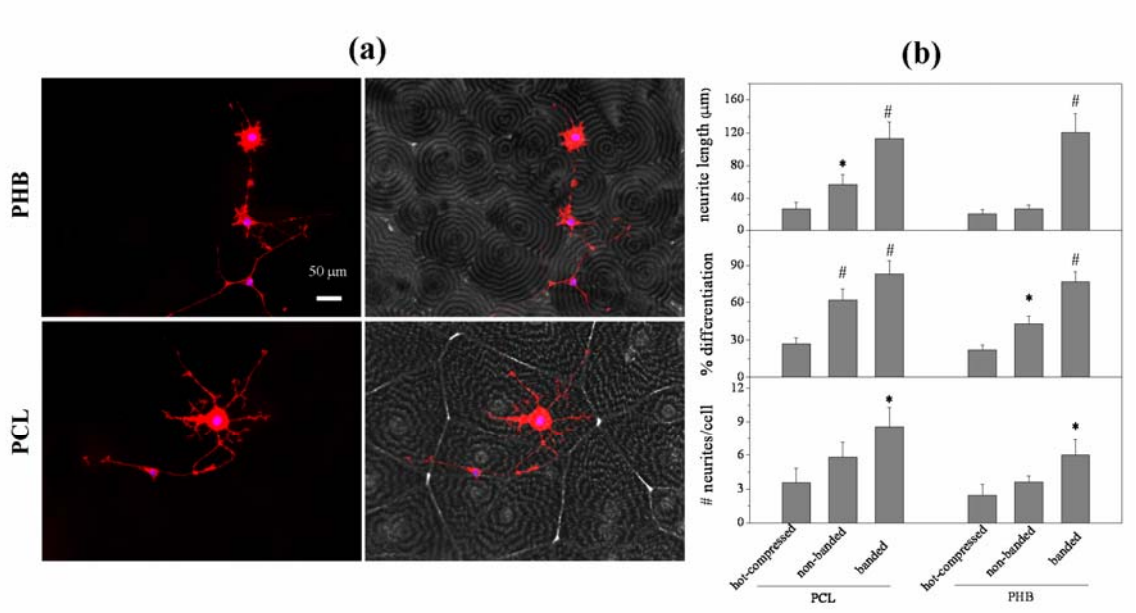

Figure 10.7 (a) Fluorescence images of PC12 cell neurite extension stained with RP (red) and DAPI (blue) after exposure to NGF for 7 days and the distribution of neurite extension on the banded spherulites of PCL and PHB. Magnification: × 20. Scale bar or 50 mm is applicable to all the images. (b) Quantification of PC12 cell neurites on the hot-compressed films, non-banded spherulites, and banded spherulites of PCL and PHB. *: $p < 0.05$ relative to the hot-compressed films; #: $p < 0.01$ relative to the others.

The different neurite outgrowth on the hot-compressed samples and banded and non-banded spherulites was attributed to the surface topographical guidance through pathfinding, in which integrin-based focal adhesions (FAs) play an essential role.[7,8,14,32] The topography of the non-banded spherulites was irregular microgrooves consisting of discontinuous, nanometer-scale small ridges radiating from the spherulite centers. The topography of the banded spherulites was typical circular microgrooves with a groove width of ~10 μm for both polymer and groove depths of ~200 nm and ~80 nm for PCL and PHB, respectively.

FAs, the closest contacts between cells and the substrate surfaces with micron dimension, attended to spread on the ridges in an aligned manner, especially when the

groove dimension was smaller than the FA size, which in turn induced the alignment of actin filaments in the same direction.[33,34] Microgrooves also affect the distribution of ECM proteins on the substrate surface in terms of their composition and conformation.[34] The distinction of ECM proteins along the ridges and valleys caused the preferential formation of FAs on the ridges, which also induced the cell alignment along the ridge. However, topographical guidance of cells on microgrooved substrates is highly dependent on cell type and groove dimensions. For example, our previous study showed that MC3T3-E1 cells cultured on $CaCO_3$ concentric microgrooved substrates with a groove depth of ~5 μm and a groove width of ~5 or ~10 μm were both aligned but the cell nuclei were only aligned on the 10 μm-wide one.[35] Our research group also used photocrosslinked PCLTA substrates with 10 μm-deep concentric microgrooves to regulate MC3T3-E1 cells and found that the narrowest width in the range of 7.5-91.2 μm could orient the cytoskeleton and nuclei most.[36] As discussed earlier, our research group found that MC3T3-E1 cells cultured on PCL banded spherulites similar to the ones here did not show clear cytoskeleton alignment and attributed this finding to too shallow valleys and also too low aspect ratio (width divided by depth) of the grooves.[19] This was in good agreement with the present result that PC12 cells were not aligned on the banded spherulites before the outgrowth of neurites. Nevertheless, the neurites generated in PC12 cell differentiation could sense the surface topography in a more sensitive manner. In pathfinding of the neurites, the filopodia and lamellipodia located at the leading edge of the neurites dominated in sensing topography through FAs and neurite outgrowth was driven by the traction forces via microtubules and actin filaments which

were inflexible, causing neurite extension only along one or two directions.[37] This can explain why the spherulites with more roughness or ridge-like topography in this study provided partial guidance for neurite outgrowth, even though the ridges were irregular, and why the neurites on the banded spherulites preferentially but not absolutely grew along the ridge direction. .

10.4 Conclusions

Banded and non-banded spherulitic surfaces of PCL and PHB prepared through isothermal crystallization as well as their hot-compressed samples demonstrated their distinct influence on rat PC12 cell behavior. PC12 cell attachment and proliferation were higher on the spherulites of PCL, especially on the banded spherulites, than on the hot-compressed sample. In contrast, the trend was opposite on the PHB samples, i.e., spherulites inhibited PC12 cell attachment and proliferation. In addition, the spherulites of both PCL and PHB promoted NGF-induced neurite outgrowth of PC12 cells and the banded spherulites showed evident neurite guidance along the groove direction.

References

[1] Discher, D. E.; Janmey, P.; Wang, Y. *Science* **2005**, 310, 1139.

[2] Yu, L. M. Y.; Leipzig, N. D.; Shoichet, M. S. *Mater. Today* **2008**, 11, 36.

[3] Harbers, G. M.; Grainger, D. W. Cell-matetial interactions: fundamental design issues for tissue engineering and clinical considerations. In Introduction to Biomaterials; Guelcher, S. A., Hollinger, J. O., Eds.; CRC Press: Boca Raton, FL, 2005; pp 15-45.

[4] Bettinger, C. J.; Langer, R.; Borenstein, J. T. *Angew. Chem., Int. Edit.* **2009**, *48*, 5406-5415.

[5] Flemming, R. G.; Murphy, C. J.; Abrams, G. A.; Goodman, S. L.; Nealey, P. F. *Biomaterials* **1999**, *20*, 573-588.

[6] Anselme, K.; Bigerelle, M. *Int. Mater. Rev.* **2011**, *56*, 243-266.

[7] Dalby, M. J. *Med. Eng. Phys.* **2005**, *27*, 730-742.

[8] Ferrari, A.; Faraci, P.; Cecchini, M.; Beltram, F. *Biomaterials* **2010**, 31, 2573.

[9] Huang, C.; Borchers, C. H.; Schaller, M. D.; Jacobson, K. *J. Cell Biol.* **2004**, 164, 593.

[10] Woo, S.; Gomez, T. M. *J. Neurosci.* **2006**, 26, 1418.

[11] Dalby, M. J. *Med. Eng. Phys.* **2005**, 27, 730.

[12] Allen, J.; Chilton, J. K. *Dev. Biol.* **2009**, 327, 4.

[13] Cecchini, M.; Ferrari, A.; Beltram, F. *J. Phys Confer Ser.* **2008**, 100, 012003.

[14] Kim, J. A.; Lee, N.; Kim, B. H.; Rhee, W. J.; Yoon, S.; Hyeon, T. *Biomaterials* **2011**, 32, 2871.

[15] Bechara, S. L.; Judson, A.; Popat, K. C. *Biomaterials* **2010**, 31, 3492

[16] Lopez, C. A.; Fleischman, A. J.; Roy, S.; Desai, T. A. *Biomaterials* **2006**, 27, 3075.

[17] Cai, L.; Zhang, L.; Dong, J.; Wang, S. *Langmuir* **2012**, 28, 12557.

[18] Cai, L.; Wang, S. *Polymer* **2010**, 51, 164.

[19] Wang, K.; Cai, L.; Jesse, S.; Wang, S. *Langmuir* **2012**, 28, 4382.

[20] Washburn, N. R.; Yamada, K. M.; Simon Jr, C. G.; Kennedy, S. B.; Amis, E. J. *Biomaterials* **2004**, 25, 1215.

[21] Simon Jr, C. G. *J. Microsc.* **2004**, 216, 153.

[22] Cai, L.; Lu, J.; Sheen, V.; Wang, S. *Biomacromolecules* **2012**, 13, 342.

[23] Gunn, J. W.; Turner, S. D.; Mann, B. K.; *J. Biomed. Mater. Res.* **2005**, 72A, 91.

[24] Jiang, Y.; Luo, Y.; Fan, Z.; Wang, X.; Xu, J.; Guo, B.; Li, L. *Sci China Ser B* **2003**, 46, 152.

[25] Xu, J.; Guo, B.; Zhou, J.; Li, L.; Wu, J.; Kowalczuk, M. *Polymer* **2005**, 46, 9176.

[26] Hobbs, J. K.; Binger, D. R.; Keller, A.; Barham, P. J. *J. Polym. Sci., Part B: Polym. Phys.* **2000**, 38, 1575.

[27] Cheung, Z.; Ng, K.; Weng, L.; Chan, C.; Li, L. *Polymer* **2006**, 47, 3164.

[28] Cheung, Z.; Weng, L.; Chan, C.; Hou, W. M.; Li, L. *Langmuir* **2005**, 21, 7968.

[29] Jiang, Y.; Zhou, J.; Li, L. *Langmuir* **2003**, 19, 7417.

[30] Maniotis, A. J.; Chen, C. S.; Ingber, D. E. *Proc. Natl. Acad. Sci. USA* **1997**, 94, 849.

[31] Dalby, M. J.; Riehle, M. O.; Yarwood, S. J.; Wilkinson, C. D. W.; Curtis, S. G. *Exp. Cell Res.* **2003**, 284, 274.

[32] Biggs, M. J.; Dalby, M. J. *Proc Inst Mech Eng H.* **2010**, 224, 1441.

[33] Geiger, B.; Spatz, J. P.; Bershadsky, A. D. *Nat. Rev.* **2009**, 10, 21.

[34] Curtis, A.; Wilkinson, C. *Biomaterials* **1997**, 18, 1573.

[35] Wu, X.; Wang, S. *Adv. Healthcare Mater.* **2013**, 2, 326.

[36] Wang, K.; Cai, L.; Zhang, L.; Dong, J.; Wang, S. *Adv. Healthcare Mater.* **2012**, 1, 292.

[37] Cai, L.; Lu, J.; Sheen, V.; Wang, S. *Biomacromolecules* **2012**, 13, 358.

CHAPTER XI
REGULATION OF NEURAL PROGENITOR CELLS ON HONEYCOMB-PATTERNED POLYMER FILMS

11.1 Introduction

Despite some success of clinic treatments for the injuries of the peripheral nervous system (PNS) and central nervous system (CNS) using end-to-end surgical reconnection of the severed nerve ends or autologous nerve grafts, both approaches face severe limitations.[1] End-to-end reconnection treatment can only repair nerve injuries with small gaps, but not for longer gaps because the tension generated in longer gaps can negatively influence nerve regeneration.[1-3] Autologous nerve grafts generally cause the dysfunction of the donor site and the availability is limited.[1] Compared with PNS, the clinic treatments for CNS injuries are far less promising because of the poor regeneration of CNS axons, slow macrophages infiltration, and glial scars that inhibit regeneration.[1] Consequently, the imperative needs of novel and advanced therapies and devices have driven the development of synthetic biomaterials used for nerve regeneration. In addition, longer axon extension is desired to grow across the lesion site and bridge the gaps to achieve functional recovery.[4] A promising material to support nerve regeneration should promote both proliferation of nerve cells and axon extension in neurons. The surface chemistry, topography, and mechanics of biomaterials can influence cell adhesion, phenotype, proliferation, and differentiation.[5-7] Among these surface characteristics, topographical guidance of nerve cells and neurite extension is particularly attractive. The neuronal differentiation of adult rat hippocampal progenitor cells (AHPCs) on

microgrooved polystyrene substrates (groove width/spacing/depth: 16/13/4 μm) was promoted by the topography through spatial control of cell-cell interactions and neurite alignment.[8,9] Rat pheochromocytoma (PC12) cell viability, adhesion, and proliferation were improved on poly(ε-caprolactone) (PCL) nanowire surface compared with control surface without any nano-architecture and the subsequent neuronal markers and phenotypic behavior were more significant on the nanowire surfaces.[10] Three-dimensional agarose scaffolds with uniaxial linear pores fabricated using freeze-drying was also found to support axonal regeneration.[11] Rat Schwann cell precursor (SpL201) cells and PC12 cells cultured on microgrooved substrates of photo-cured PCL triacrylates (PCLTAs) were highly aligned along the groove direction and neurite extension from PC12 cells was promoted on the microgrooves, especially when they were narrower.[2] Honeycomb-patterned PCL films with controllable pore diameters of 3, 5, 8, 10, and 15 μm were prepared via the breath figure method in the presence of an amphiphilic polymer as assistance.[12,13] Neural stem cell (NSC) proliferation was enhanced on these honeycomb-patterned PCL films but the differentiation was suppressed and larger pores favored neurite pathfinding more.[12,13] However, the mechanism of how honeycomb patterns affect cell-cell interactions and the differentiation of NPCs into highly specialized cells, such as astrocytes, mature neurons, immature neurons, and oligodendrocytes is still unknown.

Previously, our research group reported that MC3T3-E1 cell attachment and proliferation were enhanced on rougher PCL spherulites compared with hot-compressed PCL,[14] different from the findings that MC3T3-E1 cell proliferation was inhibited on rougher spherulites of poly(L-lactide) (PLLA).[15,16] Thus we speculate that the thermal

properties of the substrates played a critical role in affecting MC3T3-E1 cell functions.[14] Although it is semi-crystalline with a melting temperature (T_m) of ~60 °C, PCL with a glass transition temperature (T_g) of ~-60 °C is considered as a relatively soft material at the cell culture temperature of 37 °C, while PLLA with a T_g of ~60 °C is considered as a rigid material regardless of its crystallinity. The aim of this study was to fabricate honeycomb-patterned films with controllable pore size using two tri-block amphiphilic copolymers synthesized recently by us via the breath figure method and to investigate the effect of polymer type and pore size on NPC attachment, proliferation, and differentiation. These two copolymers named as CoPLLA17200 and CoPCL17200 consisted of a linear poly(ethylene glycol) (PEG) center block and PLLA or PCL dendrons with a PLLA or PCL arm molecular weight of 17200 g/mol.

11.2 Experimental Section

11.2.1 Preparation of Honeycomb-patterned PCL and PLLA Derivative Copolymer films

CoPCL17200 and CoPLLA17200 were synthesized by us as reported previously. The honeycomb copolymer films were fabricated using the breath figure method as reported by us previously. Briefly, the copolymer was dissolved in methylene chloride (CH_2Cl_2) at a concentration of 0.01 g mL^{-1} and honeycomb-patterned films were prepared on clean glass slides in a closed chamber at a relative humidity of 80 % with assistance of moist airflow. Honeycomb films of CoPCL17200 with pore diameters of 2.5 and 5.2 μm were prepared when the airflow rate was 100 and 0 mL min^{-1}, respectively. Honeycomb

films of CoPLLA17200 with pore diameters of 0.95, 1.95, and 3.1 μm were prepared at the airflow rates of 1000, 100, and 0 mL min^{-1}, respectively. The flat controls were prepared by compressing the copolymer melts between two glass slides and cooling down the samples at room temperature.

11.2.2 Surface Morphology

The honeycomb copolymer films were fixed onto clean glass slides, dried in vacuum, and sputter-coated with a gold-palladium layer (Emscope SC 500, Elexience). A Scanning Electron Microscope (SEM; S-3500, Hitachi Instruments, Tokyo, Japan) was used to observe the surface morphology of the honeycomb copolymer films at an accelerating voltage of 5 kV.

11.2.3 Water Contact Angle

The honeycomb copolymer films were completely dried in vacuum before the measurements. Determination of water contact angles was conducted using a Ramé-Hart NRC C. A. goniometer (model 100-00-230). Briefly, 20 μL of water droplet was injected onto the film at room temperature and the water contact angle was recorded after the water droplet was stable on the surface. Meanwhile, the water droplet was photographed using a 3.0 megapixel camera (Moticam 2300, Motic).

11.2.4 Cell Culture

NPCs were cultured using the procedure reported previously.[17,18] Briefly, a serum-free growth media containing DMEM/F12 medium (Invitrogen, Carlsbad, CA), 20 ng/mL recombinant human epidermal growth factor (EGF, Invitrogen), 20 ng/mL basic

fibroblastic growth factor (bFGF, Invitrogen), 1% GlutaMAX (Invitrogen), and 1% penicillin/streptomycin (Invitrogen) was prepared prior to cell culture. The cells were cultured using this serum-free growth medium in a cell incubator with 95% relative humidity and 5% CO_2 at 37 °C and the medium was changed every other day.

11.2.5 Cell Attachment and Proliferation

The copolymer samples were punched into disks with a diameter of ~8 mm, immersed in 70% alcohol solution to remove impurities on the surface first, sterilized in 70% alcohol solution for 30 min twice, and completely dried in vacuum prior to cell studies. NPC cells were seeded on the samples at a density of ~14000 cells/cm^2 and cultured for 4 h, 1, 4, and 7 days. The cell number at each time point was counted using a colorimetric cell metabolic assay (CellTiter 96 Aqueous One Solution, Promega, Madison, WI). To visualize cells, the cells after culture for certain time were fixed in 4% paraformaldehyde (PFA) solution at room temperature for 20 min and rinsed with PBS twice. The cells subsequently were stained with 4',6-diamidino-2-phenylindole (DAPI) at room temperature and photographed using an Axiovert 25 light microscope (Carl Zeiss, Germany). To demonstrate that the cells were still in undifferentiated state at day 7, the cells fixed with 4% PFA were further blocked with PBS solution containing 1% bovine serum albumin (BSA) and in 0.3% Triton X-100 for 30 min at room temperature. Then the cells were incubated with mouse monoclonal antinestin (1:500, v/v) for 1 h and stored at 4 °C for one day. The cells were rinsed with PBS that contained 1% BSA for 10 times and then stained with goat antimouse IgG-FITC (1:100, v/v) in the cell incubator for 2 h. Following that, cells were rinsed with PBS twice and stained with DAPI at room

temperature. The Axiovert 25 light microscope was employed to photograph the cells. The percentage of nestin-positive cells to the total cell population in more than 20 cell images was counted and averaged.

11.2.6 Cell Differentiation

Cells were seeded on the samples at a density of ~6000 cells/cm^2 and cultured in the growth medium in the cell incubator. After the cells attached onto the samples, the growth medium was removed and substituted with a differentiation medium that contained DMEM/F12, 1% GlutaMAX, 1% fetal bovine serum (FBS, Gibco, Grand Island, NY), and 1% penicillin/streptomycin. The cells were cultured in the differentiation medium for another 7 days and the medium was changed every other day. After 7 days, the cells were fixed and blocked for nestin staining in the same way as used for cell attachment and proliferation. For characterizing the NPC differentiation into mature neurons, immature neurons, astrocytes, and oligodendrocytes, we used rabbit monoclonal antineurofilament 200 (NF, 1:1000, v/v), mouse monoclonal anti-β-tubulin III (1:500, v/v), rabbit monoclonal antiglial fibrillary acidic protein (GFAP, 1:500, v/v), and mouse monoclonal antioligodendrocyte marker O4 (1:1000, v/v; R&D systems, Minneapolis, MN), respectively. Goat antimouse IgG-FITC (1:100, v/v) was used as the secondary antibody for β-tubulin III and O4. CF647 goat antirabbit IgG (1:100, Biotium, Hayward, CA) was used as the secondary antibody for NF and GFAP. All the above specialized staining steps were performed together with DAPI staining. The specialized differentiation of NPCs into each lineage was quantified from 10 cell images by dividing the number of the cells expressing the corresponding marker by the total cell number

quantified using DAPI-stained nuclei. NF-stained cell images were used to evaluate the neurite outgrowth and only neurites longer than the diameter of the cell body was counted. The percentage of cells with neurites, the number of neurites per cell, the average neurite length, and the total neurite length per cell were calculated through dividing the number of cells bearing neurites by the total cell number, the total number of neurites in each image by the total cell number, the total neurite length by the total number of neurites, and the total neutite length by the total cell number, respectively.

11.2.7 Gene Expression

After NPCs were cultured in the differentiation medium for 7 days, the cells were rinsed with PBS twice and the RNA was isolated using an RNeasy Mini Kit (Oiagen, Valencia, CA) according to the manufacturer's instruction. Subsequently the cDNA was synthesized using a cDNA synthesis kit (Thermo Scientific) also according to the manufacturer's instruction. The oligonulceotide primers used in real-time ***polymerase chain reactions*** (PCR) included neuron specific enolase 2 (NSE), GFAP, myelin oligodendrocyte glycoprotein (MOG), and glyceraldehyde 3-phosphate dehydrogenase (GAPDH), as listed in Table 1. The expression levels of NSE, GFAP, MOG, and GAPDH were determined on a thermal cycler with fluorescence detection systems (PTC-200, MJ Research) using a Power SYBR Green PCR Master Mix (Applied Biosystems, Carlsbad, CA).

.

Table 11.1 Oligonucleotide primer sequences for real-time PCR.

primer	accession no.	sequence (5'-3')	template	Product size (bp)
NSE	NM_013509	TGTTCTTGTCGTCGGACTGTGT	1234-1255	73
		CCTCCTGGTGATTCCACAGT	1286-1306	
GFAP	X_02801	TGTGGAGGGTCCTGTGTGTA	7435-7454	199
		GTAGCCTGCTCCACCTTCTG	7614-7633	
MOG	NM_010814	AAATGGCAAGGACCAAGATG	240-259	140
		AGCAGGTGTAGCCTCCTTCA	360-379	
GAPDH	NM_008084	ACTTTGTCAAGCTCATTTCC	961-980	267
		TGCAGCGAACTTTATTGATG	1208-1227	

11.2.8 Statistical Analysis

Cell culture was performed in quadruplicates for each group. All the data were expressed as mean ± standard deviation. The statistical significance ($p < 0.05$ or $p < 0.01$) in the differences between groups was determined using student's *t*-test.

11.3 Results and Discussion

In the breath-figure method, the pore diameter can be tuned through controlling the fabrication parameters such as airflow rate, humidity, the concentration and volume of polymer solution cast on the substrates, and solvent type.[19-22] In this study, the honeycomb copolymer films with different pore diameters were prepared via controlling the air flow rate. When airflow rates of 1000, 100, and 0 mL min^{-1} were applied to the CoPLLA17200 solution, the as-formed average pore diameters were measured to be 1.0 ± 0.09, 1.9 ± 0.11, and 3.1 ± 0.11 μm, respectively (Figure 11.1a). When airflow rates of

100 and 0 mL min^{-1} were applied to the CoPCL17200 solution, the as-prepared average pore diameters were 2.5 ± 0.8 and 5.2 ± 1.5 μm, respectively (Figure 11.1b). Increasing the airflow rate accelerated the evaporation of solvent (CH_2Cl_2) and the temperature on the copolymer solution decreased more efficiently, leading to the formation of more water droplets arranged on the solution surface. When the airflow rate was higher, the coalescence of water droplets became more difficult and thus smaller pores could be produced. In general, when the solvent used to dissolve polymer is denser than water, the water droplets condensed from the moisture air tend to form monolayer pores on the solution surface without penetrating into the solution.[20] On the other hand, when the solvent is lighter than water, water droplets can penetrate into the solution and form multilayer pores.[23] Owing to the fact that the solvent (CH_2Cl_2) is denser than water, the pores on those copolymer films were arranged in monolayer architecture as shown in Figure 11.1a,b.

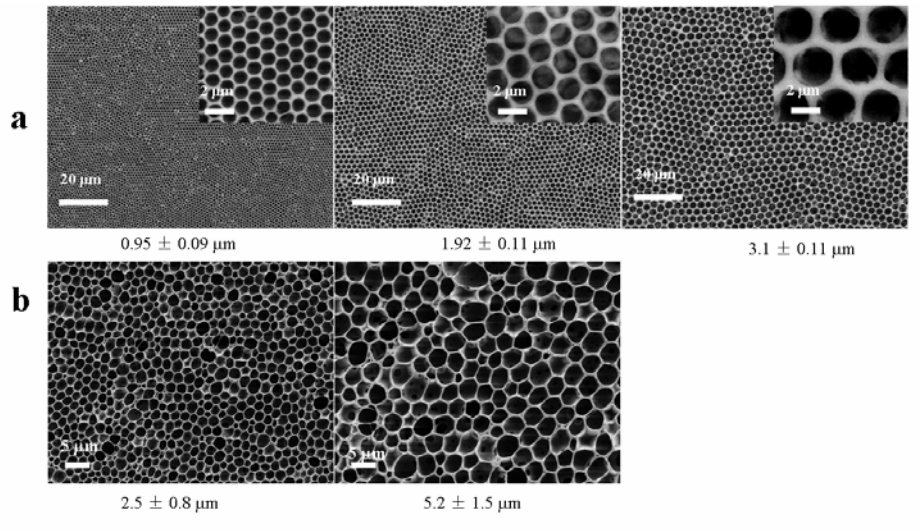

Figure 11.1 (a) SEM images of honeycomb-patterned CoPLLA17200 films with different pore diameters. Magnification: × 2000. Insets: maginification: × 10000. (b) SEM images of honeycomb-patterned CoPCL17200 films with different pore diameters.

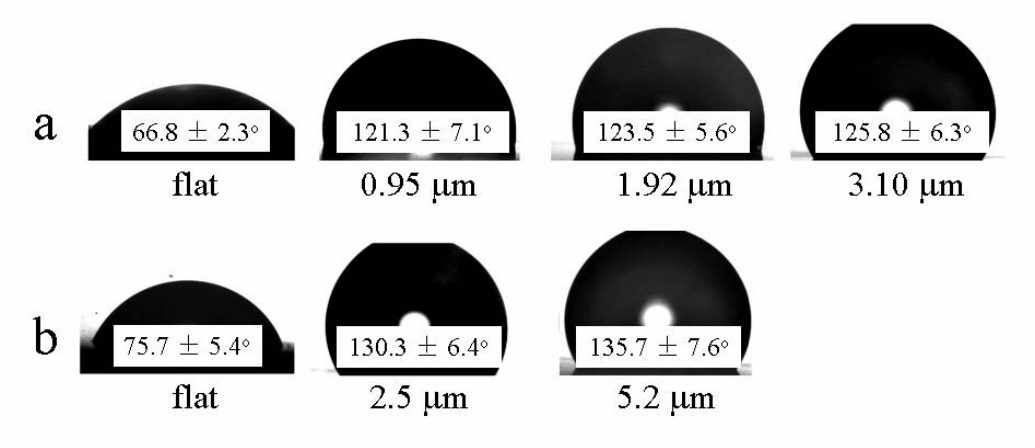

Figure 11.2 Micrographs of water droplets and contact angles on the flat and honeycomb-patterned films with different pore diameters. (a) CoPLLA17200. (b) CoPCL17200.

The surface topography can affect the wettability of polymer films.[24-26] The water contact angles on those honeycomb-patterned films and flat ones were determined as shown in Figure 11.2. The water contact angle increased sharply from 66.8 ± 2.3° on

the flat film of CoPLLA17200 to 121.3 ± 7.0°, 123.5 ± 5.6°, and 125.8 ± 6.3° on the honeycomb films of CoPLLA17200 with pore diameters of 1.0, 1.9, and 3.1 μm, respectively. Similarly, the water contact angle increased from 75.7 ± 5.4° on the flat film of CoPCL17200 to 130.3 ± 6.4° and 135.7 ± 7.6° on the honeycomb films of CoPLLA17200 with pore diameters of 2.5 and 5.2 μm, respectively. Honeycomb films have higher hydrophobicities because of the formation of air pockets between the substrate surface and water droplets when the water droplets are much bigger than the pore size. In this case, the Cassie and Baxter model in eq. 1 can be used to theoretically predict the water contact angles (θ).[24-27]

$$\cos\theta = (1 - f_o)\cos\theta_s + f_o\cos\theta_o \qquad (1)$$

where f_o is the fractional flat geometrical area of liquid-air interface beneath a water droplet, θ_o is the water contact angle on the pore filled with air and is considered as 180°, and θ_s is the water contact angle on the smooth surface, which was determined to be 66.8 ± 2.3° and 75.7 ± 5.4° for CoPLLA17200 and CoPCL17200, respectively. For CoPLLA17200 films, when the pore diameters were 1.0, 1.9, and 3.1 μm, the rim sizes were measured from the SEM images using ImageJ software to be 0.15 ± 0.02, 0.31 ± 0.05, and 0.42 ± 0.04. Then the f_o values were calculated to be 0.587, 0.586, and 0.598 for the honeycomb films of CoPLLA17200 with pore diameters of 1.0, 1.9, and 3.1 μm, respectively. For CoPCL17200 films, when the pore diameter increased from 2.5 to 5.2 μm, the rim size increased from 0.14 ± 0.03 to 0.21 ± 0.05 μm and then the f_o value increased from 0.705 to 0.744. Using Eq. 1, the water contact angles were calculated to be 115°, 115°, and 116° on the honeycomb films of CoPLLA17200 with pore diameters

of 1.0, 1.9, and 3.1 μm and 129° and 133° on the honeycomb films of CoPCL17200 with pore diameters of 2.5 and 5.2 μm, respectively. Clearly, all the predicted water contact angles were smaller than experimental values and they did show strong dependence on the pore diameter, especially for the CoPLLA17200 films. However, this prediction provided theoretical support for explaining the pore-diameter dependence of wettability. Prominently, the f_o values of honeycomb-patterned CoPCL17200 films were higher than those of honeycomb-patterned CoPLLA17200 films because of the much narrower rims on the CoPCL17200 films compared with the CoPLLA17200 ones. In addition, on the films of both CoPLLA17200 and CoPCL17200, the f_o value increased with increasing the pore diameter, which is in contrast with our previous study that the f_o value increased from 0.528 on the honeycomb PCL films with 10.0 μm pores to 0.553 and 0.592 on the films with 6.0 μm and 3.5 μm pores, respectively.[17]

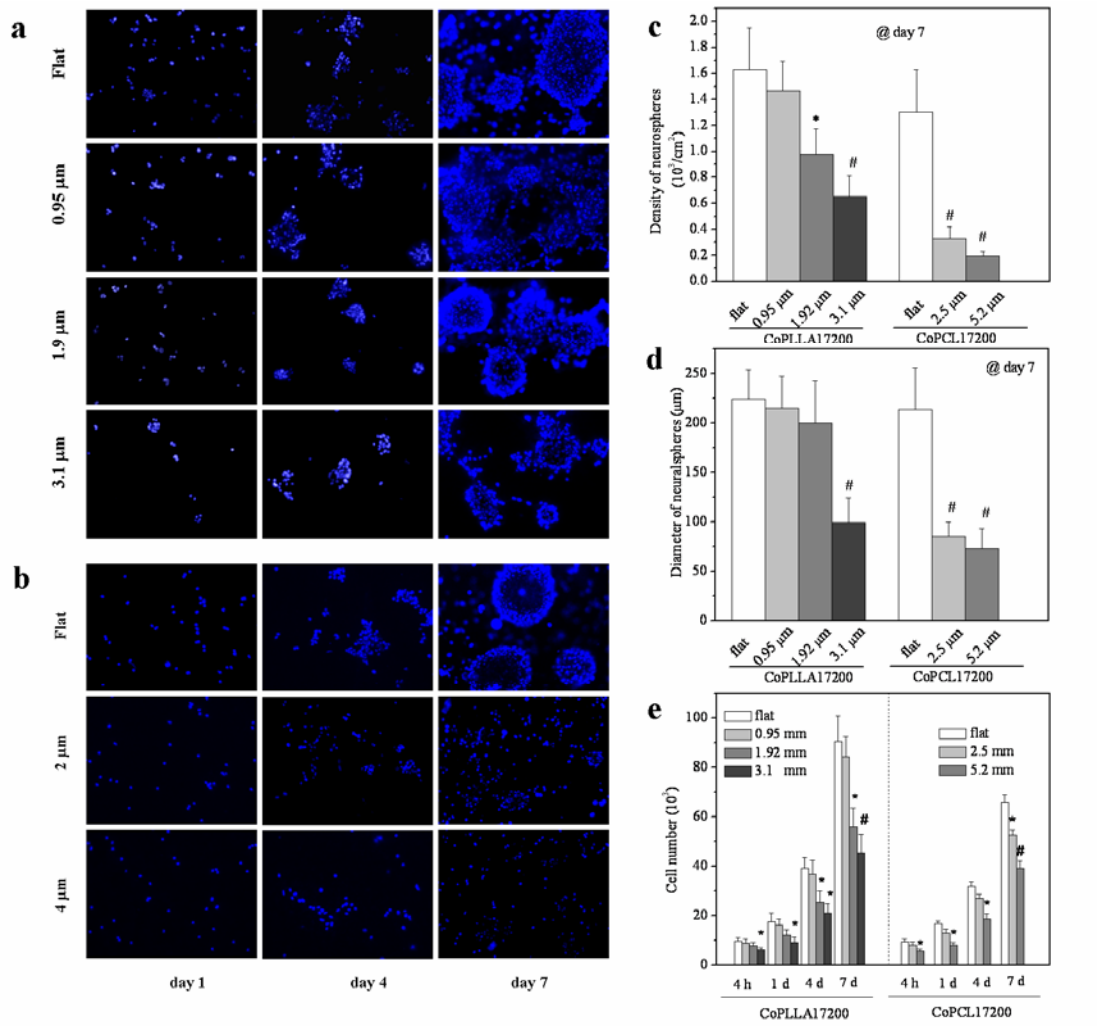

Figure 11.3 E14 mouse NPC proliferation on flat film and honeycomb-patterned films. (a) fluorescent images of neurospheres stained with DAPI (blue) at days 1, 4, and 7 on CoPLLA17200 films. (b) fluorescent images of neurospheres stained with DAPI (blue) at days 1, 4, and 7 on CoPCL17200 films. (c) density of neurospheres on films at day 7. *: $p < 0.05$ relative to flat, 0.95, and 3.1 μm films; #: $p < 0.01$ relative to flat and 0.95 μm films for CoPLLA17200 and flat film for CoPCL17200. (d) diameter of neurospheres on films at day 7. #: $p < 0.01$ relative to other films. (e) cell numbers at 4h, days 1, 2, and 4 on films determined by MTS assay. *: $p < 0.05$ and #: $p < 0.01$ relative to flat and 0.95 μm films for CoPLLA17200 and flat and 2.5 μm films for CoPCL17200.

The pore-size dependence of NPC attachment and proliferation was investigated by culturing NPCs in serum-free media to exclude the effect of adsorbed serum proteins on cell behavior. As demonstrated in Figure 11.3a,b, the flat films supported more neurospheres than the honeycomb ones for both CoPLLA17200 and CoPCL17200,

indicating that NPC proliferation was suppressed on the honeycomb films. By comparing the NPC proliferation on the honeycomb films, we found that NPCs on the smaller pores formed more neurospheres and fewer neurospheres were observed on honeycomb films of CoPCL17200 than those of CoPLLA17200. From the DAPI-stained cell images, the average number of neurospheres per image and the average diameter of neurospheres were quantified from more than 20 images. Consistent with the observation in Figure 11.3a,b, the average number of neurospheres per image was lower on the honeycomb films and the smaller pores supported fewer neurospheres for both CoPLLA17200 and CoPCL17200 (Figure 11.3c). Compared with the honeycomb films of CoPLLA17200, the CoPCL17200 films had lower neurosphere numbers per image. The diameter of neurospheres shown in Figure 11.3d presented a trend similar to that was seen in Figure 11.3c. NPC attachment at 4 h and proliferation over 7 days were quantified using the MTS assay, as shown in Figure 11.3d. NPC attachment on the honeycomb film of CoPLLA17200 with 3.1 μm pores and the honeycomb film of CoPCL17200 with 5.2 μm pores was significantly lower than that on flat CoPLLA17200 and flat CoPCL17200 films, respectively. The NPC attachment on the honeycomb films of CoPLLA17200 with 1.0 μm and 1.9 μm pores was slightly lower than that on the flat CoPLLA17200 film without significant difference and the larger pores suppressed the attachment more. This trend was also found between the honeycomb film with 2.5 μm pores and the flat one of CoPCL17200. When the NPCs were cultured for longer time, these differences became more prominent. The above result agreed with a previous finding that chondrocyte proliferated more slowly on honeycomb films of poly(lactic acid) (PLA) with 5 μm pores

than on the flat one;[28] however, different from some other findings, e.g., MC3T3-E1 cells, epidermal keratinocytes, and dermal fibroblasts showed better adhesion and proliferation on honeycomb-patterned PCL films with pore diameters of a few microns compared with the flat control.[17,27,29] In one report, it was even suggested that honeycomb films promoted NPC proliferation compared with the flat one.[30]

The main factor to affect NPC attachment and proliferation in this study was the topography available on the film surface, namely, the honeycomb pores. The pore diameter and the rim size might play a critical role in the cell-substrate interactions. The diameter of single NPC at 4 h was 7~10 μm. When NPCs were seeded on the copolymer films, the cells first found attaching sites where the force balance was achieved. Owing to the presence of pores and rims on the copolymer films, NPCs preferred to be localized in pores to avoid the rims because the latter possibly caused force unbalance. Hence, when the pore diameter was more comparable to or larger than a single NPC, NPCs tended to be separated on the honeycomb films. As confirmed in Figure 11.3a,b, the larger pores resulted in more separated cells that were randomly distributed on the films instead of forming neurospheres. In particular, the NPCs were extremely separated from each other on the honeycomb films of CoPCL17200 with 2.5 and 5.2 μm pores, which was more significant than on the honeycomb films of CoPLLA17200. This difference might be ascribed to the narrower rims on the honeycomb films of CoPCL17200, especially the one with 5.2 μm pores, than on the honeycomb films of CoPLLA17200. Single NPC on the narrower rims more tended to be localized in pores to obtain force equilibrium and those cells were separated more easily with forming fewer neurospheres.

NPCs cultured on the copolymer samples for 7 days were also immunostained with nestin to verify the progenitor nature of NPCs prior to the studies of differentiation into various lineages and gene expression. On all the copolymer films, 100% of NPCs were nestin-positive, demonstrating that NPCs remained immature and undifferentiated at this stage. Previously our research group reported that MC3T3-E1 cell attachment and proliferation were enhanced on rougher PCL spherulites compared with hot-compressed PCL,[14] whereas MC3T3-E1 cell proliferation was inhibited on rougher spherulites and surfaces of PLLA.[15,16] As discussed in Introduction, the thermal properties of the substrates might be important for regulating MC3T3-E1 cells because PCL was relatively soft and PLLA was rigid at 37 °C.[14] However, in this study, NPCs responded to the films of CoPLLA17200 and CoPCL17200 in the same way in terms of attachment and proliferation possibly because the topography instead of polymer type dominated in determining the cell-material interactions.

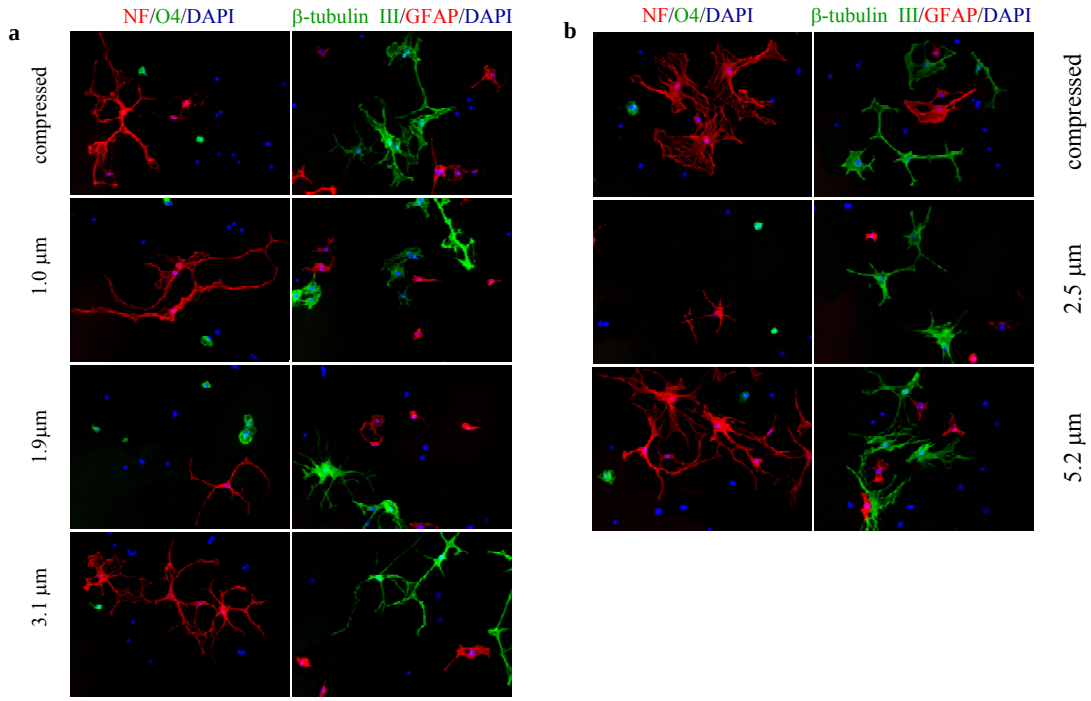

Figure 11.4 Fluorescent images of NPCs differentiated on flat film and honeycomb-patterned films with different pore diameters of (a) CoPLLA17200 and (b) CoPCL17200. Differentiated NPCs were immunostained with anti-NF (red, mature neurons), anti-O4 (green, oligodendrocytes), anti-β-tubulin III (green, immature neurons), and anti-GFAP (red, astrocytes) and counter-stained with DAPI (blue).

NPC differentiation into neurons, astrocytes, and oligodendrocytes, primary CNS lineages, were characterized on the copolymer films, as demonstrated in Figure 11.4. For CoPLLA17200, NPCs stained with mature neural marker NF showed typical and much better neurite outgrowth on the flat film and the honeycomb film with 1.0 and 3.1 μm pores than those on the honeycomb film with 1.9 μm pores. NPCs stained with immature neural marker β-tubulin III showed the same trend. The number of NPCs stained with astrocyte marker GFAP per image did not show significant difference on the CoPLLA17200 films, whereas the number of NPCs stained with oligodendrocyte marker

O4 in each image was slightly higher on the flat film and the honeycomb film with 1.0 and 1.9 μm pores than those on the honeycomb film with 3.1 μm pores. For CoPCL17200, NPCs stained with NF and β-tubulin III showed more prominent neuronal differentiation r the flat film and the honeycomb film with 5.2 μm pores, in particular, the latter, than on the honeycomb film with 2.5 μm pores. Slightly better astrocyte differentiation of NPCs as indicated by GFAP staining was also found on the flat film and the honeycomb film with 5.2 μm pores of CoPCL17200 than on the honeycomb film with 2.5 μm pores. Differently, oligodendrocyte differentiation marked with O4 did not show significant differences on those CoPCL17200 films.

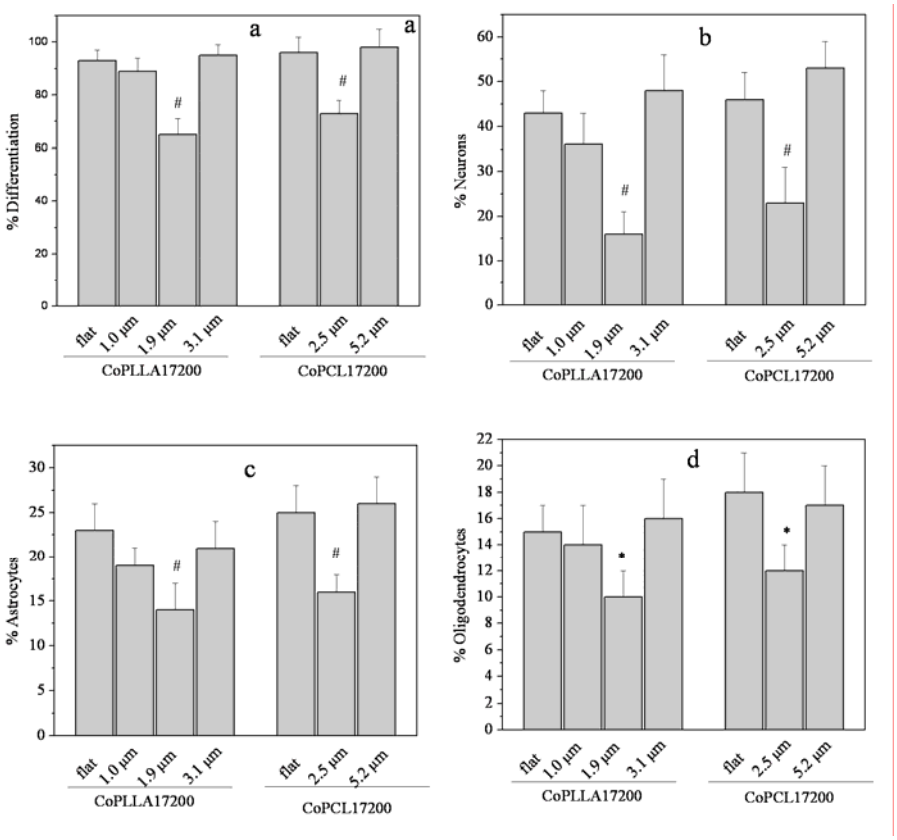

Figure 11.5 Percentages of differentiated (a) NPCs, (b) neurons (NF-positive), (c) astrocytes (GFAP-positive), and (d) oligodendrocytes (O4-positive) on flat film and honeycomb-patterned films with different pore diameters after 7 days of culture in differentiation media. *: $p < 0.05$ and #: $P < 0.01$ relative to other films.

The total percentage of differentiated NPCs and the percentages of differentiation into neurons, astrocytes, and oligodendrocytes were quantified from fluorescent images, as shown in Figure 11.5. The total percentages of differentiated NPCs was 93 ± 4%, 89 ± 5%, 65 ± 6%, and 95 ± 4% on the flat film and the honeycomb films with 1.0, 1.9, and 3.1 μm pores of CoPLLA17200, and 96 ± 6%, 73 ± 5%, and 98 ± 7% on the flat film and the honeycomb films with 2.5 and 5.2 μm pores of CoPCL17200, respectively. The neuronal differentiation of NPCs on the honeycomb film with 1.9 μm pores of CoPLLA17200 showed a significantly lower percentage of ~15% than the values of

~42%, ~35%, and ~47% on the flat film and the honeycomb films with 1.0 and 3.1 μm pores. Similarly, the percentages of the neuronal differentiation on the flat film and the honeycomb films with 2.5 and 5.2 μm pores of CoPCL17200 were ~44%, ~16%, and ~50%, respectively. The astrocyte differentiation and oligodendrocyte differentiation of NPCs also demonstrated the same trend as they were suppressed on the honeycomb films with 1.9 μm pores for CoPLLA17200 and with 2.5 μm pores for CoPCL17200. As discussed earlier, the number of NPCs stained with GFAP per image did not show significant difference on the CoPLLA17200 films; however, the differentiation percentages were significantly lower on the honeycomb films with 1.9 μm pores than on the other films. This can be ascribed to the difference in the cell density among different films and the value was lower on the honeycomb films, especially when the pores were larger, as discussed earlier in NPC proliferation. This phenomenon was further confirmed by the percentage of the oligodendrocyte differentiation, which was much lower on the honeycomb film with 1.9 μm pores than on the other films although the number of NPCs stained with O4 per image was slightly higher on the flat film and the honeycomb films with 1.0 and 1.9 μm pores than on the honeycomb film with 3.1 μm pores. This explanation was also applicable to the result of oligodendrocyte differentiation on the CoPCL17200 films.

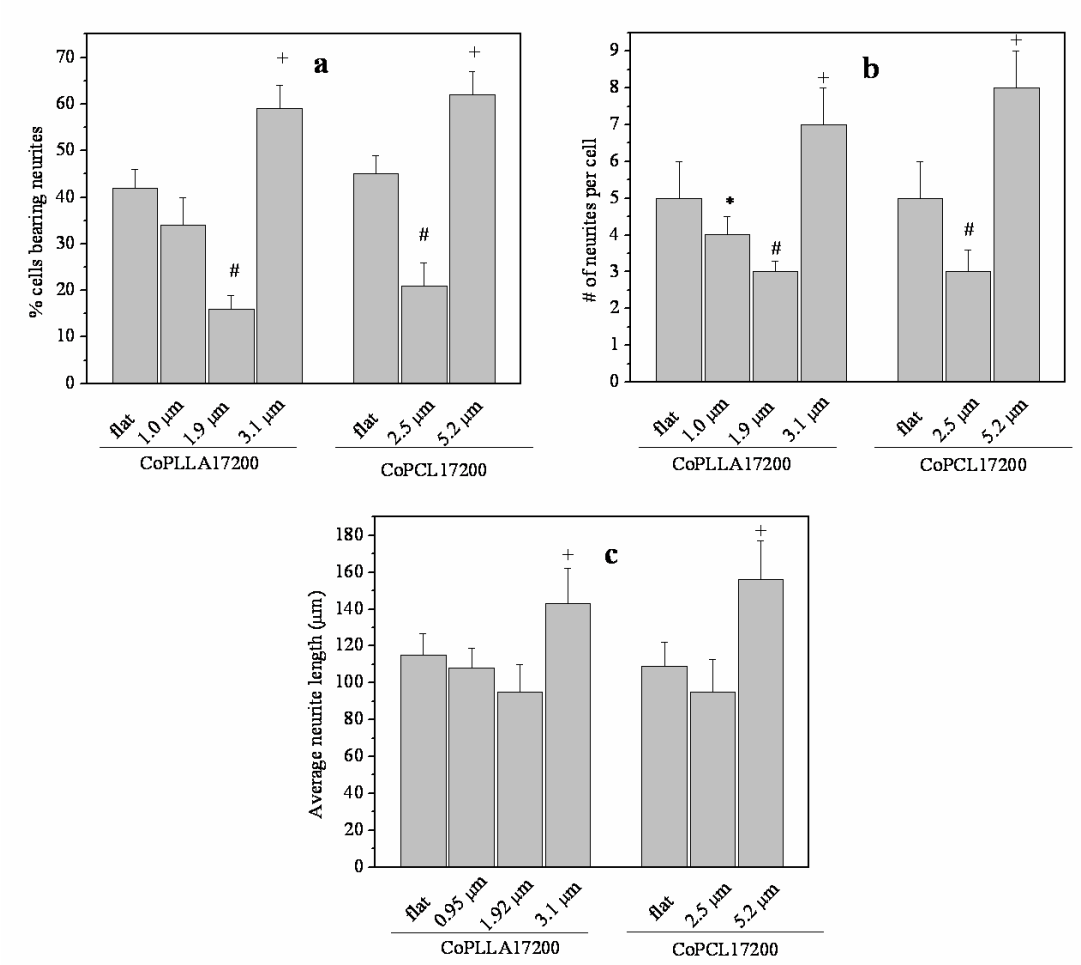

Figure 11.6 (a) Percentage of cells bearing neurites. #: $P < 0.01$ and +: $P < 0.01$ relative to other films. (b) Number of neurites per cell.*: $P < 0.05$ relative to flat CoPLLA17200 films; #: $P < 0.01$ and +: $P < 0.01$ relative to other films. (c) Average neurite length. +: $P < 0.01$ relative to other films.

In addition to the percentage of NPC differentiation into specific lineage, the percentage of cells bearing neurites, the number of neurites per cell, and average neurite length were also quantified from NF-immunostained fluorescent images, as shown in Figure 11.7. The percentage of cells bearing neurites on the honeycomb film with 3.1 μm pores ofCoPLLA17200 was significantly higher than on other CoPLLA17200 films, and it was much lower on the honeycomb film with 1.9 μm pores than on the flat and the

honeycomb film with 1.0 μm pores. The percentage of cells bearing neurites on the honeycomb film with 2.5 μm pores of CoPCL17200 was prominently lower than the values on the other CoPCL17200 films, and it was also much lower on the flat film than on the honeycomb film with 5.2 μm pores. For both CoPLLA17200 and CoPCL17200, the number of neurites per cell was much higher on the flat films and the honeycomb films with the largest pores than those on the honeycomb films with smaller pores. The average neurite length was remarkably bigger on the honeycomb films with the largest pores than the values on the other films for both CoPLLA17200 and CoPCL17200. There was no significant difference between the flat film and the honeycomb film with 1.9 μm pores for CoPLLA17200 or the flat film and the honeycomb film with 2.5 μm pores for CoPCL17200, although it was slightly higher on the flat films.

Evidently, compared with the flat films, the honeycomb film with 3.1 μm pores for CoPLLA17200 and the honeycomb film with 5.2 μm pores for CoPCL17200 promoted neurite outgrowth instead of suppressing NPC differentiation, although NPC attachment and proliferation were suppressed. When the pores were smaller than ~3.0 μm, for examples, the honeycomb films with 1.0 and 1.9 μm pores for CoPLLA17200 and with 2.5 μm pores for CoPCL17200, the NPC differentiation was suppressed and smaller pores supported better differentiation.

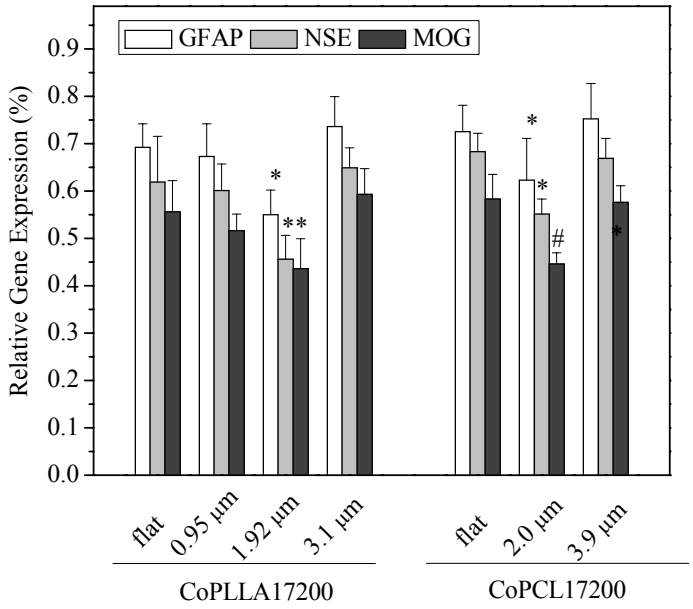

Figure 11.7 Gene expression levels of GFAP, NSE, and MOG, relative to GAPDH for NPCs cultured on flat and honeycomb-patterned films in differentiation media for 7 days. *: $P < 0.05$ and #: $P < 0.01$ relative to other films.

The differentiation of NPCs into mature neurons, astrocytes, and oligodendrocytes was also evaluated using expression of gene markers, NSE, GFAP, and MOG, respectively. Consistently, the expression levels of these three markers were lower on the honeycomb CoPLLA17200 films with 1.0 and 1.9 μm pores than on the flat one, and the bigger pores resulted in lower expression levels, whereas this trend was not monotonic and these expression levels sharply increased on the honeycomb CoPLLA17200 film with 3.1 μm pores, which were even slightly better than those on the flat film. Similarly, these three expression levels were significantly suppressed on the honeycomb CoPCL17200 film with 2.5 μm pores than those on the flat film, which then sharply increased on the honeycomb film with 5.2 μm pores.

Although the NPC attachment and proliferation were inhibited on the honeycomb copolymer films because of the poorer cell-cell communications caused by separation of the cells from each other compared with those on the flat ones, topographical guidance played a critical role in neurite outgrowth. During neuronal polarization accomplished through the generation of long cellular protrusions from cells, namely, neurites, the topographical feature of substrates provided guidance for formation and stabilization of focal adhesions which dominated the neurite initiation and outgrowth.[31-33] The neurites grew and proceeded toward specific targets in a process called pathfinding.[34] The efficient neurite alignment was induced on nanogratings with a linewidth of 500 nm and a depth of 350 nm.[32] In this study, the pore rims on the honeycomb films can be considered as circular groove ridges, which might provide the main topographical guidance during neurite outgrowth. However, because microtubules and actin filaments are inflexible, neurite pathfinding tends to develop in one or two directions. Consequently, neurite outgrowth could only be guided and promoted on the rims when the pores were large enough to reduce the directional confinement of neurites. For example, the honeycomb CoPLLA17200 film with 3.1 μm pores and the honeycomb CoPCL17200 films with 5.2 μm pores supported better neurite growth. Because the honeycomb CoPCL17200 film with 5.2 μm pores had a larger pore size than the honeycomb CoPLLA17200 film with 3.1 μm pores, the neurites grew slightly better on the former, as confirmed in earlier discussion. In contrast, when the pores were sufficiently small, for example, < 3.0 μm, the pore rims could not guide the neurite growth efficiently and poor cell-cell communications dominated the cell behavior to suppress NPC differentiation

than on the flat films. When the pore diameter was larger, poorer cell-cell communications resulted in lower neurite growth. Therefore, the honeycomb CoPLLA17200 film with 1.0 μm pores showed better neurite growth than on the honeycomb film with 1.9 μm pores. Our results were in agreement with previous findings that neural stem cell differentiation was suppressed on honeycomb-patterned PCL films with diameters of 3, 5, 8, and 10 μm, especially on the films with 3 μm pores.[12] Their findings also indicated that neurites grew along the pore rims and the protrusion extension was much better than on the flat films.

11.4 Conclusions

Honeycomb-patterned CoPLLA17200 films with diameters of 1.0, 1.9, and 3.1 μm and honeycomb-patterned CoPCL17200 films with diameters of 2.5 and 5.2 μm were fabricated using the breath-figure method. NPC attachment and proliferation were prohibited on honeycomb-patterned films, especially when pore diameters were larger due to the poorer cell-cell communication caused by cell separation on pores. However, NPC differentiation was promoted on the honeycomb CoPLLA17200 films with 3.1 μm pores and the honeycomb CoPCL17200 films with 5.2 μm pores compared with that on the flat ones, even though it was suppressed on the honeycomb films with smaller pores, for example, 1.0 and 1.9 μm for CoPLLA17200 and 2.5 μm for CoPCL17200.

References

[1] Schmidt, C. E.; Leach, J. B. *Annu. Rev. Biomed. Eng.* **2003**, 5, 293.

[2] Cai, L.; Zhang, L.; Dong, J.; Wang, S. *Langmuir* **2012**, 28, 12557.

[3] Hoffman-Kim, D.; Mitchel, J. A.; Bellamkonda, R. V. *Annu. Rev. Biomed. Eng.* **2010**, 12, 203.

[4] Stokols, S.; Tuszynski, M. H. *Biomaterials* **2004**, 25, 5839.

[5] Yu, L. M. Y.; Leipzig, N. D.; Shoichet, M. S. *Mater. Today* **2008**, 11, 36.

[6] Harbers, G. M.; Grainger, D. W. Cell-matetial interactions: fundamental design issues for tissue engineering and clinical considerations. In Introduction to Biomaterials; Guelcher, S. A., Hollinger, J. O., Eds.; CRC Press: Boca Raton, FL, 2005; pp 15-45.

[7] Discher, D. E.; Janmey, P.; Wang, Y. *Science* **2005**, 310, 1139.

[8] Recknor, J. B.; Sakaguchi, D. S.; Mallapragada, S. K. *Ann. N. Y. Acad. Sci.* **2005**, 1049, 24.

[9] Recknor, J. B.; Sakaguchi, D. S.; Mallapragada, S. K. *Biomaterials* **2006**, 27, 4098.

[10] Bechara, S. L.; Judson, A.; Popat, K. C. *Biomaterials* **2010**, 31, 3492.

[11] Tsuruma, A.; Tanaka, M.; Yamamoto, S.; Shimomura, M. *Colloids and Surfaces A: Physicochem. Eng. Aspects* **2008**, 313-314, 536.

[12] Tsuruma, A.; Tanaka, M.; Yamamoto, S.; Shimomura, M. *IFMBE Proceedings* **2007**, 14, 3558.

[13] Wang, K.; Cai, L.; Jesse, S.; Wang, S. *Langmuir* **2012**, 28, 4382.

[14] Simon Jr, C. G. *Journal of Microscopy* **2004**, 216, 153.

[15] Washburn, N. R.; Yamada, K. M.; Simon Jr, C.G.; Kennedy, S. B.; Amis, E. J. *Biomaterials* **2004**, 25, 1215.

[16] Wu, X.; Wang, S. *ACS Appl. Mater. Interfaces* **2012**, 4, 4966.

[17] Wu, X.; Wang, S. *Adv. Healthcare Mater.* **2013**, 2, 326.

[18] Madej, W.; Budkowski, A.; Raczkowska, J.; Rysz, J. *Langmuir* **2008**, 24, 3517.

[19] Bunz, U. H. F. *Adv. Mater.* **2006**, 18, 973.

[20] Stenzel, M. H.; Barner-Kowollik, C.; Davis, T. P. *Journal of Polymer Science: Part A: Polymer Chemistry* **2006**, 44, 2363.

[21] Saunders, A. E.; Dickson, J. L.; Shah, P. S.; Lee, M. Y.; Lim, K. T.; Johnston, K. P.; Korgel, B. A. *Physical Review E* **2006**, 73, 031608.

[22] Park, M. S.; Kim, J. K. *Langmuir* **2004**, 20, 5347.

[23] Murray, M. D.; Darvell, B. W. *J. Phys. D: Appl. Phys.* **1990**, 23, 1150.

[24] Min, E.; Wong, K. H.; Stenzel, M. H. *Adv. Mater.* **2008**, 20, 3550.

[25] Cassie, A. B. D.; Baxter, S. *Trans. Faraday Soc.* **1944**, 40, 546.

[26] Wang, B.; Mao, Z.; Meng, X.; Tong, W.; Gao, C. *Colloids and Surfaces B: Biointerfaces* **2010**, 76, 38.

[27] Fukuhira, Y.; Kaneko, H.; Yamaga, M.; Tanaka, M.; Yamamoto, S.; Shimomura, M. *Colloids and Surfaces A: Physicochem. Eng. Aspects* **2008**, 313-314, 520.

[28] Mcmillan, J. R.; Akiyama, M.; Tanaka, M.; Yamamoto, S.; Goto, M.; Abe, R.; Sawamura, D.; Shimomura, M.; Shimizu, H. *Tissue Engineering* **2007**, 13, 789.

[30] Woo, S.; Gomez, T. M. *J. Neurosci.* **2006**, 26, 1418.

[31] Ferrari, A.; Faraci, P.; Cecchini, M.; Beltram, F. *Biomaterials* **2010**, 31, 2565.

[32] Huang, C.; Borchers, C. H.; Schaller, M. D.; Jacobson, K. *J. Cell Biol.* **2004**, 164, 593.

[33] Allen, J.; Chilton, J. K. *Dev. Biol.* **2009**, 327, 4.

[34] Cai, L.; Zhang, L.; Dong, J.; Wang, S. *Langmuir* **2012**, 28, 12557.

CHAPTER XII
CONCLUSIONS

I present a divergent method to prepare two series of well-defined comb-dendritic tri-block copolymers via divergent synthesis of dendritic PEG with four generations using acetonide-protected anhydride derivative of 2,2-bis(hydroxymethyl)propionic acid and ring-opening polymerization (ROP) of ε-caprolactone or L-lactide monomers. The composition of copolymers was varied by controlling the feed ratio of monomers to hydroxyl groups to give variable PLLA or PCL arm lengths. The chemical structures were confirmed by ^{1}H NMR, FTIR, and GPC measurements. DSC and DMA measurements were used to study the thermal and mechanical properties, respectively. POM and AFM were used to oberve the crystalline morphology of copolymers with different molecular weights. GIXRD study on copolymer films demonstrated that crystallite size, lattice constants a, b, and c, and the crystallinity of copolymers were strongly influenced by the penetration depth and increased with the penetration depth. The MC3T3-E1 cell attachment and proliferation were regulated by the hydrophilicity of the copolymers. For both CoPCL polymers and CoPLLA polymers, the cells had the best response when the arm molecular weight was 4500 g/mol. Cell attachment and proliferation were promoted when the CoPCL polymer with arm molecular weight of 17200 g/mol was crystallized from 35 ^{o}C to 45 ^{o}C, however, they did show significant difference when the CoPLLA polymer with arm molecular weight of 17200 g/mol was crystallized from 110 ^{o}C to 145 ^{o}C. Cells on CoPCL polymers with arm molecular weights of 4500 g/mol and 17200 g/mol crystallized at 50 ^{o}C, as well as CoPLLA polymers with arm molecular weights of 17200 g/mol crystallized at 145 ^{o}C and 4500,

17200, and 28500 g/mol crystallized at 130 ^{o}C could feel the small ridges formed by the lamellae radiating and were strongly aligned along radius direction of spherulites.

I elucidate the mechanism of how honeycomb substrates with tunable pore diameters influenced MC3T3-E1 cell functions. For example, honeycomb-patterned PCL films with controllable diameters from 10 to 6.0 and 3.5 μm and photo-cured honeycomb-patterned PCLTA films with controllable diameters from 3.0 to 5.6 μm were fabricated, respectively. Compared with the flat control, the honeycomb films significantly promoted mouse MC3T3-E1 cell adhesion, spreading, proliferation, alkaline ALP activity, calcium content, and gene expression of bone-specific differentiation markers, ALP, COL I, OCN, and OPN, especially when the pores were smaller. The promotion originated from enhanced expression of integrin subunits of α_1, α_2, β_1. Honeycomb PCL films could also be stretched into groove-like structures. Compared with stretched flat films, stretched honeycomb films could elongate F-actin filaments of MC3T3-E1 cells significantly and the effect was more prominent when the pore diameter was smaller. These honeycomb PCL films can supply an efficient platform for bone tissue engineering applications. In addition to the films with micron scale pores, honeycomb-patterned photocrosslinked PCLTA films with pore diameters of 43, 93, 322, and 725 nm were also fabricated using monodisperse silica nanoparticles as templates to study the effect of honeycomb pores at submicron scale on MC3T3-E1 cell functions. Compared with the solid film of photocrosslinked PCLTA, these honeycomb films promoted MC3T3-E1cell adhesion, spreading, proliferation, and differentiation and this promotion was more prominent on the films with smaller pores. These honeycomb films with submicron pores serve as excellent platform for investigating cell-material

interactions and also promising materials for bone tissue engineering applications.

To investigate the effect of honeycomb-patterned microgrooves with various groove widths of ~5, ~15, and ~45 μm and depth of ~ 8 μm on MC3T3-E1 cell functions. Honeycomb-patterned microgrooves were fabricated using breath figure method. the alignment of cell filaments and nuclei, ALP activity and calcium content of cells, and expression of ALP, OCN, and OPN were promoted on honeycomb-patterned microgrooves compared with regular microgrooves without pores. Furthermore, the smaller groove width induced better results. However, the cell proliferation on honeycomb-patterned microgrooves was inhibited compared with honeycomb-patterned films without microgrooves.

Besides, the effect of surface energy on MC3T3-E1 cell functions was also investigated. Hot-compressed, edge-on, and flat-on PCL films were prepared via simple crystallization process and the surface morphology was observed by AFM scanning. Flat-on surface had higher surface free energy compared with hot-compressed and edge-on surface. MC3T3-E1 attachment, adhesion, spreading, proliferation, mineralization, and gene expression were evaluated systemtically. The flat-on samples with a much higher surface free energy could dramatically promote MC3T3-E1 cell adhesion and subsequent spreading, proliferation, mineralization, and expression of gene markers related to osteogenesis.

Microgrooved feature is another main topography which plays a great role in regulating MC3T3-E1 cell functions. To mimic the surface feature of banded spherulites generated from semi-crystalline polymers, $CaCO_3$ concentric microgrooves with groove widths of 5.0 and 10 μm were fabricated through modulating incubation temperature.

MC3T3-E1 cells cultured on flat and microgrooved substrates of $CaCO_3$ demonstrated that the microgrooves could dramatically enhance their adhesion, spreading, proliferation, and differentiation, especially on the narrower ones. In addition, cell nuclear distortion, either being aligned or stretched, and distribution were also studied and more aligned cell nuclei were trapped in 10-μm-wide $CaCO_3$ grooves because of their comparable dimensions. This study showed the great promise of using biomimetic $CaCO_3$ concentric microgrooved topography in bone tissue engineering applications. Besides, uniaxially and biaxially stretched PCL films were prepared. The S600 film showed an evident groove-like view along the stretching direction while the S1000 and BS films showed a fibril-like view. Stretching enhanced the substrate stiffness dramatically, especially for the S1000 film, but did not alter their thermal properties significantly. The S1000 and BS films, especially the S1000 one, promoted mouse MC3T3-E1 cell adhesion, attachment, proliferation, and mineralization, than the original film. The S600 film did not promote MC3T3-E1 cell attachment and proliferation but enhanced its differentiation because of the groove-like topography compared with the original film.

The effect of topographical features was studied not only on MC3T3-E1 cell behavior for bone regeneration, but also on nerve cells, such as PC12 and NPC cells for potential application in nerve regeneration. Banded and non-banded spherulitic surfaces of PCL and PHB prepared through isothermal crystallization as well as their hot-compressed samples demonstrated their distinct influence on rat PC12 cell behavior. PC12 cell attachment and proliferation were higher on the spherulites of PCL, especially on the banded spherulites, than on the hot-compressed sample. In contrast, the trend was opposite on the PHB samples, i.e., spherulites inhibited PC12 cell attachment and

proliferation. In addition, the spherulites of both PCL and PHB promoted NGF-induced neurite outgrowth of PC12 cells and the banded spherulites showed evident neurite guidance along the groove direction. Honeycomb-patterned CoPLLA17200 films with diameters of 1.0, 1.9, and 3.1 μm and honeycomb-patterned CoPCL17200 films with diameters of 2.5 and 5.2 μm were fabricated using breath-figure method. NPC attachment and proliferation were prohibited on honeycomb-patterned films, especially when pore diameters were larger due to the poorer cell-cell communication caused by cell separation on pores. However, NPC differentiation on 3.1-μm CoPLLA17200 films and 5.2-μm CoPCL17200 ones was promoted compared with flat ones, even though it was suppressed on 1.0-μm CoPLLA17200 films, 1.9-μm CoPLLA17200 films, and 2.5-μm CoPCL17200 films. Our study provided one potential mechanism in which the engineering devices for nerve regeneration applications can be achieved by tuning the pore size on honeycomb-patterned films.

VITA

Xiaohui Wu was born in Luan, Anhui, China. He earned his B.S. degree in Polymer Science and Engineering and M.S. degree in Materials Science and Engineering at the East China University of Science and Technology in 2007 and 2010, respectively. In the fall of 2010, he was admitted into the doctoral program and joined Prof. Shanfeng Wang's group in the Department of Materials Science and Engineering at the University of Tennessee, Knoxville. He received a Doctor of Philosophy Degree in Polymer Engineering from the University of Tennessee, Knoxville in August 2013.